A Two-dimensional Study of Green-Water Loading

A thesis submitted in partial fulfillment of the
requirements for the degree of Doktor Ingeniør
by

Marilena Greco

Trondheim, 2001

Department of Marine Hydrodynamics
Faculty of Marine Technology
Norwegian University of Science and Technology

URN:NBN:no-1305

Ai miei genitori, aura del mio cammino
(To my parents)

URN:NBN:no-1305

Acknowledgements

I wish to thank my supervisor Prof. Odd M. Faltinsen, for his special way to guide students, and me in particular, and his constant and patient presence and help. After a so careful education and training, it is only my fault if I still do not understand so many things.

An important role has been played by Dr. Maurizio Landrini. First, it is mainly because of him if I started my "adventure" in Norway. Second, luckily for me, he considered this as a cross he had to carry on. To his marvelous generosity and help, I can only reply with my deeper gratitude.

I also wish to warmly thank Prof. Dag Myrhaug, Dr. Carl T. Stansberg, and Tone M. Vestbøstad, for the many inspiring discussions and suggestions.

I thank Olaf F. Rognebakke for his generous help in the set-up of the two-dimensional water-on-deck experiments, and his incredible kindness and patience in making me familiar with this important aspect of the research.

I'm indebted with Norway for the chance this country gave me to meet so many friends. Among them, I like to mention my "Norwegian mum" Marianne Kjøl°as, who made me feel always at home from the very first day, and Lihua Wang and Gro Sagli Baarholm, for their wonderful moral support. These three women were so important to me that I'm sure the other friends will understand this special mention.

Many other people contributed in various way to my education and to this work. I thank infinitely all of them.

I thank Dr. Paolo Bulgarelli, the Research Director of INSEAN, *The Italian Ship Model Basin*, where I'm now permanently employed, because he encouraged me to undertake the Ph.D. studies, and for the freedom he gave in the final part of this activity.

This Dr.Ing Fellowship has been given by the Strong Point Centre on Hydroelasticity at NTNU / SINTEF in Trondheim, Norway.

URN:NBN:no-1305

Abstract

Large relative motions between the ship and the water may cause water shipping on the main deck. In this thesis, the fundamental features of water-on-deck phenomena are investigated, together with the "green" water loading on a deck house in the bow region. The studies are relevant for a stationary ship like a FPSO in head sea waves.

Potential flow theory is used to study numerically a nonlinear two-dimensional problem in a plane containing the ship's centerplane. The developed model is verified by various test cases, and validated by published as well as new experimental data.

The influence of wave parameters, ship motions and hull geometry is investigated. Relevance of three-dimensional effects is discussed.

Dedicated two-dimensional model tests have been performed, both to elucidate the fluid mechanics involved in the water shipping and to validate the numerical method. It is found that the water shipping starts in the form of a plunging wave hitting the deck. This could cause structural damages. Most often, the plunging is localized in the bow region and do not affect the main flow at a later stage. In a few cases, larger masses of water bluntly impacting with the deck have been observed. The latter is consistent with seldom observations reported in 3-D experiments, with large and steep waves plunging directly onto the deck. More often the water flow along the deck resembles the one subsequent to a dam breaking. Both types of events are investigated numerically. The impact pressures on a vertical wall in the bow area are measured and compare well with the boundary element method.

The reliability of a dam-breaking model and shallow-water approximation to study the propagation of water on the deck is examined. The former can only qualitatively describe the flow evolution. The latter can in principle be used but needs information from the exterior flow and, thus, the solution of the complete ship-wave interaction problem.

Water impacts with a deck house in the bow area are studied in details. Use of a similarity solution for a water wedge hitting a rigid wall at 90° is compared with the fully numerical solution. The method predicts correctly the first stages of the impact with a smaller computational effort. Influence of local flow conditions and wall slope on hydrodynamic loads is discussed. Importance of hydroelasticity is investigated in case of realistic structural parameters for the deck house. This shows a limited role of structural deformations in determining the maximum loads.

Nomenclature

General Rules

- Only the most used symbols are listed in the following sections
- Meaning of symbols is given at least when introduced in the thesis
- Sometimes the same symbol is used to indicate different things
- Vectors are represented by introducing a right arrow above the symbols

Subscripts

cav	Cavity
db	Dam breaking
imp	Impact
in	Initial
max	Maximum
shw	Shallow
sto	Stokes
ver	Vertical
wet	Wetted
wod	Water on deck

Roman Letters

A	Amplitude of heave motion
d_s	Horizontal distance of superstructure from the bow
D	Ship draft
E	Youngs modulus

EI	Beam bending stiffness
f	Freeboard
F_x	Horizontal force
$\vec{g}$	Gravitational acceleration
h	Height of water reservoir. Water depth
h_w	Water level along the deck
H	Incoming wave height
I	Beam cross-sectional area moment of inertia per unit width about neutral axis
k_θ	Spring constant
l_{cav}	Cavity length
L	Ship length
L_{beam}	Beam length
m	Beam structural mass per unit length and unit width
$\vec{n}$	normal unit vector
p	Pressure
p_a	Atmospheric pressure
$P_{\max}$	Maximum pressure
Q	Volume of shipped water
Q_0	Number characterizing amount of water of the incident waves, defined as water volume above the mean free surface over one wavelength
r	Radius
R	Maximum vertical run-up
R_j	J-th natural wetted-period to j-th natural dry-period ratio
t	Time
t_{imp}	Time of initial water impact
t_{wod}	Time when water on deck starts
t_{last}	Time of zero water flux onto the deck
T	Incoming wave period
$T_{j\text{dry}}$	J-th beam natural dry-period
$T_{j\text{wet}}$	J-th beam natural wetted-period
$\vec{u}$	Fluid velocity
u	Horizontal velocity component. Velocity magnitude
v	Vertical velocity component
V	Impact velocity
w	Beam deformation
x	Horizontal axis
x_{shw}	Distance from the bow from where shallow water theory is applicable
z	Vertical axis

Greek Letters

α	Stem angle. Superstructure inclination
β	Semi-angle of fluid wedge

Δ	Difference between two quantities
ζ_j	Amplitude of j-th beam eigenmode
η	Free surface elevation
η_{sto}	Stokes wave elevation
λ	Incoming wavelength
$\sigma_{\max}$	Maximum stress
φ	Velocity potential
φ_{sto}	Stokes wave velocity potential
ρ	Water density
ψ_j	J-th beam eigenmode
τ	Non-dimensional time
ω	Wave frequency (rad/s)

Contents

Acknowledgements i

Abstract iii

Nomenclature v

1 Introduction 1
- 1.1 Green-Water Loads . . . 1
  - 1.1.1 Framework and Scope of the Present Analysis . . . 2
  - 1.1.2 Historical Developments . . . 5
- 1.2 Present Work . . . 7
  - 1.2.1 Structure of the Thesis . . . 7
  - 1.2.2 Major Findings . . . 8

2 Mathematical Model 11
- 2.1 General Assumptions . . . 11
- 2.2 Statement of the Mathematical Problem . . . 12
- 2.3 Modeling of the Hydroelastic Problem . . . 15

3 Numerical Solution 19
- 3.1 Solution Algorithm . . . 19
  - 3.1.1 Kinetic Problem . . . 20
  - 3.1.2 Evaluation of $\partial\varphi/\partial t$ . . . 22
  - 3.1.3 Time Integration . . . 23
- 3.2 Generation of Incoming Waves . . . 24
  - 3.2.1 Use of the Analytical Incident-Wave Solution . . . 25
  - 3.2.2 Wavemaker . . . 26
- 3.3 Modeling of the Flow Field during Water Shipping . . . 27
- 3.4 Absorbing Boundary Conditions . . . 28

4 Water on Deck 31
- 4.1 General Remarks . . . 31
- 4.2 Preliminary Studies and Validation . . . 32
- 4.3 Influence of Main Geometric Parameters . . . 35

4.4 Influence of Body Motions 41
4.5 Occurrence of Waves Plunging on the Deck 43

5 Dam Breaking and Water Impact **47**
5.1 Dam Breaking and Water Impact 47
5.2 Parameters Influencing the Impact 53
5.2.1 Angle of the Incoming Water Flow and Impact Velocity 53
5.2.2 Slope of the Wall 56
5.2.3 Fluid-Structure Interaction 57

6 Approximated Methods for the Water Flow along the Deck **63**
6.1 Shallow-Water Approximation 63
6.2 Dam-Breaking Model 65

7 Two-Dimensional Water-on-Deck Experiments **67**
7.1 Choice of Relevant Parameters 67
7.2 Description of the Experimental Set-up 69
7.2.1 Equipment 69
7.3 Reliability and Repeatability of the Measurements 72
7.4 Error Sources in the Measurements 77
7.4.1 Flume 77
7.4.2 Instrumentation 79
7.4.3 Model 82
7.4.4 Human Errors 84

8 Water-on-Deck Experiments: Analysis **85**
8.1 General Remarks 85
8.2 Water shipping: First Stages 87
8.2.1 General Description 87
8.2.2 Vortex Shedding at the Edge of the Deck 88
8.2.3 Wave Plunging Evolution 89
8.2.4 Water Impact with the Deck 93
8.3 Water Shipping: Later Stages 98
8.3.1 General Description 98
8.3.2 Wave Parameter Analysis 99
8.4 Influence of the Stem Angle 101
8.5 Impact with a Vertical Wall 105
8.5.1 Water Evolution 105
8.5.2 Pressure along the Vertical Wall 108

9 Summary and Future Perspectives **111**
9.1 Future Perspectives 114

References **117**

A Details of the Numerical Method **123**
A.1 Tangential Velocity along the Domain Boundary 123
A.2 Velocity Potential and Velocity Components 124
A.3 Numerical Features of the Method 125
A.4 Example of Convergence Test 126

B Boundary Value Problem for ψ **127**

C Verification and Validation of the Method in Shallow-Water Conditions **129**
C.1 Case 1: Collapse of a Semi-Circular Water Column 129
C.2 Case 2: Collapse of a Rectangular Water Column 132
C.3 Case 3: Dam Breaking with an Semi-Infinite Water Reservoir 134
C.4 Case 4: Run-up of Long Waves on a Flat Wall 136

D Liquid Wedge-Flat Wall Impact: Similarity Solution **139**

E Simplified Method for Water-Wedge Impacts **143**

F Simplified Problem to Evaluate the Added Masses **147**

G Wavemaker: Experimental Time Histories **149**

Chapter 1

Introduction

1.1 Green-Water Loads

In rough-sea conditions, both moored and/or dynamically positioned vessels and ships in transit can suffer shipping of water on the deck. This phenomenon can occur everywhere along the hull and it is a consequence of freeboard magnitude and large relative motions between the ship and the water. The picture in figure 1.1 shows an incident occurred to the tanker Golar Siri in the

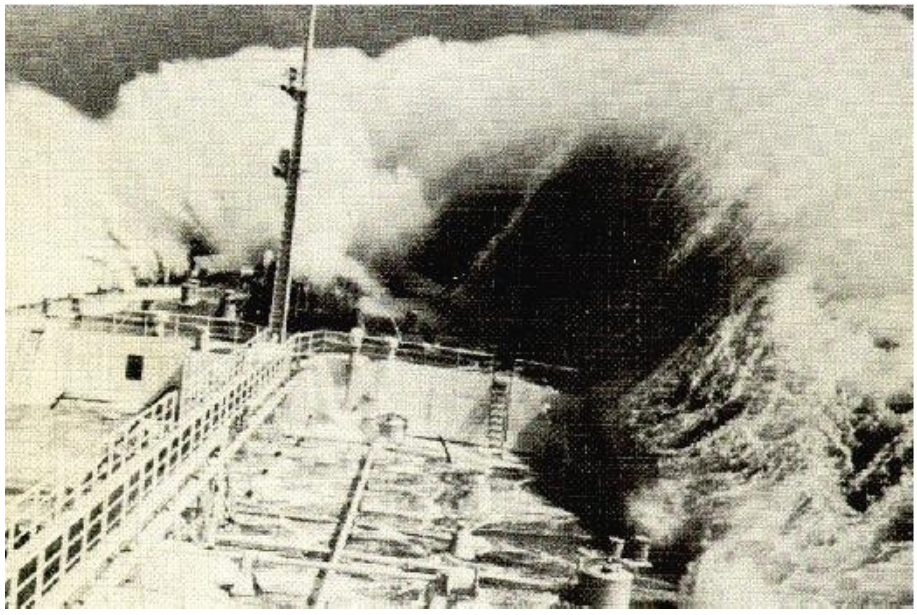

Figure 1.1 The tanker Golar Siri meets the hurricane "Judy", 1963 (photo by Per Meidel).

h urricane" Judy" in 1963. The water shipping, from the captain's view, appears dramatic: the water enters the deck non-uniformly along the fore part of the ship, and the worst conditions are concentrated at the front of the bow. Here, the water surface is very steep, and in the form

of a wall of water high relative to the ship dimensions. The consequence is a compact mass of water flowing over the deck ("green" water, "heavy" wetness). Head-sea waves represent a common sea condition in bad weather. This implies that the more severe situations are normally localized in the bow region of the ship, as in the shown incident. When a sufficient amount of water comes onto the deck, a flow with increasing velocity develops, possibly hitting obstacles on its way. Water impacting against the deck and superstructures may cause both high pressures in confined regions and contribute to global ship loads.

Several water-on-deck casualties have also been documented for smaller ships, such as fishing vessels (*cf.* Storch 1978). A main concern is roll stability. During water on deck, loads distribution along the vessel changes. Large lateral motions can follow and be responsible of ship capsizing. The ship instability is mainly caused by a critical reduction of $\overline{\mathrm{GM}}$ due to the mass of shipped water and consequent free surface area. However, water sloshing on the deck can also matter.

In this context, water on deck is critical for loaded vessels due to the smaller mean ship freeboard. An increase of forward ship velocity can either be positive or negative for the vessel safety, depending on the ship conditions. For instance, in Grochowalski (1989) it was observed that for fishing vessels the increase of forward speed supports the ship capsizing in unloaded conditions. Conversely, a greater speed appeared beneficial for a loaded vessel, and in particular counteracted the occurrence of water shipping.

Forward speed is a relevant factor also for larger vessels, influencing mean sinkage and trim and ship motions. Moreover, the steady wave pattern decreases the freeboard in the bow and increases the probability of deck wetness from the ship sides. Higher forward velocities can more easily lead to "light" wetness ("white" water). The latter means a large amount of spray during the water shipping. This can be a danger for the visibility on board and consequently affect deck operations.

1.1.1 Framework and Scope of the Present Analysis

The work reported in this thesis concerns water-on-deck phenomena for Floating Production Storage and Offloading (FPSO) units. These represent a relatively new concept of oil platforms, where a floating unit (see left plot in figure 1.2) is used for production, storage and offloading operations. This concept has been adopted in different parts of the world (see right map in figure 1.2). In practice, a FPSO is a ship. It is less expensive than traditional platforms. FPSOs are supposed to be weather-vaning, *i.e.* that head sea is the most-occurring weather condition. Dynamic positioning may be used to assist the station-keeping. Clearly, the seakeeping properties of a stationary ship are quite different from ships with forward speed. In this context, many factors have to be accounted for, such as wave-frequency motions, station-keeping and mean and slow drift motions induced by current, wind and second order wave-body interactions. Examples of important sea loads to consider in a structural analysis are bow stem slamming, green water loads, and global induced bending moments and shear forces.

Water on deck is now considered an important risk for this type of ship, and started to be a factor in defining operational strategies and ship design. Green-water accidents documented both deck wetnesses in the bow region and from the ship sides, with damages for deck house and equipments. The location of the deck house can vary .FPSOs working in the North Sea usually

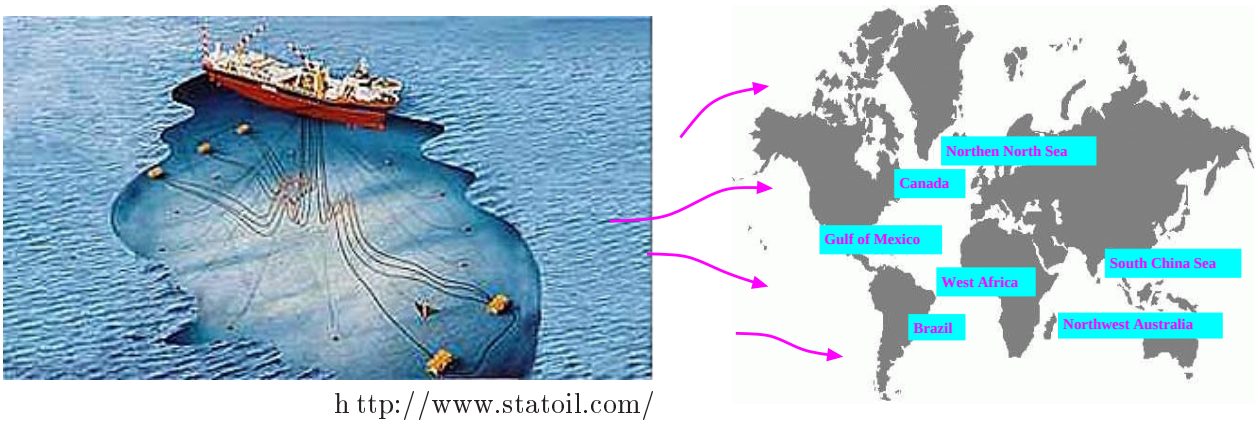

http://www.statoil.com/

Figure 1.2 Left: concept of a FPSO unit. Right: map of the FPSO operations.

have the deck house in the bow region. FPSOs operating in South America have the deck house near the stern.

The occurred water-on-deck casualties in North Sea motivated experimental investigations and suggested some modifications of design rules and operational restrictions. An overview of the most important accidents and of the subsequent requirements of the Norwegian Petroleum Directorate are given by Ersdal and Kvitrud (2000).

On the above ground, the present work is focused on green-water phenomena occurring in the bow region. These do not cover all the possible wetness features, but the most severe events may

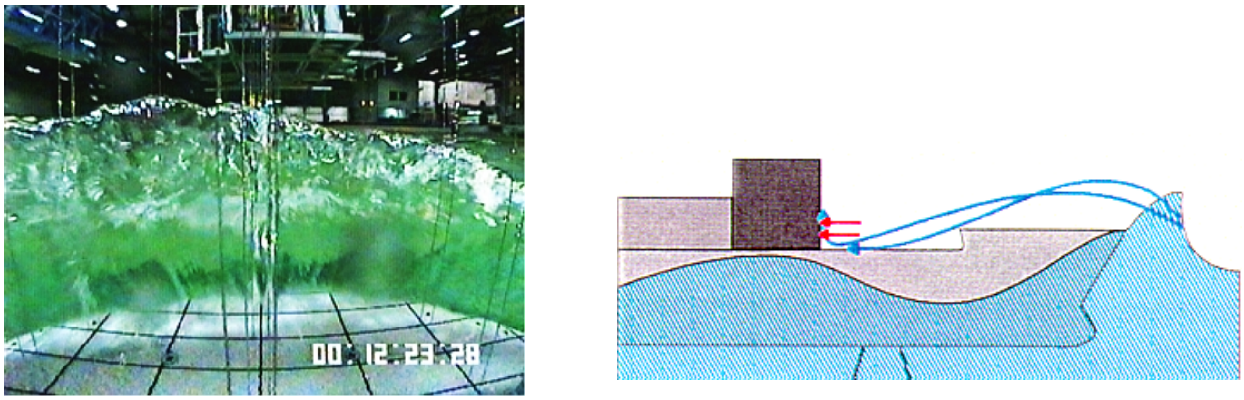

Figure 1.3 Dam breaking-type water on deck. Left: captain view from 3-D experiments (Marintek, 2000). Right: sketch of the phenomenon from side view.

occur in head-sea conditions. In this case, after the water exceeds the freeboard, two scenarios can take place:

(i) More commonly, the water flows along the deck and resembles the flow generated after the breaking of a dam (see figure 1.3, MARINTEK 2000).

(ii) Occasionally, large breaking waves plunge directly on the deck house (see figure 1.4, MARINTEK 2000). This event has been detected in recent model experiments (MARINTEK 2000) and appears typically more severe and dangerous than the type (i).

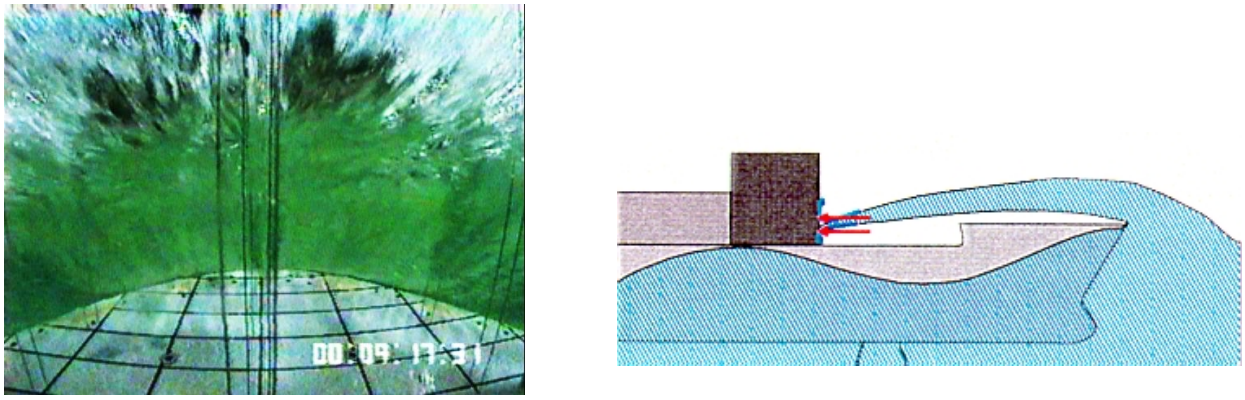

Figure 1.4 Plunging wave-type water on deck. Left: captain view from 3-D experiments (Marintek, 2000). Right: sketch of the phenomenon from side view.

As we will see later, also type (i) starts in the form of a plunging wave hitting the deck, near the bow. However, this initial phase is localized in time and space relative to the scale of the water shipping itself.

Many physical aspects determine and affect the water-on-deck phenomenon. Wave-ship interactions (*cf.* figure 1.5.A) modify significantly the wave pattern with respect to that of the incident waves. This is related both to local effects and to wave reflection, which in rough sea

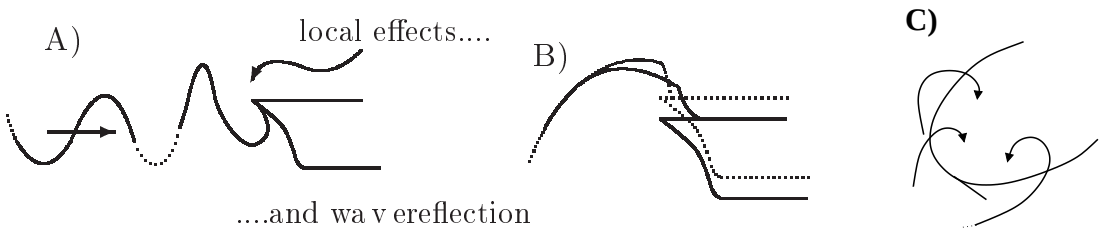

Figure 1.5 Some physical aspects involved in the water-on-deck phenomenon: wave-body interaction (A), body motions (B), three-dimensional effects (C).

are highly nonlinear phenomena. Ship motions (figure 1.5.B) can either enhance or prevent the deck-wetness occurrence. Three-dimensional effects are relevant (figure 1.5.C) though less than for cases with forward speed. These factors make it difficult to clearly identify the design parameters relevant for occurrence and severity of water on deck, and for its consequences on the ship.

Obviously the ship freeboard is important. However the effect of other parameters characterizing the ship-bow geometry is far from being clarified. Sometimes, it is not even clear whether they enhance or reduce the deck wetness. As an example, O'Dea and Walden's (1984) experiments in regular waves and with forward speed showed that larger bow flare angles reduce the deck wetness, while Lloyd *et al.* (1985) experiments in irregular waves and with forward speed observed more frequent freeboard exceedances and deck wetness with more heavily flared bows. Newton's (1960) experiments in regular waves and with forward speed documented that increase of flare, obtained by introducing a knuckle without changing the actual freeboard, is equally effective, as increasing the latter, in counteracting water shipping. The bow bulb is usu-

ally considered non relevant for the wave induced body motions. However a bulb may increase the fluid velocities in the bow region and steepen the local waves. This would support deck wetness. On this ground, investigations of fundamental type are requested to overcome this lack of knowledge and to develop numerical tools of practical use.

Finally, the present analysis deals mainly with local loads in the deck area. However, global effects in terms of, for instance, midship bending moment should be investigated. This may not be dominant (*cf.* Wang *et al.* 1998). In this context, the relative phasing between green-water loads and the maximum values of the bending moment is crucial.

1.1.2 Historical Developments

Extensive experimental studies of deck wetness have been carried out in the past. Some of the most important ones will be briefly described.

Ships with forward speed. Regular head-sea waves have been used by Newton (1960) to study the influence of freeboard and flare on deck wetness. A basic model geometry has been varied to identify the relative role of each parameter. Same environmental conditions characterized the model tests by O'Dea and Walden (1984). Here a model of a frigate has been altered in the above-water bow shape. Then, absolute and relative motion near the bow and deck wetness were measured. An analysis of these quantities as a function of freeboard, flare and knuckles was carried out. Lloyd *et al.* (1985) performed experiments in irregular sea states. A frigate model was systematically varied to investigate the influence of freeboard, flare, stem overhang and stem sharpness. The results were presented in terms of bow wave height, frequency of freeboard exceedance, impact frequency and swell-up coefficient.

FPSO units. Buchner (1995) reported head-sea regular wave model tests. Relation between relative ship motions and deck wetness was investigated, as well as behavior of the green water along the deck and water-impact phenomena with superstructures.

All mentioned studies are relevant for understanding the phenomenon. However, they are not conclusive and give in some cases contradictory results in terms of parameter influence. Alternative approximated analyses have also been developed and used to predict green-water loading. In this context experimental observations played a fundamental role.

The conventional way of estimating water-on-deck occurrence in a short-term sea state is to combine a probabilistic analysis (*cf.* Ochi 1964) with a linear hydrodynamic analysis. It implies that the above-water hull form is not included in the hydrodynamic analysis. The important hydrodynamic variable is the linear relative vertical motion between the ship and the water. Often only the incident wave and not the local wave accounting for the presence of the ship is used in this context. An effective freeboard is sometimes introduced for a ship with forward speed. This accounts empirically for the steady wave profile and the sinkage of the ship.

In the previous stochastic analysis, the hydrodynamic phenomenon is treated as a black-box. For a real improvement of the design strategies, the stochastic analysis has to be combined with a hydrodynamic analysis. In the framework of the potential flow theory, a fully-nonlinear analysis was carried out by Maruo and Song (1994). There, the water-shipping phenomenon of high-speed vessels was analyzed by using $2\frac{1}{2}$-D Slender-Body Theory. This method may also have relevance for slender-ship bows at moderate forward speed. Buchner and Cozijn (1997) analyzed the bow deck wetness for moored ships, assuming a two-dimensional problem in the

longitudinal ship direction. They presented both numerical simulations and experiments for a simple prototype problem, but no comparisons between simulations and measurements have been shown.

In case of dam breaking-type water on deck, some authors studied the motion of the shipped water along the deck by using shallow-water models. The reliability of this type of approach is dependent on how the initial conditions as well as the inflow boundary conditions are determined. A sensitivity analysis in terms of the inflow velocities was carried out in Mizogushi (1989) by comparing numerical results and experimental data for the S-175 container ship. The shallow-water equations have been solved for the three-dimensional problem, using experimental results for the water height at the inflow boundary. In the simulation, the ship motion is not taken into account. The author concluded that the flow interactions (between flow on the deck and flow outside the ship) and the efflux occurring between the deck area and the outer region represent important items in the water-on-deck phenomena.

Wan and Wu (1999) studied the water on deck for a moored ship in shallow water due to solitary waves. Three-dimensional effects have been neglected and the problem was solved with the Volume-of-Fluid method (VOF). The adopted solver was, in principle, a Navier-Stokes solver but apparently the used resolution was not enough to capture viscous effects at the body boundary and at the free surface. Results have been presented in terms of velocity field, wave profile and pressure evolution along the deck house. The authors stressed some numerical difficulties in evaluating the latter quantity. Two main issues have been pointed out: (i) importance of small time steps in the simulation to properly capture rapid pressure changes during the impact, and (ii) limitations of the used first-order pressure differential scheme. No discussion was presented about the importance of the boundary layer developing near the deck during the water shipping. In particular in terms of reduction of the water front velocity relative to the inviscid case. The same method was applied by Fekken *et al.* (1999) for studying the three-dimensional flow of water along the deck. This was made by considering an equivalent dam-breaking problem. Comparisons with 3-D experiments of water on deck on a FPSO were shown for the water front contours and for the pressure evolution along superstructures with different shapes (flat vertical wall, wedged vertical wall, cylindrical vertical wall). Numerical and experimental water fronts showed clear differences though with a certain global similarity. Numerical and experimental evolutions of the pressure and total loads were in reasonable agreement, both in magnitude and time duration, in the case of flat vertical superstructure. The agreement in magnitude was not satisfactory for the other studied geometries.

Specific studies of the later water flows along the deck can explain many phenomena and give some important suggestion for an improved ship stability. This is relevant for smaller vessels. Much research effort has been spent for this topic. Dillingham (1981) analyzed the phenomenon of interest by solving numerically the two-dimensional shallow-water flow with the Glimm's method (Glimm 1965), that can efficiently capture jump phenomena (discontinuity of some variable of interest). According to the author, this approach should be suitable for this kind of physical problems where the flow can be characterized by quite steep waves moving back and forth between the lateral barriers. In Dillingham (1981) beam-sea conditions were assumed as incident wave system and the linear strip theory by Salvesen *et al.* (1970) was used to evaluate the hydrodynamic coefficients. The vessel was considered as a two-degrees-of-freedom system in sway and roll and the rigid-body motions were coupled with the water sloshing on the

deck. The flow of water onto or off the deck was evaluated in a simplified way, by comparing the instantaneous body configuration and the undisturbed incoming waves. Glimm's method was extended to nonlinear three-dimensional water flows onto the deck by Pantazopoulos (1987) and by Dillingham and Falzarano (1988). In both cases, coupling of the water sloshing with the body motions, and on deck-off deck flows of water, are not accounted for. A qualitative study of the water-on-deck effect on response and stability of the vessel is carried out in Pantazopoulos (1987) by using simple energy and stability principles. Some numerical shortcomings of the Glimm's method motivated the development of more robust and accurate methodologies (see *e.g.* Huang and Hsiung 1996).

1.2 Present Work

Wave-body interaction, shipping, subsequent flowing of water onto the deck and impact with superstructures, are strongly coupled stages of the problem. Localized structural damages as well as excitation of global response of the ship may occur. The importance of hydroelasticity during water impacts with superstructures needs to be assessed. The main objective of present work is to gain a better understanding of this complicated picture and give answers to some of the related question marks.

Our investigation is centered on the deck wetness at the bow region of a FPSO in head-sea. Therefore, forward-speed effects are not investigated. The phenomenon is further idealized by considering the two-dimensional flow in the longitudinal plane of the ship. The resulting problem is studied both numerically and experimentally. In the former case, a fully-nonlinear unsteady problem is solved by assuming inviscid fluid dynamics.

1.2.1 Structure of the Thesis

The prototype two-dimensional problem, representative of a FPSO in head-sea conditions, is stated in the next chapter, while the numerical procedure is given and discussed in chapter 3. The obtained formulation is applied to study the water-on-deck phenomenon due to regular incoming waves. The influence of main wave and ship parameters on the occurrence and characteristics of water shipping is analyzed in chapter 4.

Water impact with superstructures along the deck is then considered by using a dam breaking-flow as initial condition for the shipped water flow. The resulting problem is numerically solved and discussed. The obtained results are compared with analytical solutions and experimental data. A parametric analysis for the impact phenomenon is also carried out in terms of local water details at the impact instant, wall slope and hydroelastic behavior of the structure.

After numerical solutions of the "exact" problem have been obtained, in chapter 6 simplified methods for the water flow along the deck are discussed and judged. In particular, the shallow-water theory and the dam-breaking model are considered, and their advantages and shortcomings are pointed out.

Two-dimensional water-on-deck experiments performed at the Dept. of Marine Hydrodynamics of NTNU are described in chapter 7. The experimental set-up is discussed, and possible error

sources in the tests are indicated.

The main physical aspects of the initial stages of water shipping and its late evolution are discussed in chapter 8, where experimental data and numerical results are used in a combined way to gain a deeper understanding of the basic physics. In the same chapter, a simplified water-on-deck analysis in terms of incoming wave parameters and ship-stem overhang is also carried out.

Significant information gained from this study is summarized in chapter 9. Some suggestions for future work are also outlined.

1.2.2 Major Findings

As stated, the present analysis is limited to the shipping of water in the bow region of a FPSO in head-sea conditions, and without forward-speed. A simplified two-dimensional problem is considered and investigated by numerics and a dedicated experimental activity. The major findings of present study are summarized as follows.

Global features of water shipping Occurrence of plunging of large waves on the deck (*cf.* figure 1.4) seems to be related to the interaction of steep waves already prone to break, more than to the wave-body interaction by itself. However, the influence of severe ship motions can not be excluded.

From our model experiments, we discovered that the dam breaking-type water on deck starts also as a plunging wave hitting the deck. This phase is rather spatially confined around the bow and takes place in a short time relative to the whole water-shipping event, and may cause local damages in the deck. To our knowledge, this phenomenon has not been reported before.

Deck wetness analysis. The effect of the main parameters causing and affecting the shipping of water are analyzed numerically. The steepness of incident waves results to be the main wave parameter. Stem overhang reduces the relative amount of shipped water, though less efficiently than the freeboard. A trim angle (a quasi-steady pitch angle) has a small effect on the amount of shipped water. The influence of normal type of bulb is limited.

Impact with the deck house. The impact of shipped water against a deck house in the bow area is investigated by quasi-two dimensional experiments and by numerics. For dam breaking-type water on deck, the numerical wave front has a wedge form. This is also observed in the experiments, with the exception of the rather small tip region, where the free surface meets the deck and the front is rounded because of viscous and surface tension effects. This small detail is not important for structural loads, as confirmed by the agreement between numerics and experiments. Also, in the first stages of the impact, gravity does not matter.

In particular, it is shown that the water front velocity V and the angle β between the free surface and the deck at the impact instant, characterizing the wedge-shaped front, are the main water-impact parameters. For $\beta <\sim 40°$, V represents the dominant parameter.

The stem overhang reduces the water level along the deck, but increases the involved flow velocities. Due to this, it is hard to find a conclusive statement about its positive or negative effects on water impacts with a superstructure.

A trim angle (a quasi-steady pitch angle) has a small influence on the water impact with the deck house. A reduced inclination of the impacted wall reduces the loads during the run-up of water along the structure. When an angle $\alpha = 40°$ (relative to the vertical direction) is

considered, the maximum normal force becomes $\sim 50\%$ of the maximum normal force in the case of vertical wall. In the analyzed range of angles, the force reduction seems almost linear with α.

It is shown that the effect of hydroelasticity may in general be neglected.

Simplified methods for the water flows on the deck. A theoretical dam-breaking model gives only a qualitative description of the flow features, and should be considered only in a preliminary study. In fact, the actual wave conditions determining the water shipping are not properly described. Therefore, ambiguities exist when choosing the height of the "equivalent" reservoir of water and the time instant when the dam breaks. Moreover, in principle shallow-water approximations are appropriate and accurate in certain domains along the deck. However, in practice, they would need data that are unavailable without solving the complete ship-wave interaction problem.

As an example, among the simplified approaches, Ritter's model (*cf.* Ritter 1892) would lead to too conservative estimates of impact loads on a deck house in the bow area. For the dam-breaking problem, with an initial reservoir of height h, this solution would predict a constant water front velocity $V = 2\sqrt{gh}$, g being the gravity acceleration. Actually, the "exact" dam-breaking solution shows an initially zero velocity, increasing as the water front evolves. The evolution of the ratio $V/2\sqrt{gh}$ is given in figure 1.6 as a function of the distance x covered by the water, and is smaller than one for $x \leq 3\ h$. Thus the shallow-water solution over-estimates

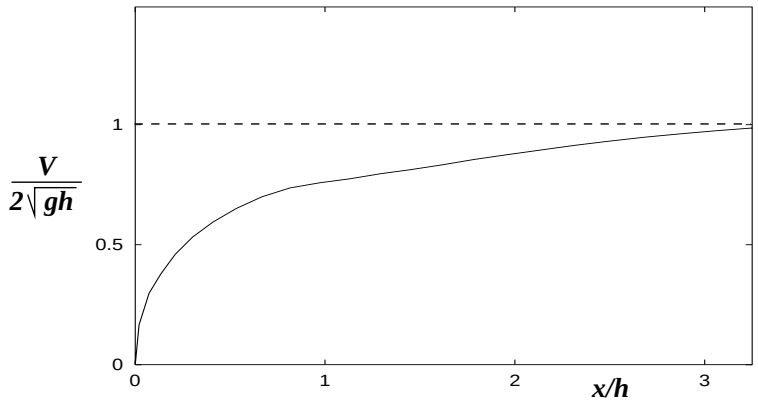

Figure 1.6 Evolution of the water-front velocity V along the deck due to the breaking of a dam with height h. g is the gravity acceleration. The solid line shows the numerical solution of the "exact" problem. The value $V/2\sqrt{gh} = 1$ results from the approximate Ritter's shallow-water method.

the impact velocity if the superstructure is located at $x \leq 3\ h$ from the dam. Since h is a measure of the freeboard exceedance during the water shipping, and it is large for significant water-on-deck events, $x \leq 3\ h$ is a reasonable condition in practical cases.

The impact phenomenon is not handled by the shallow water approximation and requires the combination with suitable local solutions, such as a similarity solution. Actually, the water front predicted by the shallow water solution is not wedge shaped, but, neglecting the detail of the tip, the wave profile at the front is well enveloped by a wedge, and a comparison is still possible. In general both V and β must be considered to estimate, for instance, the maximum pressure along the wall. However, if β is smaller than $\sim 40°$, which occurs for $x > \sim 0.65\ h$ in the "exact" problem, V is the main parameter and the squared ratio $(V/2\sqrt{gh})^2$ can be interpreted as ratio

between "exact" and shallow-water maximum pressures.

Chapter 2

Mathematical Model

In the following, the wave-ship interaction in the bow region of a FPSO is idealized in the form of a two-dimensional problem. The general physical assumptions are discussed and the corresponding mathematical problem is stated. The model is described in detail in case of a rigid body. The fluid-structure coupling to account for hydroelastic effects during impact is discussed in the final section.

2.1 General Assumptions

As already discussed, the present analysis is limited to the case of a ship in head-sea conditions with zero forward speed. This is the rather common case of a FPSO unit, which is typically characterized by a blunt bow.

In this framework, the problem is idealized by considering the two-dimensional flow in the longitudinal plane of the ship. In reality, the neglected three-dimensional effects are relevant, though less than for the case with non-zero forward speed. In the latter situation, additional sources of three-dimensionality come from the interaction with the steady and unsteady wave patterns. In fact, when the ship advances the freeboard along the vessel is more non-uniform because of the steady wavepattern and it is generally reduced with respect to the zeroforward speed case, at least in the bow region. The forward speed will also influence mean sinkage and trim of the ship. Finally, the run-up at the bow of ambient waves is generally larger in case of an advancing body.
In spite of the above limitations, a two-dimensional analysis gives important insights of the water-on-deck phenomenon, and useful information about the role of the many parameters involved.

In practical cases, the Reynolds number of the flow is high. Therefore, for unseparated flows, the vorticity is concentrated in the thin boundary layer at thebody boundary, and a potential-flow model can be used to describe quantitatively the main features of the flow field, including the wave evolution around the hull and the induced pressure distribution. Boundary layer effects may be relevant also in case of thin fluid layers on solid boundaries, as in case of the water front

propagating on the deck. Moreover, the edge of the ship deck may induce separation and large vortex shedding. In present analysis, such phenomena are not modeled *a priori*.
In general, surface-tension effects are negligible because of the relatively large spatial scales involved in practical cases. However, high curvature of the free surface may exist at the body-free surface intersection and in plunging waves. There surface tension may be relevant.
Finally, unless otherwise stated, structural elastic deformations are not considered and the body is assumed perfectly rigid.

With these premises, a potential flow model is adopted and the "heavy" water-on-deck is analyzed by fully retaining the nonlinearities associated with body and free-surface motions. This physical model is applied to solve several two-dimensional prototype problems, related to the topic of our interest. The objectives are (i) to verify and validate the method by comparisons with published analytical, numerical and experimental results, and (ii) to gain a physical and quantitative understanding of the water-on-deck phenomenon and of the role of the many parameters affecting it.
In the next section, the mathematical formulation is described in a general way. Problem-dependent variables and treatments are detailed in the sections where specific cases are studied.

2.2 Statement of the Mathematical Problem

A two-dimensional problem (*cf.* figure 2.1) is studied, where the fluid domain, $\Omega(t)$, is bounded by the free surface $\partial\Omega_{FS}$, the wetted surface of a rigid body $\partial\Omega_{BO}$, and a control surface $\partial\Omega_{\infty}$.

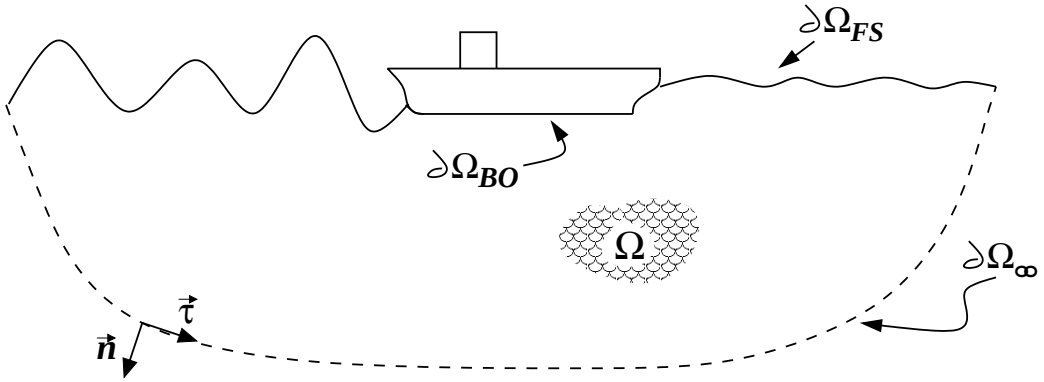

Figure 2.1 Sketch of the two-dimensional problem of interest.

In general, the boundary $\partial\Omega$ varies with time because of

- free-surface motion
- pressure distribution along $\partial\Omega_{FS}$
- rigid-body motions at $\partial\Omega_{BO}$
- non-zero or prescribed fluid motion at portions of the control surface $\partial\Omega_{\infty}$

These disturbances propagate through the fluid, in particular causing loads on the body and motions, if the body is not restrained to move.

We assume the fluid to be incompressible, inviscid, and in irrotational motion. A potential-flow model is therefore applicable. The velocity potential $\varphi(\vec{P},t)$, defined as $\vec{u}=\nabla\varphi$ where $\vec{u}$ is the fluid velocity, satisfies the Laplace equation

$$\nabla^2\varphi \;=\; 0 \tag{2.1}$$

everywhere in the fluid domain.

Kinematic condition at boundaries Fluid particles cannot cross the portion $\partial\Omega-\partial\Omega_\infty$ of the domain boundary, therefore

$$\frac{\partial\varphi}{\partial n}=\vec{V}_{(\partial\Omega-\partial\Omega_\infty)}\cdot\vec{n} \qquad\qquad \forall t,\ \forall\vec{P}\in\partial\Omega-\partial\Omega_\infty\ , \tag{2.2}$$

where $\vec{n}$ is the unit normal vector to the surface assumed pointing out of the fluid domain. In equation (2.2) $\vec{V}_{(\partial\Omega-\partial\Omega_\infty)}$ is the velocity associated with a geometric point along the surface, and a separate discussion is needed for the body boundary and for the free surface.

Body boundary The velocity on the instantaneous wetted surface of the body is

$$\vec{V}_P=\vec{V}_G+\vec{\omega}\times\vec{GP}\ . \tag{2.3}$$

Here G is the center of mass of the structure, $\vec{V}_G$ is the translatory velocity of G and $\vec{\omega}$ is the angular velocity of the rigid body. In case of captive body motions, $\vec{V}_P$ is *a priori* known. In case of a floating structure, $\vec{V}_P$ has to be determined by solving the equations of body motion, coupled with the fluid dynamic problem through the pressure

$$p\;=\;p_e\;-\rho\left(\frac{\partial\varphi}{\partial t}+\frac{1}{2}\mid\nabla\varphi\mid^2+gz\right) \tag{2.4}$$

acting along the wetted surface $\partial\Omega_{BO}$[1]. More precisely, the pressure acting along $\partial\Omega_{BO}$ gives the hydrodynamic force $\vec{F}$ and moment $\vec{M}_G$ about G

$$\begin{aligned}\vec{F}\;&=\;\int_{\partial\Omega_{BO}}p\,\vec{n}\,\mathrm{d}\ell\\ \vec{M}_G\;&=\;\int_{\partial\Omega_{BO}}p\,\vec{GP}\;\times\;\vec{n}\mathrm{d}\ell\end{aligned} \tag{2.5}$$

which depend on the body position, on the rigid body velocity and acceleration and are in general a function of the previous time history of the fluid motion. The hydrodynamic loads enter explicitly into the equations of body motion which therefore have to be solved simultaneously with the fluid dynamic problem. In practice, we may have to account also for viscous loads due to current, wind and viscous damping of the body motions. Mooring and/or thruster forces have to be considered in a station-keeping analysis.

[1] In equation (2.4) p_e is the external pressure, ρ is the mass density of the fluid, g means the gravity acceleration, $z=0$ corresponds to the mean free surface and z is a vertical coordinate positive upwards.

Conditions at the free surface The free surface configuration, $\partial\Omega_{FS}$, is in general unknown and the kinematic condition given above has to be complemented by a dynamic condition. Upon neglecting surface tension effects, the free-surface dynamic condition enforces the pressure to be continuous across $\partial\Omega_{FS}$:

$$p = p_e(\vec{P}, t) \qquad \forall t,\ \forall \vec{P} \in \partial\Omega_{FS} \ . \tag{2.6}$$

For the cases of interest p_e coincides with the atmospheric pressure, p_a, which is set equal to zero. Through the Bernoulli equation (2.4) and by using a Lagrangian description (the motion of the fluid particles is followed), we can write the free-surface conditions as

$$\begin{cases} \dfrac{D\vec{P}}{Dt} = \nabla\varphi \\ \dfrac{D\varphi}{Dt} = \dfrac{1}{2}\left|\nabla\varphi\right|^2 - g\,\eta - \dfrac{1}{\rho}p_e \end{cases} \qquad \forall t,\ \forall \vec{P} \in \partial\Omega_{FS} \ , \tag{2.7}$$

where η is the wave elevation. Equations (2.7) are well known and simply state that the free surface is made by fluid particles moving with the fluid velocity $\nabla\varphi$ and carrying a value of the potential φ which evolves according to the second equation. Consistently, $D/Dt = \partial/\partial t + \nabla\varphi\cdot\nabla$ is the standard total, or *material*, derivative. Finally, it is worth to mention that the first equation of (2.7) is consistent with the kinematic condition (2.2).

Conditions at control surfaces The geometry and location of the control surface $\partial\Omega_\infty$ are *a priori* known, and for the problems of interest are time independent. In the case of a ship in a region of water with depth h this surface can be made by two vertical barriers, upstream and downstream the body, and by the portion of the bottom between them. Along the bottom the velocity potential is unknown, while its normal derivative is zero due to the impermeability of the surface.

On the lateral portions both φ and $\partial\varphi/\partial n$ would be in general unknown. However, simplified assumptions can be made if these surfaces are chosen far enough from the body. In fact, let us assume the two-dimensional initial value problem is characterized by an impulsive pressure acting on the free surface. In this case, for a finite time t asymptotically zero motion is felt at great distance from the initial disturbance (Mei 1983). This implies that the velocity potential is asymptotically zero as the distance from the disturbance goes to infinity. This argument can be applied to the present problem since the body disturbance may be described as a distributed pressure disturbance along the free surface. Actually, the disturbances expected in the present case are weaker than in the impulsive problem referred to above. Therefore, a faster decaying asymptotic behavior of the velocity potential is expected.

In a finite interval of time, the leading disturbances due to the body remain spatially confined, and become practically negligible beyond a suitable large horizontal distance, say d, from the body. This implies a small error when setting them equal to zero from d on. Clearly, the distance d increases with time as radiated or reflected waves propagate outwards, and, in numerical computations, one should use a large domain compared with the considered time scale for the introduced errors to be small. This could represent a severe difficulty in terms of computational costs. To limit the horizontal extension of the fluid domain the free-surface conditions are

modified to damp out outgoing waves and to prevent unphysical reflections. The use of damping layers at the edges of the computational domain is described in the next chapter.

From the above discussion, the lateral portions of $\partial\Omega_\infty$ are placed at a suitable distance d, and φ and $\partial\varphi/\partial n$ are prescribed. In particular, at the downstream barrier both functions are assumed to be zero. The same treatment would be used at the upstream barrier in case of a radiation problem, while, for the case of head-sea incident waves, the solution is analytically prescribed consistently with the desired waves.

For deep-water conditions, we assume the horizontal portion of the control surface at a depth large enough to neglect its influence. This implies both $\partial\varphi/\partial n$ and φ are zero. Strictly speaking, nonlinear interactions among wave components can give rise to a slow decay of the potential and, in particular, the asymptotic value of the potential is non-zero (while $\nabla\varphi \to 0$). This behaviour can have a special importance in case of microseism, as discussed by Longuett-Higgins (1953). Despite this special case, in the present work we use also $\varphi = 0$ along the horizontal portion of the control surface without influencing the solution of the considered problem.

A different treatment of the boundary $\partial\Omega_\infty$ is adopted for the simulation of a physical wave flume, shown in section 3.2.2, where the wavemaker and the bottom of the channel have to be modeled. The treatment is more conventional, with the velocity component normal to such boundaries *a priori* known. In the specific case, due to the presence of the wavemaker, $\partial\Omega_\infty$ is time dependent.

2.3 Modeling of the Hydroelastic Problem

To a certain extent, all structures deform under the action of fluid loads. In many cases, structural deformations are not relevant to determine the fluid flow and the problem can be treated as that of a perfectly rigid body. In other circumstances, the motion of the body boundary due to elastic deformations takes place on spatial scales and frequencies suitable to significantly influence the fluid motion. In this context it is fundamental that the time scale of the considered fluid motion (loading time) is comparable with structural elastic natural periods. When this occurs, the fluid dynamic problem and the structural problem are coupled and have to be simultaneously solved (hydroelastic problem).

In the present context, when the shipped water hits structures along the deck, elastic deformations may have a certain importance and may influence the flow conditions. To assess the role of hydroelasticity, analyzed in chapter 5, we need to formulate a hydroelastic model. In particular, within the present two-dimensional analysis, the fluid-structure interaction is studied by coupling the nonlinear potential flow model with a linear Euler beam to represent a portion of the deck house under the action of the shipped water.

The use of a rather simple structural model makes the analysis rather faster and easier. For a more realistic treatment, one should use a more complicated structural model. However main focus is to assess the importance of hydroelasticity for a stiffened flat steel panel, and the beam model represents a satisfactory approximation for the considered structure. Small beam deformations are assumed and, consistently with the Euler beam model, rotations of the beam sections are neglected. Finally, structural damping is assumed negligible.

Let us consider a Cartesian frame of reference (χ, ξ), with the ξ-axis along the undeformed

beam (see sketch 2.2). The transverse deformation $w(\xi, t)$ of the beam is approximated as

$$w(\xi, t) \simeq \sum_{j=1}^{N} \zeta_j(t)\, \psi_j(\xi)\,, \tag{2.8}$$

with $N < \infty$. Here $\psi_j(\xi)$ is the j-th dry mode of the beam and $\zeta_j(t)$ its amplitude. The former can be analytically determined according to the specific boundary conditions at the beam ends,

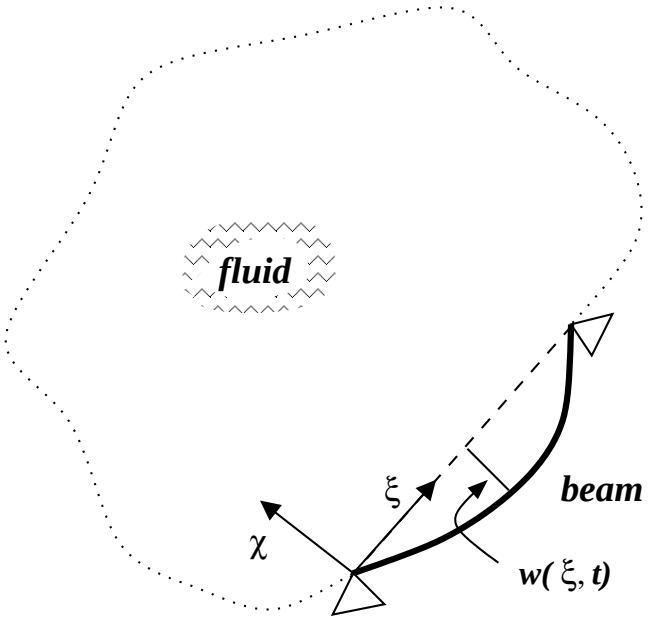

Figure 2.2 Sketch of the two-dimensional problem of interest.

$\xi = 0$ and $\xi = L_{\text{beam}}$, L_{beam} being the beam length. The modal amplitudes are the unknowns of the problem.

The algorithm used for solving the described problem is the following. At a given instant of time, the beam geometry, w, and the deformation velocity, $\partial w/\partial t$, are known and the boundary-value problem for the potential φ can be solved by imposing the impermeability condition

$$\frac{\partial \varphi}{\partial n} = \frac{\partial w}{\partial t}$$

along the instantaneous wetted portion of the beam. It is worth to stress that in the fluid-dynamic computations, in spite of the linearized structural model, the beam is deformed according to $w(\xi, t)$.

The rate of change of the potential, $\partial\varphi/\partial t$, is also needed to evaluate the hydrodynamic pressure (*cf.* equation (2.4)) forcing the beam to deform (see equation (2.11) below). Since $\partial\varphi/\partial t$ is a harmonic function, it can be found by solving a suitable boundary-value problem for the Laplace equation $\nabla^2 [\partial\varphi/\partial t] = 0$. The boundary conditions on the free and rigid boundaries follow from the Bernoulli equation and from the no-penetration boundary condition, respectively. A boundary condition on the instantaneous wetted portion of the beam is also requested, having

the less common form of a non-homogeneous Robin condition:

$$\frac{\partial^2\varphi}{\partial t\partial n} = -\frac{\rho}{m}\frac{\partial\varphi}{\partial t} + b_1 + b_2\,. \tag{2.9}$$

Here ρ is the water density, m the structural mass per unit length and unit width of the beam and b_1 and b_2 are known functions of the longitudinal coordinate ξ. Equation (2.9) follows by inserting the condition for $\partial^2\varphi/\partial t\partial n$ (*cf.* Tanizawa 1999)

$$\frac{\partial^2\varphi}{\partial t\,\partial n} = \frac{\partial^2 w}{\partial t^2} - k\left(\frac{\partial w}{\partial t}\right)^2 - \frac{\partial}{\partial n}\left(\frac{1}{2}|\nabla\varphi|^2\right), \tag{2.10}$$

into the beam equation

$$\begin{aligned} m\,\frac{\partial^2 w}{\partial t^2} + \mathrm{EI}\,\frac{\partial^4 w}{\partial\xi^4} &= p\left(w,\,\frac{\partial w}{\partial t},\,\frac{\partial^2 w}{\partial t^2}\right) \\ &= -\rho\left(\frac{1}{2}|\nabla\varphi|^2 + \frac{\partial\varphi}{\partial t} - \vec{g}\cdot\vec{P}\right). \end{aligned} \tag{2.11}$$

In condition (2.10), $k = |\partial^2 w/\partial\xi^2|/[1+(\partial w/\partial\xi)^2]^{3/2}$ is the local curvature of the beam. In equation (2.11) $\vec{g}$ is the gravity acceleration, $\vec{P}$ represents a generic point (χ,ξ) of the deformed beam and EI is the beam bending stiffness, where E is the Youngs modulus and I the area moment of inertia per unit width of the beam about the neutral axis. Therefore, b_1 and b_2 are given by

$$\begin{cases} b_1 = -k\left(\dfrac{\partial w}{\partial t}\right)^2 - \dfrac{\partial}{\partial n}\left(\dfrac{1}{2}|\nabla\varphi|^2\right) \\ b_2 = -\dfrac{1}{m}\left(\mathrm{EI}\,\dfrac{\partial^4 w}{\partial\xi^4} + \rho\,\dfrac{1}{2}|\nabla\varphi|^2 - \rho\,\vec{g}\cdot\vec{P}\right) \end{cases}. \tag{2.12}$$

From the assumption of small structural deformations the local curvature k can be approximated as $\sim|\partial^2 w/\partial\xi^2|$. This term is multiplied by $(\partial w/\partial t)^2$ in (2.10) thus the resulting contribution is $\mathcal{O}(|w|^3)$ and can be neglected consistently with the assumption of linear beam.
Once $\partial\varphi/\partial t$ is known, $\partial^2 w/\partial^2 t$ can be evaluated and fluid motion and structural deformation can be updated in time. A procedure, similar to the one discussed above, has been introduced in Tanizawa (1999) to analyze the impact of a flexible body with the free surface.

Similarly to the case of rigid-body motions, the right-hand-side of equation (2.11) depends also on terms proportional to the acceleration. This may lead to numerical instabilities in the time integration.

Chapter 3

Numerical Solution

In the following, a numerical procedure to solve the mathematical problem stated in the previous chapter is described. The adopted algorithm, presented in section 3.1, is the well known Mixed Eulerian-Lagrangian method, where the problem is split into a two-step procedure: the evaluation of the velocity field ("kinetic problem" or "Eulerian step"), and a time-evolution problem (the "Lagrangian step"). Motivations and limits related to the present implementation are discussed. Practical details of the numerical procedure are reported in appendix A.

3.1 Solution Algorithm

As discussed in the previous chapter, the two-dimensional free-surface flow around a surface-piercing body is studied within the framework of inviscid irrotational fluid mechanics.
In this context, a possible strategy to numerically solve the problem consists in the following procedure.

0 Let us assume that, at a given instant of time t_0, the boundary geometry $\partial\Omega$ is known together with the potential along the free surface, and the component of the velocity normal to impermeable boundaries.

1 A boundary value problem (b.v.p.) for the Laplace equation can be stated as:

$$\begin{cases} \nabla^2\varphi = 0 \\ \varphi \quad \text{given on} \partial\Omega_{\mathcal{D}} \\ \frac{\partial\varphi}{\partial n} \quad \text{given on } \partial\Omega_{\mathcal{N}} \end{cases} . \tag{3.1}$$

In general, the Dirichlet boundary $\partial\Omega_{\mathcal{D}}$ and the Neumann boundary $\partial\Omega_{\mathcal{N}}$ are only a subset of the domain boundary, since along some parts of $\partial\Omega$ both φ and its normal derivative are known.

By solving the b.v.p. (3.1), we determine the fluid velocity, and (3.1) can be referred to as the "kinetic problem". This is also said to be the "Eulerian step" of the procedure because the problem (3.1) is solved for a frozen configuration of the flow field.

As we will discuss, at this stage the term $\partial\varphi/\partial t$, necessary for the pressure evaluation, can also be calculated.

2 The kinematic and dynamic conditions giving, respectively, the evolution of the free-surface geometry and of the free-surface potential can be stepped forward in time. If a Lagrangian formulation for the free surface is used this step can be properly defined as the "Lagrangian step" of the procedure.

The pressure along the instantaneous wetted surface of the body can be evaluated and the body motions, if not restrained, can be calculated.

This provides new values for the boundary data along the Dirichlet and the Neumann boundaries, and the procedure can be repeated from Step 1 above.

The described solution strategy was elaborated in Ogilvie (1967), but was introduced into practical numerical calculations by Longuett-Higgins and Cokelet (1976) and by Faltinsen (1977), independently. For the specific considered cases, the portion $\partial\Omega_\infty$ of the boundary can be of Dirichlet type, Neumann type, or can be a boundary where the boundary data are entirely specified.

3.1.1 Kinetic Problem

In the present approach, the kinetic problem

$$\begin{cases} \nabla^2\varphi = 0 & \forall\vec{P}\in\Omega \\ \varphi = f(\vec{P}) & \forall\vec{P}\in\partial\Omega_{\mathcal{D}} \\ \dfrac{\partial\varphi}{\partial n} = g(\vec{P}) & \forall\vec{P}\in\partial\Omega_{\mathcal{N}} \end{cases} \tag{3.2}$$

is recast in terms of boundary-integral equations, and solved by a boundary-element method (BEM).

Features and drawbacks of using boundary-integral equations for free-surface flows have been discussed at length by many authors (see *e.g.* Yeung 1982). Here, we only mention that the simplicity of handling highly distorted configurations such those appearing during water shipping, formation of plunging waves, and impact against structures gives a decisive advantage over discretization-field methods, where a grid covering the whole fluid domain is required[1].

[1] The accuracy of field-discretization methods depends on the "quality" of the grid, and not only on the grid-refinement. This limits the use of surface-tracking methods. Also surface-capturing methods (*e.g.* level-set method, Volume-of-Fluid method (VOF), *cf.* Kothe 1998) are based on an underlying grid to solve the fluid dynamic equations and, unless using local grid refinement, suffer of unphysical numerical smoothing of the solution. Lagrangian-meshless methods (*e.g.* Smooth Particle Hydrodynamics (SPH), Reproducing Kernel Particle Method (RKPM), *cf.* Belytschko *et al.* 1996) seem promising but still need verification for the problems presently considered.

To derive suitable integral equations, we consider the Green's second identity

$$c(\vec{P})\,\varphi(\vec{P}) \;=\; \int_{\partial\Omega}(\varphi\frac{\partial G}{\partial n_Q} - \frac{\partial\varphi}{\partial n_Q}G)\mathrm{d}\ell_Q \;. \tag{3.3}$$

Here

$$c(\vec{P}) \;=\; \begin{cases} 2\pi & \vec{P}\in\Omega \\ 0 & \vec{P}\notin\Omega\cup\partial\Omega \\ \theta & \vec{P}\in\partial\Omega \end{cases} \tag{3.4}$$

In (3.3), $\vec{Q}$ is a point along the domain boundary, $\vec{n}_Q$ is the unit normal vector along the boundary pointing out of the fluid domain (see figure 2.1), and

$$G(\vec{P},\vec{Q}) \;=\; \ln(R) \qquad\qquad R=|\vec{P}-\vec{Q}| \tag{3.5}$$

is the two-dimensional free-space Green function. Finally, θ is the inner angle (relative to the fluid domain) at point $\vec{P}$ along the boundary.

The integral representation (3.3) gives the velocity potential within the fluid domain, once φ and $\partial\varphi/\partial n$ are known along the boundary. Conversely, for points $\vec{P}$ on the boundary, (3.3) gives a compatibility condition on the boundary data. In particular, if only some of them are known we can write integral equations to determine the remaining unknown boundary data. More specifically, for points belonging to Dirichlet and Neumann boundaries, respectively, we have

$$\begin{aligned} -\int_{\partial\Omega_{\mathcal{D}}}\frac{\partial\varphi}{\partial n_Q}G\mathrm{d}\ell_Q \;+\; \int_{\partial\Omega_{\mathcal{N}}}\varphi\frac{\partial G}{\partial n_Q}\mathrm{d}\ell_Q \;&=\; \mathcal{T}_{\mathcal{D}} \qquad \vec{P}\in\partial\Omega_{\mathcal{D}} \\ -\int_{\partial\Omega_{\mathcal{D}}}\frac{\partial\varphi}{\partial n_Q}G\mathrm{d}\ell_Q - c\,\varphi(\vec{P}) \;+\; \int_{\partial\Omega_{\mathcal{N}}}\varphi\frac{\partial G}{\partial n_Q}\mathrm{d}\ell_Q \;&=\; \mathcal{T}_{\mathcal{N}} \qquad \vec{P}\in\partial\Omega_{\mathcal{N}} \end{aligned} \tag{3.6}$$

The functions in the right-hand-sides are

$$\begin{aligned} \mathcal{T}_{\mathcal{D}} \;&=\; cf(\vec{P}) - \int_{\partial\Omega_{\mathcal{D}}} f(\vec{Q})\frac{\partial G}{\partial n_Q}\mathrm{d}\ell_Q \;+\; \int_{\partial\Omega_{\mathcal{N}}} g(\vec{Q})G\mathrm{d}\ell_Q \\ \mathcal{T}_{\mathcal{N}} \;&=\; -\int_{\partial\Omega_{\mathcal{D}}} f(\vec{Q})\frac{\partial G}{\partial n_Q}\mathrm{d}\ell_Q \;+\; \int_{\partial\Omega_{\mathcal{N}}} g(\vec{Q})G\mathrm{d}\ell_Q \end{aligned} \tag{3.7}$$

In this work, the integral equations (3.6) are solved by a panel method with piecewise-linear shape functions both for geometry and for boundary data. This was preferred to higher-order schemes (*e.g.* Landrini *et al.* 1999) which may lead to numerical difficulties at the body-free surface intersection point. Clearly, a lower-order method requires a finer discretization in regions with high curvature of the boundary. In particular, it is important to satisfy conservation of fluid mass. Therefore, an accurate tracking of the free boundary is crucial in areas with high free-surface curvature. During the simulation, this has been achieved by inserting dynamically new points where appropriate.

In the present implementation of the method, the collocation points are placed at the edges of each element. This results in a smoother distribution of the velocity potential along the free

surface with respect to piecewise constant panel methods. Continuity of the velocity potential is assumed at those points where the free surface meets a solid boundary. Though no rigorous justification is available, this procedure gives convergence of the numerical results under grid refinement (*cf.* Dommermuth and Yue 1987). Occasionally, when the contact angle becomes too small, numerical problems still may occur and the jet-like flow created during a water-entry phase is partially cut (*cf.* Zhao and Faltinsen 1993).

The discretization procedure by the boundary element method is well known, and we give just few details. The boundaries $\partial\Omega_{\mathcal{D}}$ and $\partial\Omega_{\mathcal{N}}$ are divided into $N_{\mathcal{D}}$ and $N_{\mathcal{N}}$ elements, respectively, and the discretization of the contour integrals in (3.6-3.7) leads to the system of linear algebraic equations

$$\begin{bmatrix} A_{ij} & B_{ij} \\ C_{ij} & D_{ij} \end{bmatrix} \begin{Bmatrix} \frac{\partial\varphi}{\partial n}_{\mathcal{D}\,j} \\ \varphi_{\mathcal{N}\,j} \end{Bmatrix} = \begin{Bmatrix} f_i \\ g_i \end{Bmatrix} \tag{3.8}$$

where the unknown vector $\{\,\partial\varphi/\partial n|_{\mathcal{D}} \quad \varphi|_{\mathcal{N}}\}^T$ has $N = N_{\mathcal{D}} + N_{\mathcal{N}}$ components.
We remark that in a fully-nonlinear simulation, the right-hand-side of (3.8), as well as the matrix coefficients on the left-hand-side, have to be evaluated each time the geometry and the boundary data change.
Once the system (3.8) has been solved, φ and its normal derivative become available along the whole boundary. Differently, the tangential velocity $\partial\varphi/\partial\tau$ along $\partial\Omega$ is determined by using finite-difference operators. The two velocity components are then used for the Lagrangian tracking of the free surface, as described in section 3.1.3.

3.1.2 Evaluation of $\partial\varphi/\partial t$

The evaluation of the pressure along the body-wetted surface, $\partial\Omega_{BO}$, requires the rate-of-change $\partial\varphi/\partial t$ of the velocity potential. However, with moving boundaries (*e.g.* the free surface, or the body boundary when motions are not restrained), the Eulerian derivative $\partial\varphi(\vec{P},t)/\partial t$ is not even defined because the point $\vec{P}$ on the considered boundary is changing in time. Therefore, some practical difficulties are expected.

Rigid body motions Cointe (1989b) observed that $\partial\varphi/\partial t$ is solution of the Laplace equation with a Dirichlet condition on the free surface and a Neumann condition on the body boundary. The latter requires high-order derivatives of the fluid velocity along the body. The problem is formally equivalent to the kinetic problem discussed above and the computation of $\partial\varphi/\partial t$ by BEM does not change significantly the computational effort.

In a different approach, the time derivative following the rigid body motion is introduced

$$\frac{D_{BO}\,\varphi}{Dt} = \frac{\partial\varphi}{\partial t} + \vec{V}_P \cdot \nabla\varphi \;, \tag{3.9}$$

with $\vec{V}_P$ given by equation (2.3). The left-hand side can be evaluated even by numerical differentiation, and the $\partial\varphi/\partial t$ is obtained by subtracting the transfer term $\vec{V}_P \cdot \nabla\varphi$.

In this work, we use the property that the function $\psi(\vec{P},t) = \partial\varphi/\partial t + \vec{V}_P \cdot \nabla\varphi$ is a harmonic function that satisfies a boundary value problem formally identical to the problem (3.1) for the

velocity potential φ (see appendix B). In this case, the body Neumann condition is simpler to evaluate than in the Cointe's approach. By using the boundary-element method already described, we obtain a system of linear algebraic equations with the same matrix as in case of φ and no additional computational effort is requested. In fact, at each time instant we can factorize once and for all the common matrix, and perform two back-substitutions for the φ and for the $D_{BO}\ \varphi/Dt$ problem, respectively.

Hydroelastic problem In this case $\partial\varphi/\partial t$ is determined by solving at each time instant the b.v.p. described in section 2.3. Due to the Robin boundary condition along the beam wetted length, the latter is not formally the same as the problem for the velocity potential. As a result, in the discrete form, the matrix associated with the system to solve is different and additional CPU-time is needed.

3.1.3 Time Integration

A standard fourth-order Runge-Kutta scheme is adopted to step forward in time the evolution equations associated with the problem. This method represents a good compromise between accuracy and computational costs. Its stability limits usually are not very severe. In particular, in a linear stability analysis we can show that the scheme becomes unstable only by using very large time step Δt, which is never adopted because the tracking of the fast physical dynamics of water shipping limits more severely the choice of the time step. Finally, the method is slightly dissipative. The dissipation rate decreases as the time step decreases, and for the global time scales here analyzed (of the order of few periods of the incoming wave) this is negligible.

The scheme is well known. Let us consider equations of the form $\partial y/\partial t = f(\vec{P}, t)$, where y is the variable of interest and $f(\vec{P}, t)$ is a known function of space and time. This gives

$$y^{n+1} \;=\; y^n \;+\; \frac{1}{6}\,k_1 \;+\; \frac{1}{3}\,k_2 \;+\; \frac{1}{3}\,k_3 \;+\; \frac{1}{6}\,k_4 \;,$$

with

$$\begin{cases} k_1 \;=\; \Delta t\, f(t^n\,,\, y^n) \\ k_2 \;=\; \Delta t\, f(t^n \;+\; \dfrac{1}{2}\,\Delta t,\; y^n \;+\; \dfrac{1}{2}\,k_1) \\ k_3 \;=\; \Delta t\, f(t^n \;+\; \dfrac{1}{2}\,\Delta t,\; y^n \;+\; \dfrac{1}{2}\,k_2) \\ k_4 \;=\; \Delta t\, f(t^n \;+\; \Delta t,\; y^n \;+\; k_3) \end{cases}$$

This scheme requires the solution of four kinetic problems for each physical time interval due to the introduced (fictitious) auxiliary time instants. For a linearized problem, this procedure would be equivalent to a fourth-order Taylor expansion in time with an error of $\mathcal{O}\,(\Delta t^5)$. Though less demanding schemes are conceivable, we adopted the described scheme because of the simplicity in changing dynamically the time step. This was found crucial to keep under control the accuracy of the solution during the development of jet flows, impacts, and breaking waves.

3.2 Generation of Incoming Waves

The incident waves are far from being *regular* in the real case. This means they are associated with a certain spectrum of energy distributed along a continuous range of frequencies. Despite this fact, in this work regular incoming waves have been considered because it is simpler to link wave parameters, such as wavelength λ and wave height H, with occurrence and severity of the phenomenon. Present study is useful when specified design conditions are analyzed. In this case the regular wave conditions can be applied to describe the sea state of interest. However one must note that the numerical method described in this work can also be applied in the case of a more general type of incoming wave system.

In an ideally unbounded domain, regular incident waves are *permanent* in shape, namely the wave profile remains unchanged in a frame of reference moving with the phase velocity. The latter is not only a function of the wave number $k = 2\pi/\lambda$ but also of the wave steepness ka, a being the wave amplitude, so that the different Fourier components of the wave are phase bounded with each other. Permanent wave forms have been analytically discovered by Stokes. They may be generated experimentally but it has been proved by Benjamin and Feir (1967), for deep water, and by Benjamin (1967), for arbitrary water depth, that Stokes waves can be unstable when perturbed. Benjamin and Feir discovered theoretically the instability by considering the problem of a periodic wave train, with frequency ω, perturbed by side-band frequencies $\omega(1 \pm \delta)$. This gave that Stokes waves where $kh < 1.363$, are stable. Here h is the water depth. Differently, those propagating in sufficiently deep water, so that $kh > 1.363$, can be unstable. In particular this occurs when the condition of instability

$$0 \; < \; \delta \; < \; k\,a\,\sqrt{2\frac{X(kh)}{Y(kh)}} \; = \; \delta_c \tag{3.10}$$

is satisfied. Here X and Y are two known functions of kh. Condition (3.10) implies that, for unstable growth, the side-band frequencies need to be sufficiently close to the fundamental frequency. The asymptotic growth of the side-band amplitudes is

$$\sim \exp\{\tfrac{1}{2}\,\delta\,\sqrt{Y\,(2\,k^2\,a^2\,X \; - \; \delta^2\,Y)}\,\omega\,t\} \quad \text{as} \quad t \to \infty\,.$$

This has a maximum value for $\delta = \delta_c/\sqrt{2}$. The growth rate of the Benjamin and Feir instability decreases as the steepness of the carrier decreases. In addition to these longitudinal instabilities, Stokes waves are also subjected to cross-wise instabilities (*cf.* McLean *et al.* 1981).
In this work, the incoming waves are generated in two alternative ways:

1. Stokes waves are analytically prescribed at the upstream barrier of $\partial\Omega_\infty$, or
2. a wave flume is numerically simulated and the upstream barrier is replaced by a wavemaker.

The first strategy is used both in deep water and finite water depth and it is used to carry out the parametric analysis in terms of the deck wetness, as described in chapter 4, and in general in the conducted studies of water-on-deck phenomena.
The second approach has been applied for finite water depth to reproduce the experiments carried out at NTNU, discussed in chapter 8.

3.2.1 Use of the Analytical Incident-Wave Solution

The vertical downstream portion of the surface $\partial\Omega_\infty$ is chosen far enough from the body to give negligible contributions in terms of disturbances generated by wave-body interactions (*cf.* section 2.2). Along the vertical upstream barrier, both φ and $\partial\varphi/\partial n$ are specified by a truncated Fourier representation of the Stokes wave for arbitrary steepness (Bryant 1983, see also Rienecker and Fenton 1981 for finite water depth). The horizontal location of this barrier is chosen far enough (order of ten wavelengths) from the body so that within the time scale of the simulation (at most the order of ten wave periods) disturbances due to wave reflection are small in proximity of the inflow boundary. For deep water problems its vertical extent is truncated at a suitable large depth, and the contribution from the horizontal bottom boundary is neglected. No approximations are introduced in case of finite water depth, and the no-penetration boundary condition is enforced on the bottom.

Semi-analytical solutions of the two-dimensional problem of nonlinear gravity waves can be derived by using perturbation expansion in terms of a small parameter ϵ involved in the problem. In this way the nonlinear solution is expressed as a power series $\sum \epsilon^i \varphi_i$, where each term φ_i is the solution of a linear mathematical problem. For water waves, this approach has been introduced by Stokes, who chose as small parameter the amplitude a_1 of the first harmonic in the Fourier expansion of the wave elevation. Later on it was proved by Schwartz (1974) that the convergence of the related power series is not ensured for each value of a_1 and that a more suitable parameter is the wave steepness $\epsilon = 2\pi a/\lambda$.

For deepwater, the solution of the problem

$$
\begin{aligned}
&\nabla^2\varphi \;=\; 0 && \forall\; z \;<\; \varepsilon\,\eta(x,t)\\
&\frac{\partial\varphi}{\partial x},\,\frac{\partial\varphi}{\partial z} \;\rightarrow\; 0, && \forall\; z \;\rightarrow\; -\infty\\
&\begin{cases} \dfrac{\partial\eta}{\partial t} - \dfrac{\partial\varphi}{\partial z} + \varepsilon\,\nabla\eta\cdot\nabla\varphi \;=\; 0\\[2ex] \eta + \dfrac{\partial\varphi}{\partial t} + \dfrac{1}{2}\,\varepsilon|\nabla\varphi|^2 \;=\; 0 \end{cases} && \forall\; z \;=\; \varepsilon\,\eta(x,t)
\end{aligned}
\tag{3.11}
$$

has been obtained following Bryant (1983). An earth-fixed frame of reference is assumed, with the z-axis parallel and opposite to the gravity acceleration $\vec{g}$, $z = 0$ corresponds to mean water level. The equations of the problem and the solution are given in terms of the non-dimensional variables:

$$
\begin{cases}
(x,\,z,\,\eta)_{\mathrm{dim}} &=& (x,\,z,\,\eta)\,\frac{\lambda}{2\,\pi}\\
t_{\mathrm{dim}} &=& t\,\sqrt{\frac{\lambda}{2\,\pi\,g}}\\
\varphi_{\mathrm{dim}} &=& \varphi\,a\sqrt{\frac{g\lambda}{2\,\pi}}
\end{cases}
\quad .
$$

In the numerical method the solution of the problem is expressed in terms of truncated Fourier

series for the wave elevation and the velocity potential,

$$\begin{cases} \eta &= \displaystyle\sum_{k=1}^{N} a_k \cos[k(x-ct)] \\ \varphi &= \displaystyle\sum_{k=1}^{N} b_k \, e^{kz} \sin[k(x-ct)] \end{cases} . \tag{3.12}$$

Here, the phase velocity c depends on the steepness ϵ, and the number N of harmonic components results from the computation so that the approximate solution satisfies the nonlinear problem within an accuracy δ decided *ab initio*. This means that the contribution of the first harmonic neglected is smaller than δ. When expressions (3.12) are substituted into the problem (3.11), a Newton-Raphson method can be applied to determine c and the amplitudes a_k and b_k with the specified error.

For finite water depth, say when the depth h is less than $\frac{1}{2}\lambda$, the problem (3.11) is modified by the impermeability condition along the bottom, and the solution procedure adopted, here not described, can be found in Fenton(1988).

3.2.2 Wavemaker

A water region with finite depth h is considered. The boundary surface $\partial\Omega_\infty$ is formed by a straight vertical downstream portion (1), an upstream portion (3) containing the instantaneous wetted surface of the wavemaker and a straight horizontal portion between them (2), see figure 3.1. As discussed in section 2.2, the portion (1) is a control surface taken far enough from the

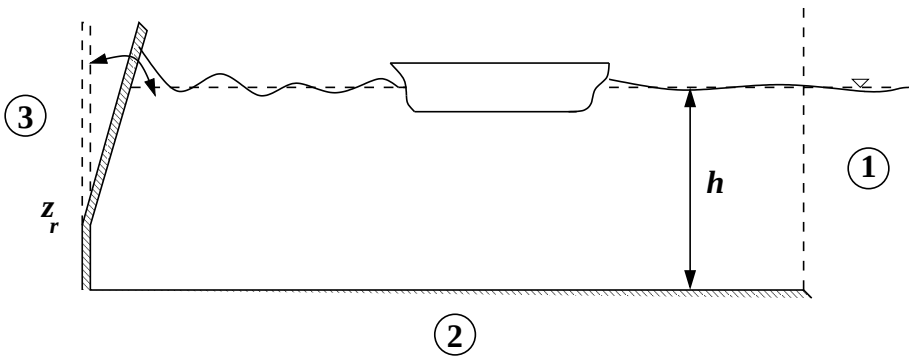

Figure 3.1 Flap wavemaker: sketch of the numerical two-dimensional problem.

body so that both the velocity potential and its normal derivative can be set equal to zero along it. The remaining two parts of $\partial\Omega_\infty$ are physical boundaries, where the impermeability condition applies, and φ follows from the solution of the integral equations (3.6). In the studied cases, the geometry of the upstream boundary reproduces that of the physical wave flume at NTNU, where a flap wavemaker is hinged at a distance z_r from the bottom (the portion underneath is vertical and fixed). The motion of the wavemaker can be freely prescribed to produce different kind of waves. In particular, for the purpose of comparison with experiments, the motion of the wavemaker is directly defined by using the recorded motion of the physical wave flume.

3.3 Modeling of the Flow Field during Water Shipping

A crucial aspect of the water-on-deck problem is represented by the prediction of the shipping occurrence. Also, the behaviour of the fluid flow during the initial stage, when freeboard is exceeded, represents a physical interesting and still rather unclear stage of the whole event. Therefore, numerical modeling has to rely upon experimental observations in the hope to grasp correctly the physics.

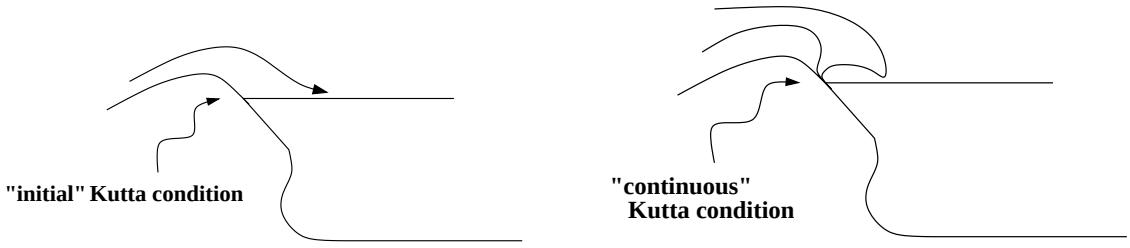

Figure 3.2 Left: "initial" Kutta-like condition at the edge of the deck. Right: "continuous" Kutta-like condition at the edge of the deck.

"Initial" Kutta-like condition At the beginning of the present work, the quasi-two dimensional experiments reported in Cozijn (1995) has been used as a guidance. From these studies, after the freeboard is exceeded and in case of water shipping, it resulted that the fluid flows tangentially along the deck, resembling the fluid motion after a dam breaking.

On this ground, we devised a first modeling of the flow at the edge of the deck, which is sketched in the left plot of figure 3.2. In particular, the fluid is allowed to leave tangentially the bow when water reaches the instantaneous freeboard. After this initial event, once the freeboard is exceeded, the fluid velocity relative to the ship determines whether the deck will be wetted or the water will be diverted in the opposite direction. In the first case, the fluid particle closest to the deck is allowed to move tangentially along it.
We verified *a posteriori* that this treatment allows a good prediction of water-on-deck occurrence, and of the subsequent evolution of the flow field along the deck.

"Continuous" Kutta-like condition Two-dimensional experiments performed in a small wave flume at the Hydrodynamics Department of NTNU, highlighted the local behavior of the water during the first stage of the shipping. In particular, it has been observed that the beginning of water shipping initiates in the form of a wave crest plunging onto the deck. In most observations, the spatial scale involved is small (compared with the ship draft), as well as the time scale for the impact to occur. After that the flow field evolves according to the "usual" description of dam breaking-type water-on-deck. Our experimental observations will be better discussed in chapter 8, and for the present purpose the above description suffices to justify a second treatment we devised for the flow at the bow edge. This is drawn in the right plot of figure 3.2, and consists in enforcing the fluid to leave tangentially the bow continuously during the whole evolution. We named this treatment "continuous" Kutta-like condition.

This description turned out to be quite successful in describing the formation of the wave plunging onto the deck, although the numerical simulation breaks down when the free surface hits the solid boundary. A description of the following impact flow is possible, for example by matching with a local high-speed solution, although it has not been presently attempted.

As we already stressed, after the initial impact, the long-time evolution of the flow field follows the better known dam breaking-type water-on-deck (*cf.* chapter 1). Therefore, phenomena occurring on a larger time scale than the initial plunging breaking wave can be studied by applying the initial Kutta-like condition, while we limited the use of the continuous Kutta-like condition to describe the initial water impact with the deck.

3.4 Absorbing Boundary Conditions

We will study water-on-deck induced by head-sea regular waves, with either incident waves analytically prescribed or generated by a given motion of a wavemaker. In the former case, the distance d of the vertical portions of the control surface $\partial\Omega_\infty$ from the body can not be taken arbitrarily large due to obvious limitations of memory requirements and computational time. Therefore, disturbances radiated by, as well as transmitted and reflected waves due to the body may reach the edges of the computational domain within a time-scale smaller than that needed by the simulation. This can cause unphysical reflections, and hamper the results.

To prevent this problem, damping layers are used in proximity of the lateral boundaries of the computational domain to damp out progressively the outgoing wave motion. In practice this is obtained by modifying the free-surface conditions. This represents a pragmatic solution, apparently without any assumption that the flow is linear or nonlinear (*cf.* Ohkusu 1996). In this way, although the wave evolution is altered along the damping region, the solution is not modified within the inner computational domain where the "physical" free-surface conditions are used. Many ways exist for applying a damping region: apparently, Israeli and Orszag (1989) introduced the idea in a general framework, probably Cointe (1989a) was the first to apply it for studying wave-body interactions. Further Clément (1996) pointed out the need of complementing the damping layer with piston-like conditions to increase the effectiveness in the low-frequency regime.

Both the free-surface conditions are modified in the present work. In particular, close to the barrier downstream of the body, the dynamic condition in (2.7) is altered by introducing a damping term proportional to φ, namely

$$\frac{D\varphi}{Dt} \;=\; \frac{1}{2}|\,\vec{u}|^2 \;-\; g\eta \;-\; \nu(\vec{P})\varphi \qquad \forall t,\ \forall \vec{P} \in \partial\Omega_{FS}\ . \tag{3.13}$$

A damping term proportional to the free surface elevation η is introduced in the kinematic condition

$$\frac{D\vec{P}}{Dt} \;=\; \nabla\varphi \;-\; \nu(\vec{P})\,\eta\,\vec{e}_z \qquad \forall t,\ \forall \vec{P} \in \partial\Omega_{FS}\ \ , \tag{3.14}$$

where $\vec{e}_z$ is the unit vector along z-axis. Some stretching of the panels is used to obtain a large reduction of the low-frequency components (*cf.* Cao *et al.* 1993).

The treatment of the upstream edge of the computational domain is slightly modified because of the generation of incoming Stokes waves. In facts, in this case the damping terms are proportional to the perturbation variables $(\varphi - \varphi_{\text{sto}})$ and $(\eta - \eta_{\text{sto}})$, respectively. Here φ_{sto} and η_{sto} are the velocity potential and wave elevation of the unperturbed Stokes wave, respectively. For the damping coefficient $\nu(\vec{P})$, we adopted the following expression

$$\nu(\vec{P}) = \begin{cases} 0 & \forall \vec{P} \in \partial\Omega_{FS} - \mathcal{L} \\ \nu_{max}\,(-2\,\xi^3 + 3\,\xi^2) & \forall \vec{P} \in \mathcal{L}_1 \\ \nu_{max} & \forall \vec{P} \in \mathcal{L}_2 \end{cases} , \tag{3.15}$$

where

$$\xi = \frac{d - d_0}{meas(\mathcal{L}_1)} .$$

Here, d is the horizontal distance from the body of a generic point $\vec{P} \in \partial\Omega_{FS}$, d_0 is the horizontal distance from the body where the damping region begins and $meas(\mathcal{L}_1)$ is the length dimension of $\mathcal{L}_1$. Thus, the numerical "beach" $\mathcal{L} = \mathcal{L}_1 \cup \mathcal{L}_2$ is made by a first portion $\mathcal{L}_1$, where the damping coefficient increases smoothly as a cubic function of the distance from d_0, reaching a maximum value ν_{max} (see sketch 3.3). The latter represents the constant value of ν in the second

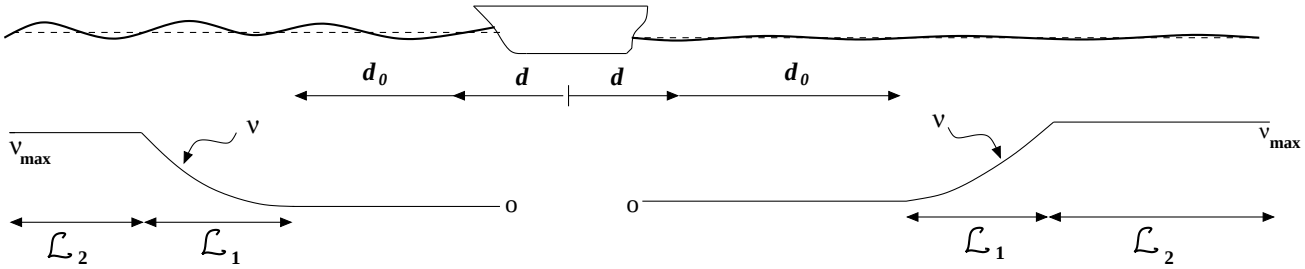

Figure 3.3 Sketch of the numerical damping region. The horizontal distances are compressed with respect to those adopted in actual computations.

portion $\mathcal{L}_2$. Clearly, ν is zero for points $\vec{P}$ outside the numerical beach, where the free-surface conditions reduce to the original ones.

The length of the numerical beach, as well as the value of ν_{max}, have to be empirically determined. In this work, $meas(\mathcal{L}_1)$ has been chosen at least equal to twice the incoming wave length λ, while $meas(\mathcal{L}_2)$ could be much larger, in particular in the downstream region, to damp out low-frequency components. In fact, analogously to the physical case, the shorter the wavelength is relative to $\mathcal{L}$, the more efficiently the wave motion is damped out. It is worth to mention that for green-water loading long waves compared with the ship draft are of interest. This requires a suitable "design" of the computational domain and of the duration of the simulation to balance the computational effort with the quality of the results needed.

The damping term $\nu_{\max}$, which has the same dimensions as frequency, was chosen in the form

$$\frac{\nu_{\max}}{\sqrt{gk}} = \frac{1}{\sqrt{2\pi}}\sqrt{\frac{\lambda}{D}} , \tag{3.16}$$

where k is the wave number and D the ship draft. This choice is based on empirical studies conducted by Greco (1997). This procedure worked efficiently for the considered cases, as confirmed by the good agreement of the numerical simulations with experimental data, reported later.

The Lagrangian drift of surface points is eliminated through periodic regridding of the upstream region. Invarianceof the results have been checked by increasing the upstream length of the domain. The reproduction of exact Stokes wave conditions have been checked inside the domain Ω in absence of the body.

Finally, in case of the numerical simulation of the NTNU wave flume we did not use damping layer in proximity of the wavemaker. In facts, in the physical wave flume an automatic control system adjusts thewavemaker motion to absorb reflected waves and to ensure the desired wave conditions. We used the actual wavemaker motion during the experiments to drive our numerical wavemaker and absorption of reflected wavesfrom the ship to the same degree as in the experiments is expected also in the simulations.

Chapter 4

Water on Deck

In this chapter the water-on-deck phenomenon is analyzed. A parametric analysis of the water shipping is carried out by varying incoming waves and main ship parameters. The influence of body motions on the amount of shipped water and on the occurrence of the plunging wave-type water on deck (see section 1.1) is also discussed.

4.1 General Remarks

Water-on-deck is a complex phenomenon. Roughly speaking, we may distinguish three different stages: i) the run-up of the water at the bow, ii) the water shipping onto the deck, iii) the subsequent flow developing along the deck. In practical cases, also iv) the impact with ship equipments or deck house can be observed.
When the wave elevation exceeds the freeboard, two main scenarios have been observed:

> Type I: the water-on-deck is characterized by a large wave plunging directly against the deck house or equipments. We will refer to this event as "plunging wave-type water on deck".
>
> Type II: the mass of water above the deck level flows along the deck and resembles the flow field after a dam breaking. In the following, we will refer to this scenario as "dam breaking-type water on deck".

In principle, although less commonly observed, the Type I water-on-deck is more dangerous for ship structures than the Type II because of the more violent impact of water.

Two-dimensional water-on-deck experiments performed at the Department of Marine Hydrodynamics of NTNU revealed that also the Type II water-on-deck starts in the form of a plunging breaker hitting the deck. These observations are extensively described in chapter 8, and here we simply anticipate that the observed phenomenon takes place in small time and space scales relative to those of the water shipping itself. Probably, because of its localized character and

therefore of the difficulties to detect it, this plunging-wave phase has not been documented in previous two-dimensional experiments reported in Cozijn (1995), discussed in the following section. In any event, after this initial stage, the water shipping has been observed to develop in the Type II form, *i.e.* as a dam breaking-type water on deck.

As anticipated in the previous chapter, comparisons with experiments have shown that small-scale details of the flow at the bow are properly modeled and recovered by a "continuous" Kutta-like condition. The following long-time evolution is not affected by these small details which can be neglected, and the use of the "initial" Kutta-like condition allows to describe efficiently the water shipping.
Therefore, throughout the following sections, the initial Kutta-like condition has been solely applied to focus on the global features of water-on-deck. A parameter analysis is carried out in terms of the amount of shipped water in the first part. Then the occurrence of the less common Type I water-on-deck is investigated.

4.2 Preliminary Studies and Validation

In the following, regular waves incident on a fixed rectangular body are considered. The initial Kutta-like condition that enforces the flow to leave tangentially the bow when the water reaches the instantaneous freeboard, f, is adopted. Once the freeboard is exceeded, the fluid velocity relative to the ship determines whether the deck will be wetted or the water will be diverted in the opposite direction.

Numerical solutions have been compared with two-dimensional experiments by Cozijn (1995). In the experiment, sketched in figure 4.1, a wavemaker was used to generate regular waves

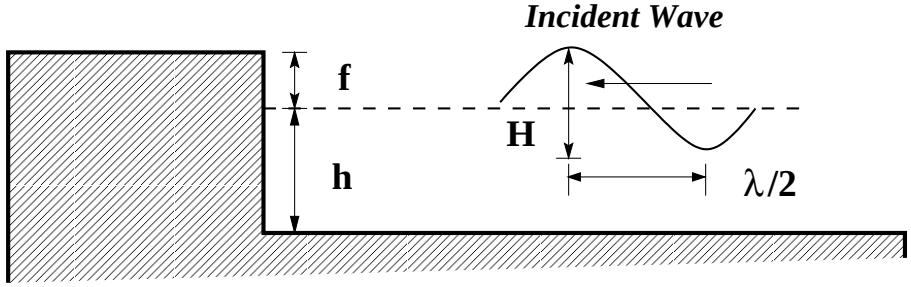

Figure 4.1 Sketch of the two-dimensional experimental set-up by Cozijn (1995) and definition of main parameters.

interacting with a rectangular bottom-mounted structure, placed at the opposite end of the tank, 1.028 m (h) deep. The freeboard f was 0.1 m, and water-on-deck events have been recorded by a video camera.
Figure 4.2 shows the comparison between numerical, solid lines, and experimental, circles, free-surfaces profiles for the case with wave height $H = 0.128$ m and frequency $\omega = 5$ rad/s, corresponding to $\lambda = 2.50$ m. Linear theory would in this case give $\lambda = 2.44$ m. The reported experimental sequence is coded 5:36:12-19 from test No. A03 of Cozijn's data. The snapshots, labeled 1 through 8, give the free surface as time increases, showing the occurrence of a dam

breaking-type water on deck. The first frame (*cf.* figure 4.2.1) reproduces the free-surface configuration just before the shipping of water. The following wave profiles are reported for a time interval of $\Delta t = 0.04$ s. The global behavior of the free surface is well reproduced by the nu-

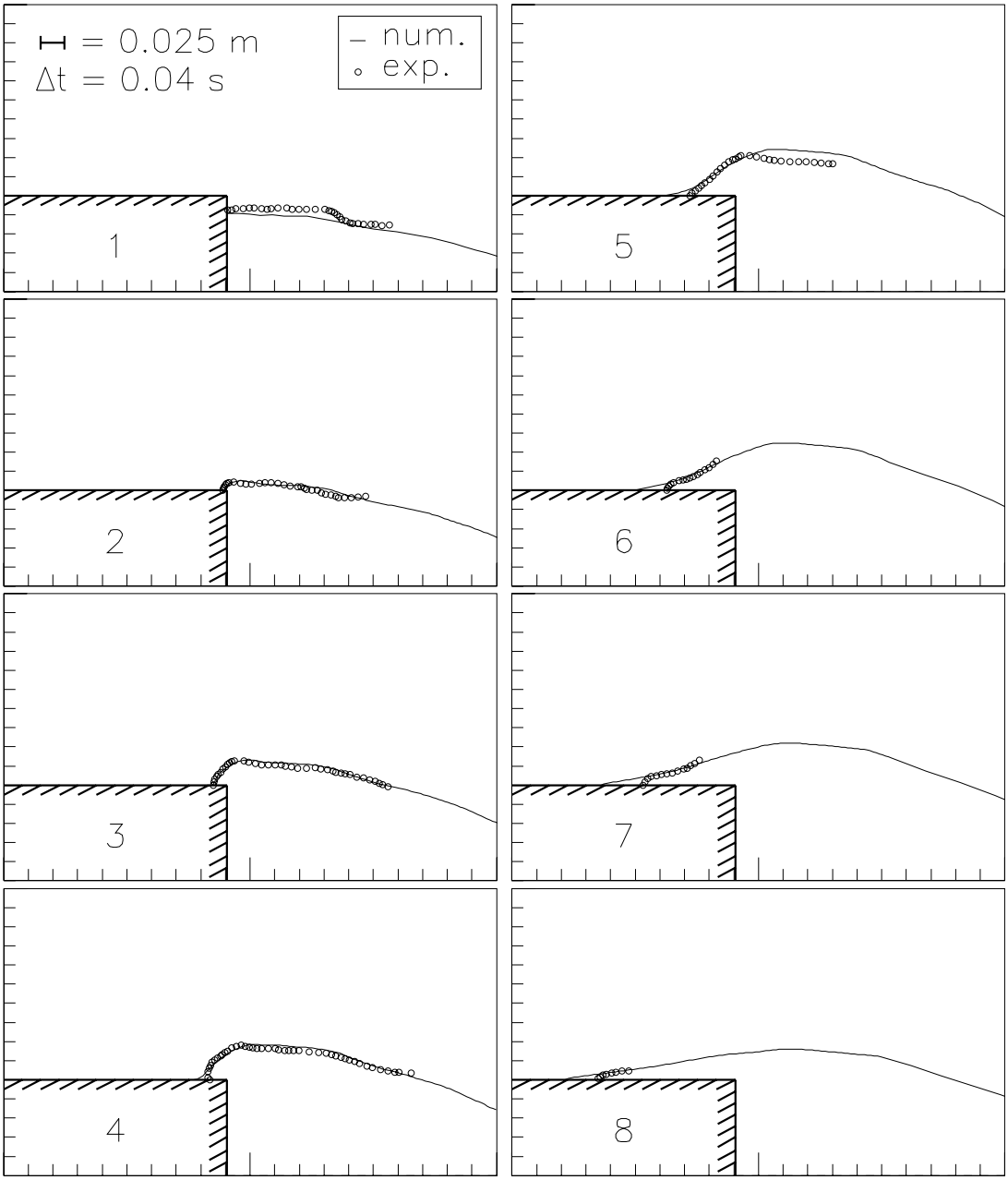

Figure 4.2 Water-on-deck on a rectangular structure caused by incoming regular waves ($H = 0.128$ m, $\omega = 5$ rad/s). The initial freeboard is $f = 0.1$ m. The snapshots are enumerated as the time increases. Experimental data (circles) are from Cozijn (1995, experimental sequence coded 5:36:12-19 from test No. A03).

merical solution, even if the local details of the flow at the edge of the deck are approximated.

In the late evolution, the numerical solution predicts a fluid front moving faster than in the experiments. Nevertheless, the water level along the deck is rather similar for the two results.

A possible explanation of the differences could be given by surface tension effects which are not modeled by present method. In facts, the thickness of the fluid layer is of the order of 0.01 m, and the high curvature of the free surface at the water front requires a more complex description of the dynamics of the contact point (*cf.* Dussan 1979). This is supported by the observation that the measured shape appears "rounded" and highly curved in proximity of the contact point.

Viscous effects and turbulent resistance could also matter. Dressler (1954) performed two-dimensional model tests for the dam-breaking problem. The experiments showed a division of the flow evolution into distinct regimes. At the beginning the flow was dominated by laminar viscous effects, and the related importance grew with decreasing the scale of the experiment. In the second regime, the flow was dominated by inviscid hydrostatic pressure effects. Finally, turbulent effects became important and tended to slow down the wave front velocity. The speed reduction occurred sooner when the bottom roughness was increased. Qualitatively these results can be applied to interpret the considered water-on-deck experiments. In particular, a non sufficiently smooth deck can cause a non-negligible decrease of the wave-front velocity with respect to the inviscid solution.

Anyway, since the deviation between the two results is strongly localized, it is believed unimportant in terms of effects for the possible impact problem where a superstructure is hit by the water flowing along the deck. On this ground, differences in the pressure over the structure are expected during the very initial time scale, which is unimportant from the structural reaction point of view.

A more realistic set of parameters is analyzed in the following. A FPSO in long and steep head-sea regular waves (Buchner 1995) is considered to determine the main parameters for the two-dimensional simulations. The draft of the ship is $D = 17.52$ m, while the relative length and freeboard are respectively $L = 14.86D$ and $f = 0.507D$. In the experiments, a superstructure is located at a distance $d_s = 2.05D$ from the bow. For simplicity, a straight vertical bow and restrained body motions are assumed. The following analysis is for the first water-on-deck occurrence caused by incident waves with wavelength $\lambda = 0.75L$ and wave steepness $H/\lambda = 0.09$. The top plot of figure 4.3 shows the free surface just after the initiation of the water shipping, and some following configurations. The latest is after the shipped water has impacted against the vertical superstructure. At first, a steep water front grows at the bow (dash-dotted line), then the flow develops along the deck (dotted line), eventually hitting the deck house (solid line). The four bottom plots report the time evolution of the water level at the locations A through D along the deck, shown in the top plot. The numerical results are compared with the (three-dimensional) experiments by Buchner (1995). In the experimental set-up, the water level sensors were located along the centerplane of the ship. In spite of the three-dimensionality of the phenomenon, and that in our simulation body motions are restrained, the numerical simulation reproduces reasonably well the propagation of the water front. We observe that the scale of this experiment is much larger than that used by Cozijn (1995). This supports our speculations about the role of surface tension in the previous case.

In more detail, in location A we observe a strong local effect associated with the first event of water on deck and a clear overprediction of h_w relative to the experiments. One must recall that geometrical details of the bow, and the wave-induced body motions prevent us from making a

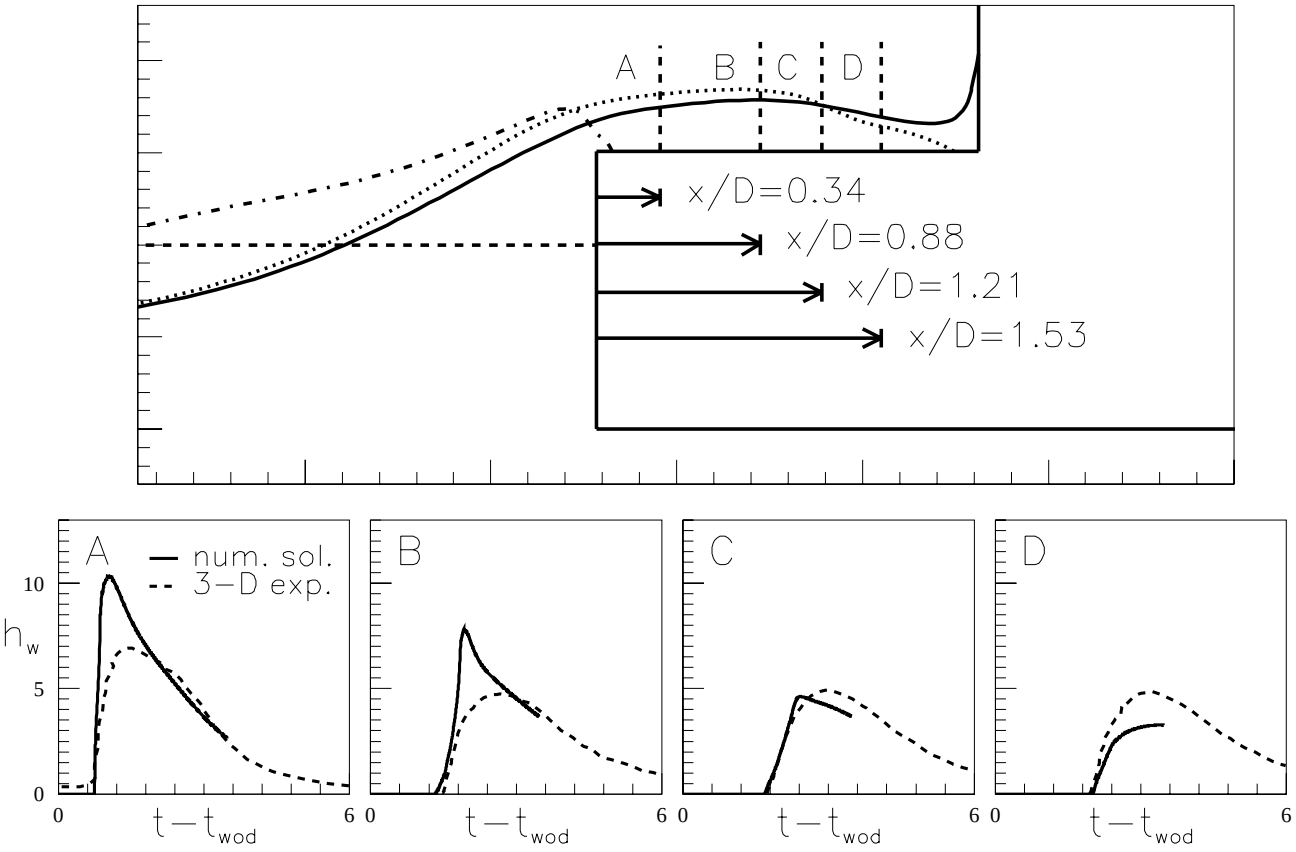

Figure 4.3 Top: sketch and free-surface evolution during the shipping of water. Bottom: history of waterlevel h_w (meters) at locations A-D along the deck. Numerical results (solid lines) and three-dimensional experiments (dashed lines) by Buchner (1995). Time is expressed in seconds and t_{wod} is the instant when the water shipping starts.

finer comparison. The relative difference is smaller for locations C-D, where numerical results underpredict the experimental values. This suggests an increasing three-dimensional behavior of the flow developing along the deck, in particular because of the additional contributions to the water level coming from thelateral sides of the ship.
Finally, for this particular choice of the parameters, the local wavesteepness in the bow region, the amount of water shipped on deck and the propagating flow velocity are observed to decrease when then umber of shipping even tsincreases. We will see in the next section that this is not a general result.

4.3 Influence of Main Geometric Parameters

A simplified parametric analysis of deck wetness has been made by using the amount of shipped water during one water-on-deck cycle, Q, as a measure of the water-on-deck severity. Q is the integratedflux of water overthe freeboard during one single water-shipping event, without any further consideration about residue of water from previous events. Therefore, at each water-

shipping cycle the deck is modeled as perfectly dry. In this way, it is assumed that the fluid flowing back along and outside the deck is not relevant for the free-surface dynamics and the back flow is not modeled at all. This means that we neglect (i) the interaction of the water leaving the deck and returning to the sea with the bow-flow region, and (ii) the interaction of fresh shipped water with residual water from a previous water-on-deck event. However, (i) in the real case the water leaves the deck mainly from the ship sides, and only a minor percentage leaves the deck along the ship centerplane. Thus we expect the committed error to be small. Furthermore, (ii) we will see how the water on deck events occur approximatively with the period of the incoming waves, while usually almost all the water leaves the deck in a shorter time (*cf.* Zhou *et al.* 1999). Thus also in this case we expect a small error.

Systematic variations of body geometry and of incoming-wave characteristics have been considered. In particular, the geometric parameters shown in figure 4.4 are examined, with the ship

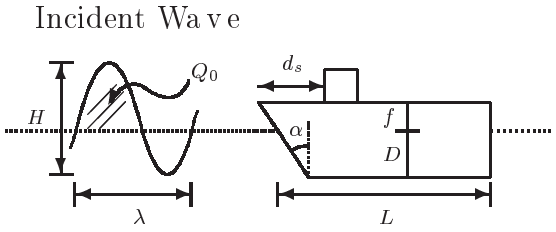

Figure 4.4 Sketch of the main geometrical parameters considered.

draft used as reference length. The shipped water Q is made non dimensional by the amount of water Q_0 within a crest of the incoming wave and above the mean free-surface level (see figure 4.4).

Ship parameters At first, we analyze cases where the body motion is restrained. Four freeboard-to-wave height ratios (f/H =0.05, 0.24, 0.36 and 0.55) are considered and the influence of the stem overhang angle α and of the length-to-draft ratio L/D of the ship is studied

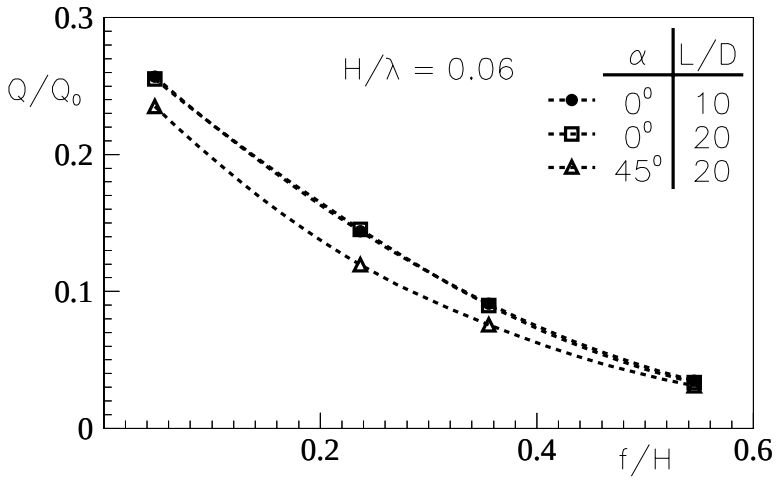

Figure 4.5 Influence of ship length and stem overhang on the bow deck wetness.

for waves with $H/\lambda = 0.06$ and $\lambda/D = 6.6$. Results are presented in figure 4.5, where the relative amount of shipped water is plotted versus f/H. As it can be expected, Q/Q_0 is strongly influenced by the freeboard of the ship. The length L does not significantly affect the deck wetness severity. However, if wave-induced body motions were considered, we would expect a stronger influence of the ship length.

A positive bow stem overhang reduces the relative amount of shipped water due to a larger wave reflection by the ship. However, in the present case, the deck-wetness severity does not dramatically change in the two considered geometries ($\alpha = 0°$, $45°$). This is more evident for larger values of f/H. But, if we interpret f as the instantaneous freeboard due to heave and pitch, f/H can be quite small. This shows that the stem-angle effect could have some importance, depending also on the actual ship loading conditions.

According to recent proprietary experimental studies (Korbijn, personal communication), a bulbous bow may influence the water-on-deck phenomenon. Intuitively this can qualitatively be explained by considering the effect of the bulb on the flow equivalent to the disturbance caused by sources centered along the bulb axis. In particular, this means that the bulb causes

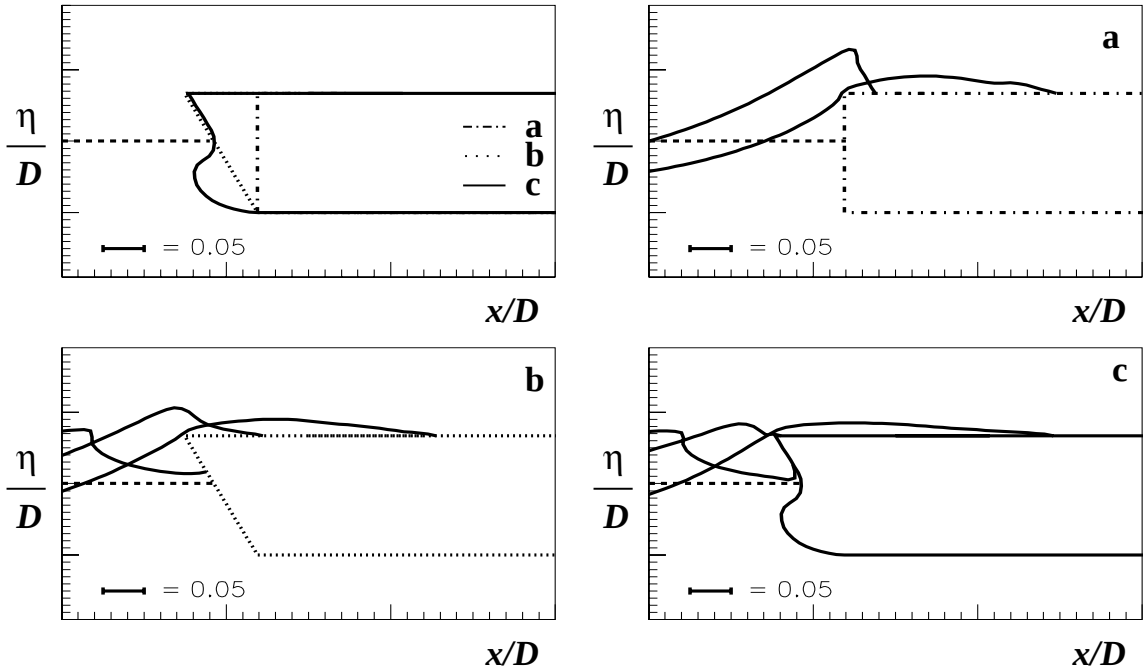

Figure 4.6 Influence of bulb at the bow on the deck wetness. Left top plot: analyzed bow geometries. Case a: vertical bow. Case b: bow with stem angle $\alpha = 28°$. Case c: bulb bow.

an additional vertical flow velocity at the free surface which can affect also the steepness of free-surface waves and, therefore, the water shipping may increase because of the bulb. This explanation does not account for the presence of the free surface. The latter can either magnify (the high frequency limit gives $\varphi = 0$ as combined free surface condition) or reduce (the low frequency limit gives $\partial\varphi/\partial z = 0$ as combined free surface condition) the influence of the bulb. For the specific study, wavelengths long relative to the ship draft are of interest. This means that the free surface tends to reduce the effects of the bulb on the local flow conditions.

As a simple heuristic study of the influence of bow geometry, we compared the flow in case of a vertical bow, a bow with stem angle $\alpha = 28°$, and a bow with bulb (cases a through c shown in the top left plot of figure 4.6). The main parameters used in the analysis are: $L/D \simeq 15.24, f/D = 0.67$, $D = 16.5$ m, for the ship, and $H/\lambda = 0.095$ and $\lambda/L = 1$, for the chosen regular incoming waves. In figures 4.6.a-.c free-surface configurations during the first water-on-deck event are shown for the three geometries. In all cases, the latest reported configuration refers to the end of water shipping, *i.e.* when the fluid at the bow edge ceases to move rightwards. The role of stem overhang alone can be inferred by comparing cases a and b.

From a global point of view the three cases are quite similar, with Q about 13% of Q_0. A more local analysis would show that the water level for cases b and c is smaller than in case a, while the water-front velocity is larger. The slope of the water front along the deck is always rather small, though it is slightly larger in case a. As it will be discussed in chapter 5, the slope of the water front affects the severity of the impact with deck structures. However for slopes less than approximatively 40° it does not represent anymore an important factor for the effects of the water impact with a superstructure. On the other hand, the loads depend strongly on the impact velocity, thus on the wave-front velocity. Therefore, in this respect, the water impact due to an inclined bow can be worse even if the amount of shipped water remains roughly the same. Cases b and c do not exhibit a marked difference between them. Therefore, within the present two-dimensional analysis, the considered rather standard bulb does not seem to significantly influence the green-water loading.

Incoming wave parameters In the following, the body parameters are kept fixed, and the influence of steepness, H/λ, and wavelength-to-draft ratio, λ/D, on the relative amount of shipped water Q/Q$_0$ are discussed in left and right plots of figure 4.7, respectively. As expected,

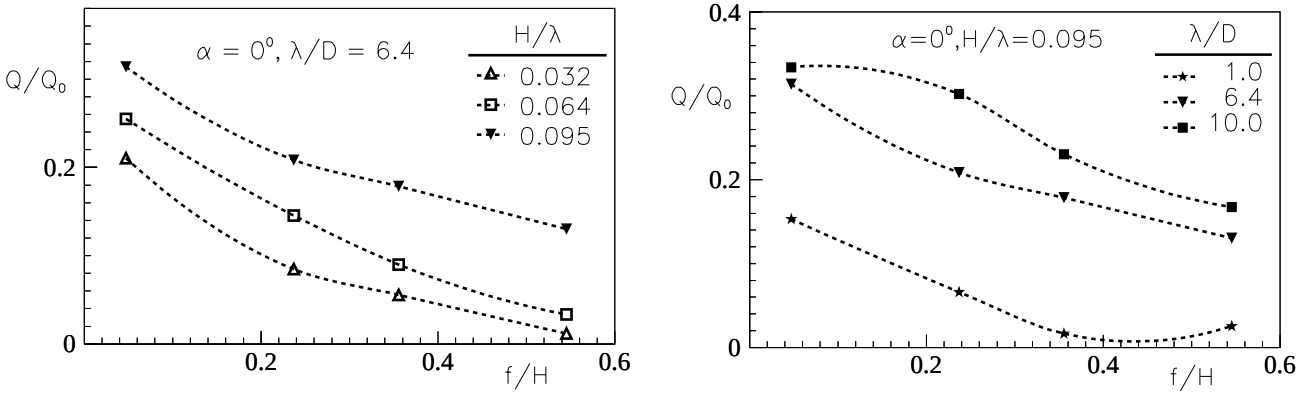

Figure 4.7 Left: influence of nonlinearity of incoming waves on the bow-deck wetness. Right: influence of wavelength-to-draft ratio on the bow-deck wetness.

by increasing H/λ we observe a larger amount of shipped water. There is an almost linear trend for small f/H. When f/H is larger, the nonlinear dependence of Q/Q_0 on the wave steepness is more pronounced. The reason is that Q becomes more strongly dependent on the wave crest flow, which will have an increased nonlinear behavior with increased wave steepness.

In the second plot, the effect of the wavelength-to-draft ratio is shown for a constant wave steepness and zero stem overhang. The deck-wetness severity changes a lot from case to case,

though the nonlinearities associated with the incoming waves are the same. The worst conditions occur for large wavelength-to-draft ratios where a smaller wave reflection is observed. The long wavelength case is also the more interesting from a practical point of view.

Time history of water-on-deck events In the previous analysis, only the first water-on-deck occurrence has been considered. Longer evolutions are now examined, and the history of shipping events is analyzed. In particular, figure 4.8 gives the amount of shipped water Q/Q_0 as a function of the time. The time origin has been shifted to coincide with the instant t_{wod1}

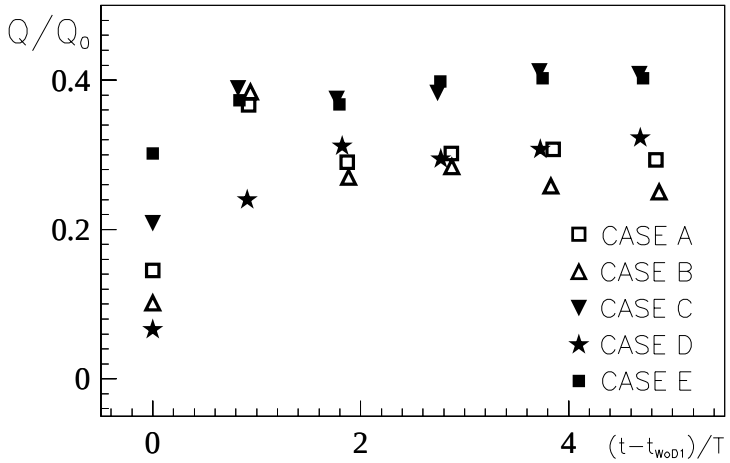

Figure 4.8 Time evolution of the relative amount of shipped water Q/Q_0. The considered cases A-E are described in table 4.1. For all the test-conditions $f/H = 0.24$.

of the first water-shipping event and the time is normalized by the wave period. For all the cases summarized in table 4.1, the same freeboard relative to the wave height $f/H = 0.24$ has

case	α	λ/L	H/λ
A	0^0	0.33	0.064
B	45^0	0.33	0.064
C	0^0	0.33	0.095
D	0^0	0.05	0.095
E	0^0	0.67	0.095

Table 4.1 Synopsis of cases considered for studying the history of water shipping.

been considered. Even if the chosen λ/L are small relative to design conditions, we should recall the previous shown insensitivity of Q/Q_0 to λ/L. Water-on-deck events (represented by the symbols) occur approximatively with the period of the incoming waves. Large changes of Q/Q_0 with respect to the first occurrence are observed in all cases. On a long time-scale Q/Q_0 seems to attain a nearly constant value. Clearly, this result is not general because more realistic sea-state conditions are characterized by irregular waves. However, large waves may reach the ship in groups and, in this context, the present result becomes relevant. Figure 4.8 indicates that if two succeeding waves with nearly the same height and wavelength cause deck wetness, the last one gives the most severe condition.

In more details, the figure shows that the worst water shippings happen for the steepest conditions (cases C and E). The corresponding Q/Q_0 tend almost to the same value, confirming the steepness as the most important wave parameter for long waves (in both cases the wavelength is large with respect to the draft). In case D, the steepness is the same but with shorter wavelength, equal to the draft, and the shipped water is comparable with that computed for a longer and less steep wave (case A). Case B (same parameters as case A but with $\alpha = 45°$) shows a certain effect of the stem overhang in reducing the severity of the deck wetness.

Figure 4.9 shows the free-surface profiles for cases A and B, left and right plots respectively, corresponding to the first four water-shipping events. Two configurations are given in each plot:

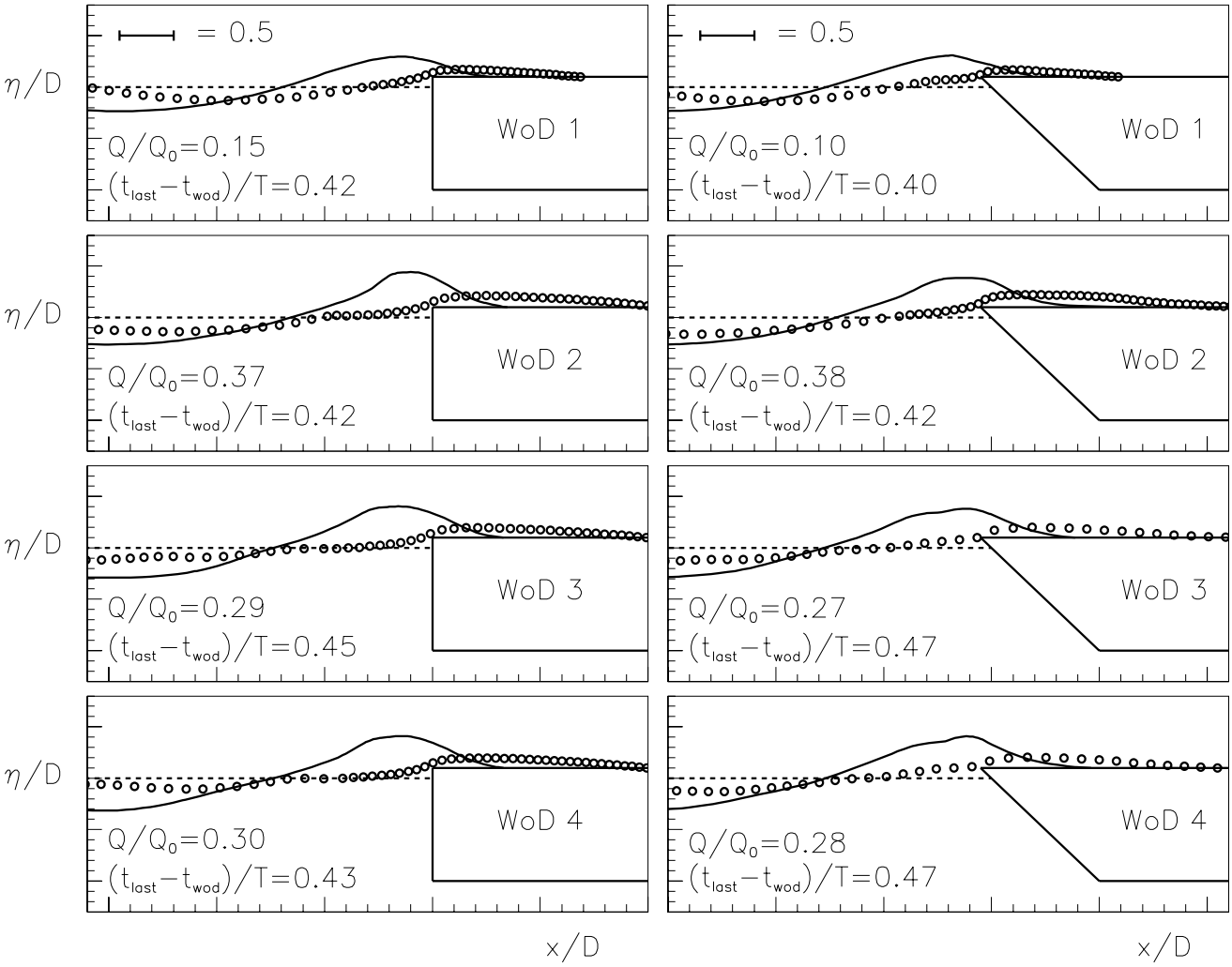

Figure 4.9 First four water-shipping events for cases A, left, and B, right. For each event, the free-surface configurations reported correspond to the maximum freeboard exceedance (solid line), and to zero-water flux entering the deck (circles).

the one with maximum freeboard exceedance (solid lines), and the one with zero flux of water onto the deck (circles).

Focusing on case A (left plots), we observe that the wave pattern in front of the body does not reproduce itself at each water-shipping cycle. This is reasonable because of the complexity of

wa v ereflection, with higher harmonics generated and reflected with non-trivial phase relations. In spite of this, the wa v eforms in the v ery near field and on the deck are rather similar for all the three latest even ts,consistently with the observation that an almost constant value of Q/Q_0 is measured. Here, t_{wod} is the time just after the freeboard exceedance, for which there is a positive inflow onto the deck, and t_{last} is the time when the shipping of water stops. With these definitions, we observe that the time duration of a water-on-deck cycle is roughly constant and about 40% of the wa v eperiod T.
Case B refers to a geometry with stem angle of 45°. From a global point of view, the relative amount of shipped water is not significantly affected by the stem angle (*cf.* right plots of figure 4.8), at least for the present choice of α.
The local details of the flow on the deck are more clearly influenced b y the stem o v erhang. F or both A and B cases, a wedge-like water front is observed but with a smaller interior angle and higher v elocity for the geometry with 45° stem o v erhang. The water level along the deck is smaller. As we will discuss in chapter 5, the impact pressures on a deck house are most sensitive to the impact v elocity, but are also influenced b y the other flow characteristics. Therefore, it is hard to giv econclusive arguments about possible positive or negative effects of α from the impact-problem point of view. We may be naively tempted to believe that a large stem ov erhang prevents the water for coming on deck. On the other hand, it seems difficult that geometrical details could counteract effectively the large horizontal velocity in the incident wa v e,especially for long wa v es.

Of course, in this respect, the limitations of present inv estigation should be noted. The analysis is two-dimensional and the body motions are not included. The stem o v erhangor the flare may affect the ship motions, and in turn the interaction with wa ves. F orinstance, Lloyd *et al.* (1985) reported model-test results where the bow flare caused a clear increase of the relative v ertical motions in the bow area. The stem o v erhangmatters also in the case of breaking wa v es hitting close to the bow. During the two-dimensional water on deck experiments discussed in chapters 7 and 8, the effects of larger bow forces were noted when a v ertical bow was substituted with a 45° stem angle bow. However bow impact phenomena are not focused on in the present work.

4.4 Influence of Body Motions

Body motions play a major role in determining the occurrence and severity of water on deck. Here, we are not solving the problem for a floating body free to respond to incoming wa v es. More simply, the body motion is prescribed *a priori*. In particular, since the present work deals with bow-deck wetness in head sea, the effect of forced heav e motion is studied. We have had in mind the relevant local heav e at the bow. The effect of the pitch angle both on the outer wa v e field and on the flow along the deck is neglected. Since the stem o v erhangangle has a small influence, one could argue that the pitch angle should not be important for shipping of water on the deck. On the other hand, the pitch angle may effect the flow on the deck. The influence of this parameter is studied at the end of this section.

The top left plot of figure 4.10 gives the first water-on-deck occurrence for the case E from the table 4.1, with a freeboard ratio $f/H = 0.55$. The body is constrained and $Q \simeq 16\,\%$ of Q_0.

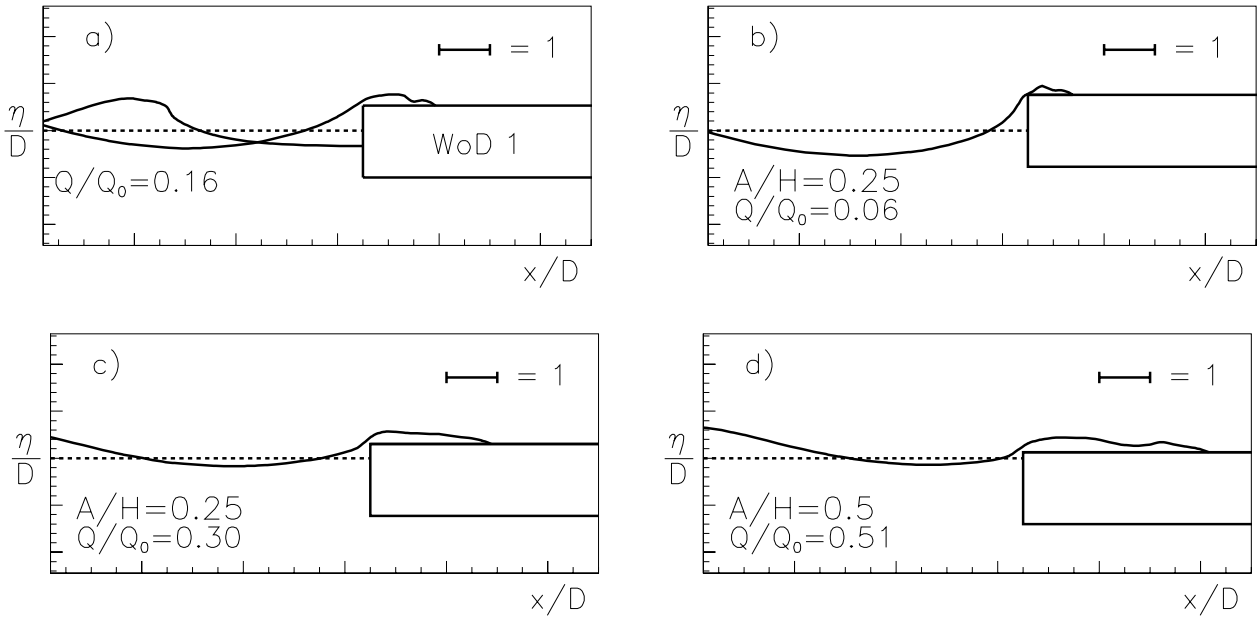

Figure 4.10 Influence of body motion. a) restrained body conditions, b) forced heave initially in phase with the water at the bow, c) and d) forced heave initially out-of-phase with the water at the bow.

For the same parameters, the plots b) through d) show the flow when a forced heave motion is excited at the beginning of the water shipping. The adopted law of the motion is

$$\zeta_3(t) = \pm A\mathcal{H}[t - t_{wod}] \sin\left[\frac{2\pi}{T}(t - t_{wod})\right], \tag{4.1}$$

where $\mathcal{H}$ is the Heaviside function. In all cases the free-surface configuration with almost zero water flux on the deck is shown.

In plot 4.10.b the motion is initially in phase with local wave motion, corresponding to the plus sign in equation (4.1). The amplitude-to-wave height ratio A/H is 0.25. The phenomenon appeared qualitatively less severe, with the amount of shipped water $Q \simeq 6\%$ of Q_0. However this nice situation is unlikely to occur in the case of a FPSO unit for the chosen wave-body parameters. Conditions of out-of-phase body motions are more reasonable and can make the water on deck much more severe than in the restrained body case. In facts, a heave amplitude $A = 0.25H$, plot 4.10.c, increases the amount of shipped water by a factor 1.9 relative to case a). When $A/H = 0.5$ (see plot 4.10.d), the factor becomes 3.2 and reaches 6.2 in the case, not shown, with $A/H = 1$.

In the following the role of pitch angle is examined. Even if the time scales of the water on deck before the water hits the deck house could be O(25%) with respect to the incident wave period, we have considered a "quasi-steady" approach as first approximation and studied the influence of a constant pitch angle. In this way the pitch angle is considered as a trim angle, in practice. The studied case is defined in the left sketch of figure 4.11. In the right of the same figure the first (top) and the second (bottom) water-on-deck events are examined in the case of zero trim angle (dashed lines) and trim angle $\zeta = -5°$ (solid lines), with two time instants for each event increasing from left to right. Restrained body conditions and vertical bow at zero

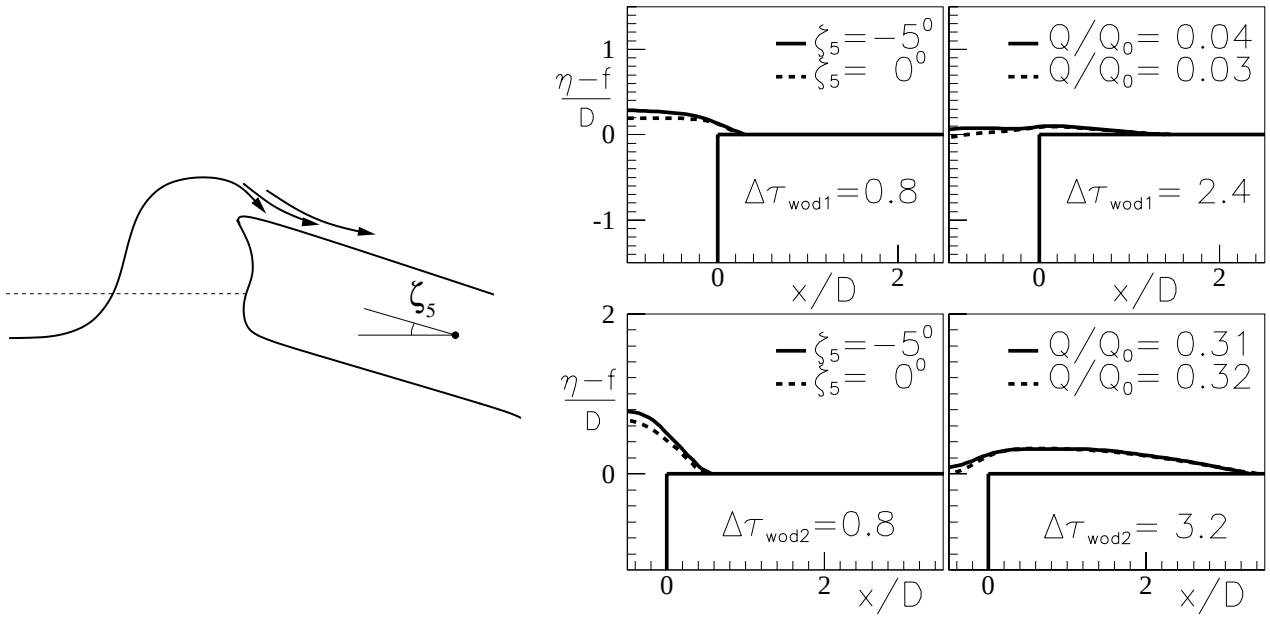

Figure 4.11 Influence of trim angle. Left: sk etch of the problem. Right: cases $\zeta_5 = -5$ and 0 degrees are compared for the first (top) and the second (bottom) w ater-on-deck even ts and restrained body conditions. $\alpha = 0°$, $L/D = 10$, $\lambda/L = 1.5$, $H/\lambda = 0.064$ and $f/H = 0.38$. $\Delta\tau_{\text{wod}} = (t - t_{\text{wod}})\sqrt{g/D}$.

trim, $L/D = 10$, $\lambda/L = 1.5$, $H/\lambda = 0.064$ and $f/H = 0.38$, are assumed. A negative trim angle (see sketc h in figure 4.11) should qualitatively increase the wa v e reflection from the body in the same wa y as a positive stem angle. Further, since the component of the gravity acceleration $\vec{g}$ parallel to the inclined deck counteracts the water shipping in the case of a negative trim angle, one should expect reduced wa v efront velocity along the deck. F romthe results, however, both the amount of shipped water, the water level and the velocity of the water flow propagating along the deck are practically unaffected b y the trim angle.

4.5 Occurrence of Waves Plunging on the Deck

The flow along the deck resembles the one after a dam breaking in the most common type of green water even t. Recent experiments in irregular seas (MARINTEK 2000) showed that water on deck can also occur in the form of large wa v es plunging directly on the deck or superstructures. This phenomenon appears lik e a "single" even t associated with a v ery steep, almost breaking, incoming wa v e, usually propagating in small background wa v es. Actually, one cannot classify this as "freak wa v e", but it is known that instability and modulation of wa v egroups in open sea can lead to the formation of steep highly energetic wa v es. Their interaction with structures is a known cause of highly nonlinear force components (Chaplin *et al.* 1997, Welc h *et al.* 1999). Similar circumstances in complex combination with ship motions can cause these extreme events. In this work only regular steep wa v eshav e been modeled. In spite of this, some extreme cases with emphasis on the effect of body motions hav e been analyzed to gain insights in to this aspect. The geometric parameters hav e been deduced from the MARINTEK experiments ($L/D = 13.75$, $f/D = 0.8$, $d_s/D = 1.0625$). Due to the limited role of the stem o verhang, the bow was

approximated with a straight vertical wall. Further, a wave train of long steep (eventually) regular waves with $\lambda/L = 1.022$ and $H/\lambda = 0.095$ is considered. The focus is on the interaction of the body with the leading wave which is characterized by high steepness and strong tendency to break. This makes the analysis more consistent with the features observed in the experiments. Forced heave motion is excited at a time instant t_0 with an amplitude A and a phase β, in the form

$$\zeta_3(t) = A\mathcal{H}[t - t_0] \sin\left[\frac{2\pi}{T}(t - t_0) + \beta\right] . \tag{4.2}$$

Here T is the wave period. Wave generation starts at $t = 0$, with the upstream vertical boundary (*cf.* section 2.2) located 5 wavelengths ahead of the bow. The phase angle β is selected to give a sudden vertical displacement of the ship at $t = t_0$. Some of the studied cases, and discussed in the following, are summarized in table 4.2.

case	f/H	A/H	β	t_0/T	t_{wod}/T
a	0.6	0.	–	–	10.795
b	0.6	0.5	-90^0	10.626	10.841
c	0.6	0.5	-5^0	10.783	10.844
c1	0.6	0.25	-10^0	10.783	10.795
c2	0.6	0.125	-20.5^0	10.783	10.790
d	0.6	0.5	-11^0	10.783	10.783

Table 4.2 Plunging wave analysis: summary of presented cases.

In left plot of figure 4.12, restrained body conditions are considered, and some free surface configurations are presented. The wave, reaching the bow, is steep and unsymmetric but its tendency to break is reduced during the run-up along the bow. The water shipping starts with already quite large horizontal velocities of the fluid making the phenomenon less similar to the dam breaking problem. Though the shallower water conditions on the deck would amplify the original tendency to wave breaking, the fast motion of the wave front has opposite effect and is the main reason why the wave is not breaking before the water impacts on the deck house.

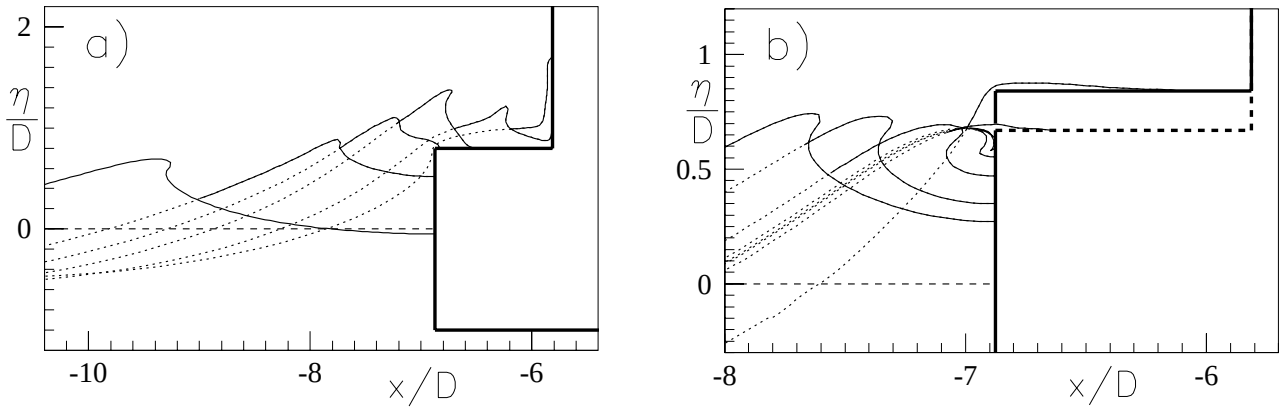

Figure 4.12 Plunging wave analysis: case a (left) and case b (right) in table 4.2.

The heave motion largely affects the phenomenon. In the next figures (right plot of figure 4.12 and plots of figure 4.13), a heave with amplitude $A/H = 0.5$ is considered (see table 4.2 for the other parameters). In case b (right plot of figure 4.12), the motion is excited with a phase such that the instantaneous freeboard at $t = t_0$ is higher than the wave elevation at the bow. By "instantaneous freeboard" is meant the mean freeboard plus the change in vertical position due to heave. The upward motion of the bow causes lower trough ahead of the breaking wave and a bow impact occurs. Air entrapment and (probably) a complex two phase flow are expected to occur. By neglecting these phenomena and "stretching" the simulation further, it appeared that the shipping of water is not particularly severe. The upward motion of the bow, in facts, limits the increase of the vertical velocity of the fluid after the impact.
In the plots of figure 4.13 the heave motion is excited later than in the previous case. This is done in both situations at the same instant but with different initial phase. This means a different instantaneous freeboard, in particular for case d the wave elevation at the bow is equal to the instantaneous freeboard. The larger t_0 eliminated the bow impact. However other interesting

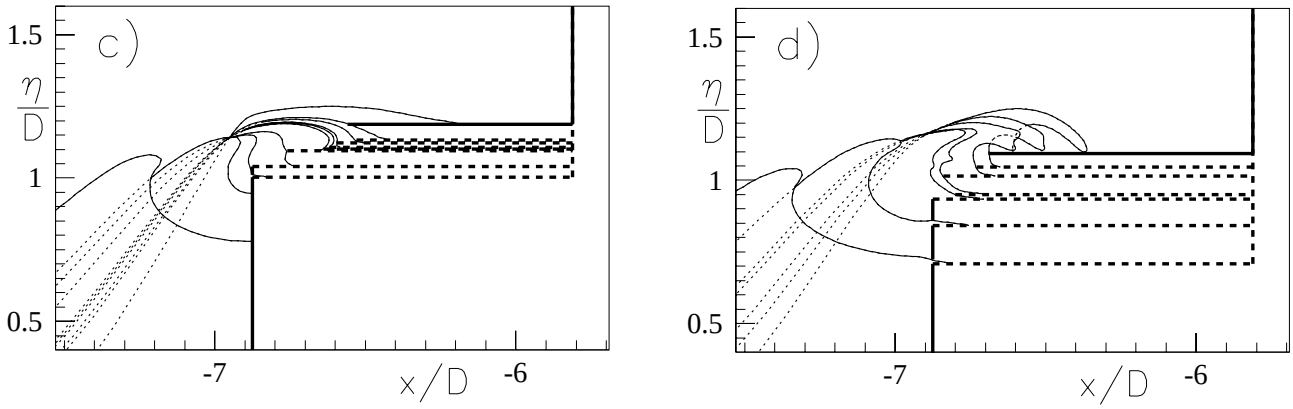

Figure 4.13 Plunging wave analysis: case c (left) and case d (right) in table 4.2.

phenomena occurred. In case c, an initial local breaking tendency of the water along the deck is observed. But this is prevented by an increase of the horizontal velocity of the contact point between water and deck. The subsequent flow is like the one after a dam breaking. In case d, the amount of shipped water is larger and the upward motion of the ship results in a wave plunging onto the deck. The three considered situations could have quite different consequences on the ship.
If case c is modified by taking a heave amplitude $A/H = 0.25$ and $A/H = 0.125$ but maintaining the same instantaneous freeboard at $t = t_0$, the results shown respectively in left and right plots of figure 4.14 follow. The water on deck is still quite serious but the consequences are more dangerous for the superstructure than for the bow or the deck. With $A/H = 0.25$, in particular, the faster rate of the water region to become shallower steepens the wave propagating along the deck. A rather thin jet develops. The jet evolves faster than the water-deck contact point and eventually hits the superstructure. After the impact the simulation was continued by a local matching with the similarity solution by Zhang *et al.* (1996) for an infinite asymmetric fluid wedge hitting a flat wall (see sketch D.1 in appendix D). If the heave amplitude is further decreased (case c2, right plot of figure 4.14), the velocity of the wave front becomes larger relative

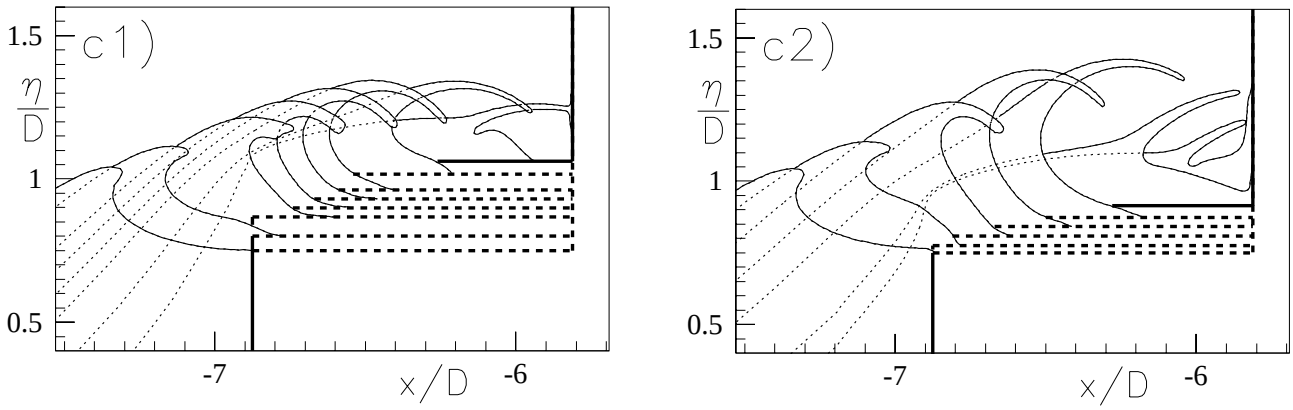

Figure 4.14 Plunging wa v e analysis: case c1 (left) and case c2 (right) in table 4.2.

to the plunging jet v elocity . This implies that the impact with the superstructure occurs from the deck. The plunging wa v e hits the water mass rising along the vertical wall after the impact. This causes an air pock et to be formed. The relative velocity between the developing plunging jet and the wa v efront depends on the rising rate of the deck. This has an important influence on the possibility of a plunging breaker hitting the superstructure.

F romthe n umerical inv estigations, the occurrence of this extreme event seems to be related to the in teraction with a steep wa v ealmost breaking, more than to the wa ve-body interaction b y itself. Howev er, the influence of ship motion to enhance or reduce its severit y can not be excluded, as suggested, for instance, b y case d (see figure 4.13.d), though the wa v eplunges far from the superstructure.

Chapter 5

Dam Breaking and Water Impact

In this chapter, a dam-breaking flow is used as a prototype problem to investigate the flow along the deck and the subsequent water impact against vertical structures, usually built on decks of ships. Secondly, a parametric analysis of the water impact against a wall is carried out by varying the wall slope and the local characteristics of the incoming flow. The latter are characterized by the wavefront velocity and the local free-surface geometry close to the intersection point with the deck. Finally, the influence of the hydroelastic interaction between the structure and the surrounding fluid is discussed by using a linear Euler beam model for the wall.

We briefly mention that other prototype problems have also been investigated, such as the collapse of water columns, the water run-up along straight walls with different slopes, the initial and the later stages of the flow generated after the breaking of a dam, which served to verify the numerical model and to gain confidence with the physical problem. These cases are collected in appendix C.

5.1 Dam Breaking and Water Impact

As we discussed, when the wave elevation exceeds the freeboard, the water can flow over the deck. Very often, the resulting flow field resembles the one after a dam breaking (*cf.* section 1.1). Therefore, the dam-breaking flow represents a natural prototype problem to gain physical understanding of our (more general) problem. Moreover, the simpler flow conditions allows to better verify and validate our numerical model, and finally a large set of data are available in the literature.

In the following, we consider in details the problem sketched in figure 5.1. A reservoir of water with height h and length $2h$, closed by a dam, is placed at a distance $3.366\,h$ from a vertical obstacle. With the present choice of geometrical parameters, the considered problem reproduces the experimental conditions adopted by Zhou *et al.* (1999). In particular, the authors made available measurements of the wave height at the locations marked by A and B in the figure, and the pressure induced on the vertical wall at location C.

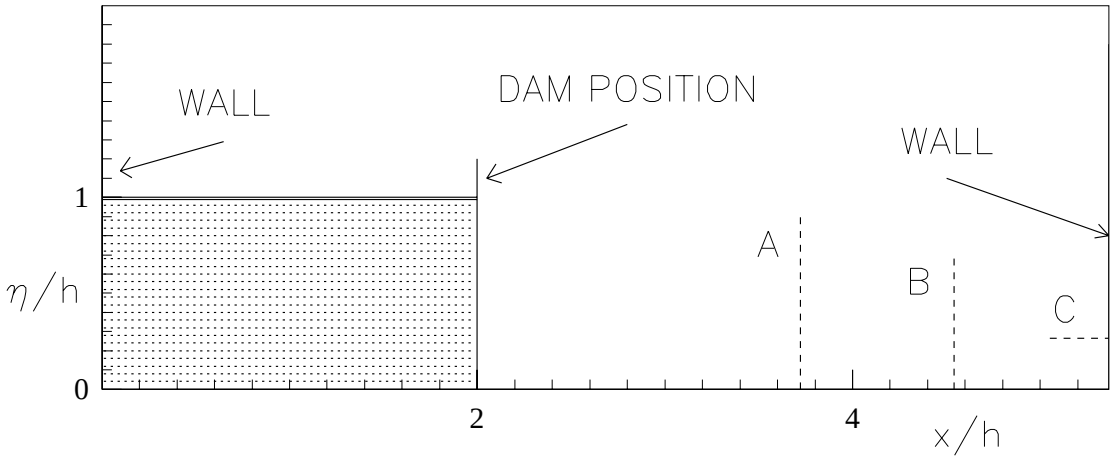

Figure 5.1 Dam-breaking problem and impact against a vertical rigid wall. Sketch of the problem and of the experiment performed by Zhou *et al.* (1999) with $h = 0.6$ m. Wave-gauge locations A and B, and pressure-transducer location C, are shown.

At the beginning, say $t = 0$, the dam is suddenly removed and the flow develops along the horizontal deck, figure 5.2.a, finally impacting against the vertical wall. The fluid is violently

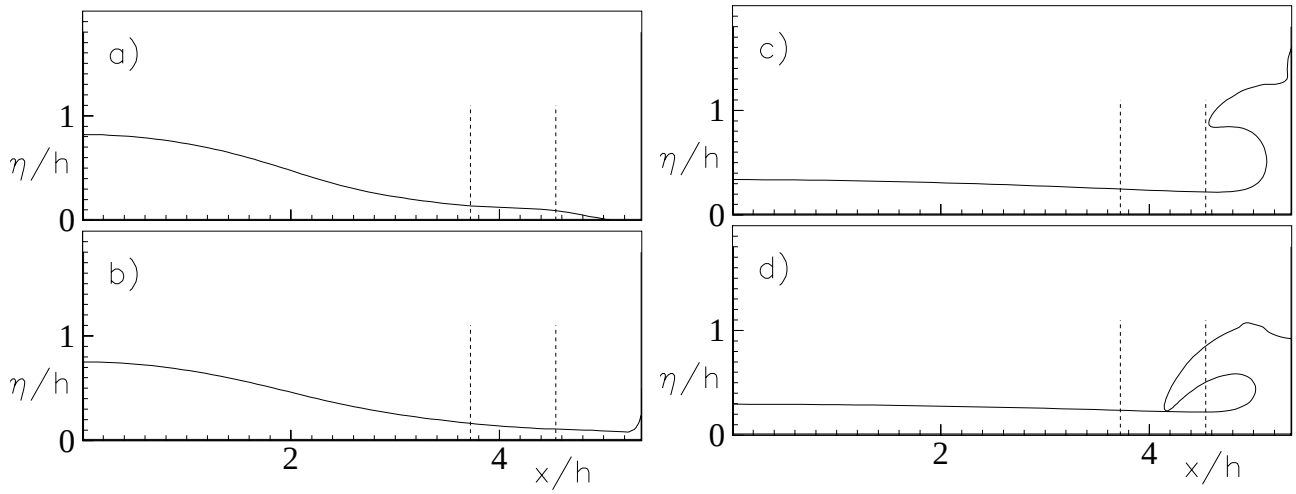

Figure 5.2 Free-surface flow and impact against the vertical wall following the breaking of the dam (cf. figure 5.1). $\tau = t\sqrt{g/h}$ (t) 2.2 (0.54 s), 2.6 (0.643 s), 5.6 (1.385 s), 6.2 (1.534 s).

deviated vertically upwards, figure 5.2.b, rising along the wall in the form of a thin layer of fluid. At this stage, formation of spray and fragmentation of the free surface may occur. These finer details cannot be handled by the present method. However, it is believed they are irrelevant for computing structural loads. As time increases, under the restoring action of gravity, the fluid acceleration decreases and the upward velocity in the jet decreases until it becomes negative. The motion of the water is reversed in a waterfall, figure 5.2.c, overturning in the form of a wave plunging onto the deck, figure 5.2.d. The numerical simulation has then to be stopped.

The plots in figure 5.3 give the time evolution of the water height h_w at the locations $(x/h)_{\mathrm{A}} = 3.721$ and $(x/h)_{\mathrm{B}} = 4.542$ along the deck (*cf.* figure 5.1). Both the experiments and our numerical

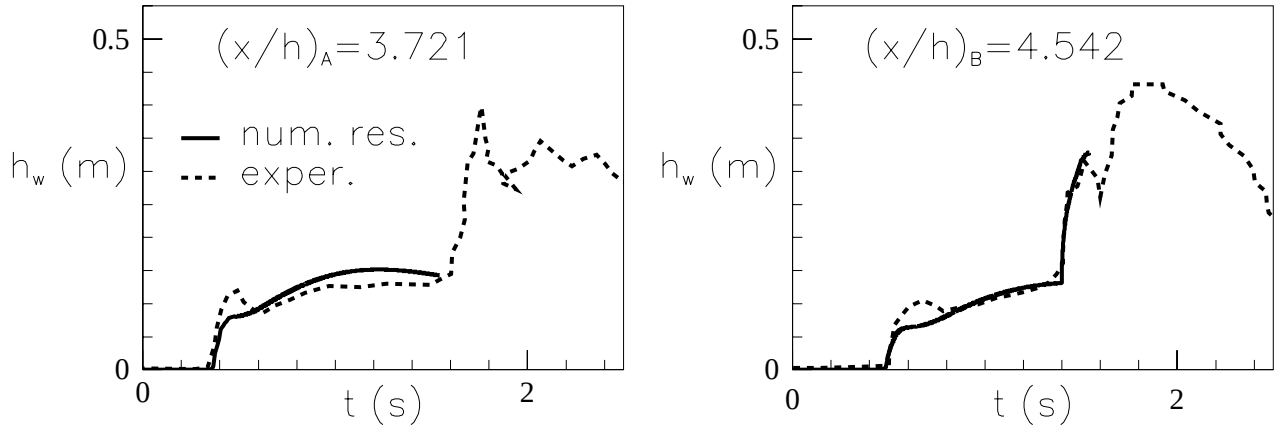

Figure 5.3 Time evolution of the experimental (Zhou *et al.* 1999) and numerical water levels h_w at $(x/h)_{\rm A} = 3.721$ and $(x/h)_{\rm B} = 4.542$. Wave-gauge locations A and B are shown in figure 5.1.

simulation allow to identify the three fundamental stages in the evolution of the flow field. The Stage I is characterized by the sudden rise of the water level h_w, due to the transition from dry-deck conditions to wet-deck conditions. Clearly, the shape of the water front determines the growth rate of h_w, and some differences can be detected between the numerical solution and the experimental measurements, which we will comment later on.

The main feature of the following Stage II is the much slower growth rate of the water level because of the almost flat free surface above the wave gauges. This is well confirmed by plots b and c in figure 5.2, which correspond to the physical times of 0.643 s and 1.385 s, respectively.

Finally, the numerical simulation allows to understand the origin of Stage III, characterized by a new steep increase of h_w. This is apparently due to the water overturning (*cf.* plots 5.3.c and 5.3.d) which gives an additional contribution to the wave height measured at the location B. Later on, also the signal recorded by the gauge located in A displays this phenomenon, which cannot be followed further on by the present numerical method which breaks down when the free surface plunges on itself.

Due to lack of details about the experiments, the numerical simulation and the experimental record at location A have been synchronized when h_w attains a non-zero value.

We discuss now the impact of the water front against the vertical structure. During the first stage of the impact, the flow resembles that due to a (half) wedge of fluid hitting a straight wall. Apparently, the rest of the flow field is nearly unaffected by the impact. Since the vertical acceleration of the fluid around the contact point is $\mathcal{O}(5g)$, the gravity plays a minor role. This is better shown in plots 5.4.a1-a4, where the free surface near the wall, after the impact, is plotted together with the zero-gravity similarity solution by Zhang *et al.* (1996), where we considered an infinite wedge of fluid hitting the wall at 90°. Plots are progressively enumerated as the time increases. More specifically, by defining $\tau_{\rm imp} = t_{\rm imp}\sqrt{g/h}$ as the initial non-dimensional impact time, we report the time instants $\Delta\tau_{\rm imp} = \tau - \tau_{\rm imp} = 0.0138, 0.0243, 0.0738$ and 0.1338. The two solutions remain in qualitative agreement even for a non-dimensional time $\Delta\tau_{\rm imp} = 0.1338$ after the impact, confirming a limited role of the gravity in the early stage of the impact.

The impact pressures are now discussed in more detail. Plots b1-b4 in figure 5.4 present the pressure distributions corresponding to the free-surfaces configurations a1-a4. According to the

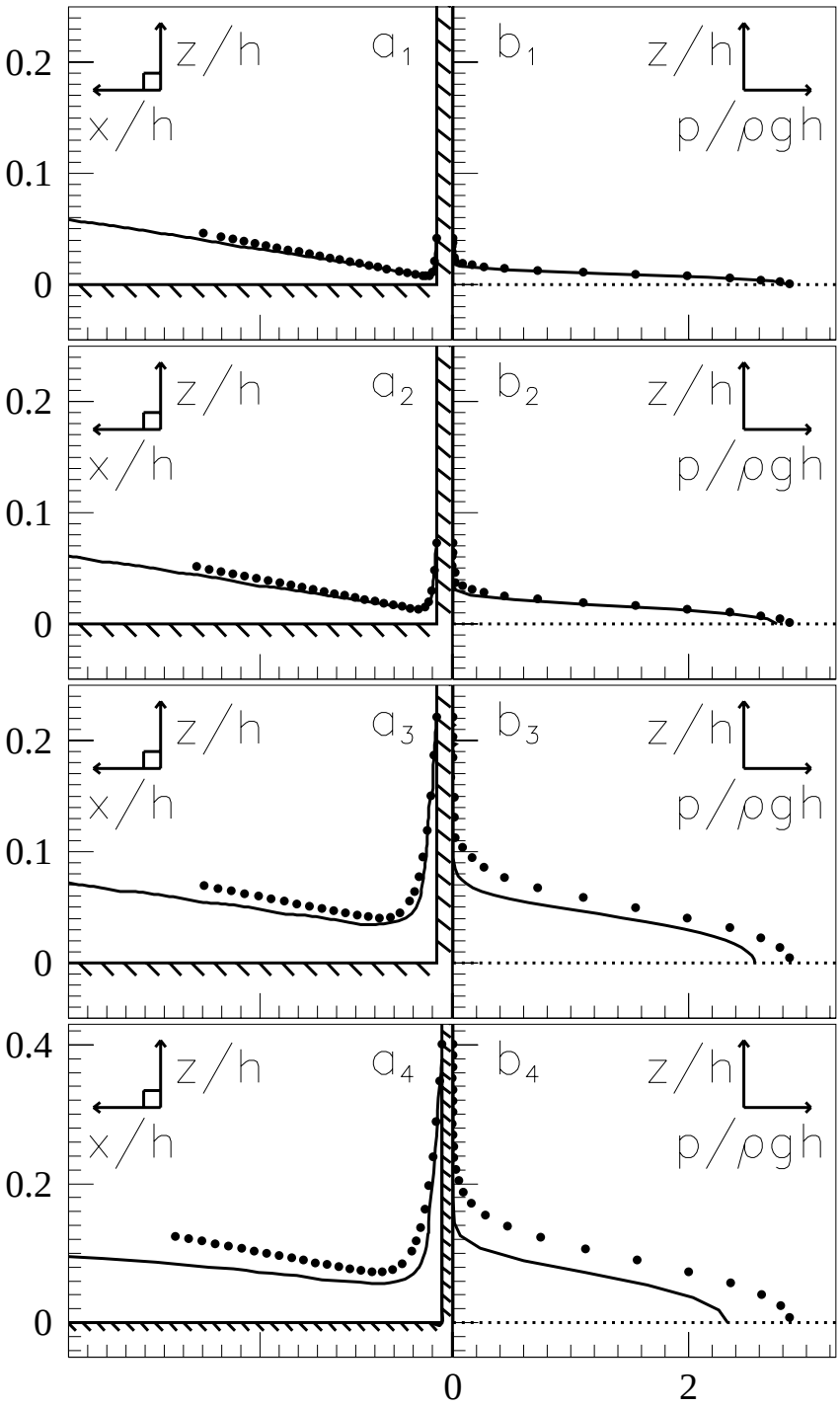

Figure 5.4 Free-surface profiles (a1-a4) and pressure distributions (b1-b4) during the initial stage of the impact against the vertical wall. Solid lines: present numerical simulations; •: similarity solution from Zhang *et al.* (1996); $\Delta\tau_{\text{imp}} = \tau - \tau_{\text{imp}} = 0.0138, 0.0243, 0.0738, 0.1338$. τ_{imp} is the initial non-dimensional impact time. Plots are progressively enumerated as the time increases.

numerical results (solid lines), at each time instant the maximum value of the pressure is located at the initial impact position and attains the highest values just after the impact. In the region

of the thin jet along the wall, the pressure is almost equal to the atmospheric one, which we conventionally set to zero.
The symbols represent the pressure distribution from the gravity-less solution of a fluid wedge hitting a flat wall. A formula for the pressure distribution is not available in the original paper by Zhang *et al.* (1996), and this has been evaluated by solving numerically the integral equation for the velocity potential along the wall, where the boundary data on the free surface have been taken from the similarity solution of Zhang *et al.* (1996). Details on this procedure and the correction of some misprints in the original paper by Zhang *et al.* (1996) are reported in appendix D.

At the beginning, the agreement between the two different analyses is good (solid lines *vs* circles), consistently with the agreement between the corresponding free surfaces. As time goes on, pressure distributions seem to disagree more rapidly than the free-surface profiles, although they qualitatively remain of the same shape for all the considered time instants. To be noted, in particular, is the tendency of the gravity to weaken the maximum pressure, while it remains constant in the zero-gravity case. This is due to a reduction of the $-\rho\,\partial\varphi/\partial t$ contribution to

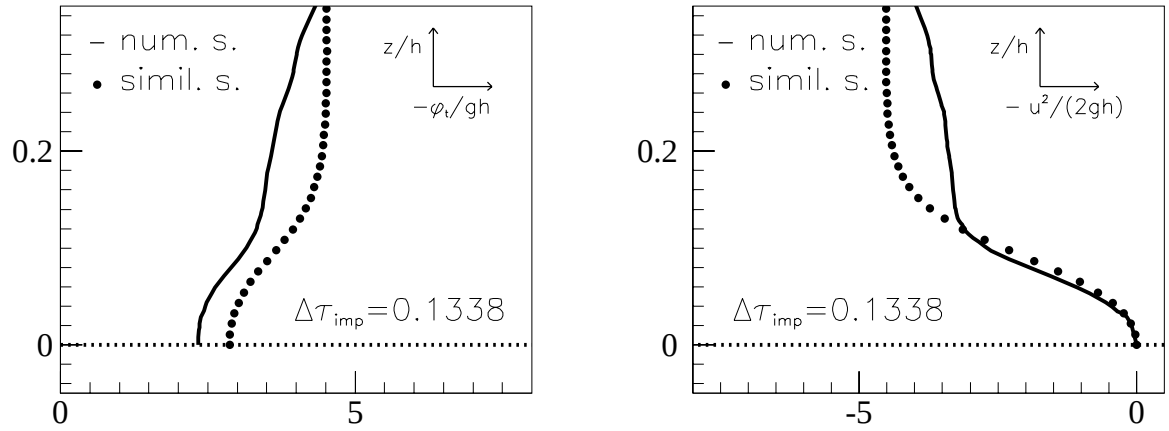

Figure 5.5 Water impact against the vertical wall. Terms contributing to the dynamic pressure along the wall: comparison between the numerical solution with gravity, solid lines, and without gravity (with free surface data from the similarity solution by Zhang *et al.* 1996), bullet symbols. Left plot: $-\partial\varphi/\partial t/gh$. Right plot: $-u^2/2/gh = -|\nabla\varphi|^2/2/gh$. $\Delta\tau_{\rm imp} = \tau - \tau_{\rm imp}$. $\tau_{\rm imp}$ = initial non-dimensional impact time.

the pressure (*cf.* left plot of figure 5.5 for $\Delta\tau_{\rm imp} = 0.1338$), as we can infer by looking at the $-\rho\,|\nabla\varphi|^2/2$ term, plotted in the right of figure 5.5. Near the initial impact position, the difference in the prediction of the $-\rho\,\partial\varphi/\partial t$ term is more pronounced than that of the velocity contribution to the pressure. In the latter case, near the initial impact position the two solutions are roughly superimposed.

The numerical solution was verified by comparing the horizontal force $F_x(t)$ exerted on the wall as evaluated by direct pressure integration and by conservation of fluid momentum (see *e.g.* Faltinsen 1990). In the latter case, a control volume bounded by the instantaneous wetted surface of the wall, l_W, a vertical control surface, l_C, at a distance $x/h = 1$ from the wall, and the portions of free surface, l_{FS}, and deck, l_B, between them, has been considered (see left plot of figure 5.6). The two results agree well, except at the very beginning (*cf.* right plot of figure 5.6).

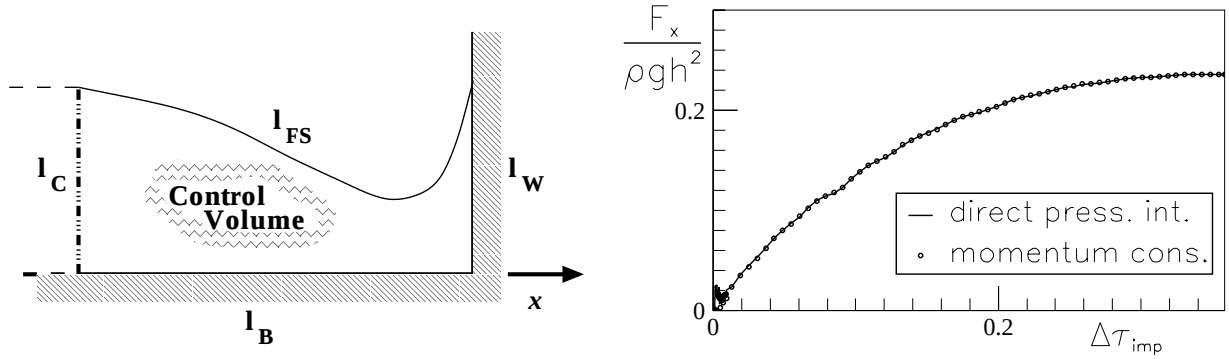

Figure 5.6 Left: control volume where the conservation of the fluid momentum is applied. Right: time history of the horizontal force F_x on the vertical wall shown in figure 5.1. Numerical results obtained with direct pressure integration (solid lines) and conservation of fluid momentum (circles).

Zhou *et al.* (1999) measured the wave pressure on the vertical wall during the impact by a circular shaped gauge, with diameter 0.09 m and centered at the location C on the wall (see figure 5.1) and sketched on the left of the figure 5.7. In the right plot, the time evolution of the measured pressure (dashed line) is given together with the pressure obtained by the present numerical simulations.

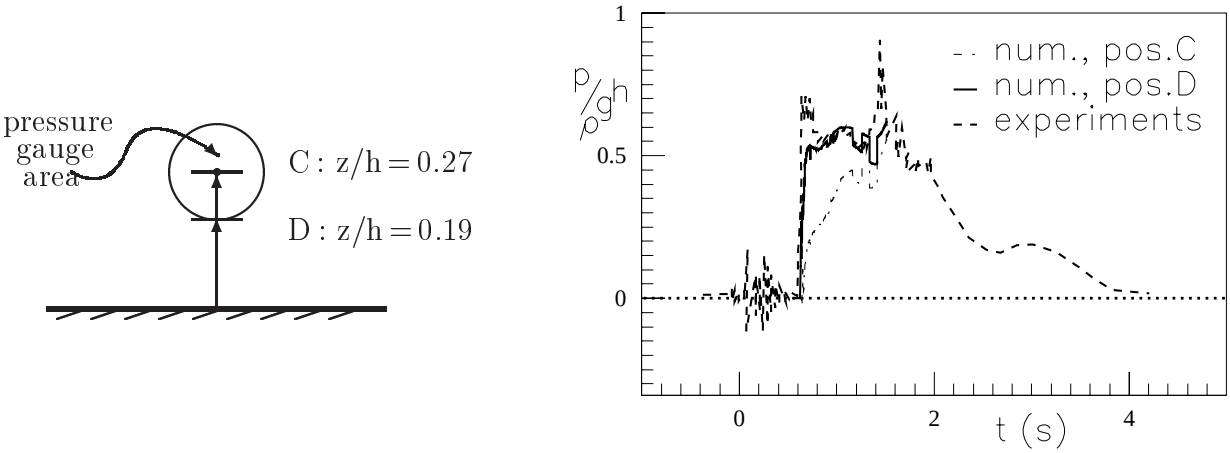

Figure 5.7 Left: position of the pressure gauge in experiments by Zhou *et al.* (1999, $h = 0.6$ m). Right: experimental and numerical evolutions of the pressure along the vertical wall (see sketch 5.1).

The dash-dotted line refers exactly to location C. The two curves attain non-zero values almost at the same instant, confirming the global agreement between the numerical simulation and the experiment. It is worth stressing that the two signal have been shifted consistently with the shift used to synchronize the wave data at location A.

A certain difference between theory and experiments is apparent, though mesh refinement and local regridding have been used to achieve invariance of the solution and to rule out the dependence on the discretization parameters. On the other hand, the complexity of the experiment makes it difficult to identify the error sources. Actually Zhou *et al.* (1999) commented that it was difficult to achieve repeatability of the results. Similar difficulties have also been observed during the two-dimensional water-on-deck experiments described in chapters 7 and 8. In the latter case, the main error source was the sensitivity of the pressure gauges to temperature

changes, primarily caused by dry-wet-dry cycles in the sensors conditions.

It can be observed that, for the actual scales of the experiment by Zhou *et al.* (1999), even a non perfectly dry deck (for example because of a previous experiment) can introduce significant differences in the measured data. This seems plausible also in the present case if we observe the water level comparison in figure 5.3. In facts, though the experimental and numerical evolutions are globally in satisfactory agreement, the numerical solution underpredicts the measured data in proximity of the instant of time when the water level attains non-zero value. In particular, the measured h_w has a maximum (for example around $t = 0.4$ s for the location A) which is not present in the numerical results. This experimental feature can be converted from a temporal to a spatial point of view and, in particular, suggests a hump in the free surface close to the contact point. This is not visible in the dam-breaking free-surface profiles reported in Dressler (1954), and could be due to the presence of a layer of water before the dam breaks. Dam-breaking experiments by Stansby *et al.* (1998) show that, if the deck is not perfectly dry due to leakage (in those experiments a film of water with a thickness about 1-2 mm was present downstream of the dam) a horizontal bulge of fluid develops just after the dam release, resulting in a small hump around the water front. This very peculiar local flow is consistent with the recorded water levels taken by Zhou *et al.* (1999). Unfortunately, the limited set of data available does not allow for a better verification of the present speculation.

Finally, we observe that the pressure undergoes large variation within the area of the transducers, and indeed the experimental pressure curve is closer to the pressure computed at the lower location of the transducer, indicated with the letter D in the sketch of figure 5.7.

5.2 Parameters Influencing the Impact

5.2.1 Angle of the Incoming Water Flow and Impact Velocity

Previous results for the impacting flow against the wall suggest the possibility of using a gravity-less similarity solution to explore the parameters influencing the impact, at least for the initial stage when the acceleration is large compared with gravity. In this respect, this simplified approach is equivalent with that used to deal with slamming problems.

On this ground, we will consider the problem of a semi-infinite wedge of fluid impacting on a vertical wall at 90° incidence. Under the zero-gravity assumption, the problem is completely specified by the velocity V of the wedge and by its angle β (see sketch in figure 5.8). In the actual problem, we will consider V as representative of the velocity of the water front along the deck, and β as the slope of the free surface at the contact point with the deck.
With this approximate model (similarity solution by Zhang *et al.* 1996 *plus* numerical pressure evaluation, see appendix D), we obtained the non-dimensional maximum pressure $P_{\max}/\rho V^2$ as function of β shown in the center plot of figure 5.8. As it can be expected, the maximum pressure increases as the wedge becomes wider. The spatial distribution of the pressure is given in the right plot. When $\beta < 35°$, the peak pressure occurs at the intersection between the wall and the deck, while for larger angles $P_{\max}$ is shifted upwards along the wall. Also the shape of the pressure distribution changes gradually as β increases, leaving a plateau between the pressure peak and the intersection of the wall with the deck.

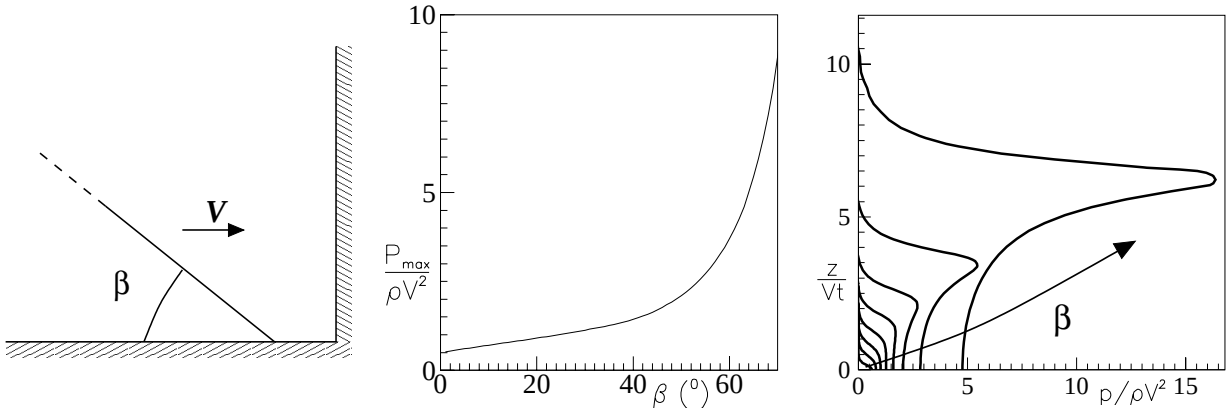

Figure 5.8 Left: sketch of the equivalent problem of a fluid (half) wedge impacting a flat wall at 90 degrees. Center: maximum pressure on a wall due to the waterimpact. Right: pressure distribution along the vertical wall for $5° \leq \beta \leq 75°$ with increment $\Delta\beta = 10°$. The results are numerically obtained by using the similarity solution by Zhang *et al.* (1996) for the free surface conditions.

It can be seen, that the derivative $d[P_{\max}/\rho V^2)]/d\beta$ is large only for $\beta >\sim 60°$, and becomes quite small for $\beta <\sim 40°$. Therefore, below such angle, the pressure is mainly influenced by the velocity V.

When β is large enough, the results agree qualitatively with a Wagner (1932)-type analysis (*cf.* figure 5.9). This analysis implies that the examined fluid particles at initial time of impact are on the surface of the fluid wedge, and that they will move normally to the wall with the initial velocity V increased by a contribution due to the impact against the wall. The Wagner-type

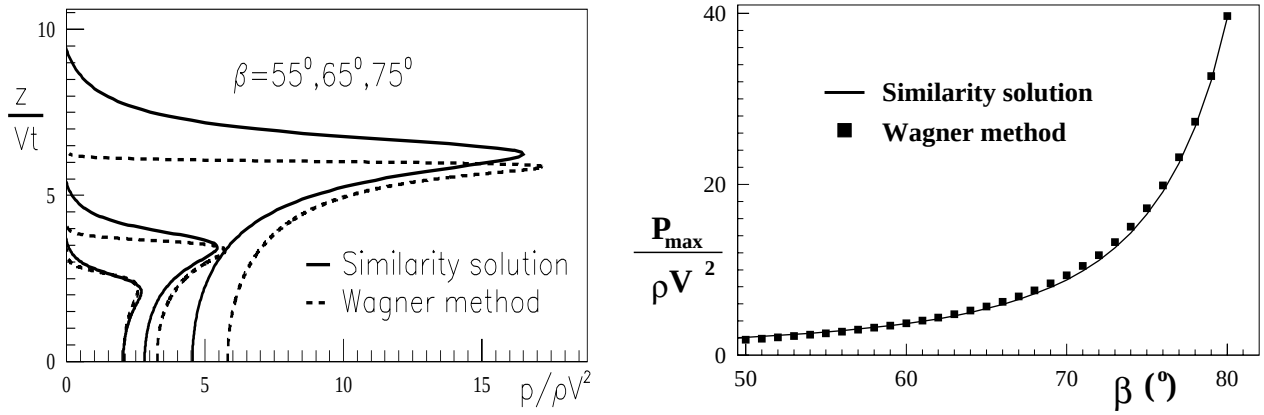

Figure 5.9 Left: distributions of pressure p along a vertical wall due to the impact of an infinite (half) wedgeof fluid. Similarity solution by Zhang *et al.* (1996), solid lines, Wagner method, dashed lines. Right: maximum pressure along the wall. Similarity solution, solid line, and Wagner method, black squares. V: impact velocity,β: angle of the (half) wedge.

solution is calculated by a flat-plate approximation, with dynamic free-surface condition $\varphi = 0$, where φ is the (perturbation) velocity potential caused by the impact. The intersection between the fluid particles and the wall determines the length of wetted wall in an outer-flow domain, which can be matched with an inner-flow domain solution at the spray root. A composite

pressure distribution can be obtained as described by Zhao and Faltinsen (1993).

Comparisons between a Wagner-type analysis and the similarity solution are presented in figure 5.9 in terms of pressure distribution (left plot) and maximum pressure along the wall (right plot). The position and the value of the maximum pressure agree well. Differences occur at the upper part of the jet. One reason may be related to the fact that, in the similarity solution by Zhang *et al.* (1996), the shape of the free surface in proximity of the wall is not consistent with the local free surface in the Wagner-type analysis. On the other hand, the latter does not ensure the conservation of fluid mass when applied to the problem of a fluid wedge hitting a rigid flat wall.

A simplified solution for small interior wedge angles has been derived in appendix E, and the free surface elevation simply reads:

$$\eta \;=\; (x + Vt)\tan\beta \;-\; \int_0^t \frac{2V}{\pi} \ln\left(\tanh\frac{\pi x}{2a}\right) \mathrm{d}t\,, \tag{5.1}$$

with $a = 2Vt\,\tan\beta$. Figure 5.10 shows a good agreement between the free-surface elevation predicted by the simplified method and the similarity solution.

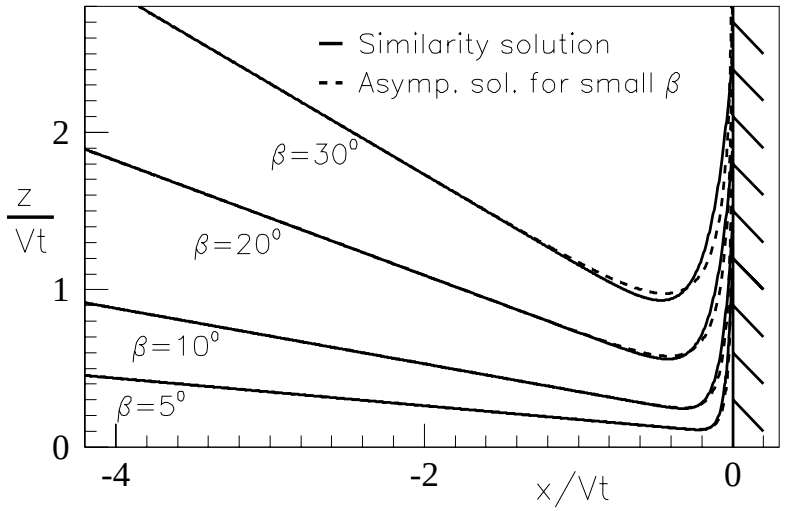

Figure 5.10 Free surface elevation close to a wall hit by an infinite fluid wedge with impact velocity V and semi-angle β. Asymptotic solution for small β, dashed lines, similarity solution by Zhang *et al.* (1996), solid lines.

Finally, figure 5.11 shows the comparison of the maximum pressure $P_{\max}$ between the similarity solution, the Wagner method and the asymptotic solution for small β. It is apparent how the small-β solution gives good predictions approximatively up to $\beta = 30°$, while the Wagner-type method agrees satisfactorily for β between $\sim 45°$ and $90°$ (*cf.* also right plot of figure 5.9). The asymptotic value for $\beta = 0°$ is the stagnation pressure $0.5\rho V^2$. The $-\rho\partial\varphi/\partial t$ term in the Bernoulli equation plays in general an important role in determining the maximum pressure.

It is then instructive coming back to the dam-breaking problem analyzed at the beginning of this chapter. In this case, the slope of the water front at a distance $\Delta x = 0.65h$ from the dam is $\beta \simeq 40°$ and decreases as the ratio $\Delta x/h$ increases. Therefore, for obstacles located farther than

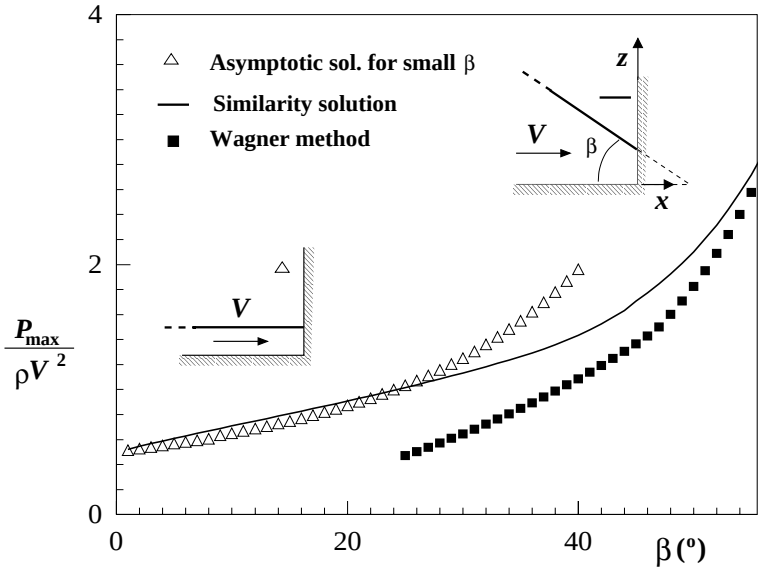

Figure 5.11 Maximum pressure on a wall hit by an infinite fluid wedge with impact velocity V and semi-angle β. Asymptotic solution for small β, triangles, pressure evaluated numerically by using the zero-gravity similarity solution by Zhang *et al.* (1996), solid line, Wagner method, full squares.

$\Delta x = 0.65h$ the maximum pressure exerted on the wall is not sensitive to the actual impact angle (see left plot of figure 5.8). In this range, from a practical point of view, an upper bound to the pressure $P_{\max} = f(V, \beta)$ is given by $P_{\max}(V) \simeq 1.4\rho V^2$.

It is worth stressing that in actual structural-response calculations the estimate of the maximum pressure only is not enough, and the entire (time dependent) pressure distribution on the wall has to be evaluated. In this respect, the pressure based on the similarity solution (*cf.* figure 5.4) has the advantage of a simpler numerical evaluation, though for increasing time overpredicts the exact results.

5.2.2 Slope of the Wall

It is known that the use of inclined structures reduces the pressure at the impact. This is confirmed by the following computations, reported in figures 5.12-5.13, where the exact dam-breaking problem has been solved to fully include the gravitational effects. For the case studied in section 5.1, the resulting impact parameters are $\beta = 11°$, and $V = 1.983\sqrt{gh}$, while the slope of the wall α (see sketch of figure 5.12) is varied between 0 and 40 degrees. The right plot in figure 5.12 shows the normal force acting on the wall for increasing values of α. In particular, as α increases, the force component increases with a smaller rate, resulting in a weaker load for a given time. As an example, when $\alpha = 40°$, at the end of the simulation, $F^{\alpha}_{n,\max}$ is about 50% of the value $F^{0}_{n,\max}$ obtained for the vertical wall ($\alpha = 0°$). In general, the ratio $F^{\alpha}_{n,\max}/F^{\alpha=0}_{n,\max}$ decreases almost linearly with α. The pressure values along the wall (*cf.* figure 5.13), and in particular the maximum pressure occurring at the position of first impact, decrease as α increases. The differences among the pressure profiles reduce as time increases.

Finally, we stress that in the simulation a rigid wall has been assumed, though the pressure distribution could be influenced by hydroelastic effects. In this case, it is important to introduce

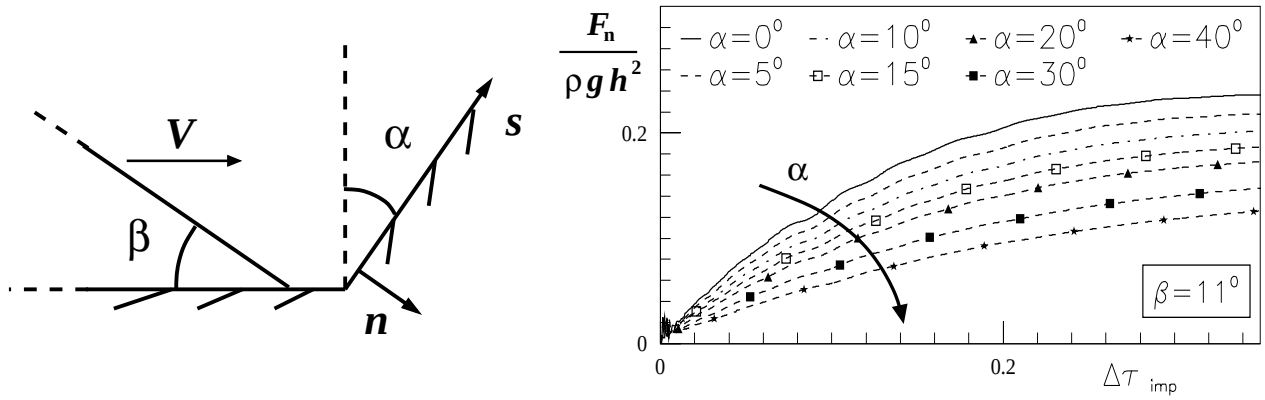

Figure 5.12 Water impacting against an inclined wall. Left: sketch of the problem. Right: time evolution of the normal force acting on the structure for increasing α. The "inflow" conditions are those relative to the case of figure 5.1, where $\beta = 11°$ and $V = 1.983\sqrt{gh}$. The results are obtained by solving numerically the "exact" problem.

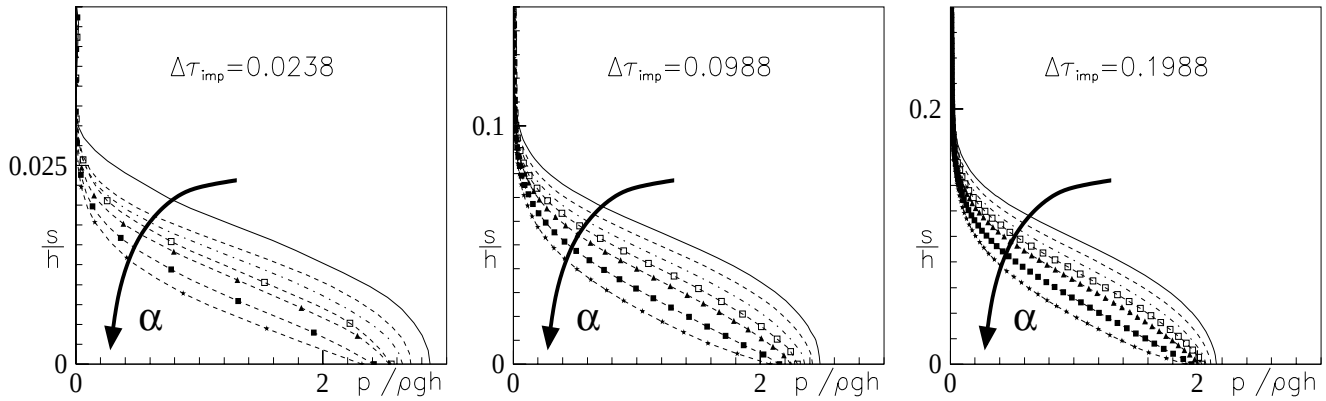

Figure 5.13 Water flow impacting a structure with angle $\beta = 11°$ and impact velocity $V = 1.983\sqrt{gh}$. The wall has an arbitrary slope α. Pressure distributions, related to the values of α considered in figure 5.12, are shown at three time instants after the impact.

the generalized force $\int p\,\psi_j \mathrm{d}l$, where ψ_j is an eigenmode for the local structural vibration. While the generalized forces related to the high initial values are modest ($z = 0$ is a structural node), smaller (but large enough) values of the pressure, distributed on a larger portion of the wall, may excite a hydroelastic response of the structure. On this ground, both the pressure distribution and its time evolution are important for the structural analysis. Hydroelastic effects should be considered if the time duration of the loading over the analyzed structural part is the same order or smaller than the highest natural period for the considered structural part (Faltinsen2001). These aspects are analyzed in the next section.

5.2.3 Fluid-Structure Interaction

In the following the influence of the hydroelasticity is investigated. Top sketch in figure 5.14 gives an example of longitudinal steel stiffeners adopted for the deck house in the bow region of a FPSO. The focus is on the effects on the stiffeners between deck 8 and deck 9 in the figure. This

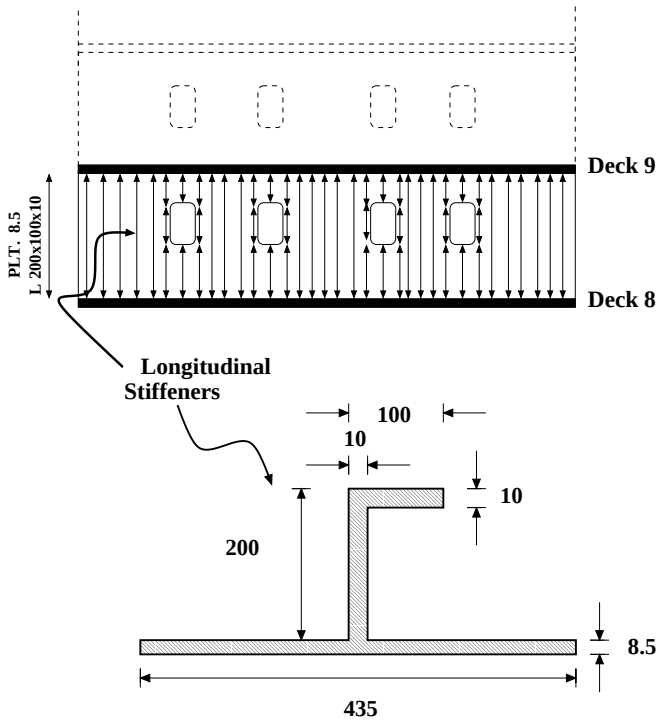

Figure 5.14 Example of stiffeners of a deck house and cross-section of equivalent beam. Lengths are in millimeters.

is done by using an equivalent Euler beam. The stiffener cross section is shown in the bottom sketch. The upper portion of the deck house is assumed rigid.

Recent accidents for FPSO units documented in Ersdal and Kvitrud (2000), suggest to use a freeboard exceedance of 10 m. Here, the flow is started as the breaking of a dam located at the bow section, with a water reservoir $h = 10$ m high and $2h$ long (*cf.* figure 5.15). The beam, representing the wall of a deck house, is placed at $d_s = 2.139h$ from the dam, with length $L_{\text{beam}} = 0.311h$. The lower edge is clamped, while rotations at the upper edge are constrained by a spring with elastic constant k_θ.

The deformation $w(z,t)$ of the beam is expressed in terms of the known dry modes $\psi_j(z)$ of the beam with unknown amplitudes $\zeta_j(t)$. Then the fluid-structure interaction is studied by coupling the nonlinear potential-fluid model with the linear-beam model by using the method explained in section 2.3. In the computations shown afterwards, the actual deformation $w(z,t)$ of the beam has been considered, *i.e.* the no-penetration boundary condition is enforced on the instantaneous configuration attained by the beam. We have also tested the effect of enforcing $\partial\varphi/\partial n = \partial w/\partial t$ on the undeformed beam and the results (not reported) are practically unchanged.

Left plot of figure 5.15 shows the initial condition, $\tau = t\sqrt{g/h} = 0$, and a later free-surface configuration, corresponding to a run-up along the vertical wall of about $3L_{\text{beam}}$. The flow generated after the impact is characterized by a narrow jet of water rising along the wall, also observed in the case of rigid wall studied in section 5.1.

The numerical solution can be negatively affected by a variety of difficulties. For instance spatial and time resolutions decrease progressively for higher-order modes. Further confluence of different boundary conditions at the edges of the beam implies locally a poorer convergence.

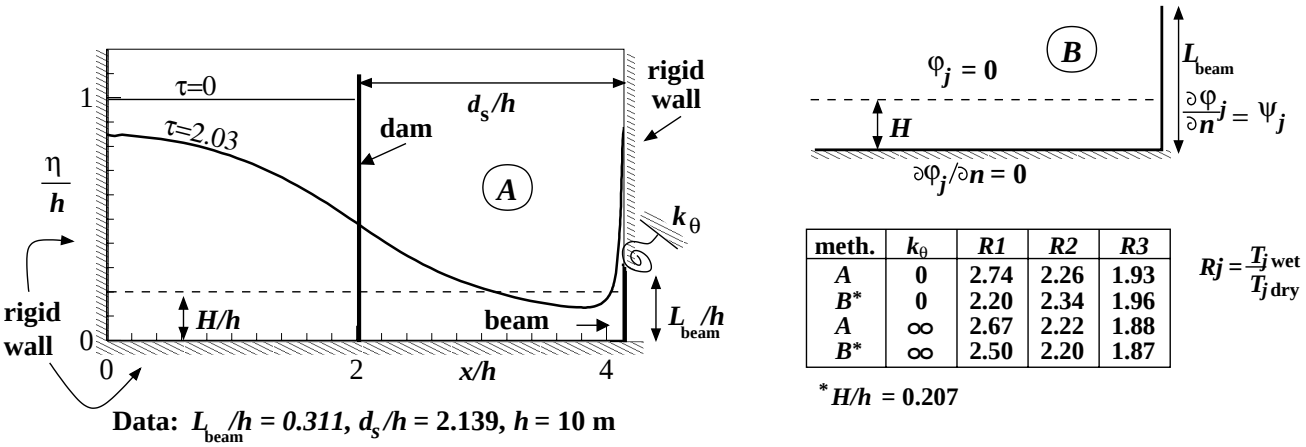

meth.	k_θ	R1	R2	R3
A	0	2.74	2.26	1.93
B*	0	2.20	2.34	1.96
A	∞	2.67	2.22	1.88
B*	∞	2.50	2.20	1.87

$Rj = T_{j\,wet}/T_{j\,dry}$

*$H/h = 0.207$

Figure 5.15 Flow impacting with a vertical flexible wall after a dam breaking. Left: sketch of the problem and nomenclature adopted. Right: in the table, the "exact" solutions, A, for natural periods are compared with results from the simplified analysis, B, obtained by solving the problem shown in the top plot.

Therefore, a simplified analytical analysis (top-right plot in figure 5.15) is also considered to qualitatively check the present results. The incoming water is approximated by a strip of fluid with constant height H, and the potential φ_j due to j-th mode oscillations with unit amplitude is computed with $\varphi_j = 0$ along the free surface. A solution is found by separation of variables and a Fourier expansion of the mode over the wetted surface. The related expressions are reported in appendix F. The height H is a free parameter chosen by the following considerations. In the approximate problem, it is found that the fluid further away than $\sim 0.8 L_{\rm beam}$ from the beam is practically unaffected by the vibrations. Therefore H is determined by imposing that masses of fluid involved in the approximate and exact problems are the same. In this procedure, particles above the beam are neglected because their role in the hydroelastic problem is expected to be small. This procedure gives $H/h = 0.207$. One can of course question this procedure but the objective is to show that the numerical results are reasonable.

The ratio natural wetted-period to natural dry-period $Rj = T_{j\rm wet}/T_{j\rm dry}$ is computed and compared with results obtained by the "exact" problem. This comparison is tabulated for $j = 1, 2, 3$ in the right of figure 5.15 for $k_\theta = 0, \infty$ and shows a reasonable agreement, more evident for the higher modes, as one can expect since their sensitivity to the fluid details is smaller. Left plots in figure 5.16 give the time evolution of ζ_j for the first two modes, in the case of $k_\theta = 0$[1]. Late stages are presented in the right of the same figure for $j = 1, \ldots, 4$. After the beam is completely wetted, $\Delta\tau_{\rm imp} \simeq 0.12$, the modes oscillate with almost constant period and amplitude. Both the value of ζ_j and the amplitude of oscillations decrease as the order of mode increases. This behavior does not change significantly when the parameter $K_\theta = k_\theta L_{\rm beam}/{\rm EI}$ is varied, where EI is the beam bending stiffness. Qualitatively, as K_θ increases the amplitudes decrease. The influence appears minor for the higher modes which are less sensitive to the boundary conditions. In general, Rj decreases as K_θ increases and is smaller for higher j (see table in figure 5.15). The highest natural wetted-period changes from ~ 0.018 to $\sim 0.026\sqrt{h/g}$ as one goes from $K_\theta = \infty$ to 0. This means $T_{1\rm wet}$ is small relative to the time to wet the beam.

[1] $\tau_{\rm imp}$ is the non-dimensional impact instant and $\Delta\tau_{\rm imp} = \tau - \tau_{\rm imp}$.

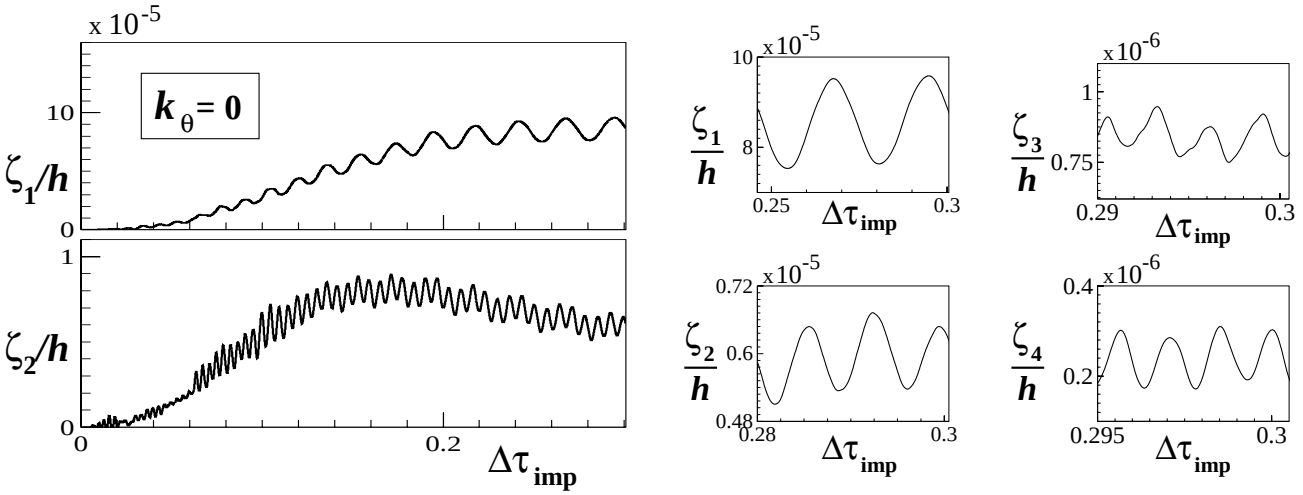

Figure 5.16 Modal amplitude as a function of time. Left: Time evolution of the first two modes. Right: Enlarged view of the amplitude of the first four modes at large times after the impact.

K_θ	0	6	24	∞
R1	2.74	2.73	2.67	2.67
R2	2.26	2.25	2.23	2.22
R3	1.93	1.93	1.88	1.88
R4	1.71	1.70	1.67	1.67

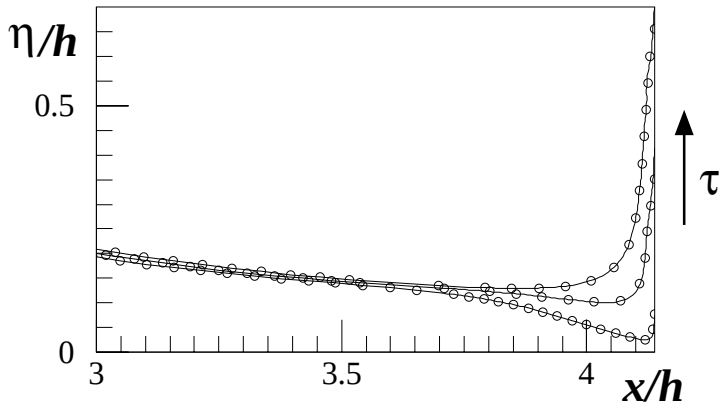

Figure 5.17 Left: ratio of natural wetted-periods to natural dry-periods for the first four modes of the beam. $K_\theta = k_\theta L_{\text{beam}}/EI$. Right: free surface for three different instants after the impact. Solid lines: rigid wall, ∘: hydroelastic solution with $k_\theta = 0$. $\Delta\tau_{\text{imp}} = 0.024,\ 0.13,\ 0.24$.

It implies that the hydroelasticity does not play an important role for the resulting maximum strains (*cf.* Faltinsen 2001).

The rigid wall results (solid lines) are compared with the clamped-supported beam results, ∘, in the right plot of figure 5.17. Here the free-surface configurations at three instants of time after the impact are presented. The overall pattern is not affected by wall deformation.

In figure 5.18, the maximum stresses ($\sigma_{\max}$) on the beam are presented as obtained by a hydroelastic analysis and by a quasi-steady model. In the latter, we have considered a rigid structure to solve the hydrodynamic problem, and the resulting loads are used to compute the static structural deformation. Fifteen modes have been used in the calculations.

For the considered cases, maxima are always observed at the bottom end. In particular (see left plot of figure 5.19) the fluid-induced bending moment gives tension stresses (t) in the wetted side, and compression stresses (c) in the opposite side. This is shown in the right-plot of figure 5.19 through the deformation of the beam at $\Delta\tau = 0.12$ after the impact. Here the arrow indicates the direction of the incoming water. Concerning the maximum tension and compression bending

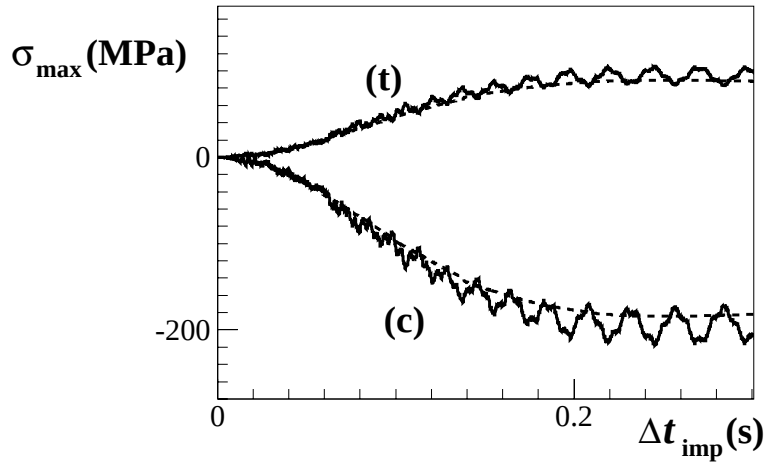

Figure 5.18 Maximum tension (t) and compression (c) stresses as a function of time. Quasi-steady (dashed lines) and hydroelastic ($k_\theta = 0$, solid lines) analyses.

stresses, the latter reach larger values than the former. This is because the cross-sectional neutral axis is closer to the wetted side. After the transient stage, the mean value of $\sigma_{\max}$ becomes nearly constant and remains with an absolute value less than 220 MPa. This is smaller than the steel yield stress but indicates that other inflow conditions may cause damage to the deck house. One notes that the magnitude of hydroelastic results oscillates around a mean value close to and slightly larger than the corresponding quasi-steady value. This confirms the unimportance of hydroelasticity in this case.

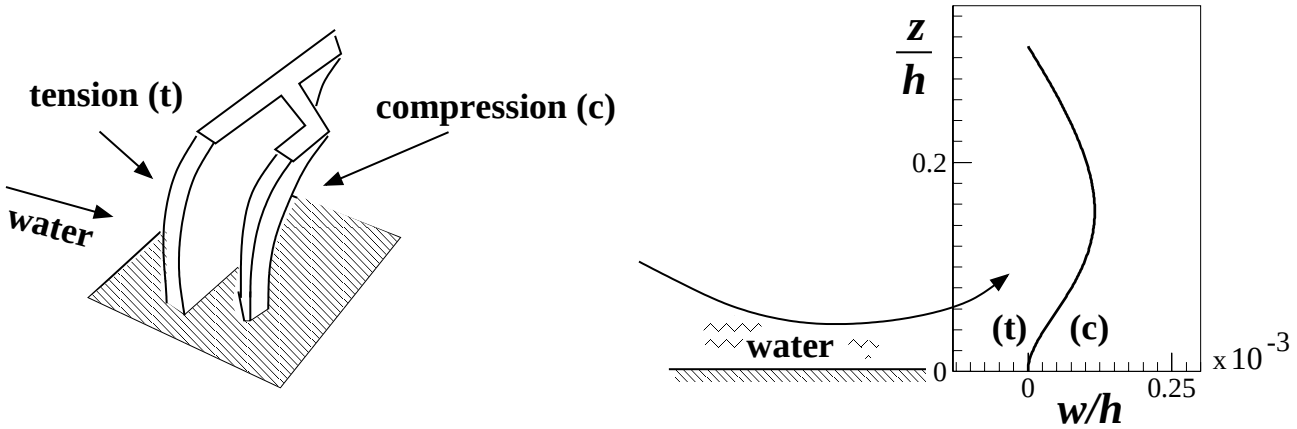

Figure 5.19 Left: sketch of the loaded beam. Right: deformation of the beam at $\Delta\tau = 0.12$ after the impact. $k_\theta = 0$.

Chapter 6

Approximated Methods for the Water Flow along the Deck

In the most common type of water on deck the water behaves qualitatively like the flow originated after the breaking of a dam. A certain region of the water will have a small depth relative to the wetted length.

These aspects leave open the possibility of using simplified approaches to analyze this phase of the complicated water-on-deck phenomenon. Questions arise, like: Can the shallow-water approximation be used for the water evolution along the deck? Does an equivalent dam-breaking problem exist for a given water shipping event? If yes, how to determine the right values of the parameters and of the conditions involved in the simplified analysis? These questions represent the topic of the next two sections where the applicability of these approximated analyses is investigated by examples. Their advantages and shortcomings are pointed out by using the numerical method described in chapter 3 as reference.

6.1 Shallow-Water Approximation

Shallow water approximation here indicates the simplified theory valid for nonlinear very long waves propagating in shallow water. This implies, nonlinearities of the problem are retained while dispersion effects are neglected. Such approximation is also referred as Airy's Theory (*cf.* Mei 1983). In the following the focus is on dam breaking-type of water on deck.

While close to the bow the dispersion effects remain in general important, a certain distance (x_{shw}) from the bow can exist from where they become negligible. The horizontal velocity becomes then almost independent of the vertical coordinate z and the flow can be described by the water height $(\eta - f)$ along the deck and the mean horizontal fluid velocity u. Here η is the local wave elevation and f is the freeboard. The shallow water equations require initial conditions for $(\eta - f)$ and u, as well as inflow boundary conditions (at x_{shw}).

This approximation has been analyzed by studying the water flow along the deck in the experimental case by Cozijn (1995), described in chapter 4. Initial and boundary conditions (see left sketch of figure 6.1) have been obtained by the present panel method and the problem has been solved numerically with the method of characteristics (see *e.g.* Mei 1983). Right plot of figure 6.1 gives the obtained results when $x_{\rm shw}/(H-f) = 2.2$ is taken as inflow boundary and $t_{\rm in} = 13.19\,T$ as initial instant in the shallow water problem. Here H is the incident wave

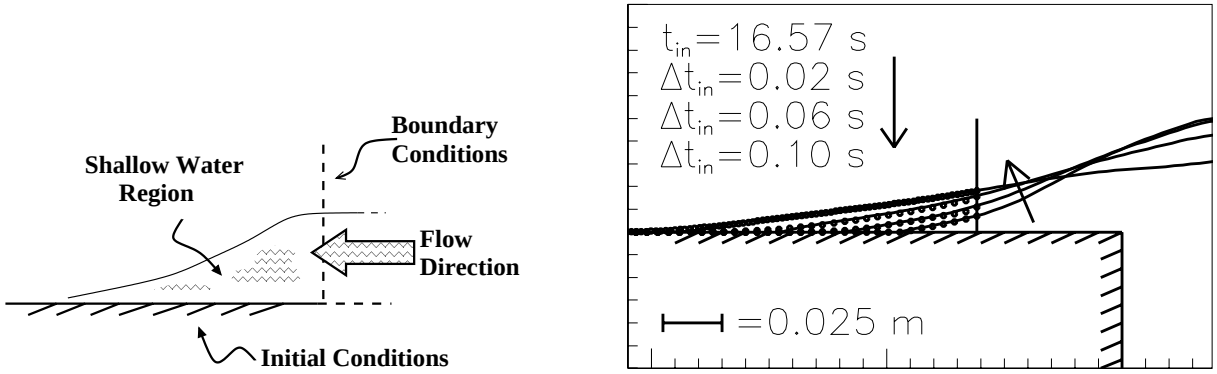

Figure 6.1 Water on deck of a rectangular structure due to incident regular waves with $H = 0.128$ m and $\omega = 5$ rad/s. Left: sketch of the shallow water problem. Right: numerical free surface profiles obtained with the panel method (solid lines) and with the shallow water approximation (black circles). $t_{\rm in}$ is the initial time for the shallow water simulation. The panel method simulation starts at $t = 0$ s.

height and T is the wave period. Further $t = 0$ is the time instant of initial generation (in the panel method simulation) of incoming waves at a position 6λ ahead of the deck structure. For this case of water on deck the maximum wave elevation in the vicinity of the bow ($\eta_{\rm max}$) was about 2.1 times the incident wave crest elevation. In the figure, the free surface profiles at three time instants after $t_{\rm in}$ are shown, given by the panel method (solid lines) and the shallow water approximation (black circles). The results agree quite well. However a major obstacle in applying the shallow water theory in practice is due to the initial and inflow boundary conditions. Since they result from the wave-ship interaction causing the water on deck, their estimate has to account for the involved nonlinearities and remains a difficult task.

An important additional limitation of the shallow water theory is the inability to handle water impacts with the deck house. The reason is simply that the resulting large variations in the vertical direction are inconsistent with the basic assumptions. The theory needs to be combined with some other method. When the flow is two-dimensional and the deck house has vertical sides at the impact position, locally the similarity solution for a fluid wedge hitting a wall at 90° (*cf.* chapter 5) can be used. The impact data, β and V (see sketch in figure 5.8), are given by the shallow water results. The impact pressure distribution along the structure can then be calculated for any structural distance from the bow. Assuming that initial and boundary conditions for the shallow water problem are properly given, the efficiency of this method depends on the importance of (i) three-dimensionality and (ii) gravity effects (neglected in the similarity solution). This importance changes according to the location of the superstructure along the deck (i) and the severity of the impact (ii).

This study documented the shallow water approximations can in principle be used in certain domains along the deck. However since they need initial and boundary conditions that are dependent on the external flow, they would in practice require data that are unavailable without solving the complete ship-wave interaction problem. This type of analysis is not suitable for solving water impacts with the deck house. In this case the coupling with a suitable local solution is necessary.

6.2 Dam-Breaking Model

An additional simplification of the problem can be obtained by studying an equivalent dam breaking problem (see left sketch of figure 6.2). As in the shallow water approximation, also

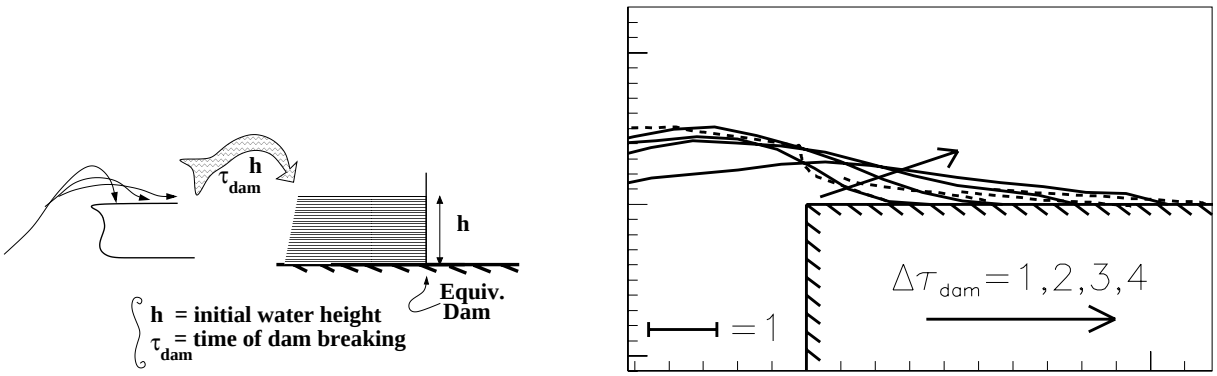

Figure 6.2 Left: water on deck and equivalent dam breaking problem. Right: water shipping due to incident regular waves with H/λ=0.06 on the deck of a "deep" rectangular structure. Numerical free surface profiles (solid lines) are compared with dam breaking experiments from Dressler (1954, dashed lines). For the numerical results the vertical axis gives $(\eta - f)/h$, where f is the freeboard, η is the wave elevation and $h = (\eta - f)_{\max}$. For the experiments the same axis shows the water level referred to the initial height of the reservoir of water, h. The related h is used in both cases to make non-dimensional the horizontal axis. The panel method simulation starts at $t = 0$ s.

in this case the dependence of the water flow along the deck from the wave-ship interaction causing the water on deck represents the main obstacle in finding the proper simplified model. This is here even more stressed. Indeed, if the height of the "equivalent" reservoir of water can be reasonably fixed by the maximum freeboard exceedance by the water, $h = (\eta - f)_{\max}$, the time instant when the dam breaks depends on the specific water on deck event due to the exterior flow. As an example, right plot of figure 6.2 shows the water on deck of a fixed structure with a "deep" (relative to the wavelength λ) vertical bow caused by incident regular waves with $H/\lambda = 0.06$. Numerical free surface profiles at four time instants (solid lines) are compared with the experimental dam-breaking results by Dressler (1954, dashed lines).

In the experiments the length of the reservoir of water is long compared with the reservoir height, and it does not influence the results. When comparing with Dressler (1954), there is an ambiguity in how to select the equivalent height h of the reservoir and when the dam breaks. Here the following decisions are taken. h is chosen equal to the maximum freeboard exceedance

by the water during the shipping, $(\eta - f)_{\max}$. The time instant of dam breaking is taken as $\sqrt{h/g}$ after the water shipping started. This value is obtained by tuning the dam-breaking and water-on-deck free surface evolutions. Its difference from the time of the shipping starting quantifies in a way the importance of the following error sources: (i) in the dam-breaking model the water reservoir has its maximum level when the dam breaks while at the beginning of the shipping the freeboard exceedance by the water at the bow is zero and increases reaching only after some time its maximum value, (ii) in the dam-breaking model the water flow is driven by the gravity while during the shipping the wave conditions outside the deck determine a more complicated driven force system.

Qualitatively the two results confirm the agreement observed experimentally in Buchner (1995), however differences exist both for the water level and for the flow velocities. These differences are clearly due to the wave kinematics involved in the water on deck. The specific local wave conditions at the bow enhance or reduce those differences. For the case shown in the right plot of figure 6.2, the differences between the flow caused by a dam breaking and the flow along the deck can be quantified in terms of the consequences on a vertical wall hit by the water. Since the angle β (*cf.* sketch of figure 5.8) is small for both the flows (less than 15^0), the velocity V is the important impact parameter. The square of the ratio between the (mean) velocities associated with the dam-breaking ($V_{\rm db}$) and the water-on-deck ($V_{\rm wod}$) problems can be interpreted as the ratio between the maximum pressures on the wall. This ratio is $(V_{\rm db}/V_{\rm wod})^2 \simeq 1.67$, indicating a large error in impact pressure predictions. It is worth noting that if the shallow water dam-breaking solution (*cf.* Ritter 1892) was used, the related impact velocity should be even higher than $V_{\rm db}$ (*cf.* figure 1.6 and section C.3). This means too conservative estimates of impact loads on a deck house in the bow area.

These results document that a theoretical dam-breaking model can only qualitatively describe the flow on the deck since it does not account for the horizontal fluid motion caused by the flow external to the ship. The latter can significantly influence the characteristics of water impacts with superstructures along the deck.

Chapter 7

Two-Dimensional Water-on-Deck Experiments

Two-dimensional water on deck model tests have been carried out in the narrow wave flume at the Department of Marine Hydrodynamics of NTNU. The general objectives of the experimental study are both the validation of the numerical model and a direct investigation of the phenomenon. In this chapter, the experimental set-up is described and observations are documented and discussed. Main error sources which may affect the experiments are also indicated and commented.

7.1 Choice of Relevant Parameters

Two-dimensional experiments have been realized to study water-on-deck phenomena for a restrained (nearly) rectangular-shaped model.

As we said, focusing our attention on FPSO-type ships, the experimental set-up has been designed by using the DWT FPSO (Buchner 1995) and the Norne (see left plot of figure 1.2, Statoil) as reference for the ship parameters. Experiments of water on deck in regular waves by Buchner (1995), on a three-dimensional model, and by Cozijn (1995), for a two-dimensional configuration, have been examined to determine the suitable wave parameters. Finally, we have also kept in mind the overview of recent FPSO accidents given by Ersdal and Kvitrud (2000). A summary of the relevant information collected from the above reference sources is presented in the following list. The used symbols are summarized in figure 7.1.

1) Ship length: L/D is $\simeq 15$ for DWT FPSO and $\simeq 13$ for Norne.

2) Freeboard: design freeboard-to-draft ratio is $\simeq 0.507$ for DWT, and $f/D \simeq 0.76$ for Norne. When Norne accident occurred on March 1998 (*cf.* Ersdal and Kvitrud 2000), the ship was almost fully loaded with a mean freeboard $f = 8$ m, resulting in $f/D \simeq 0.35$.

3) Stem angle: both ships have an almost vertical bow below mean waterplane. The upper portion of the bow is inclined outwards, with an angle of ~ 37 and ~ 36 degrees, respectively.

4) Deck house: Norne has a deck house located at $d_s/D \simeq 1.3$ from the bow.

5) Critical sea states: according to the overview of FPSO accidents by Ersdal and Kvitrud (2000), the recorded sea states responsible for water-on-deck events were normally characterized by long waves, that is wave lengths of order of the ship length, and usually greater than 200 m in the case of FPSO units. Significant wave heights associated with the critical sea states varied between 7 and 13 m. This corresponds to largest wave heights H_M of approximately 14 and 26 m, respectively. Peak periods T_p were between 11 and 13 s. With the parameters above, combinations (H_M, T_p) imply a broad range of wave steepnesses.

6) Regular wave length: in 3-D Buchner's experiments, wave length-to-ship length ratios λ/L =0.75, 1, 1.25 were considered, giving λ/D $\simeq$ 11, 15, 19, respectively.

7) Regular wave steepness: in 3-D Buchner's experiments, steepness values of $H/\lambda \simeq 0.066$, 0.088 have been analyzed. A steepness ~ 0.052 was studied during 2-D experiments by Cozijn.

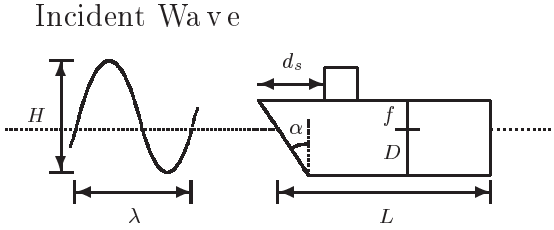

Figure 7.1 Nomenclature adopted for the main geometrical parameters considered.

In addition to data above, the two-dimensional numerical analysis discussed in chapter 4 has been taken into account. From numerical results, the ship length does not directly influence the amount of shipped water as long as it is large relative to the draft, and as long as the ship is restrained from oscillating. Since the wave-induced ship motions are not studied in the tests, this gives some freedom when deciding the ratio L/D. In particular, L/D can be chosen a bit smaller than in real cases to achieve a good compromise between test scale and flume dimensions. In particular, if the scale is too small, important surface-tension effects would significantly affect the water shipping and the flow evolution along the deck. On the other hand, for large scales, long waves have to be generated and a larger influence of the bottom of the flume would be expected, causing steeper wave conditions and occasionally wave breaking. This would prevent the comparison with our numerical simulations. In addition, for wave lengths large relative to the flume dimensions, the model would be relatively closer to the wave maker, thus implying more pronounced local effects and wave reflection.

Heave and pitch motions cause a time variation of the ship freeboard relative to the mean waterplane. This has been taken into account when deciding the freeboard of the fixed model. In particular, f has been chosen to give realistic values of freeboard exceedance during the

water shipping. The final chosen f was also based on preliminary numerical studies, resulting in freeboard smaller than the ship freeboard in calm water.

This information, together with practical aspects related to available instrumentation, wave-flume characteristics, costs and other factors determined the experimental set-up, discussed in the following sections.

7.2 Description of the Experimental Set-up

7.2.1 Equipment

The flume Two-dimensional water-on-deck model tests have been performed in a narrow wave flume. The flume is 13.5 m long, 1.035 m deep and 0.6 m wide. The sides are 19 mm thick glass-plate made to permit flow visualization during tests.
Incoming waves are generated by a flap wavemaker hinged at 0.1 m from the bottom. A parabolic beach at the opposite end of the flume reduces the wave reflection. The wavemaker is equipped with a control system constructed by Edinburgh Designs. This is based on monitoring hydrodynamic forces acting on the flap. Details of how the feedback in the system works to counteract the presence of unwanted reflected waves at the wavemaker is proprietary information.
The position of the model is determined by considering sufficient distance from the wavemaker to avoid local effects from the flap. For the considered wave periods, we placed the model at $\simeq$ 5.54 m from the wavemaker.
Another restriction is given by the optical window seen by the video equipment, with the widest observed-flow area of about 3 m.

The ship model A simplified two-dimensional ship model has been used in the tests, with three different bows, sketched in figure 7.2. The basic configuration is characterized by a trans-

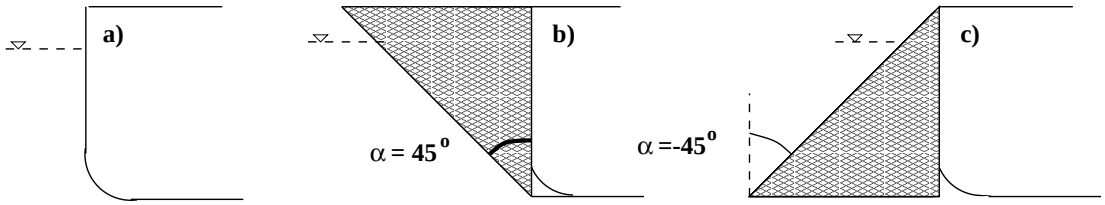

Figure 7.2 Water-on-deck at the bow of a 2-D ship. Bow geometry of the considered models. Side view.

parent nearly rectangular body (a) with draft $D = 0.198$ m, length $L = 1.5$ m, freeboard $f = 0.05$ m (*cf.* sketch in figure 7.3). This means $L/D \simeq 7.6$ and $f/D \simeq 0.253$. The model is made in plexiglas. The front part of the transparent model has been placed at $\simeq$ 5.54 m from the vertical wavemaker position ($\mathrm{wm_{ver}}$), while the aft part is about 6.46 m far from the opposite side of the flume.

Due to the chosen freeboard, the height of the glass side above the deck is $\sim$ 0.215 m, as indicated by the double arrow in the side view (right picture) in figure 7.3. In order to take

video images of the water shipping, this height has to be large enough relative to the involved water level along the deck. Also this determined the choice of the test scale.

The bottom corner at the bow has a radius of curvature $r = 0.08$ m to avoid vortex shedding. The value of r was decided by carrying out a simplified analysis. In particular, in case of oscillatory ambient flow with amplitude η_a around a fixed horizontal circular cylinder of radius r, the experimental threshold (*cf.* Faltinsen 1990) for almost-zero vortex shedding is

$$\mathrm{KC} = \frac{U_M\, T}{2\, r} = \frac{\pi\, \eta_a}{r} <\sim 3 \ ,$$

where KC is the Keulegan-Carpenter number, and T and U_M are the period and the velocity amplitude of the ambient oscillatory flow, respectively. By setting η_a equal to the largest wave amplitude considered in the tests, 0.08 m, we obtain a limit radius r of about 0.08 m. Clearly, this analysis is simplified since it does not account for the complete model shape. However flow visualization did not detect any vortex shedding during the tests.

In the other configurations, the bow has a stem angle of 45 (b) and -45 (c) degrees, respectively. The removable bow part is made by divinisel, which, although not transparent, is easier to shape.

Finally, the model is restrained from oscillating in all the tests we performed.

Side, top and lateral views of the experimental set-up together with the definition of main geometric parameters are given by figures 7.3, 7.4 and 7.5. In the case of the vertical-bow

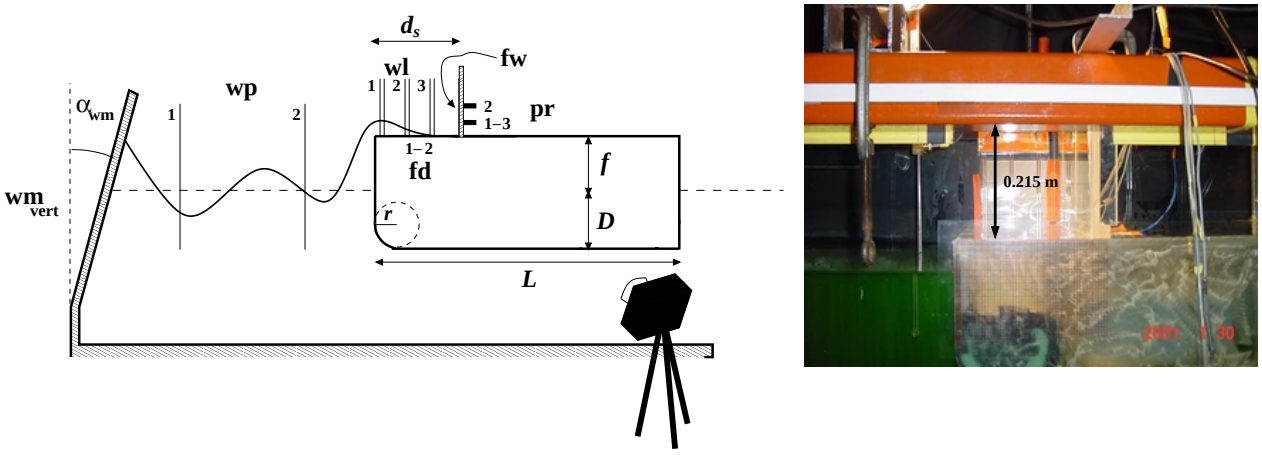

Figure 7.3 Water-on-deck at the bow of a 2-D ship. Experimental set-up, main parameters involved and used sensors. Side view.

configuration, tests have been performed both without and with a vertical wall on the deck, located at $d_s = 0.2275$ m ($d_s/D \simeq 1.15$) from the bow. Configurations (b) and (c) have been tested only without superstructure. The vertical wall is transparent and made by plexiglas. It is rectangularly shaped, ~ 0.60 m large, 0.30 m high and 0.012 m thick. Four equi-spaced vertical stiffeners on the back side of the wall (see right plot of figure 7.4 and left photos of figure 7.5) have been introduced. Among them, the most external ones are placed at the ends of the structure. The stiffeners have rectangular cross sections and the same height as the wall. The cross section is 0.033 m $\times$ 0.012 m, where 0.033 m corresponds to the side length orthogonal to the wall.

crest of a regular wavetrain. This has to be kept in mind because we will focus on the first water-on-deck event which, in our case, is determined by the interaction of the bow with a highly non uniform wavetrain. Therefore, we have accurately measured the 'actual' waves interacting with the model, characterized by the first crest steeper than the waves that would be generated by the wavemaker for the selected frequency and amplitude after a very long time, in the absence of the body. In our experiments, the latter condition has never been reached.

The instrumentation The used instrumentation is characterized by

- two capacitive wave probes (with 3 mm diameter) located along the flume: wp_1 at 0.8 m from wm_{ver} (see sketch 7.3) and wp_2 at 0.104 m from the bow.
- three capacitive wave probes spaced 0.075 m from each other and placed on top of the deck. When the superstructure is not used, the wl_1 center is at the bow. When the wall is introduced, wl_3 center is at 0.0405 m from the vertical wall.
- two capacitive wave probes *along* the deck (fd_1, fd_2).
- one capacitive wave probe along the vertical superstructure (fw).
- three piezoelectric pressure gauges (diameter of 3 mm) along the vertical superstructure: pr_1 and pr_3 at 12 mm from the deck and horizontally spaced 15 cm from each other, pr_2 at 32 mm from the deck.
- one digital video camera with a standard 25Hz sampling frequency.

Wave probes on the ship model are characterized by two thin metallic ribbons 5 mm wide glued with a separation distance of 5 mm, and finally calibrated *in situ*. These sensors are used to evaluate the water level along the deck (wl_1, wl_2, wl_3), and to measure the wave front propagation along the deck (fd_1, fd_2) and during water run-up along the vertical superstructure (fw). The sampling rate of the measured data is generally 100 Hz.

7.3 Reliability and Repeatability of the Measurements

Repeatability of the tests has been checked. Here, we consider prescribed (nominal) incoming waves with $\lambda = 2$ m and $H = 0.16$ m. Figure 7.6 shows the time histories of the wave elevation at 0.8 m from wm_{ver} (left plot, wp_1) and at 0.104 m (right plot, wp_2) from the bow. The basic model with vertical bow is used during the experiments. The curves are related to seven different tests. The measurements agree quite well, though some tests show a certain deviation from the majority. This is mostly true at the beginning of the time evolution, when the sensitivity and dependence on the initial wave conditions in the flume are the largest. The water-level evolution along the deck is presented in figure 7.7. The wave probes are placed at the bow (top left plot, wl_1) and at 0.075 m (top right plot, wl_2) and 0.15 m (bottom plot, wl_3) from the bow. The first two water-on-deck events are shown and for both of them the incoming wave is steeper than the nominal regular wave prescribed by the wavemaker settings. The second event is characterized

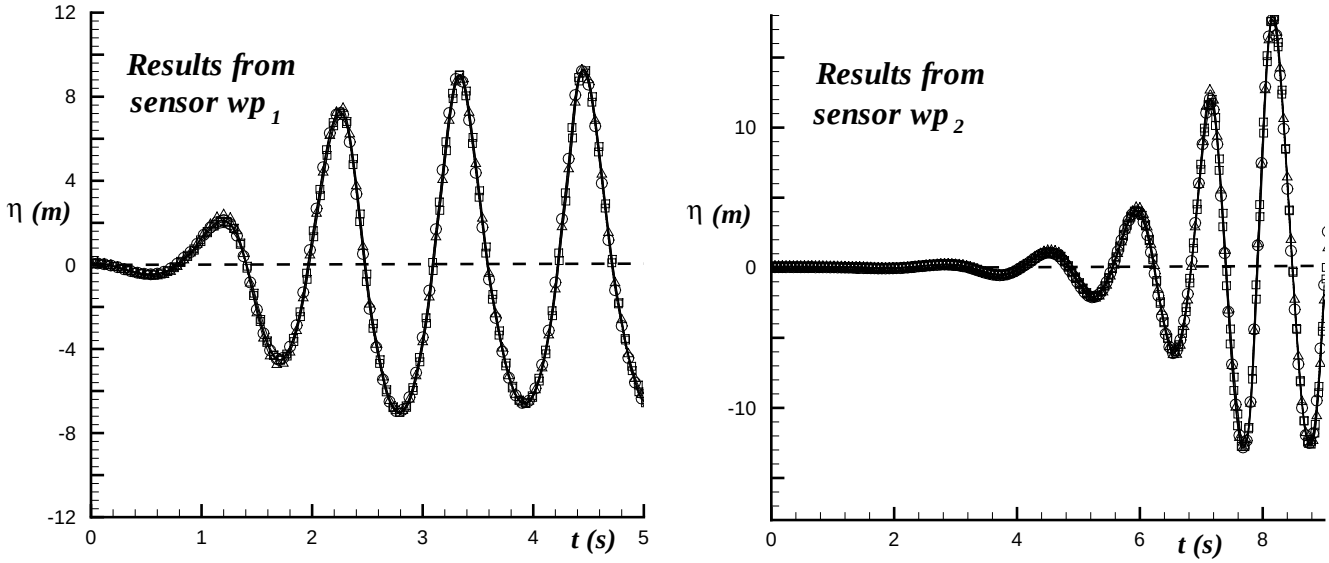

Figure 7.6 Repeatability of the wave elevation measured by wp_1 (left) and wp_2 (right). Seven test results are plotted.

by a larger amount of shipped water than the first one. This is because the wave crest reaching the bow steepens because of reflected waves. The repeatability of the measured data appears acceptable, though less good in this case. An important reason is the formation of a cavity of air at the beginning of water on deck, as it will be extensively discussed in section 8.2. In this context, important factors are represented by the high transient behaviour of the cavity and by the sensitivity of the sensors to the rate of change of the wetted length along the two strips of each sensor.

The propagation of the wave front along the deck ($\Delta x_{\text{bow}} = x_{\text{w ave front}} - x_{\text{bow}}$) is analyzed in the left plot of figure 7.8, which shows a satisfactory repeatability of the experiments. The maximum value reached by the front is about 0.25 m, which is consistent with the length of the metallic ribbons forming the sensor. The water front covers in reality a longer distance than the length of the probe. In the later stages of the first water on deck, the wetted length measured decreases reaching a minimum[1]. After that, it increases due to the starting of the next event, which follows a similar evolution cycle.

The right plot of the same figure gives the comparison between the results obtained with sensors fd_1 and fd_2, for one of the tests. The probes attain non-zero values at the same time instant, and the curves fit quite well until the end of the first water on deck. This confirms the two-dimensionality of the flow. Differences are observed during the following stages. However, as observed, in this phase the reliability of the measurements is questionable, and the difference is not related to three-dimensional effects, which are negligible according to the analysis of video

[1] One could question about the fact that a decreasing wetted length is measured, since once the probe has been wetted the signal should remain constant. However, below a certain thickness of the layer of water on the deck, capillary effects drive a contraction of the water in the form of isolated wetted regions, with rather unpredictable extent, which are seen from the probe as a reduction of the wetted length.

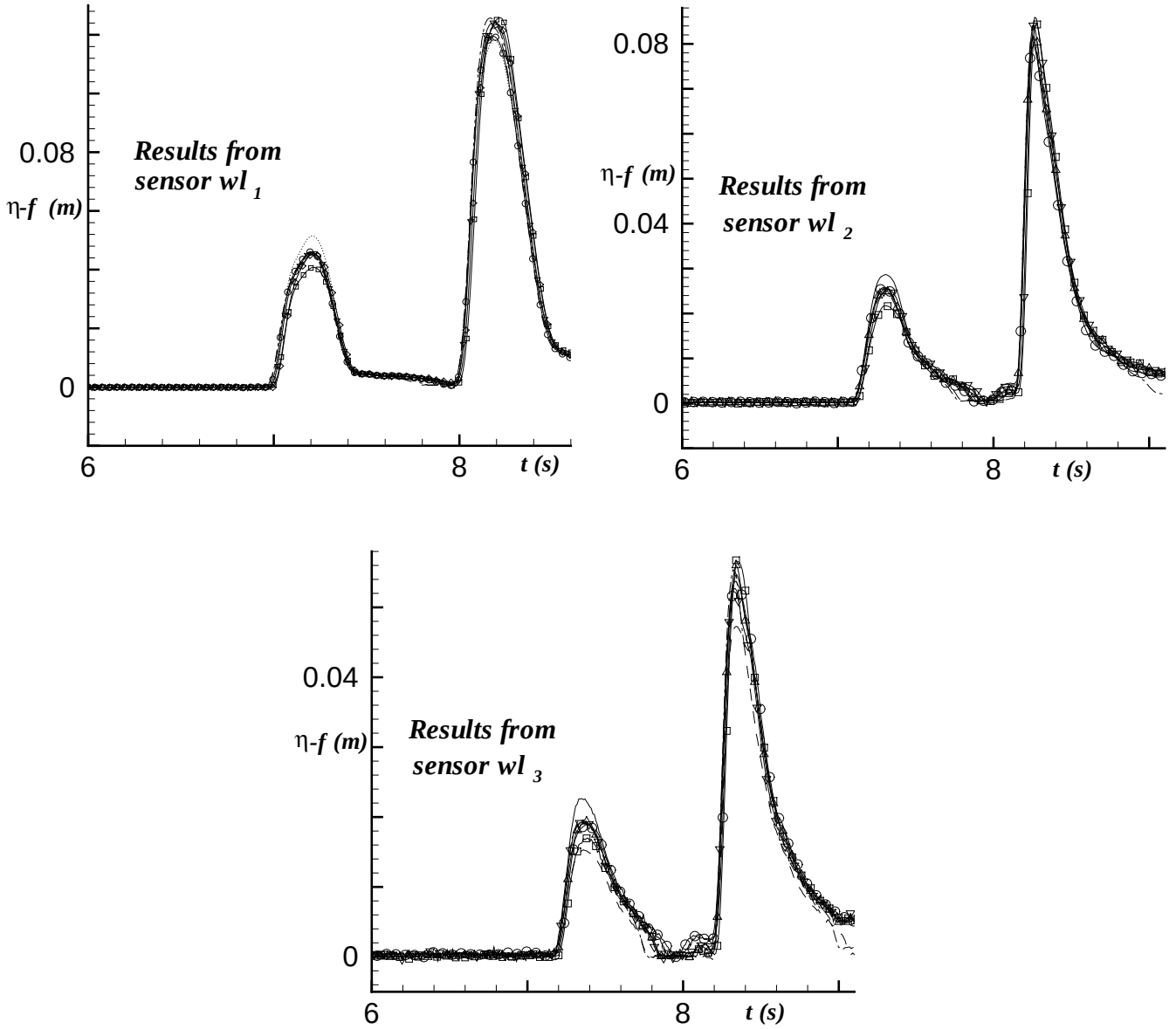

Figure 7.7 Repeatability of the water level measured by wl_1 (top left) and wl_2 (top right)and wl_3 (bottom). Seven test results are plotted.

images[2].

The measured data commented so far refer to a model without a vertical wall on the deck. In figure 7.9, we consider tests with a vertical wall at 0.2275 m from the bow. The left plot shows the evolution of the wavefront measured by fd_1. The maximum value measured of the wave front is less than the expected one (0.2275 m) in this case. The strips of the sensor are longer (0.25 m) than the wall distance from the bow. This suggests that errors in the measurements are probably associated with the specific flow details close to the wall.

[2]When small and thin wetted regions appear, the probes are working in a regime where differences in sensitivity imply significant differences in the output signal.

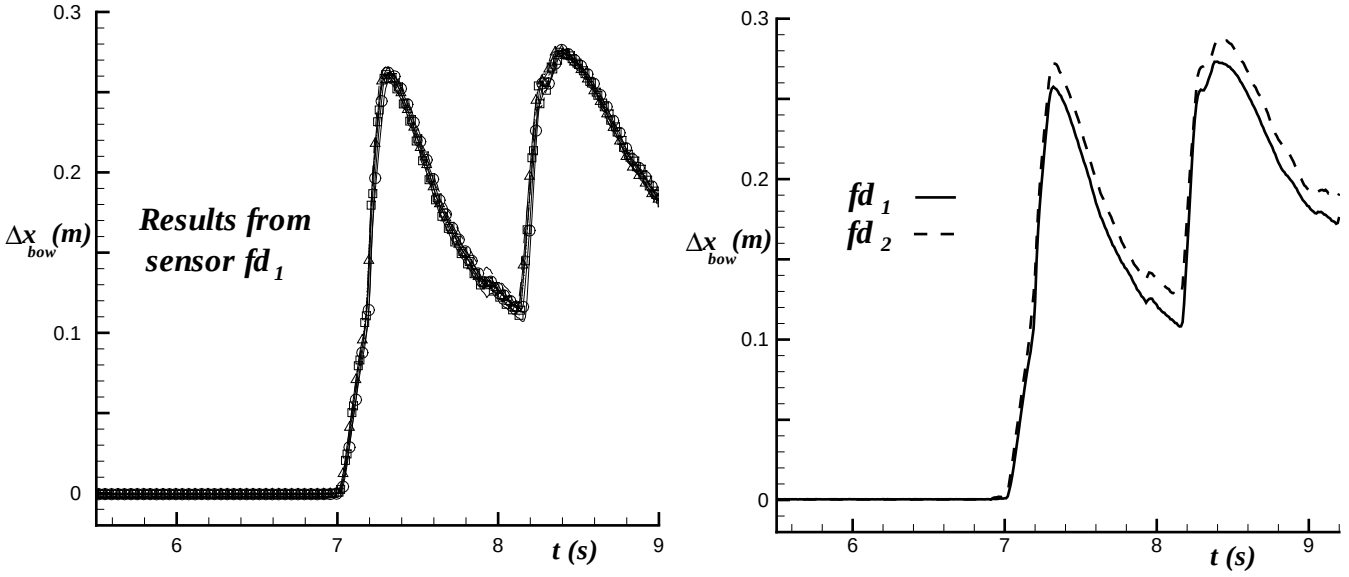

Figure 7.8 Left: repeatability of the wave front propagation measured by fd_1, without superstructure along the deck. Seven test results are shown. Right: comparison of fd_1 and fd_2 measurements for one of the tests, without superstructure along the deck. Five test results are shown.

The vertical wall reflects the water propagating along the deck. This makes the water on deck phenomenon faster relative to the case without the wall. Further the water level along the deck

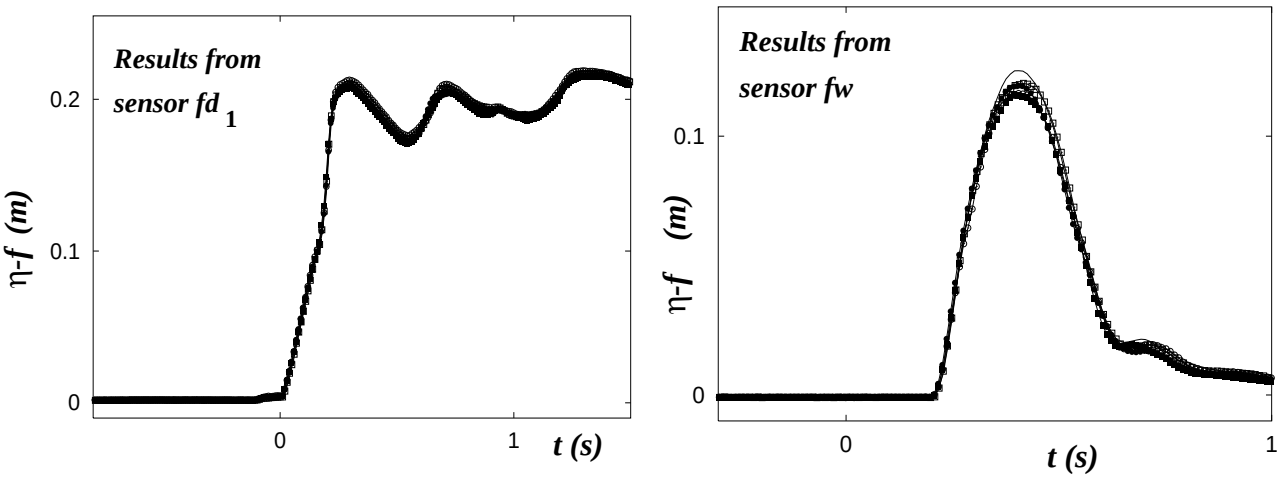

Figure 7.9 Left: repeatability of the wavefront propagation measured by fd_1, with a superstructure along the deck. Right: repeatability of the water run-up along the vertical superstructure measured by fw. Five test results are shown.

increased and does not become zero between one water-on-deck event and the next one. This is confirmed by the measurements in left plot of figure 7.9 where the wetted length remains almost constant after it has reached a maximum value.
Right plot of the same figure gives the evolution of the water run-up along the wall. Five test

results are shown. As one can observe the repeatability is quite good until the maximum is approached. Then the measurements show a certain difference. The video images show that the flow becomes unstable and three-dimensional during the water rise-up. This explains the differences in the results.
The pressure measurements are analyzed in the plots of figure 7.10. In the left, the pressure measured at 0.012 m from the deck (pr_1) is examined. F our testresults are shown. In this case

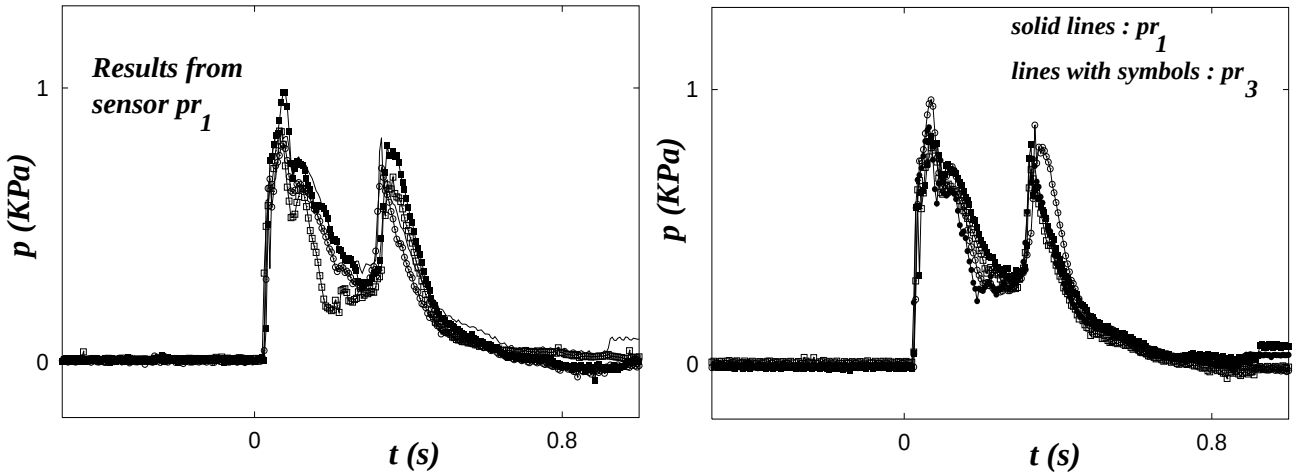

Figure 7.10 Left: repeatability of the pressure ev olution measured b y pr_1. F our test results are shown. Right: comparison of pr_1 (lines with squares) and pr_3 (lines with circles) measurements. Two test results (full and empty symbols) are shown for each gauge.

the measurements appear similar but not perfectly repeatable. This is both due to the three-dimensional effects appearing during the water run-up along the wall and to the sensitivity of the measured pressure to the specific flow and environmental conditions. The latter represents a key factor for the reliability of the pressure measurements. In the right plot, the pressure evolutions at pr_1 (lines with squares) and at pr_3 (lines with circle) are compared. Two test results (full and empty symbols) are shown for each gauge. The differences between the two sensors results are of the same order as those between results from different tests for the same gauge. This confirms the important role play ed b y the pressure sensitivity to the physical conditions, but it does not exclude the influence of three-dimensional effects. However, these start to matter when the water front, rising along the wall, is already far from the pressure sensors and, at least at the beginning, remain localized in the front region.

A cross-check of variables measured on the model was performed to guaranty their reliability. An example of this is given in figure 7.11, where a good agreement between different sensors is documented. The case refers to the first water on deck due to a nominal incoming wa v ewith length $\lambda = 2$ mdan height $H = 0.16$ m. No v ertical wall was used on the deck. Solid line gives the evolution of the wa v efront along the deck measured b y the sensor fd_1. Lines with squares, circles and rev ersedtriangles represent the water level ev olutionalong the deck measured with wl_1, wl_2 and wl_3, respectively . The center of the sensor wl_1 is at the bow and the centers of the others are respectively at 0.075 m and 0.15 m from the first one. As one can observe the fd_1 measurement becomes different than zero almost at the same time instant as the one of wl_1. The small delay in the wa v efront measurement can be explained b y the fact that (*cf.* chapter

8) the deck is not wetted just after the freeboard is exceeded, but a plunging wave is formed. When this one impacts on the deck the wetting starts. The plunging and impact phenomena are quite rapid in this case, with the impact occurring at about 0.13 s from the instant of freeboard exceedance. As a consequence of the plunging impact a cavity is formed that collapses during the water evolution. This explains the better agreement between the fd_1 and the following water level sensors. As one can observe, the wavefront measured by fd_1 reaches the values of 0.075 m and 0.15 m almost when wl_2 and wl_3, respectively, become different than zero.

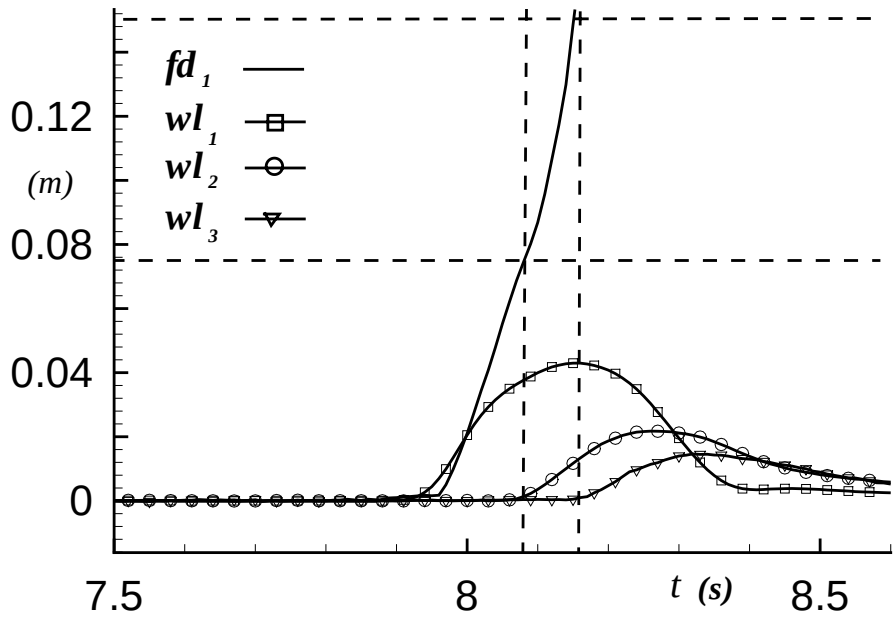

Figure 7.11 Cross-check: wave front propagation (fd_1), water level at the bow (wl_1), at 0.075 m from the bow (wl_2) and at 0.15 m from the bow (wl_3).

7.4 Error Sources in the Measurements

Both when the experimental set-up is designed and when the results from the tests are analyzed, it is crucial to determine and keep under control possible error sources in the measurements. This can give guidelines for the former process and fixes the validity and reliability limits of the experimental results. The main error sources are analyzed in the following text.

7.4.1 Flume

Seiching in the flume Seiching indicates the presence of longitudinal standing waves in the tank, with wavelength twice the tank length. Since the latter is much larger than the flume depth, this is a shallow water phenomenon. The actual length-to-depth ratio is $b/h \simeq 13.04$ in the tests, where $b = 13.5$ m and $h = 1.035$ m. Since seiching represents an error source in the

actual waves generated in the flume it is important to control this resonance phenomenon in the tank.

The parabolic beach at the opposite side of the wavemaker influences the time necessary for the standing waves to be set up (t_{sw}). However, since it is not designed for such long waves, its absorption efficiency is poor. A first estimate of t_{sw} can thus be obtained by neglecting the beach and simply considering a rectangular tank. The group velocity for shallow water waves is $c_g = \sqrt{gh}$. This means, the long disturbances generated by the wavemaker reach the opposite side in $b/c_g \simeq 4.24$ s after start up and return to the flap after $2b/c_g \simeq 8.47$ s. The latter can be taken as a measure of t_{sw}. Once the seiching is excited the waves generated by the wavemaker are altered in the flume by the standing waves. This gives a higher frequency signal modulated by a lower frequency envelope. The latter is associated with the natural period of the flume that can be evaluated by applying the shallow water expression for the highest natural (sloshing) period (*cf.* Faltinsen 1990)

$$T_N = \frac{2\,b}{\sqrt{g\,h}}\,.$$

This gives $T_N \simeq 8.5$ s in the present case. In figure 7.12 the angle of wavemaker oscillation (α) is shown for the case of nominal wave with $\lambda = 2$ m and $H = 0.16$ m. The ship model was not used during the test. α does not correspond to the prescribed wavemaker motion but has

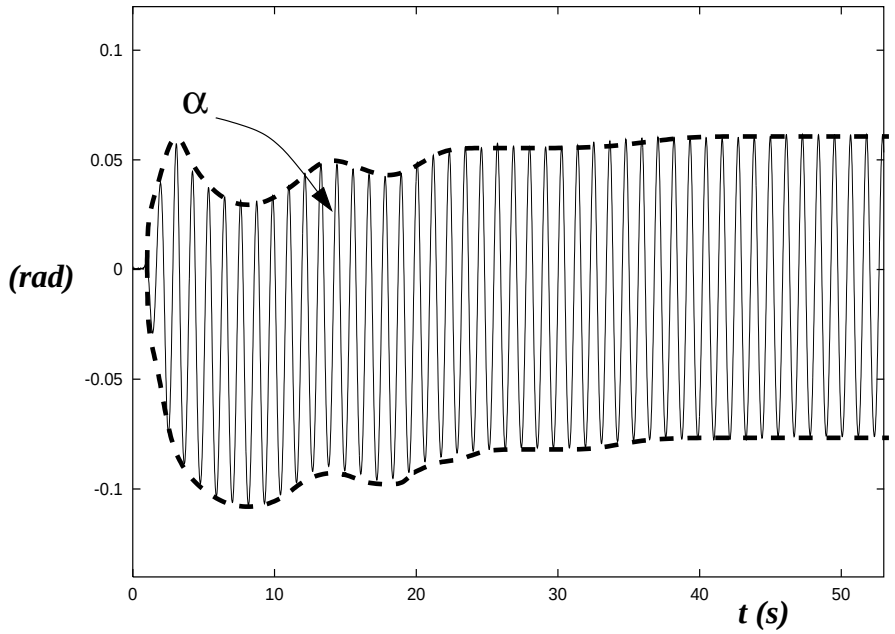

Figure 7.12 Wavemaker motion: angle of oscillation (solid line) and its envelope (dashed line). A positive angle corresponds to a flap rotation towards the tank.

been directly measured. This was done since the actual wavemaker motion does not coincide in general with the one set. Indeed, when wave reflection occurs an automatic control system adjusts the flap motion to ensure the desired wave conditions in the flume. From the figure, the first part of the time history shows clearly a modulated envelope of the wavemaker motion, with period consistent with flume natural period. It is difficult to detect when the seiching starts to influence α since the initial wavemaker motion is characterized by a ramp function of 2 s. As

the time increases, the low frequency oscillations of the envelope reduce in amplitude due to the control system. In later stages they become negligible.

Seiching modes are excited at the beginning of each experiment, regardless the ramp adopted to start the motion which has to be reasonably short to be of practical use. In principle, it could be possible to use active wave absorbers on the other side of the tank to reduce if not eliminate the seiching mode. In the absence of such devices, we cannot avoid the presence of the slowly varying oscillations due to these standing waves. The time interval from one experiment and the following can be made longer but the decay time is rather long because we are dealing with rather long waves. What matters is controlling that: (i) the residual amplitude of the seiching mode is small compared with the wave heights we are going to measure, and (ii) the time scale of the seiching period is not close to those involved in our experiments. In the specific case of our experiments, both the requirements are met well.

Initial conditions in the flume A certain time interval is necessary between each test for wave motions and parasite currents in the flume to die out, and to ensure the same initial conditions in the flume for each test. If the time interval between two following tests is not large enough, the results from test to test can vary in a percentage that depends on the error in the initial conditions and on the sensitivity of the specific measured quantity to the initial conditions. On the other hand, constraints exist also in the other direction. In particular, as it is discussed later in the section, pressure measurements require a strict control of the temperature and of the wetting of the gauges. This limits in practice the duration of the time intervals between tests. Different interval durations have been used. A mean value of 5 min was found to be a reasonable compromise of the competitive requirements.

Environmental conditions The environmental conditions are very important for the quality of the test results. The latter can not be achieved if the two following aspects are not accounted for.
First, it is crucial to keep environmental changes small during each test. From this point of view the temperature represented a key factor in the reliability of the pressure measurements.
Second, it is fundamental to control/avoid environmental disturbances in the experimental results. For instance, the 50 Hz current of the general power system may cause unphysical 50 Hz oscillations in the sensors output. Therefore 40 Hz filter was used in processing measured data to avoid this possible disturbance.

7.4.2 Instrumentation

Cavitation and ventilation of the wave probes The wave probes used in the flume are cylindrical sensors with a 3 mm diameter. In principle they are capacitive sensors measuring the wetted surface of the cylinder and giving as output the instantaneous elevation of the wave passing by as the time increases. This is given as a mean value among those measured along the circumference of the cylinder. This type of wave probe is thus not able to measure the free surface configuration in the case of breaking wave occurrence.

Close to the probe, surface tension effects matter and alter locally the free surface. This represents an error source in the wave elevation measurements. The latter is expected to be within ~ 1 mm. The environment where these sensors operate is an oscillatory motion with main period equal to the one of the wave system generated in the flume. If the ambient horizontal velocity at the wave probe is too high ventilation can occur at the wave probe. This phenomenon has been studied by Wetzel (1958) in a steady current. Related results have been applied to the wave probe by using a quasi-steady approach. The reason for doing this is that the KC-number associated with the oscillatory flow past the wave probe would be high ($83 < \mathrm{KC} < 168$). Environmental conditions have been approximated by those of a surface piercing cylinder in a slowly varying current with depth independent velocity. Limit of the velocity values exist (more precisely limit of a related Froudenumber) above which ventilation and cavitation phenomena occur on the probe. For the reliability of the experimental results it is crucial to be always under that limit. Otherwise the wavefield close to the "cylinder" is characterized not only by a local water run-up (i) in the body front but also by an important local run-down (ventilation, ii) in the downstream part. Physically this corresponds in the horizontal plane to respectively an upstream over-pressure and a downstream under-pressure. In Wetzel (1958) the threshold value for the Froudenumber defined as $U/\sqrt{gD}$ (U is the current velocity, g the gravity acceleration and D the draft of the cylinder) is given in terms of the geometric parameters of the problem. For a probe diameter of 3 mm this gives an upper limit of ~ 1.2 m/s for the current velocity without ventilation. In the performed experiments, the orbital velocity for the prescribed incoming waves was at most 0.44 m/s. This value is below the threshold velocity. As already pointed out (*cf.* section 7.2) and as it will be extensively discussed later (*cf.* section 8.1), the actual wave conditions in the flume were not the same as the prescribed ones during the tests. However, this does not compromise the obtained result.

In a preliminary step, cylindrical wave probes have also been considered for the measurements on the deck, with diameter of 2 mm. The value of the diameter was chosen as a compromise between different relevant aspects. In particular, the diameter has to be as small as possible to reduce the intrusion, namely the disturbance of the flow field during the delicate phase of the shipping. On the other hand, a too small diameter will not give a sufficiently stiff structure to withstand the hydrodynamic loads. In this case an additional support along the wave probe may be necessary. For the chosen value of the diameter the upper limit of a current velocity without ventilation is about 1.4 m/s. Clearly results in Wetzel (1958) are not directly applicable to the case of interest. However his results indicate possible problems in the measurements for flow velocities of that order of magnitude. Both preliminary numerical studies, made for dimensioning the experimental set-up, and experimental results, confirmed that during the studied water on deck phenomena the wave front velocities become order of 1 m/s. For these reasons less intrusive wave probes have been used for the evaluation of the water level evolution during the shipping, described in the following paragraph.

Wave probes on the model All the wave probes used on the model (wl_1, wl_2, wl_3, fd_1, fd_2, fw) are characterized by two metal strips 5 mm wide, placed parallel to each other with a 5 mm separation. Also these are capacitive. Main advantages of the specific set-up are the small intrusion of the probe and its versatility. The latter quality refers to the ease of using the probe in different contexts. In the present case, for example, this type of sensors is used to evaluate

the water level along the deck when the shipping occurred, the wave front propagation along the deck and its run-up along the vertical wall. The measured value corresponds to the averaged wetted length of the two strips. It is thus important to keep small their separation, otherwise the prediction, for instance, of the local water slope can not be sufficiently satisfactory when the water level is measured. Similarly as for the probes described in the previous paragraph, they can not be used to predict the real free surface configuration when breaking waves and in general cavitation phenomena occur. For the water front evolution along the deck, an error source is related to the cavity formation due to the plunging impact near the bow. This phenomenon is described in details in chapter 8. After the water hit the deck, two jets develop in opposite directions of the deck. In this phase the rate of change of the strips wetted length accounts for the evolution of both jets. Only after the cavity collapsed the strips wetted length is related to the flow going away from the bow. But bubbles, caused by the cavity collapse, are mixed to the water and represent an error source for the measurements.

Phase delays in the wave instrumentation In the present experimental arrangement, the electronic equipment driving our wave probes (both in the flume and on the ship model) introduces a frequency dependent phase shift which has not been fully characterized in our experiments (this is possible by a dynamic calibration procedure). Moreover, the phase responses of the probes, in principle, are not the same. This is the main reason for the different phase delays detected for the sensors fd_1 and fw.

Pressure gauges Changes in the temperature due to dry-wet-dry cycles of the pressure gauge conditions can cause a significant shift in the zero value given by the sensors. If this occurs during a measurement, the related results become practically unuseful. To control as much as possible this error source no lamp has been used during the tests. It implies that additional tests were performed for taking the video images. Further, a great effort was made to keep the pressure cells almost continuously wet. In particular, a wet towel was applied on the cells between a test and the next one. This was needed to ensure the same conditions and thus the same zero level before and after each test. In the later stages of the water on deck event the water level is lower than the pressure gauges. This means the sensors should measure atmospheric pressure. This is a good indication of the reliability of the pressure measurements and has been used to check the results from the data base.

Video images We found it effective to take measurements of free-surface profiles by using frames grabbed from the recorded video images. Clearly, also this procedure is affected by uncertainties and possible errors.

First of all, the axis of the video camera lens is aligned with some reference axis on the model, say the edge of the deck at the bow. Therefore, as we move from the focusing point of the lens outwards an error is introduced in the distances. Further, the focusing of the optical system, adjusted on the closest side of the water flume, is progressively not correct as we move towards the boundary of the available optical window.

Meniscus effects tend to spread the contact line between the free surface and the lateral tank wall. A similar uncertainty is introduced by the fact that glass walls remain wetted. In

particular, when the water level decreases, a thin layer of water "following" the contact line can be seen. Actually, by adjusting properly the source of light, both effects do not introduce a significant uncertainty in determining the wave profile along the wall.

We found more important error source the non-perfect perpendicularity of the lens axis to the lateral wall of the flume. In such unlucky cases, the large distortion of the lengths in the plane of the image due to the perspective error prevents completely a reliable measurement of the wave profile.

7.4.3 Model

Defects in the model set-up A gap of about 1.5 mm was caused by the imperfect connection in the middle of the deck, between the deck and the vertical wall. The gap has been covered by using copper tape, but a certain influence in the results is expected since in this way the deck is not perfectly horizontal.

An offset of ~ 2 mm was observed in the divinisel appendix with 45° (case b in figure 7.2). Due to this, the fore portion of the deck was not perfectly horizontal and the actual stem angle was reduced by 0.57 degrees. In addition, due to the connection mechanisms of the appendix with the rest of the model (only two screws aligned along a horizontal line were used) pitch motion was excited by the loading conditions during the run-up of the water along the bow and the following water shipping. Related amplitude was however small. In connection with this, leakage phenomena occurred from the model sides making practically unuseful the water level probes along the deck for the tests with this bow geometry.

Elastic behavior of the wall If the loading time of the vertical superstructure is small or comparable with the natural wetted-period of the wall, hydroelastic effects become important. Since rigid wall conditions are of interest in present experiments, the wall set-up (*cf.* section 7.2.1) has been decided to prevent this phenomenon. The fact that hydroelasticity did not matter during the experimental water impact with the wall has been verified by applying the developed numerical model to the problem. This gives ~ 0.14 s as a measure of the loading time, here taken as the time for the water to rise about the 40% of the wall. Numerical results were then used for a simplified analysis as described in the following text.

The wall is substituted by an equivalent beam described in figure 7.13, with highest natural dry-period

$$T_{1,\mathrm{dry}} \simeq 2\,\pi\,(\frac{L_{\mathrm{beam}}}{4.73\,\pi})^2\,\sqrt{\frac{\rho_{\mathrm{plex}}\,A}{\mathrm{EI}}} \simeq 0.00011\,\mathrm{s}\,.$$

Here ρ_{plex} is the plexiglas density, A is the cross-section area and L_{beam} is the beam length. $T_{1,\mathrm{dry}}$ is very small compared with the numerical loading time. This result is in principle not conservative, since one expects the natural wetted-period to be larger than $T_{1,\mathrm{dry}}$, due to the added mass contribution. However, if we use the numerical analysis conducted in chapter 5 as a reference, $T_{1,\mathrm{wet}}$ should be at the most three times $T_{1,\mathrm{dry}}$. This rough estimate suggests that with this set-up the experiments are not affected by elastic oscillations of the wall, as confirmed by the test results. In particular, the pressure recordings do not show suspicious oscillation frequencies.

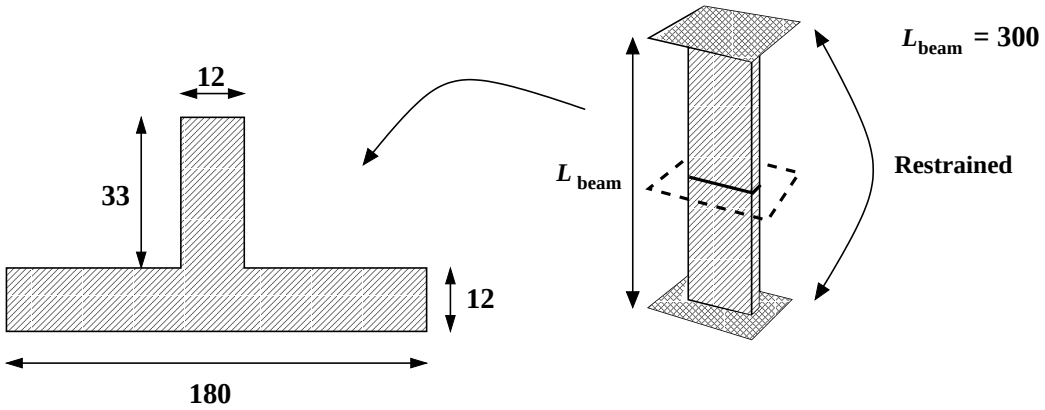

Figure 7.13 Cross section (left) and boundary conditions (right) of the equivalent beam for the vertical wall. Lengths are in millimeters.

Bubbles When the cavity caused at the beginning of the water shipping collapsed, bubbles are generated and partially convected with the flow towards the vertical wall. To these, new bubbles are added during the water rising along the vertical wall, as a consequence of the spray. The bubbles can be responsible for time dependent changes in the wall loading.

Three-dimensional effects During the rise up of the water along the vertical wall, a jet develops causing spray formation. At this stage the flow becomes unstable and three-dimensional effects start to be important (see figure 7.14, back view from the experimental video images).

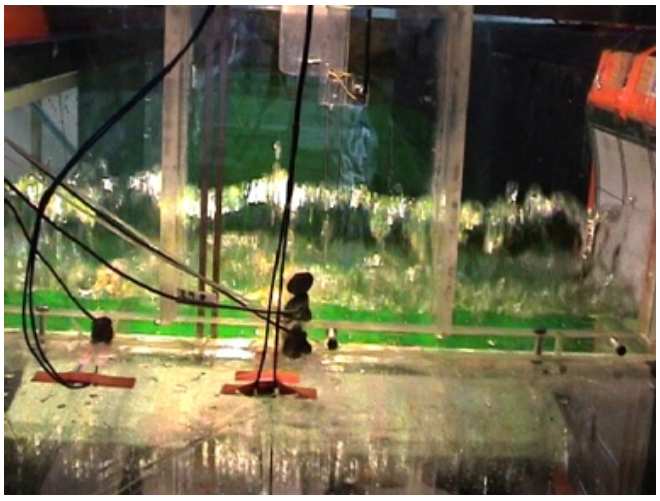

Figure 7.14 Experimental water run-up along the vertical wall (back view).

From this moment on the experimental results loose their reliability from a quantitative point of view.

7.4.4 Human Errors

Human error represents an error source difficult to quantify since it influences the test results from many points of view. These are not discussed here. It is only mentioned the one associated with the wetting of the pressure cells (*cf.* section 7.4.2) since it is specifically related to present tests.

Chapter 8

Water-on-Deck Experiments: Analysis

In this chapter, the main physical aspects of the initial stages of water shipping and its late evolution are discussed on the ground of the two-dimensional model tests described in the previous chapter, and complemented by numerical simulations. Typical time histories of the measured wavemaker motion for the cases analyzed experimentally are reported in appendix G.

8.1 General Remarks

As anticipated, in the following the experimental results are complemented and interpreted also through the use of numerical simulations. In particular (*cf.* section 3.2.2), for the purpose of comparison, the physical wave flume is numerically modeled and the measured wavemaker motion is used to drive the flap in the simulation. This motion includes the feedback action that the control system uses to minimize reflections (mainly) from the model. On the other hand, we did not attempt to model the absorbing beach at the end of the wave flume, and the mathematical damping region (*cf.* section 3.4) used in the numerics is quite different from the physical one. This represents a source of uncertainty when comparing the two results. Figure 8.1 shows the evolution of the wave elevation at two locations, 0.79 m from the flap (left plot), and at 0.104 m upstream the vertical bow (*cf.* case a in the right plot of figure 7.2). Here, the nominal incoming wavelength is $\lambda = 2$ m and the crest-to-trough waveheight is $H = 0.16$ m. The experimental data are compared with the numerical results. The agreement is rather satisfactory, though, at the beginning, a small difference could be observed from an enlarged plot (not reported). Possible explanations of the difference, concerning the experiments, are discussed in section 7.4. A possible reason could be the seiching motion, set up initially in the physical tank and not correctly reproduced in the numerical simulation because of the mentioned difference in the treatment of the downstream end of the tank. However, according to a first estimate presented in chapter 7, the standing waves would require about 8.47 s to be set up in the flume. This means a longer time interval relative to the one of interest. This estimate is quite rough since it does not account for the presence of the damping region and of the ship model. As time

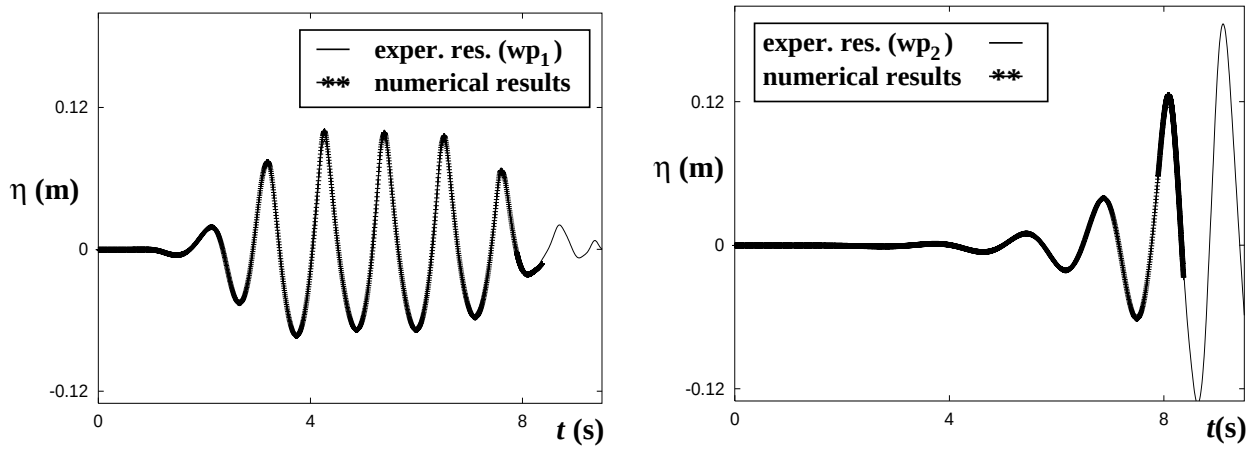

Figure 8.1 Evolution of the wave elevation recorded at 0.79 m from the flap (left plot) and at 0.104 m from the bow of the model (right plot) for case a in figure 7.2. Nominal incoming waves: $\lambda/D = 10.1$, $H/D = 0.808$. Experimental and numerical wave records are compared.

increases, the measurements would show a small phase delay relative to the numerical results. This is practically constant and is probably due to a phase lag introduced by the wave probes and their driving electronics.

In the following, the first water-on-deck event is focused on. This implies a quite transient phenomenon because the incoming waves are far from being regular. This can be appreciated in figure 8.2, which gives the numerical free-surface configurations for the same case as in the previous plots. Four time instants are considered, $t = 2.82$, 4.23, 5.63 and 7.04 s from top to bottom, respectively. The wavemaker is at the left end of each snapshot, though it is not

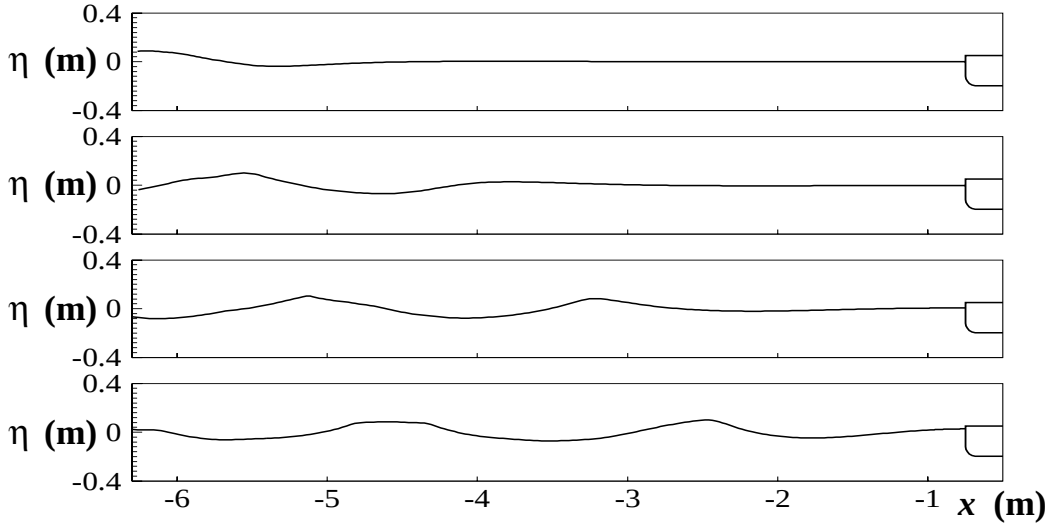

Figure 8.2 Numerical free-surface configurations before water shipping occurrence corresponding to nominal incoming waves with $\lambda/D = 10.1$ and $H/D = 0.808$. The plots are in natural scale and the time increases from top to bottom ($t = 2.82$, 4.23, 5.63 and 7.04 s).

represented for simplicity. The settings of the control system in the experiment would give waves 2 m long and with a 0.16 m crest-to-trough height. As we can see, the initial portion of the

generated wavetrain is neither symmetric nor with constant amplitude. The differences from the prescribed incoming waves are better emphasized in figure 8.3, where the portion of the free surface closer to the ship model is plotted for $t = 7.04$ and 7.66 s, respectively. In this case,

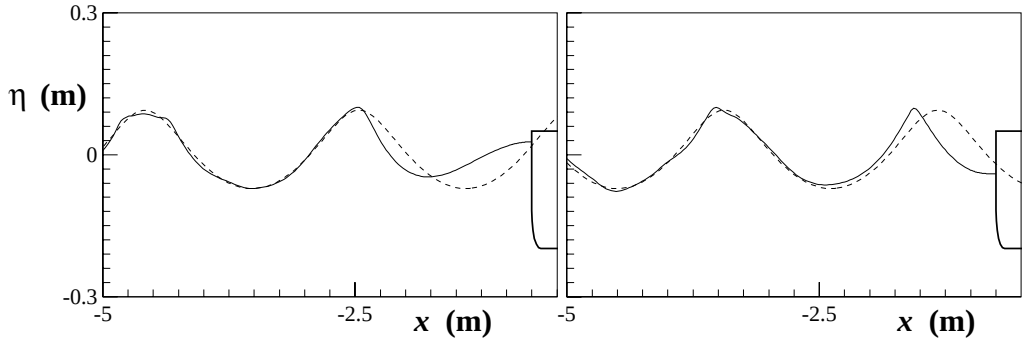

Figure 8.3 Free-surface configurations near the bow before water-shipping occurrence ($t = 7.04$ and 7.66 s, left and right plots respectively). Nominal incoming waves: $\lambda/D = 10.1$, $H/D = 0.808$. Present numerical solution (solid lines) and permanent-wave solution (dashed lines) by Fenton (1988) are compared. The plots are not in natural scale.

plots are not in natural scale. Numerical results (solid lines) are compared with the permanent-wave solution (dashed lines), obtained as in Fenton (1988, *cf.* section 3.2), corresponding to the prescribed wave conditions. Only a rough resemblance between the two solutions can be observed, with the leading wave steeper and shorter than the nominal regular wave. This becomes even more pronounced as waves approach the ship, due to wave-body interactions. Therefore, though the prescribed wave parameters will be used to identify the wave conditions, we underline the highly transient character of the flow in front of the model.

8.2 Water shipping: First Stages

8.2.1 General Description

Figure 8.4 is representative of the initial stages of water shipping. The considered ship model has a vertical bow (*cf.* case a in figure 7.2) and the prescribed incoming wave is 2 m long and with a 0.16 m crest-to-trough height. At the beginning, the fore-part of the deck remains dry, and the shipping of water starts in the form of a rounded jet plunging directly onto the deck. A cavity is formed with air trapped inside. This behavior has been observed in all the studied test conditions. Moreover, though in the particular case shown here the jet hits the deck rather close to the bow edge, cases are recorded where the fluid organizes itself to plunge on the deck further from the bow. Finally, for some wave conditions, even blunter impacts have been observed. In all cases, front-view pictures of the same event (not reported) confirmed the two-dimensionality of the phenomenon, and excluded that the cavity formation is related to localized three-dimensional instabilities. As a consequence, the initiation of deck-wetting should be characterized by localized high impact pressures.

This fluid behavior was not detected in the two-dimensional experiments reported in Cozijn (1995). This may be due to the small time and space scales involved In the reported example,

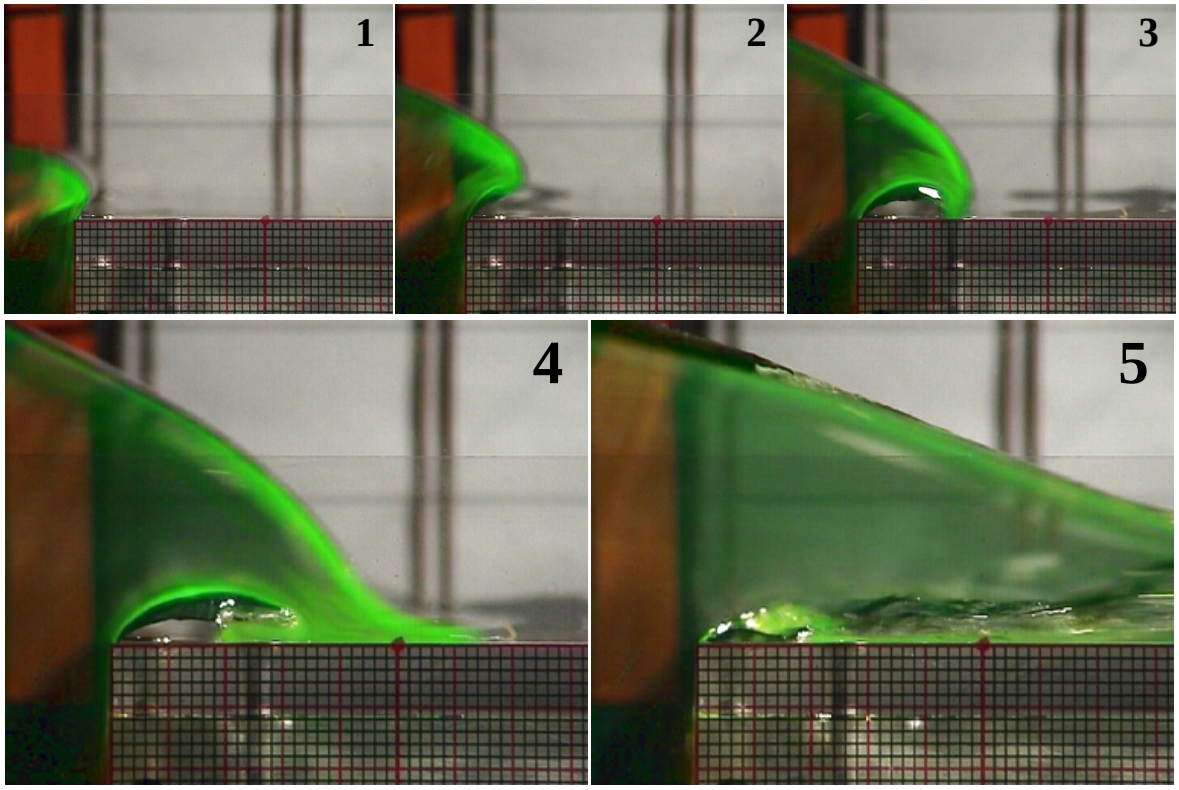

Figure 8.4 Two-dimensional water-on-deck experiments. Initial stages of the watershipping due to nominal regular waves with $\lambda/D = 10.1$ and $H/\lambda = 0.08$. The snapshots are enumerated as time increases, and the time interval is 0.04 s. The smallest grid dimension is 2 mm.

as described below, the time needed before the plunging wave hits the deck is about 0.13 s, and at the instant of impact the entrapped cavity has length $l_{\text{cav}} \simeq 0.2D$ and height $h_{\text{cav}} \simeq 0.05D$.

From the point of view of measurements, a consequence of the presence of an air cavity is that capacity wave probes do not estimate correctly the free-surface height along the deck.

After the impact of the plunging wave onto the deck, *cf.* bottom plots in Fig. 8.4, two horizontal jets develop. One of these moves backwards, reducing the cavity volume. The other one propagates forwards with higher velocity. As time passes, the whole cavity is drifted forwards, convected together with the shipped water. The water level above the cavity increases and contributes to squeeze it. These combined actions are responsible, together with surface tension, of the following fragmentation of the cavity. However, this evolution cannot be documented because of the limited frame rate of the video camera and, in any event, the late evolution of the entrapped cavity is three-dimensional.

8.2.2 Vortex Shedding at the Edge of the Deck

Natrium flourisenium powder, mixed with Dutch syrup, was used as fluorescent material to detect a possible vortex-shedding in the initial stage of the phenomenon. The resulting mixture was placed in the upper-front portion of the bow. During the tests, the running-up water slowly

dissolves the syrup and the fluorescent material is convected with the fluid wetting the deck. For cross flow past blunt bodies, Skomedal (1985) documented that this procedure is suitable for vortex-shedding visualizations. Here, by using this method, we have not detected any clearly defined vortical structure during the initial stages of water shipping.

Later on, after the air entrapment, when the cavity starts to move forwards, the gravity has already organized the run-down of the fluid in front of the model, preventing the beginning of vortex shedding, at least of strength large enough to be detected by the used method. This is qualitatively shown in figure 8.5, where an enlarged view of the flow around the bow is given

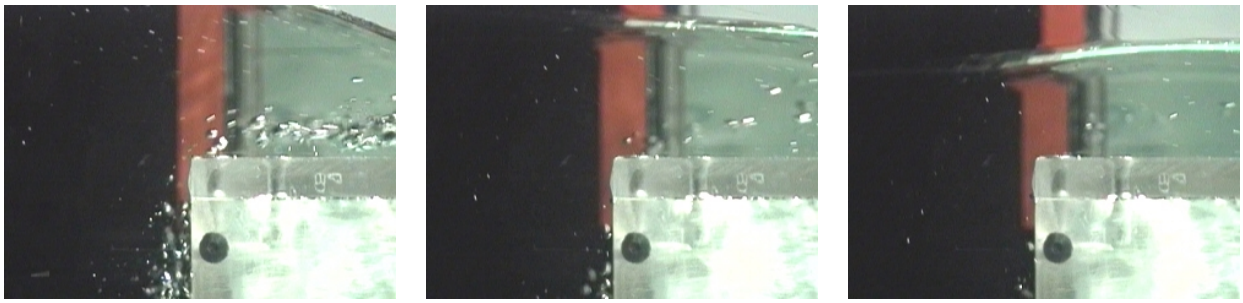

Figure 8.5 Evolution of the flowfield near the bow edge during the late stages of watershipping. The time increases from left to right with time interval of 0.04 s. Nominal regular incoming waves: $\lambda/D = 10.1$, $H/\lambda = 0.08$.

for the later stages of water shipping. The time increases from left to right, and entrapped air bubbles are clearly visible in the water. By tracking their motion, we can see that the bubbles above the deck are convected rightwards, while those in front of the bow move downwards. Therefore, grossly speaking, the flow is divided into two streams wetting the deck and involved in the run-down, respectively, with negligible cross-flow and vortex shedding effects.

8.2.3 Wave Plunging Evolution

Numerical simulation The plunging phenomenon observed in the experiments is not correctly described by the initial Kutta-like condition, introduced in section 3.3. There, a more suitable model is given through the continuous Kutta-like condition. Numerical results for the case just discussed are superimposed (red lines) to the experimental profiles in figure 8.6. The time increases from left to right with a constant interval of 0.04 s.

In the experiments, the start of the video camera is not triggered by the wavemaker motion, and the actual instant of time of the reported pictures is not known. Therefore, the corresponding numerical sequence is determined *a posteriori* in the following way. First, the numerical free surface in agreement with the *last* experimental wave profile is found. In the case presently considered, this corresponds to a time instant $t - t_{\mathrm{wod}} = \Delta t_{\mathrm{wod}} \sim 0.11$ s, where t_{wod} stands for the instant of freeboard exceedance in the numerical simulation. Then, the numerical sequence is obtained by considering the same time interval, 1/25 s, of the video camera. Therefore, the triggering between numerics and experimental data is done heuristically, and it leaves open the possibility of a time lag between experiments and numerical results. This possible error can not be quantified with the used instrumentation.

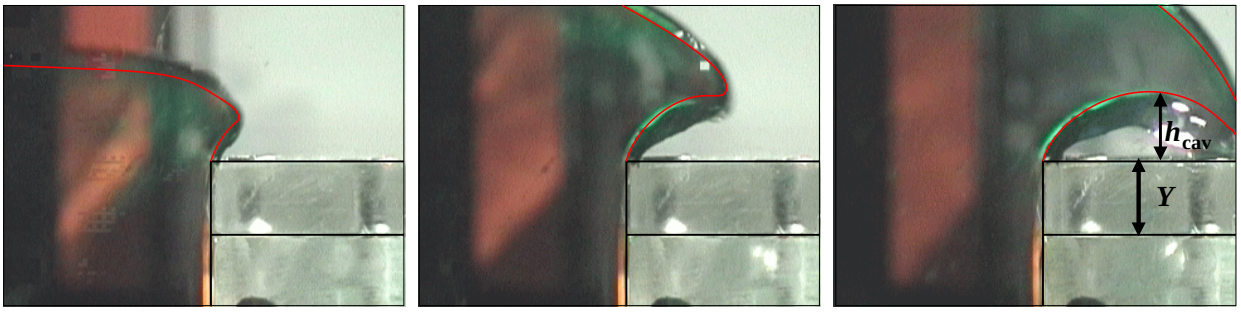

Figure 8.6 Initial stage of the watershipping. Numerical free surfaces (red lines) are superimposed to pictures from the experiment. The time interval between twosnapshots is 0.04 s. Nominal regular incoming waves: $\lambda/D = 10.1$, $H/\lambda = 0.08$.

From figure 8.6 experimental and numerical free surfaces agree quite well. In particular this is true for the time scale of the phenomenon and for the cavity dimensions. The differences visible in the sequence can partially be explained by meniscus effects at the glass side of the flume, and by three-dimensional effects in the video images. A light disturbance in the last picture makes it difficult to decide sharply if water impact with the deck already occurred.

Fromthe numericalsimulation, the impact occurs at a distance $\simeq 0.2D$ from the bow, after $\Delta t_{\mathrm{wod}} \simeq 0.13$ s from the instant of the freeboard exceedance.

Analysis of the cavity profile The fair, if not good, agreement, between experiments and numerics allows us touse the numerical meanstodiscuss in more detail the local features of the phenomenon.

In figure 8.7, the free-surface profile close to the separation point at the bow is compared with

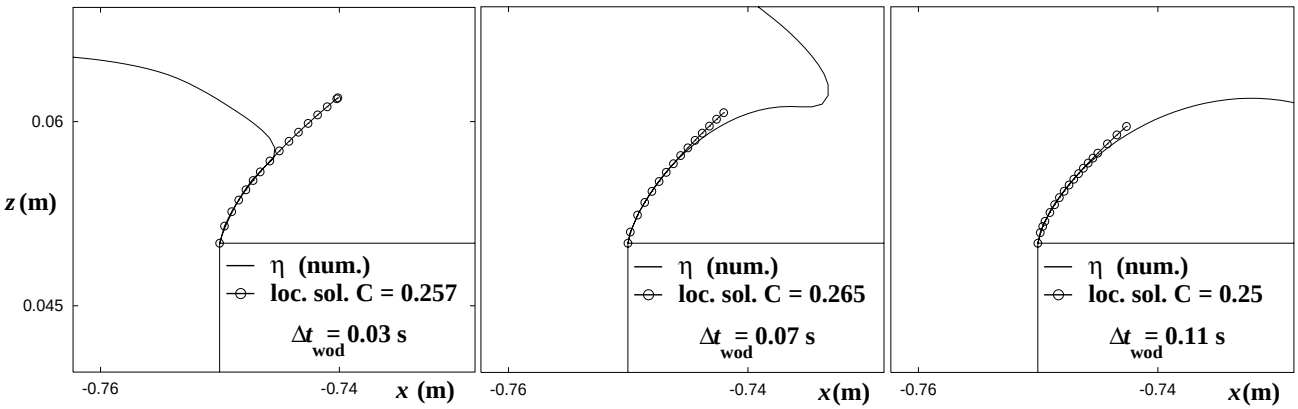

Figure 8.7 Initial stage of the water shipping. Numerical free surfaces, solid lines, and local solution (8.1), lines with circles, are compared. Nominal regular incoming waves: $\lambda/D = 10.1$, $H/\lambda = 0.08$.

the local solution (*cf.* Zhao *et al.* 1997)

$$z_1 \;=\; C(t)\, x_1^{2/3} \tag{8.1}$$

around a fixed separation point, obtained by assuming potential flow theory and zero gravity effects.

Similar result can for 2-D flow be derived for the thin free shear layer shape close to a separation point. In expression (8.1), the origin of the local coordinate system (x_1, z_1) is at the edge of the deck, the x_1-axis is along the deck and the z_1-axis is vertically upwards. The coefficient $C(t)$ is a time dependent parameter which depends on the complete flow, and therefore cannot be determined by a local flow analysis. The agreement of the local solution with the numerical data is good. In particular, the computed free-surface profiles for $\Delta t_{\rm wod} = t - t_{\rm wod} = 0.03, 0.07$ and 0.11 s fit quite well the local solution, when values $C \sim 0.26$, 0.27 and 0.25 are used, respectively.

The configuration of the free surface at the impact with the deck is analyzed in figure 8.8. Far

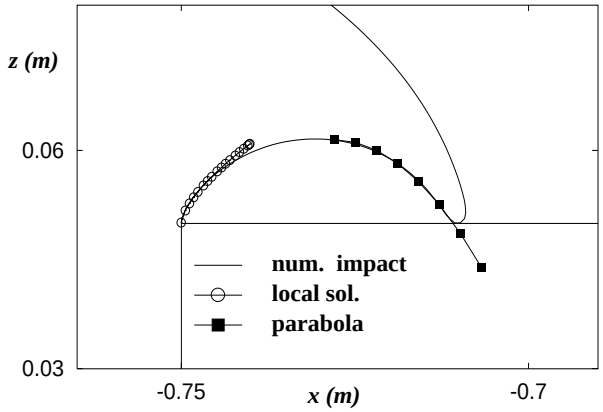

Figure 8.8 Water impact with the deck. Nominal regular incoming waves: $\lambda/D = 10.1$, $H/\lambda = 0.08$.

enough from the deck edge, and up to the impact position, the cavity profile agrees well with a parabolic contour (line with black squares). The latter would be the path of a fluid particle in free fall under the action of the gravity. This and the previous observations suggest the existence of three main stages during the flow evolution. An initial phase (i) where the gravity does not matter and a final stage (iii) with free-falling water, joined by an intermediate phase (ii), where both the gravity and the pressure gradient influence the fluid motion.

Steepness influence on the cavity Figure 8.9 shows the wave plunging on the deck during the first water shipping caused by three different wave systems. The steepness of the nominal regular incoming waves is $H/\lambda = 0.04$, 0.06 and 0.08, from left to right, respectively, with wavelength $\lambda = 10.1D$ for all the cases. The smallest steepness considered is associated with a quite gentle water on deck. As a consequence, it is practically impossible to detect the cavity formation and probably surface tension significantly affects the evolution. For larger H/λ, the cavity is visible and increases more from the second to the third case than from the first to the second one. Since the involved rate of change of the steepness is kept constant, this suggests a nonlinear dependence of the cavity dimensions from the wave steepness.

The first water-on-deck is also examined in figure 8.10. Here the wave steepness is kept fixed to $H/\lambda = 0.08$. The wavelength λ is 7.58 D, for the case A in the left picture, and 10.1 D, for the case B in the right picture, corresponding to actual wave heights $H = 0.606$ D and 0.808 D,

respectively. This implies a smaller amount of water shipped in case A. Qualitatively the two cavities have similar shapes. A more quantitative comparison is given by scaling the free-surface profile digitized from case B (*cf.* red line in the right picture) by the factor $(H-f)_{\mathrm{A}}/(H-f)_{\mathrm{B}}$, and plotting it over the case A (*cf.* the red line in the left picture). The overall agreement is

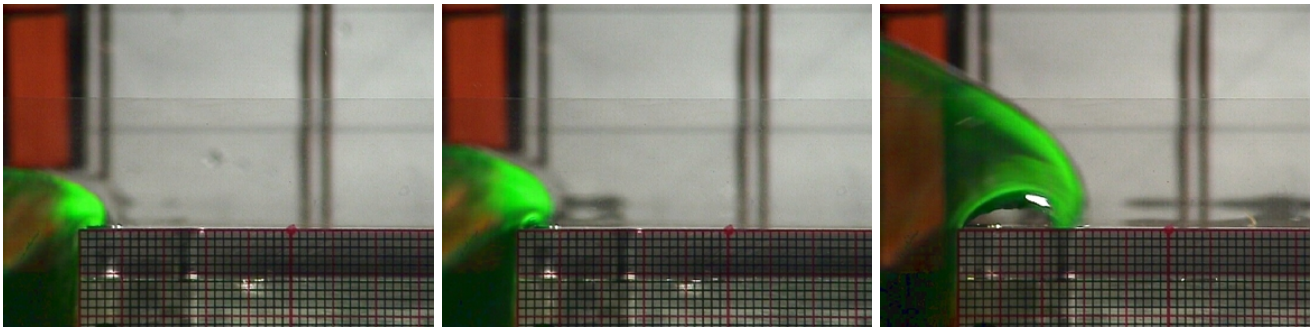

Figure 8.9 Influence of the wave steepness on the cavity. From left to right: $H/\lambda = 0.04$, 0.06, 0.08. $\lambda/D = 10.1$ for all the cases. The smallest grid dimension is 2 mm.

reasonable and suggests $(H-f)$ as a possible scaling factor. Actually, differences can be detected for the profile of the entrapped cavity which should be expected because of the different role of surface tension. Besides this, other uncertainties hamper the comparison, such as actual instant of time, optical effects, etc. The agreement between the uppermost free-surface profiles is definitely good.

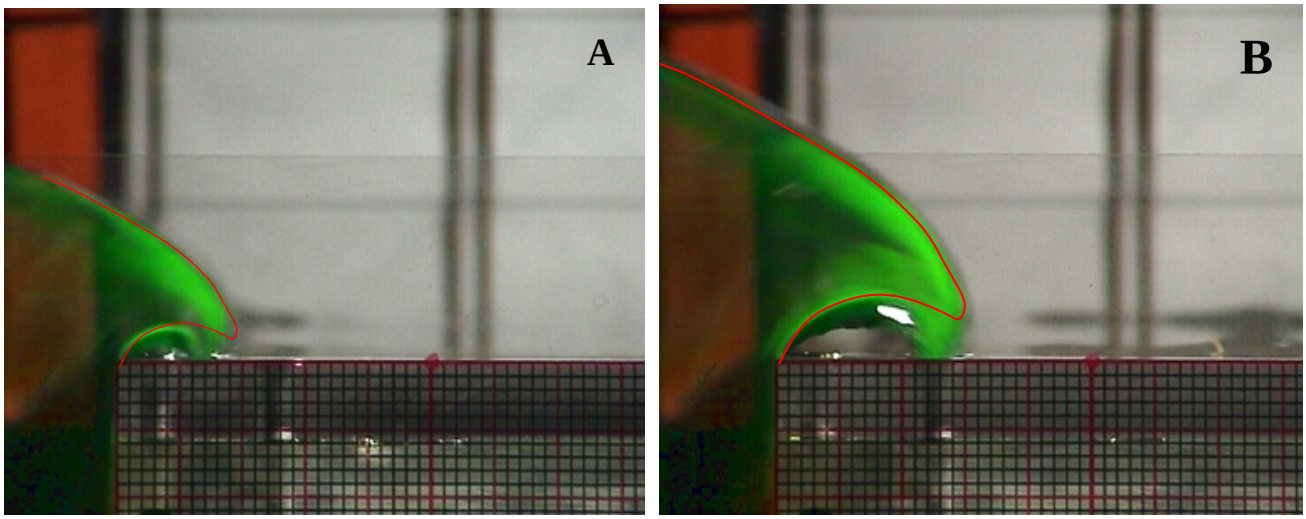

Figure 8.10 Influence of the wavelength on the cavity. Left: case A, $\lambda/D = 7.58$. Right: case B, $\lambda/D = 10.1$. The steepness is $H/\lambda = 0.08$ for both cases. The free-surface profile digitized from case B (red line in the right picture) is scaled by the factor $[(H-f)_{\mathrm{A}}/(H-f)_{\mathrm{B}}]$ and plotted over the left picture for case A. The smallest grid dimension is 2 mm.

8.2.4 Water Impact with the Deck

The previous results have shown that water shipping starts with a wave plunging on and impacting against the deck. Here, we briefly analyze the possible effects of the impact for a FPSO. Throughout the section we will refer to full scale dimensions by considering a ship draft of 18 m.

The typical steel stiffeners along the deck are sketched in the left diagram of figure 8.11. The deck is designed to stand against a maximum spatially uniform pressure of 60 KPa. In

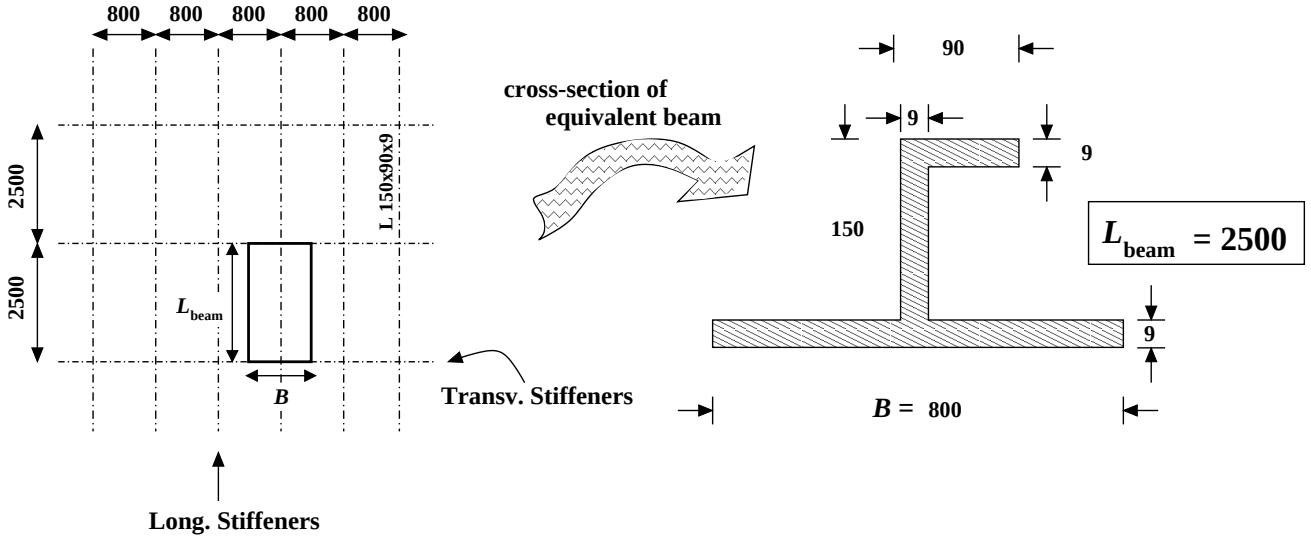

Figure 8.11 Example of stiffeners on the deck of a FPSO. Left: top view. Right: cross-section of the equivalent beam modeling the deck in the longitudinal direction. Dimensions are in millimeters.

the present two-dimensional analysis, an equivalent beam (*cf.* right sketch in figure 8.11) is used to model the deck structure along a longitudinal stiffener. The beam is assumed to be simply supported between two consecutive transverse stiffeners. In this framework, to carry out a qualitative investigation both experiments and numerical simulations are considered. In particular, the latter are used to overcome the lack of information from model tests (*e.g.* the impact velocity).

Here, we consider the water impact following the shipping of water caused by incident waves with length 182 m, and height 14.55 m ($\lambda/D = 10.1$ and $H/D = 0.808$). The free-surface configuration as obtained by the numerical simulation is given in figure 8.12. The two horizontal arrows indicate the length of the first two equivalent beams along the deck. As we can see, the impact starts close to the middle of the second one. From the numerical simulation, an impact velocity of 4.3 m/s is estimated. This value is not large, and in particular is close to the orbital velocity in free-wave conditions (4.4 m/s). The free-surface shape near the initial impact position is rather blunt with radius of curvature $r \simeq 0.1$ m.

The impact phenomenon can thus be approximated as the impact of a fluid circle against a flat wall and without gravity effects, and therefore described in the initial stage by a Wagner-type approach (*cf.* Faltinsen 1990). The related problem is sketched in figure 8.13, where the main involved parameters are indicated. The solution procedure is the same as the one described in section 5.2.1 for the impact of a fluid wedge hitting a flat wall. In particular, parameter c shown in sketch 8.13 can be obtained as $2\sqrt{Vrt}$ by locally approximating the initial circular shape of the fluid with a parabola. This approach may not be used at the very beginning of the impact,

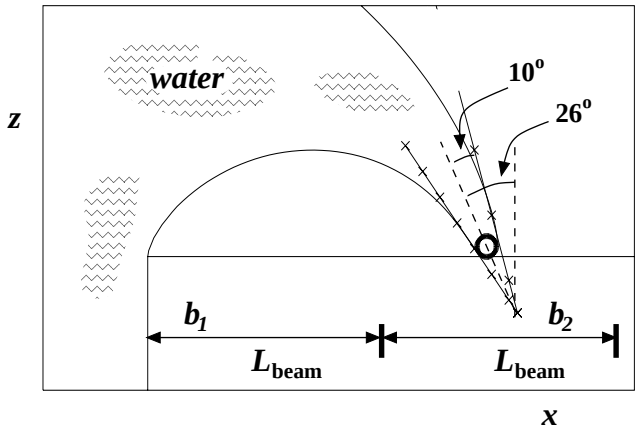

Figure 8.12 Impact with the deck (numerical simulation). Close to the impact position the free surface (solid line) is approximated by a circle with radius $r \simeq 0.1$ m. The free surface resembles a fluid wedge of ~ 20 degrees, inclined of ~ 26 degrees with respect to the vertical direction. The two horizontal arrows (b_1 and b_2) indicate the length of the first and second equivalent beams along the deck.

when infinite pressures are predicted and the method is not valid since the neglected water compressibility is important. In reality, though high, the pressure cannot exceed the acoustic pressure $p_{\rm ac} = \rho\, c_e\, V$. Here ρ is the water density, c_e is the sound velocity in water (usually varying between 1450 m/s and 1540 m/s), and V is the impact velocity. In the specific case, the maximum value of $p_{\rm ac}$ is ~ 6.6 MPa. This is much larger than the design pressure. However since the high pressures are localized in space and time, the effect on the structure is limited. The time duration of the acoustic phase can be estimated through the Wagner method by imposing the maximum pressure equal to the acoustic value

$$p_{\max} = p_{\rm ac} \quad \Longrightarrow \quad \frac{\rho}{2}\left\{\frac{d[c = 2\sqrt{V t_{\rm ac} r}]}{dt}\right\}^2 = \rho V c_e \quad \underbrace{\Longrightarrow}_{\text{Hp: } V=\text{ constant}} \quad t_{\rm ac} = \frac{r}{2c_e}\,. \tag{8.2}$$

This gives $t_{\rm ac} \sim 3.3 \cdot 10^{-5}$ s for the present case. Alternatively we can say that the acoustic phase lasts until $\mathrm{d}c_{\rm geom}/\mathrm{d}t = c_e$ (*cf.* Korobkin 1995), with $c_{\rm geom}$ obtained as geometric intersection of the fluid circle with the deck. For very small times, this gives $c = \sqrt{2Vrt}$ and $t_{\rm ac} \sim 0.9 \cdot 10^{-7}$ s. These two estimates give an indication of, respectively, the upper and the lower limit of the compressibility phase duration, and show that this phase is quite short.

For $t > t_{\rm ac}$, a Wagner-type method can be used to find the evolution of the pressure distribution along the deck. The duration of this second stage can be estimated as the time interval for half-circle of fluid to have impacted with the deck ($\beta = 90°$ in figure 8.13), from the end of the acoustic phase. In this case, by using the geometrical relationship $c = r \sin\beta$ and the solution for c ($c = 2\sqrt{Vtr}$), we find $t_{\rm circ} \sim 5.8 \cdot 10^{-3} s$. At this time, the maximum pressure becomes 37 KPa, which is smaller than the design pressure. The time duration of the second impact phase is larger than the first one, and corresponds to $\sim 37\%$ of the highest natural dry period of the equivalent beam, $T_{\rm dry1} = 0.0156$ s (*cf.* sketch 8.11). This means they are of the same order of magnitude and therefore the elastic response of the beam has to be analyzed. We must note that strictly speaking the Wagner method is valid for $\beta \leq 20°$. In paragraph 5.2.1 we have

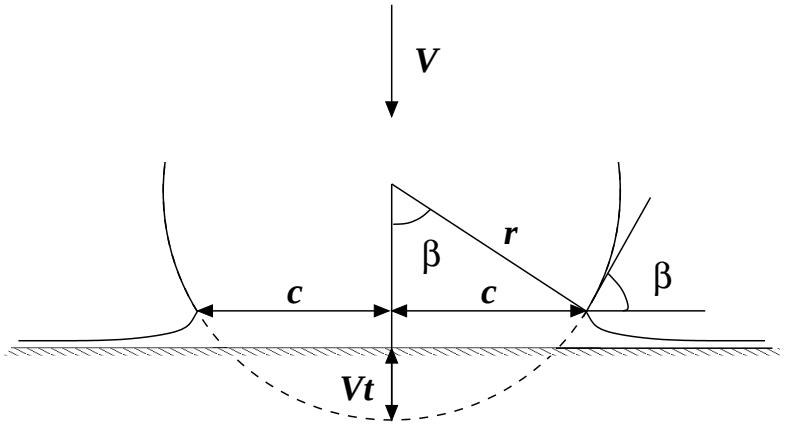

Figure 8.13 Sketch of the problem of a fluid circle hitting a flat horizontal wall.

seen that in the case of a fluid wedge hitting a flat wall, the maximum pressure predicted by the Wagner method compared well with the pressure obtained with similarity solution at least until a deadrise angle of 45°. Since here we have used this approach up to $\beta = 90°$ we can expect that t_{circ} has only been roughly estimated. During this blunt impact phase the region of the beam with important pressure loads is $\sim 2r = 0.08\ L_{\text{beam}}$, thus quite small relative to the beam length. The beam evolution and the related stresses can thus be determined in a simplified way, by considering the problem of an initially undeformed beam subjected to a spatial Dirac-delta load, $f(t)\delta(x - x_{\text{imp}})$, at the initial impact position. $f(t)$ can be estimated as vertical force on a rigid circle penetrating a flat free surface (*cf.* Faltinsen 1990) and expressed as $\rho C_s(t) r V^2$. The time dependent coefficient C_s has been derived experimentally by Campbell and Weynberg (1980) and is represented by the formula

$$C_s = \frac{5.15}{1 + 8.5\dfrac{h}{r}} + 0.275\frac{h}{r}.$$

Here $h = Vt$ is the instantaneous submergence of the circle and is equal to r when half-circle penetrated the free surface. This means that the end of the blunt impact phase should be given by $t_{\text{circ}} = r/V \sim 2.44 \cdot 10^{-2} s$ which is four times the value predicted above. Since this value is not based on the assumption of small deadrise angle, it should be considered a more realistic estimate than the previous one. An analysis like this shows that the resulting maximum stresses on the beam are safely below the yield stress.

The next stage of the evolution can be roughly approximated by the impact of a fluid wedge of 20° hitting asymmetrically the deck (see figure 8.12). In case of a rigid deck, this would give a maximum pressure of ~ 18 KPa on the assumption that the impact velocity is constant and equal to the initial value of V. This pressure value was obtained numerically, by taking the free-surface data from the similarity solution of a liquid wedge impacting nonsymmetrically a flat rigid wall (see appendix D). Clearly, this value is definitely below the safety limits for the deck. The actual evolution is however more complex. From video images of model tests, during this phase, the two jets developing in opposite directions along the deck wet completely the second beam (b_2). The portion of the deck closer to the bow is instead characterized by a cavity

originated at the impact instant, which is stretched by the flow entering the deck and above it. As a consequence, the first beam (b_1), under the action of the atmospheric pressure at the beginning of the cavity formation, suffers loads due to the compressibility of the air entrapped in the cavity. If we assume a uniform pressure in the cavity, and we model the air evolution as an adiabatic process of an ideal gas, the pressure $p(t)$ in the cavity can be obtained by

$$\frac{p(t)}{p_0} = \left\{ \frac{\mathcal{V}(t)_0}{\mathcal{V}(t)} \right\}^{\gamma}, \qquad \text{with } \gamma = 1.4\,. \tag{8.3}$$

Here, $p(t)$ and $\mathcal{V}(t)$ are the pressure and the volume at time t and p_0 and $\mathcal{V}_0$ are the corresponding reference values, *e.g.* the atmospheric pressure ($p_0 = 1\,\text{Atm} \simeq 10^5$ Pa) and the air volume in the cavity at the impact instant. As already observed, the cavity is squeezed during the following evolution, and the relation (8.3) would predict unbounded pressure above the first beam. Therefore, this simple analysis is eventually not applicable. However, from the structural point of view, the important factor is the rate of change of the pressure and this one can be predicted by using the above relation.

In the following, by using equation (8.3) and the pictures taken from the experiments, we have carried out a simplified analysis. In the sequence 8.14, the post-impact evolution is shown

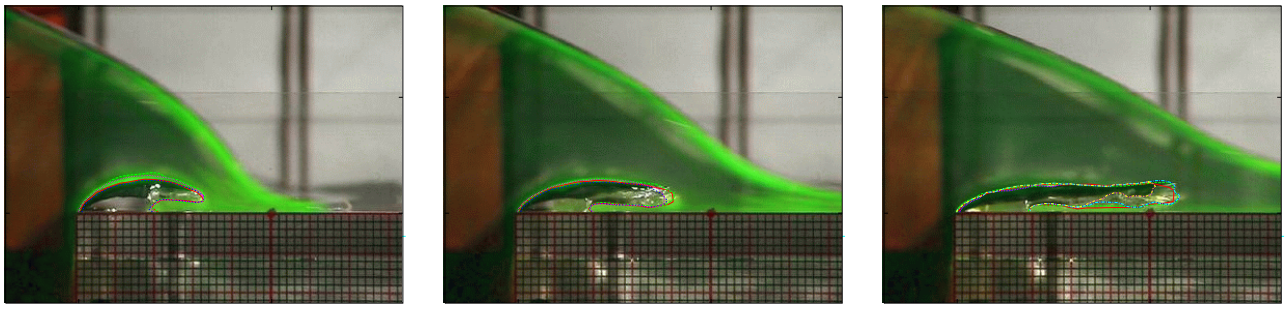

Figure 8.14 Pictures from the experiments showing the evolution of the air cavity at the bow edge. The time increases from left to right with a constant interval of 0.38 s (full scale, $D = 18$ m). The digitized cavity profiles (colored lines) are superimposed to the video images.

with snapshots separated in time by 0.38 s. Because of the relatively poor resolution of the images, at least for the present purpose, the cavity profile is not sharply detectable from the pictures (see the discussion in section 7.4), and for each snapshot several different curves are candidates as cavity boundary. Therefore, all of them have been considered and are reported, superimposed to the corresponding video images. For each instant of time, the cavity volume has been evaluated and introduced in relation (8.3) to estimate the pressure inside the cavity. Clearly, because of the uncertainty in the determination of the cavity boundary, for each time step several scattered results will be obtained.

Actually, the use of relation (8.3) requires some extra data which are not available from the experiments and our numerical simulations have been used to complement the available experimental information. In particular, the impact instant t_{imp} is not available from the video images, therefore (i) the volume $\mathcal{V}_0$ cannot be obtained from the experiments and (ii) the time interval $t - t_{\text{imp}}$ of each of the considered configurations (see sequence 8.14) is unknown. Here,

$\mathcal{V}_0$ has been evaluated by numerical simulations, and the time of the experimental snapshots is estimated by using the experimental snapshot shown in the left of figure 8.15, previous to the water impact with the deck and occurred 0.76 s before the first snapshot of figure 8.14. Blue and red curves superimposed to the picture represent the numerical free-surface configurations

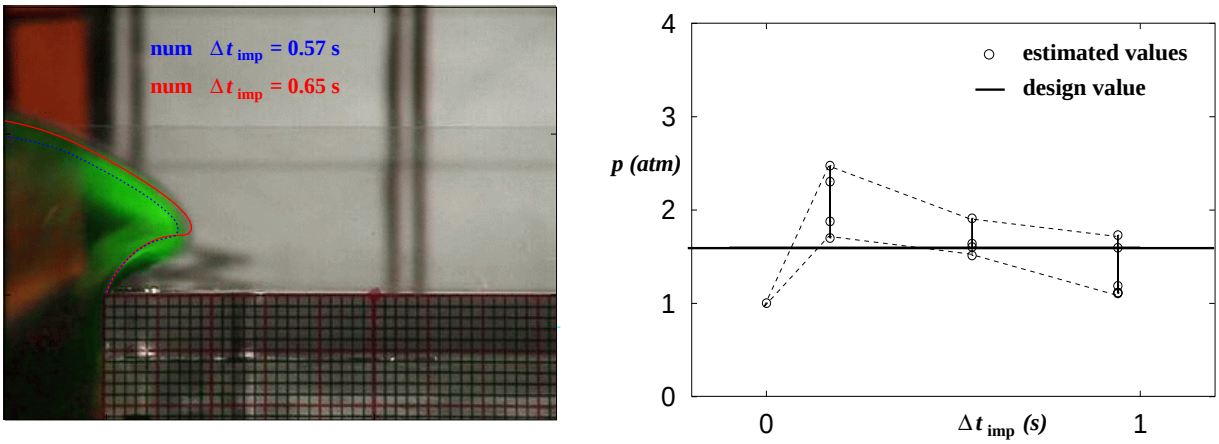

Figure 8.15 Left: estimate of the experimental time by comparing with numerical free-surface configurations at $\Delta t_{\rm imp} = 0.57$ (blue line) and 0.65 s (red line). $t_{\rm imp}$ is the numerical impact instant. Right: estimated pressure evolution by assuming valid equation (8.3). All the quantities are given in full scale ($D = 18$ m).

at, respectively, $\Delta t_{\rm wod} \simeq 0.57$ and 0.65 s from the freeboard exceedance. From this comparison, we can approximatively consider $\Delta t_{\rm wod} = 0.61$ s as the time for the experimental snapshot.

Eventually, the time instant of all the snapshots is evaluated and the pressure evolution can be computed by using relation (8.3). Results are given by the circles in the right of figure 8.15. As anticipated, different pressure values for the same instant of time refer to the different digitized cavity boundaries. The pressure bandwidth (dashed lines) gives an indication of the order of magnitude of the uncertainty involved in. In the plot, the horizontal solid line is the design pressure for the deck. It seems reasonable that this value is exceeded during the cavity evolution and likely this occurs for a time interval not small compared with, for instance, the first natural dry beam period $T_{\rm dry1}$. The cavity collapse represents thus a danger for the safety of the deck. From the tests, this phase lasts for $t_{\rm coll} - t_{\rm imp} \sim 2.57$ s - 1.2 s = 1.37 s. As all the quantities reported in the present section, also this time interval is given in full scale.

Summarizing, for the second beam (b_2), the water-impact evolution features three phases: (i) acoustic phase, (ii) blunt-impact phase, (iii) and wedge-impact phase. The beam closer to the bow (b_1) is instead subjected only to the air-compressibility phase before to be completely wetted.

During the impact, local damages of the deck as well as hydroelastic excitation can occur and need to be quantitatively investigated. We should note that equation (8.3) assumes no air leakage. This is likely to occur in a 3-D flow situation and it can be expected that pressures will be lower. The present numerical method is not able to describe the flow evolution after the impact. This could however be obtained by matching with a suitable high-speed local solution. With this procedure the impact phenomenon could be described until the cavity collapses.

8.3 Water Shipping: Later Stages

8.3.1 General Description

The sequence of pictures in figure 8.16 describes the late evolution of the flow field observed

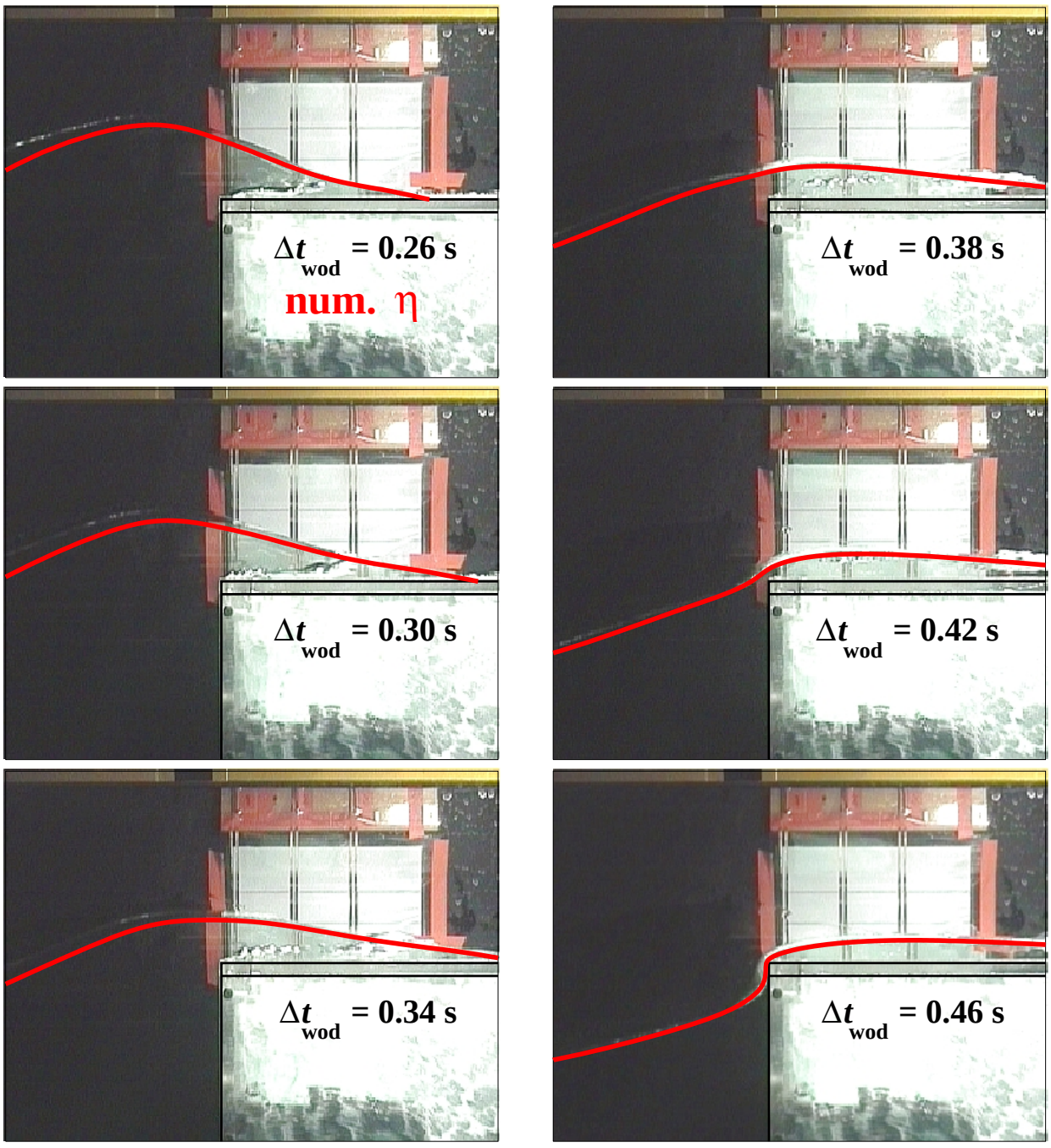

Figure 8.16 Late stages of water shipping on the basic model (case a of figure 7.2) without superstructure along the dec k. Numerical free surfaces (red lines) are superimposed to the experimental video images. Nominal incoming wav es: $\lambda = 2$ m, $H = 0.16$ m.

in the experiments in a case without superstructure on the deck. The time increases from top to bottom and from left to right, and the time interval between two consecutive snapshots is 0.04 s. The global phenomenon is a dam breaking-type water on deck. The cavity formed at the beginning of the water shipping is collapsed, and bubbles, identifiable as the white region close to the deck, are convected by the main flow propagating forwards. As the time increases, the role of the gravity becomes important causing the run-down in front of the bow. This finally leads to the end of the water shipping.

We have numerically modeled this stage of the phenomenon by neglecting the initial plunging phase, and by enforcing the initial Kutta-like condition at the edge of the deck. The obtained results are superimposed (red lines) to the experimental images in sequence 8.16. Apparently, though the details of the initial stages of water shipping are neglected, the numerical wave profiles agree well with the experimental ones, with the exception of the wavefront region where the numerical method predicts a higher propagation velocity. Therefore, the gross flow evolution is not significantly affected by the phenomena connected with the initial plunging. An ambiguity in the time correspondence between experiments and numerics has to be recalled, as already discussed in section 8.2.3.

8.3.2 Wave Parameter Analysis

Water level The water-level evolution at the bow is analyzed in figures 8.17–8.18 in terms of the nominal parameters of the incoming waves. Both first and second water-on-deck events are

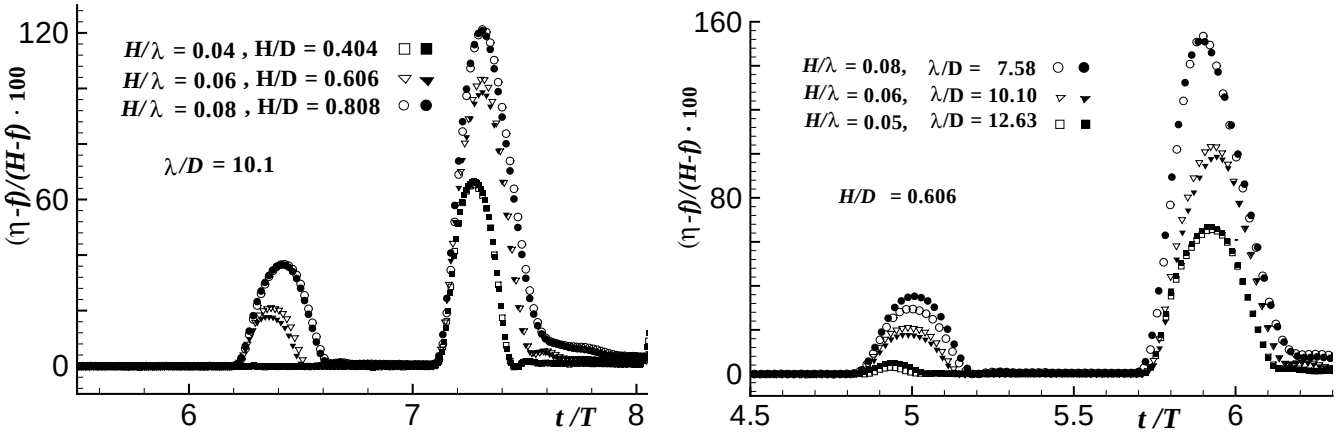

Figure 8.17 Water level at the bow. Influence of the incoming wave nonlinearities in terms of the wave height (left) and of the wavelength (right). Two test results (full and empty symbols) are given for each case.

considered for the ship model with vertical bow (case a in figure 7.2) and without superstructure along the deck. The time histories have been shifted to synchronize the first water on deck for all the cases. In the left plot of figure 8.17, the examined (nominal) wavelength is 2 m and three different wave heights (0.08, 0.12 and 0.16 m) are considered. Here, for the smallest wave height ($H/\lambda = 0.04$), only one water on deck has been observed and it has been shifted to coincide with the second shipping cycles of the other incident wave cases. In the right plot, the wave height

is constant, 0.12 m, and the wavelengthchanges assuming values of 1.5, 2 and 2.5 m. Therefore also in this case the steepness is not kept constant. For each of the considered conditions, two test results (full and empty symbols) are given showing a satisfactory repeatability of the experimental results. The water level is made non-dimensional with respect to the exceedance of the freeboard by the wave height $(H - f)$ while the time axis is made non-dimensional by the wave period T.

Both plots show an increase of the maximum relative water level at the bow with the steepness. The time interval between the first and the second water-on-deck even tsseems to scale with the wave period. In particular, it is close and smaller than T.

The left plot of figure 8.18 reports cases with constant steepness H/λ and varying the wavelength λ. The maximum relative water level during the first water on deck is almost the same,

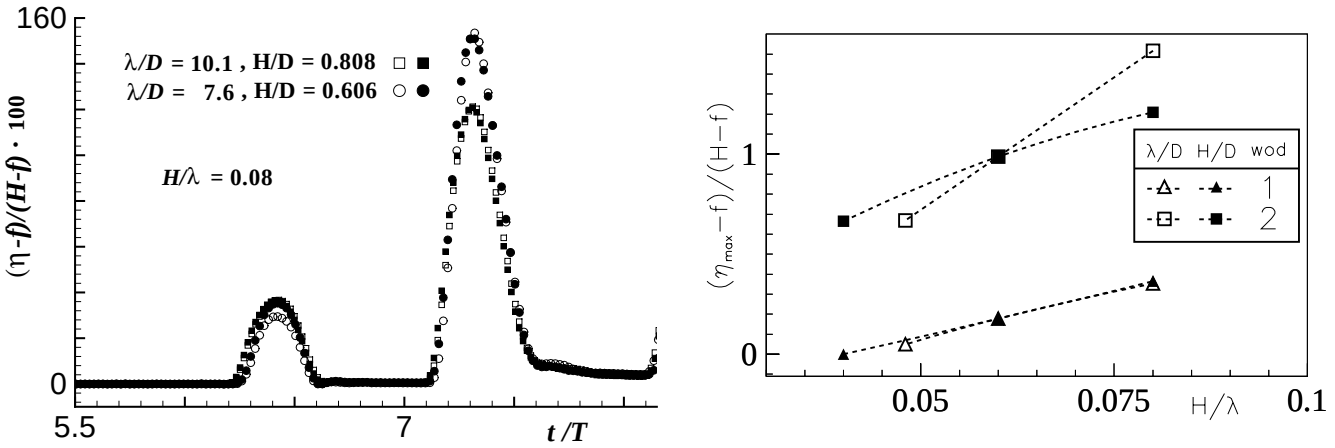

Figure 8.18 Left: water level at the bow for constant steepness. Two test results (full and empty symbols) are given for each case. Right: influence of the steepness on the maximum relative water level at the bow. Empty symbols correspond to fixed λ/D, full symbols correspond to fixed H/D. Only one test result is given for each case.

while a larger difference is observed for the second even t. However, the latter is associated with incoming waves steeper and even less related to the nominal conditions because of the strongest wave-body interaction. These results, together with those in figure 8.17, are presented in more compact way in the right plot of the same figure. Here, the non-dimensional maximum water level at the bow $(\eta_{\max} - f)/(H - f)$ is plotted *versus* the steepness H/λ. Only one test result is given for each case. During the first water on deck, $(\eta_{\max} - f)/(H - f)$ increases almost linearly with the steepness. For the second water on deck, the effect of changes in H/D and λ/D is different, and $(\eta_{\max} - f)/(H - f)$ can be different even when keeping fixed the steepness.

Water evolution along deck The influence of the nominal incoming wave parameters on the wave front propagation along the deck is considered in figure 8.19. This is made in terms of the wave height (left) and of the wavelength (right), by using the same cases considered in figure 8.17. As in that figure, the time is made non-dimensional by T and the instantaneous wetted length of the deck (Δx_{bow}, measured with sensor fd_1) is made non-dimensional by $(H - f)$. Two tests (full and empty symbols) are shown for each studied case, and the time histories are shifted

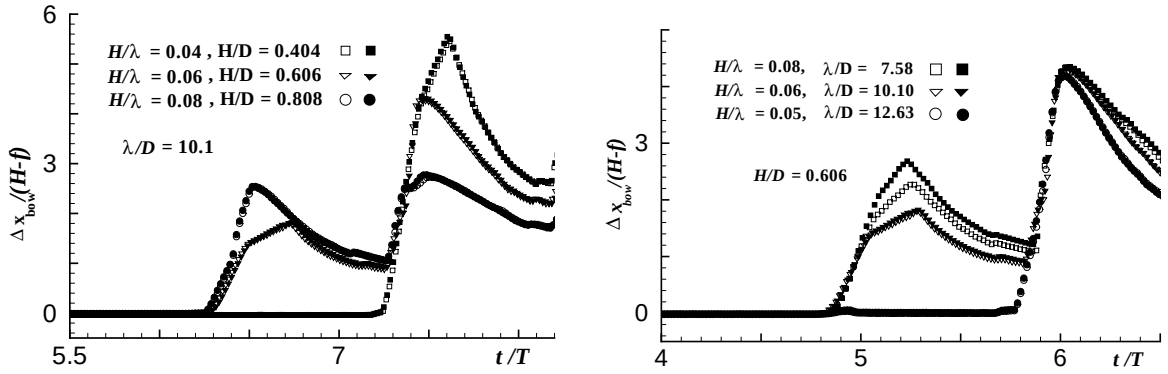

Figure 8.19 Wave front along the deck. Influence of the incoming wave nonlinearities in terms of the wave height (left) and of the wavelength (right). Two test results (full and empty symbols) are given for each case.

to have correspondence of the starting of the first water shipping. The body geometry is the basic one (case a of figure 7.2) without superstructure along the deck.

It is interesting to note that the evolution of the non-dimensional Δx_{bow} is quite similar for the different cases, both during the first and the second events. In the first water on deck, the curve for the case with steepness $H/\lambda = 0.06$ and wavelength-to-draft ratio $\lambda/D = 10.1$ (triangles) reaches a non-dimensional maximum value of ~ 1.5. This is not the real maximum distance covered by the water which is definitely larger, as observed from video recordings of the tests. The reason of the difference is explained in chapter 7 and is related to the fact that, at a certain instant during the water evolution, the flux of water invading the deck becomes zero together with the water level on the deck close to the bow. This experimental error may not be quantified *a priori* since it depends on the sensor sensitivity and on the extension of the deck region with almost-zero water level. The results suggest that the wavefront velocity along the deck behaves as $k\sqrt{g(H-f)^2/\lambda}$, k being a time dependent parameter weakly dependent on the incoming waves.

8.4 Influence of the Stem Angle

A positive stem angle should reduce the amount of shipped water by increasing the wave reflection from the ship. A negative inclination in the upper portion of the bow is however preferred in some designs. This should decrease the intensity of water bow impacts, giving more gentle water shipping, with possible lateral water deviations out of the deck. The latter aspect is intrinsically three-dimensional.

To investigate the influence of a bow stem angle, two additional bow configurations have been considered, indicated as cases b and c in figure 7.2. They have a stem angle of 45 and -45 degrees, respectively. The analysis here carried out is qualitative. This is due to the following reasons. First, in both these alternative cases the fore portion of the bow is closer to the wavemaker than when the basic model with vertical bow is used. Second, the on-model measurements during the experiments for case b are not quantitatively satisfactory because of additional relevant error

sources (*cf.* section 7.4). Despite this fact, the analysis can give useful information.

Sequences 8.20 and 8.21 show a water shipping caused by prescribed incoming waves 2 m long

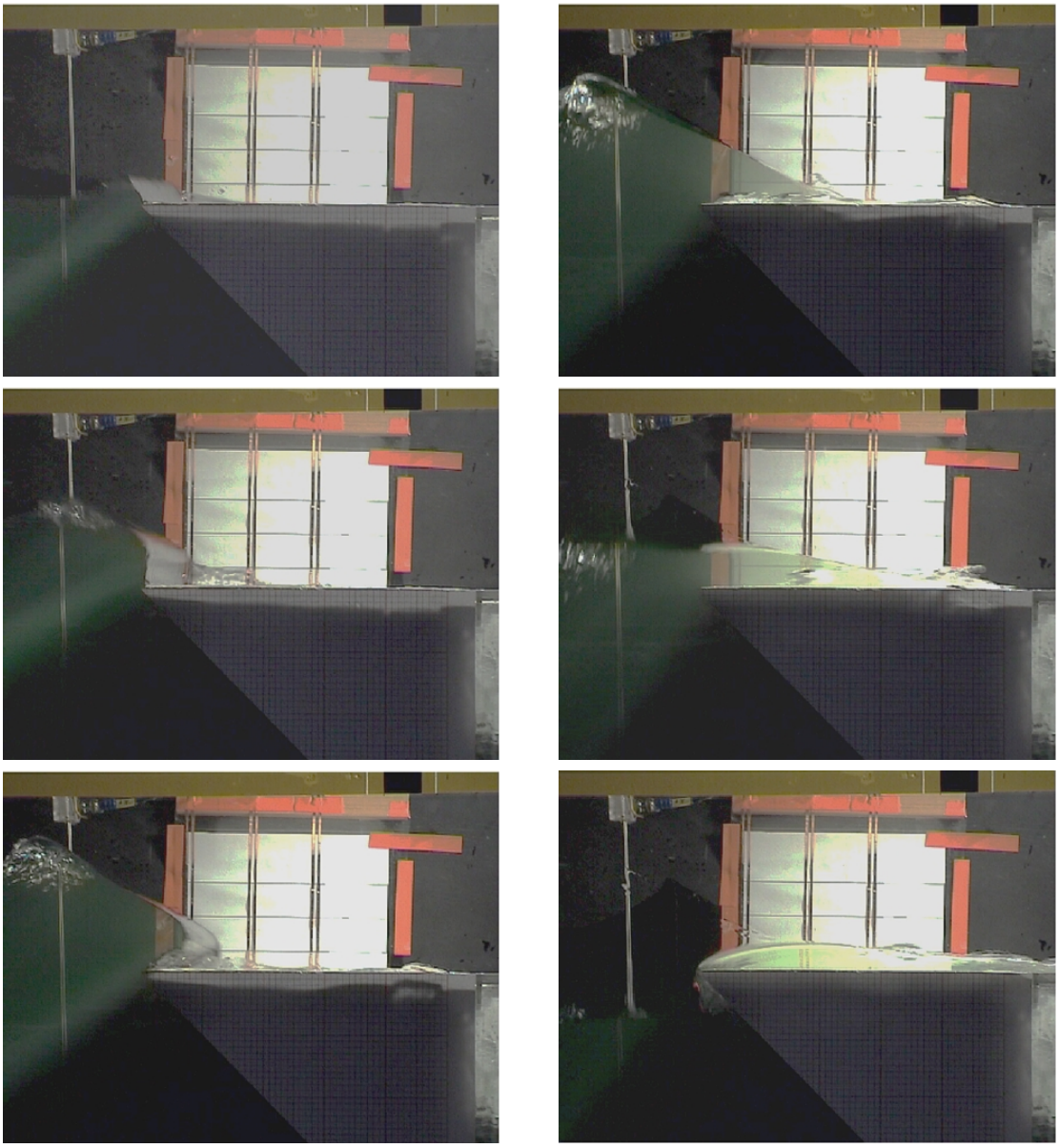

Figure 8.20 Geometry with 45° stem angle, case b in figure 7.2. Free surface evolution during the water shipping. The time increases from top to bottom and from left to right with constant time interval of 0.04 s.

and with a .16 m crest-to-trough height on the ship model with bows b and c, respectively. In both sequences the time increases from top to bottom and from left to right. The two water on deck phenomena occurred approximately after the same time interval from the beginning of the wavemaker motion in the related test. For the positive stem angle the event corresponds to the first shipping. The corresponding event in the case of ship model with vertical bow represents also the first water on deck and has been discussed in the previous sections. Differently, the

event related to the negative stem angle is the second ev en t.A previous even t occurred because

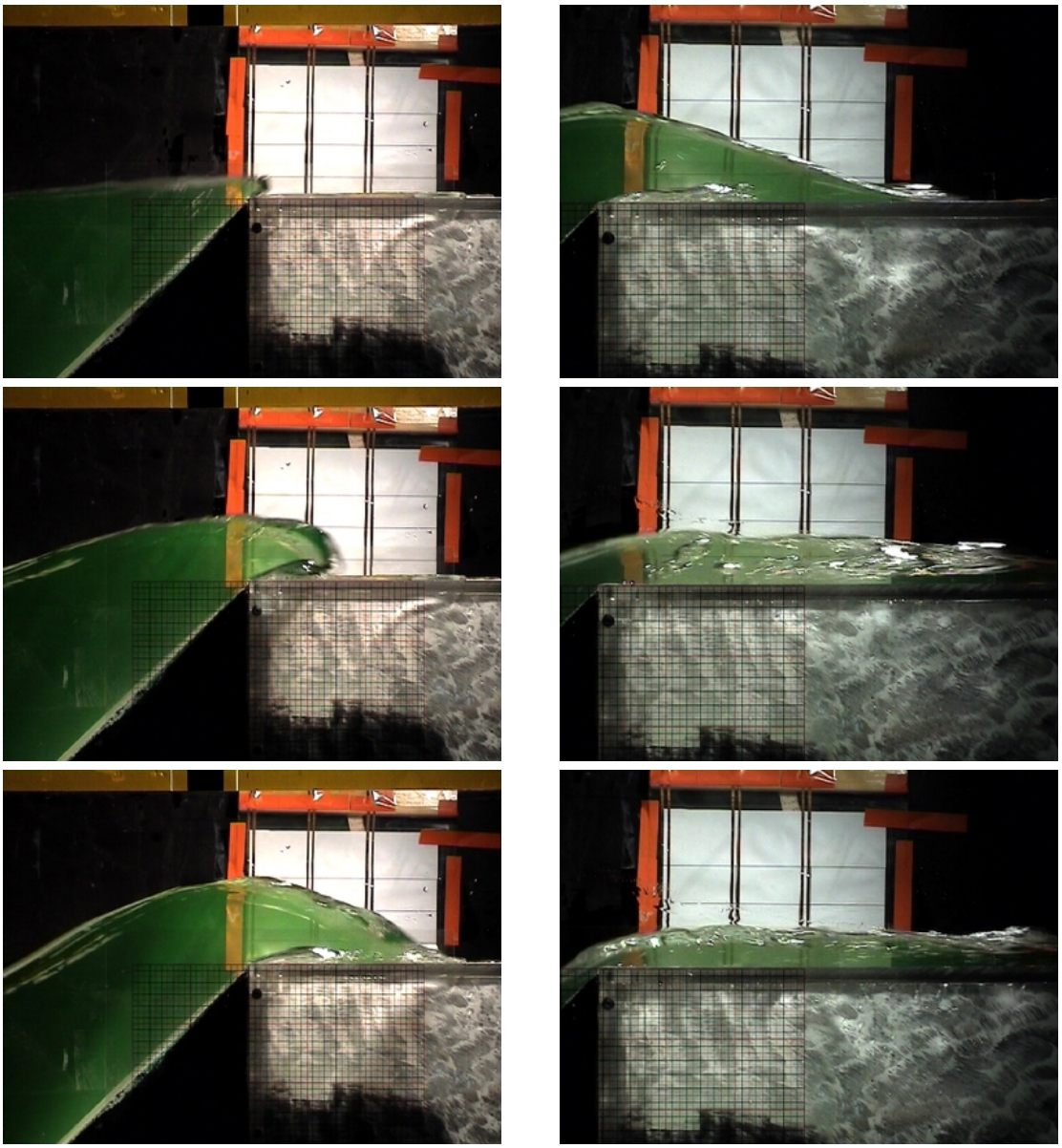

Figure 8.21 Geometry with $-45°$ stem angle, case c in figure 7.2. Free surface evolution during the w ater shipping.The time increases from top to bottom and from left to right with time interval of 0.04 s for the first three snapshots. Last three photos are related to a different test of the same case, with time intervals of 0.08 and 0.04 s, respectively.

of the reduced wa v ereflection from the bow. This was however characterized b y a quite small amount of shipped water.

Similarly to the v ertical bow also in cases b and c the water shipping starts in the form of a plunging wa v ehitting the deck. The positive stem angle causes clearly a larger w a v ereflection. Locally in front of the bow the wa v efield is more deformed and steeper than in the cases of 0 and -45 degrees stem angle. In this flow region a backward wa v eo v erturningoccurs (see third

and fourth snapshots of sequence 8.20), accompanied by spray formation. The water impact with the deck is blunter and less localized. This leads to higher pressures and greater danger of deck structural damages. The air entrapped in the cavity after the impact collapses very quickly causing bubbles. These form a thick white strip near the deck and are convected by the main flow. In case c the fore part of the bow is favorable to the wave propagation. The local crest is smaller and the water shipping starts with a larger front velocity but the resulting impact appears less severe. Summarizing. When the stem angle is reduced the water on deck starts with higher horizontal velocities but gives a less heavy impact with the deck. These two aspects are competitive in terms of the resulting wave front velocity after the impact. It is not obvious to identify the critical one in determining this quantity which represents an important parameter for the water impacts with superstructures along the deck.

The three bow geometries are compared in figure 8.22 in terms of the water front evolution

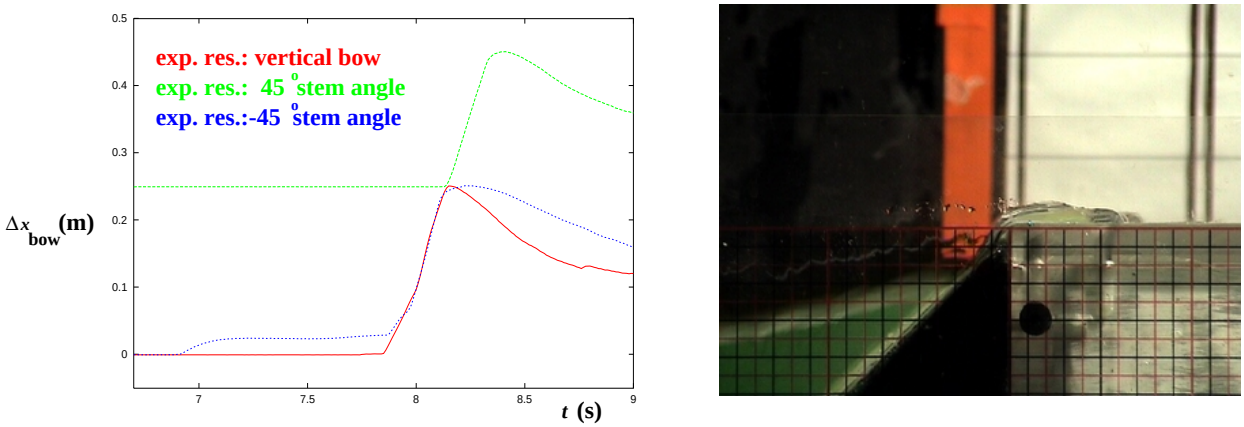

Figure 8.22 Left: wave front propagation along the deck. Geometry with vertical bow (red line, case a in figure 7.2), with 45° stem angle (green line, case b in figure 7.2) and with −45° stem angle (blue line, case c in figure 7.2). The wave sensor fd_1 starts almost at the bow for cases a and c, while starts at 0.25 m from the bow for case b. Right: geometry with −45° stem angle. Water shipped during the first water on deck. The smallest grid dimension is 5 mm.

during the water on deck. The time axis of the three curves was a little shifted to make easier the comparison of the results. In the case of positive stem angle the water sensor fd_1 gives a non-zero value after the water covered the distance of 0.25 m from the bow. For this reason, the relative measurement (green curve in the figure) has been vertically shifted to give 0.25 m as starting value of Δx_{bow}. Differently, curves for case a (red line) and case c (blue line) start from zero. Since for case "c" a previous water shipping occurred, the related curve becomes different than zero before the others. It reaches a maximum of about 0.025 m and then increases during the second water on deck. The maximum value measured during the first event is consistent with the maximum distance covered by the water at the end of the first water on deck (*cf.* right plot of figure 8.22). The water fronts for the cases a and c seem to develop with similar velocities. Further, after covered 0.25 m from the bow, their velocities seem to be of the same order of magnitude as the corresponding water front velocity for case b.

Figure 8.23 gives the free surface configurations when the water flux invading the deck is almost zero. The view is not exactly the same. However, qualitatively the amount of shipped water does not appear significantly different from case a to case c. In the case of negative

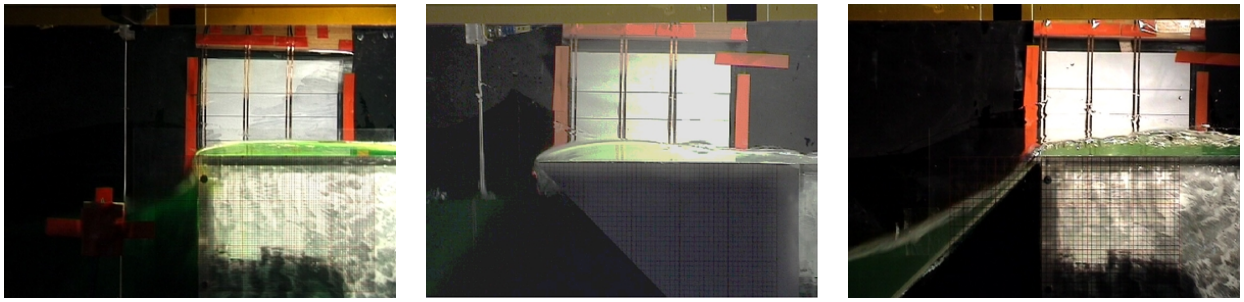

Figure 8.23 Free surface configuration when the water flux on the deck is almost zero. Cases a (left), b (center) and c (right).

stem angle, the free surface appears less smooth than in the other cases and bubbles are clearly observed, mixed with the water.

8.5 Impact with a Vertical Wall

8.5.1 Water Evolution

Figure 8.24 shows an enlarged view of the water impact occurring when a vertical wall is in-

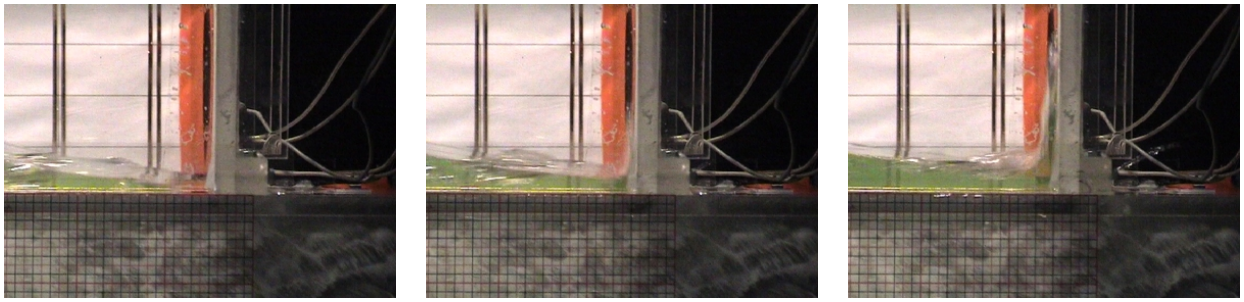

Figure 8.24 Water impact with a vertical wall at 0.2275 m from the bow. Jet evolution along the structure. Nominal incoming waves with $\lambda/D = 10.1$ and $H/D = 0.808$.

troduced along the deck, at 0.2275 m from the bow. Nominal incoming waves have $\lambda = 2$ m and $H = 0.16$ m. The flow field appears quite similar to the impact phenomenon discussed in section 5.1, where the water flow generated after the breaking of a dam hits a vertical wall. The water front approaching the structure resembles a thin half-wedge, and, at the beginning, only the small amount of the fluid sharply deviated upwards by the obstacle is affected by the phenomenon. A jet originates vertically, and some spray is formed.

Comparison with numerical results First stages of the free-surface evolution during the water impact with the vertical wall is reported in figure 8.25, where the time instant between two pictures is 0.04 s. The red lines are obtained from the numerical simulation, which includes

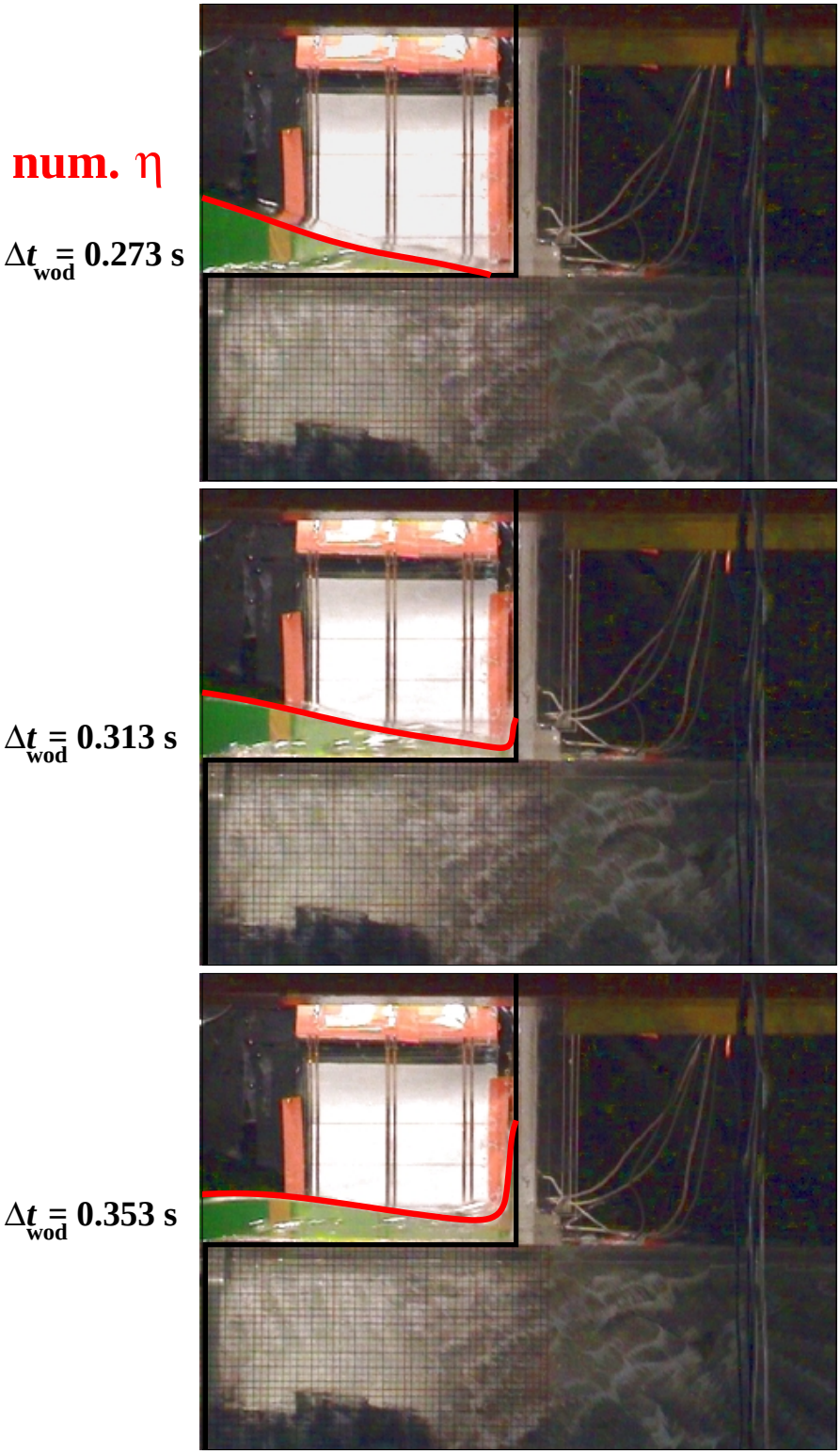

Figure 8.25 First stages of water impact with a vertical wall at 0.2275 m from the bow. Numerical free surfaces (red lines) are superimposed to the experimental video images. Time interval between two snapshots is 0.04 s. $\Delta t_{\mathrm{wod}} = t - t_{\mathrm{wod}}$. t_{wod} is the instant of water-on-deck starting in the numerical simulation.

the modeling of the water shipping at the bow. In this case, the initial Kutta-like condition at the edge of the deck has been adopted. The overall agreement between the experimental water profiles and the numerical results is rather good.

This is also confirmed by the comparison between numerical and experimental water run-up (Δz_{deck}) along the vertical wall. The latter is presented in figure 8.26 where two experimental tests (line with squares and line with circles) are compared with the numerical results (solid

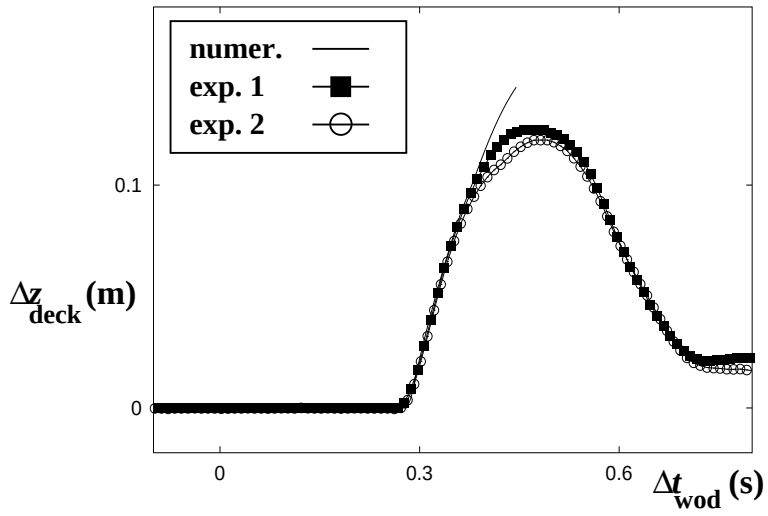

Figure 8.26 Water run-up along the vertical wall placed at 0.2275 m from the bow. Two experimental tests (line with squares and line with circles) are compared with numerical results (solid line). $\Delta t_{\mathrm{wod}} = t - t_{\mathrm{wod}}$. t_{wod} is the instant of water-on-deck starting in the numerical simulation.

line). The water run up is given as a function of $\Delta t_{\mathrm{wod}} = t - t_{\mathrm{wod}}$, t_{wod} being the instant of water-on-deck starting in the numerical simulation. During the first stages, the agreement is rather good. Later, when the experiments approach the maximum run-up along the wall, the numerical prediction overestimates the measured data. In this stage, also the two test results do not agree completely. This behavior is probably explained by three-dimensional flow instabilities following the spray formation during the rise of the water (*cf.* section 7.4.2).

Wave parameter analysis Experimental visualizations can be used to have a very rough estimate of the wave-front velocity just before the impact with the wall. The impact velocity is clearly an important parameter affecting the resulting water loading (*cf.* section 5.2.1). For instance, during the first water on deck, the impact velocity is ~ 0.67 m/s, for prescribed incoming waves with $H/D = 0.606$ and $\lambda/D = 7.58$, and ~ 1.13 m/s, for waves with $H/D = 0.808$ and $\lambda/D = 10.1$. In the latter case, the numerical solution predicts an impact velocity of 1.2 m/s. These two experimental conditions correspond to the same wave steepness $H/\lambda = 0.08$ and the non-dimensional impact velocity $V/\sqrt{g\,(H-f)^2/\lambda}$ is about 4 and 5, respectively.

The water run-up along the vertical wall is presented in figure 8.27. In the plots, the non-dimensional vertical distance from the deck wetted by the water, $\Delta z_{\mathrm{deck}}/(H-f)$, is given as a function of the non-dimensional time t/T. The wave-height influence is examined in the left plot, while three different values of the wavelength are considered in the right plot, for a fixed

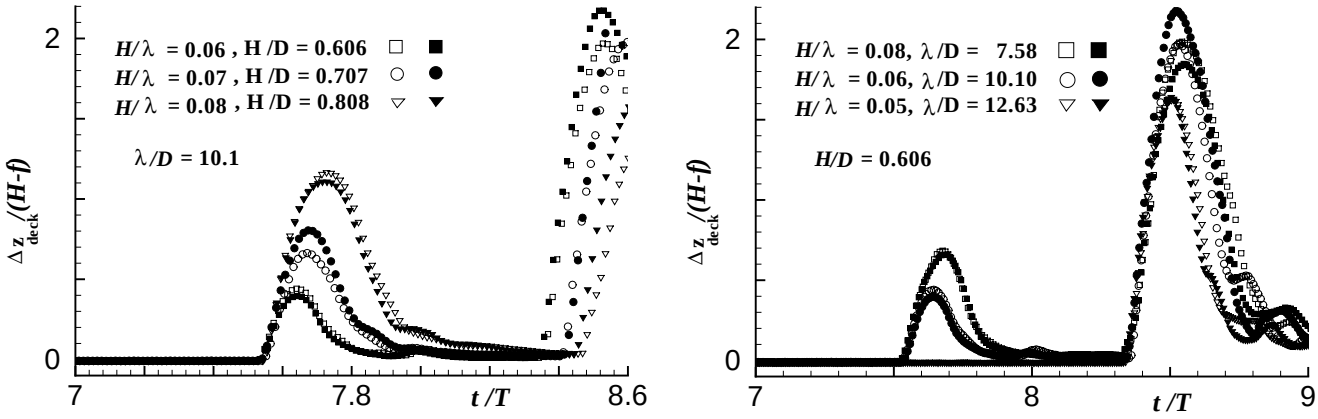

Figure 8.27 Water rise-up along the vertical wall. Influence of the incoming wave nonlinearities in terms of the wave height (left) and of the wave length (right).

wave height. As we can observe, the measurements of water run-up for the case with $H/\lambda = 0.06$ and $\lambda/D = 10.1$ do not agree with the corresponding measurements of water flow along the deck (*cf.* left plot of figure 8.19). According to sensor fd_1, during the first water on deck the shipped water should not reach the wall (the measured distance covered by the water is smaller than the wall-bow distance), conversely sensor fw records a water run-up along the wall even during the first water on deck. The disagreement is due to errors in the fd_1 measurements, as discussed in chapter 7 and recalled in section 8.3.2.

The relative wave rise-up along the wall remains qualitatively similar for all the considered cases. This suggests that the vertical water-front velocity along the superstructure behaves similarly to the horizontal water-front velocity along the deck.

8.5.2 Pressure along the Vertical Wall

Comparison with numerical results The pressure evolution on the wall, measured at 0.012 m and at 0.032 m above the deck, are reported in the left and right plots of figure 8.28, respectively. Along the horizontal axis $t = 0$ s corresponds to the time instant when the numerical pressure (thick line in each plot) at the lowest location attains a non-zero value. Two test results are shown for each pressure gauge (full and empty symbols).

Qualitatively the agreement is satisfactory, but the experimental results are not perfectly repeatable. At the lower location, the value of the first peak for two test results is roughly the same as the numerical one, while is larger for the two others. Later on, the repeatability is not exactly ensured. All the test results show two peaks of the same order at the lower location. The first one is almost disappeared at the upper location. This occurs at the beginning of the water run-up and is related to the initial water impact with the superstructure. The second one occurs in the later stages, when the gravity started to matter and is related to the occurrence of a backward water overturning and breaking. The latter phenomena are shown in the sequence 8.29 and are therefore important for green-water loading on the superstructure.

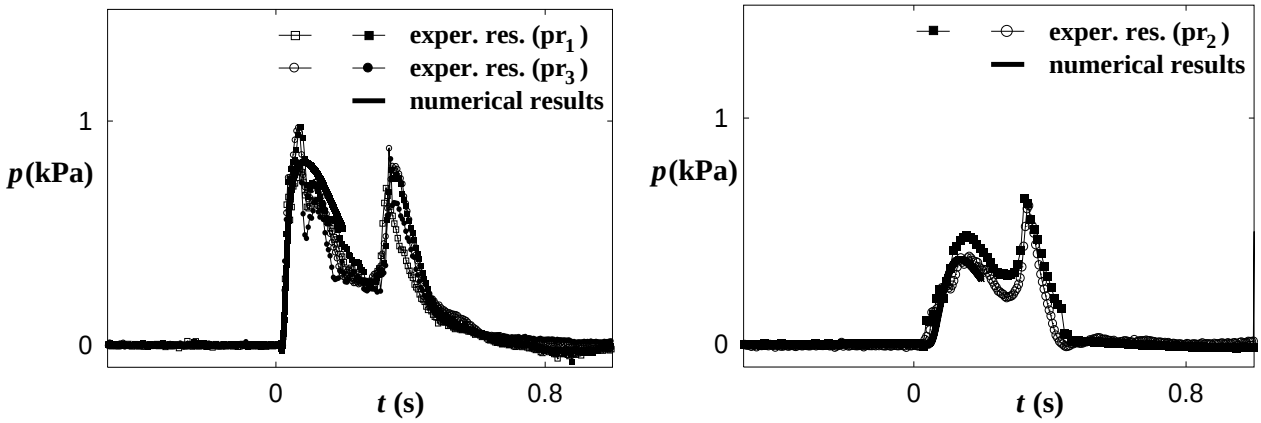

Figure 8.28 Pressure evolution on the vertical wall. Experimental and numerical data. Left: pressure measured at 0.012 m above the deck. Right: pressure measured at 0.032 m above the deck.

Figure 8.29 Water overturning and breaking after the impact. Nominal incoming waves with $\lambda/D = 10.1$ and $H/D = 0.808$.

Wave parameter analysis Time histories of the pressure on the vertical wall at locations 0.012 m ($\Delta z_{\text{bow}}/D = 0.06$) and 0.032 m ($\Delta z_{\text{bow}}/D = 0.16$) from the deck are given in figures 8.30

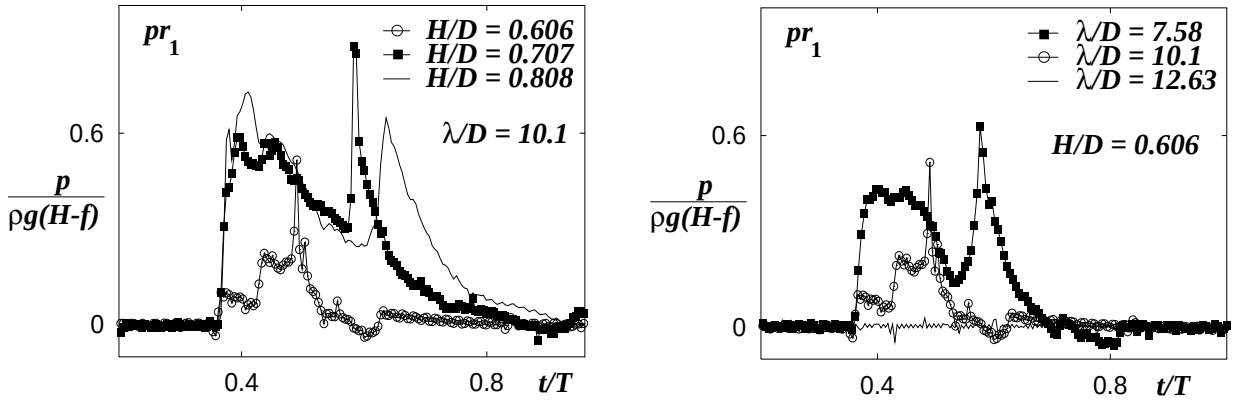

Figure 8.30 Pressure evolution at 0.012 m from the deck. Influence of the incoming wave nonlinearities in terms of the wave height (left) and of the wavelength (right).

and 8.31, respectively. For simplicity of graphical representation, only one test result is shown for each considered case, though we recall the repeatability issue, discussed in section 7.3. The

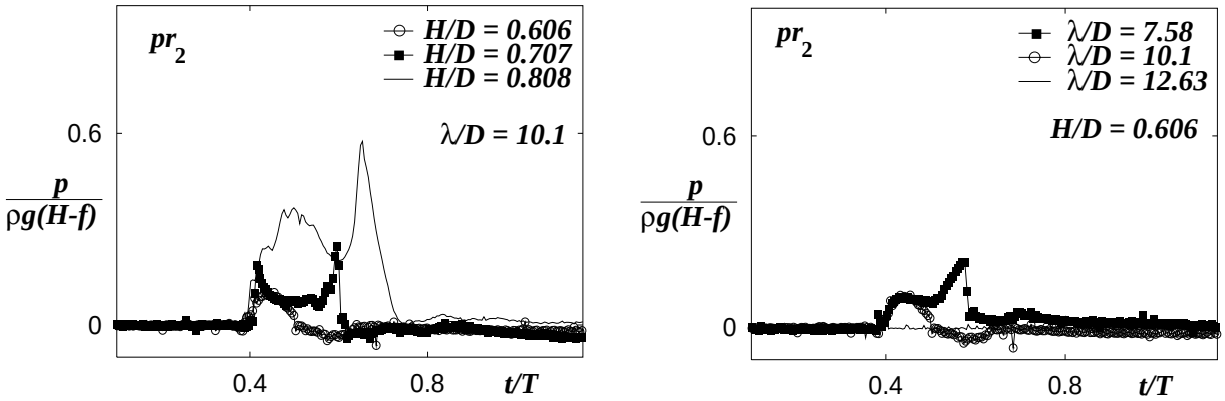

Figure 8.31 Pressure evolution at 0.032 m from the deck. Influence of the incoming wave nonlinearities in terms of the wave height (left) and of the wavelength (right).

time is made non-dimensional by the wave period, and the pressure is referred to the hydrostatic term $\rho g (H - f)$, the atmospheric pressure being set zero. Since nominal incoming waves with $\lambda/D = 12.63$ and $H/D = 0.606$ do not cause an impact with the superstructure during the first weak event (*cf.* right plot of figure 8.19), the measured pressure at both locations (pr_1 and pr_2) remains atmospheric in the examined time interval.

The non-dimensional pressure seems to be nonlinearly related to the wave steepness. Also, the second pressure peak is dominated by the local conditions at the impact, and by the subsequent occurrence of a breaking wave. This can partially explain why the maximum non-dimensional pressure associated with less steep waves can be larger than the value caused by steeper incident waves. Clearly this represents only a possible reason. Three-dimensional effects are definitely important at this stage and, close to the wall, bubbles are mixed with water. All these factors affect the pressure and make more difficult the interpretation of the experimental results.

Chapter 9

Summary and Future Perspectives

The bow deck wetness phenomenon for a moored ship, with blunt bow, in regular head waves, has been idealized and reduced to a simple two-dimensional wave-body interaction problem.

In this framework, the problem has been analyzed both by numerical simulations and by a dedicated experimental activity. On the numerical side, viscous- and surface-tension effects have been neglected, and the resulting unsteady fully-nonlinear free-surface flow has been solved by a boundary-integral equation method. Numerical results have been compared with published experimental and analytical solutions for prototype problems connected to the phenomenon of interest. Reasonable good agreement with reference results enabled us to use this model to gain fundamental insight into water-on-deck occurrence, flow field over the deck, and impact with superstructures.

The performed experiments complemented the numerical analysis, giving a closer view on several aspects, some of them unexpected.

Water on deck occurrence The first crucial aspect of the water-on-deck problem is the prediction of the shipping occurrence. This issue has been addressed numerically. The role of several wave and geometric parameter have been discussed.

Two approaches have been applied, both of them are based on the application of a Kutta-like condition at the bow edge. In the first case, the flow is enforced to leave tangentially the bow once the freeboard is reached. Then, the fluid velocity relative to the the ship determines whether the deck will be wetted or the water will be diverted in the opposite direction. In the second one, the Kutta condition is continuously imposed from that moment on.

Initial stages of the water shipping Two-dimensional water on deck model tests have revealed details of the flow when the water is initially shipped onto the deck. Within a rather small time scale, the shipping of water starts in the form of a plunging breaker, hitting the deck close to the bow. The impact causes locally high pressures and results in the formation of a cavity near the bow. The very high pressures last too short in time and are too concentrated in

space for causing important stresses in the deck. However the pressure rise due to the collapse of the cavity is significant from a structural point of view.

The experiments showed that later on there is no significant cross-flow, preventing any vortex shedding at the bow.

From these observations, the continuous Kutta-like condition represents the most appropriate condition between the two proposed and implemented. In this way, the numerical method is able to predict free-surface evolutions in reasonable agreement with that observed during the model tests. Therefore, the numerics was used to evaluate the flow conditions at the moment of the impact with the deck. The resulting impact loading has been discussed.

Later stages of the water shipping The observed initial plunging wave hitting the deck is a quite localized phenomenon. After this rapid phase, the observed water shipping develops in the form of a dam breaking-type water on deck. This behavior is also observable in our numerical simulations by enforcing the initial Kutta-like condition.

The agreement between numerics and experimental data was satisfactory in terms both of the free-surface evolution, and of the pressure evaluated on a superstructure along the deck. Therefore, the numerical method with the initial Kutta-like condition has been applied extensively to analyze: type of water shipping, amount of shipped water, and water impact with the deck house.

Global plunging-type water on deck The occurrence of the less common "plunging wave water on deck" has been detected during three-dimensional experiments (see figure 1.4), and features a non-local plunging phenomenon characterizing the whole water shipping. This possibility has been numerically investigated.

From the numerical analysis, the occurrence of this extreme and dangerous event seems to be related to the interaction with a steep wave already prone to break, more than to the wave-body interaction by itself. However, the influence of ship motion to enhance or reduce its severity can not be excluded.

Deck-wetness analysis An analysis concerning the parameters dependence of deck wetness has been carried out, showing that

- For long wavelengths λ relative to the draft D, the wave steepness H/λ mainly determines water-on-deck occurrence and severity. The relative amount of shipped water depends nonlinearly on H/λ.

- For small λ/L, where L is ship length, the bow-wave reflection reduces or prevents the shipping of water, even for large wave steepnesses.

- The stem overhang reduces the relative amount of shipped water, but its positive effect is less pronounced with respect to that of the freeboard.

- A trim angle (a quasi-steady pitch angle) has a small effect on the amount of shipped water.

Impact with the deck house The impact of shipped water against a deck house has been analyzed, showing that

- In the first stages of the impact gravity does not matter.
- For dam breaking-type water on deck, the water-front velocity (V) and the angle (β) between the free surface and the deck at the impact are the relevant parameters.
- The impact flow can be approximated by a zero-gravity similarity solution in the initial stages of the impact. In this case a fluid wedge hitting a straight wall at 90 degrees is studied with V and β as input.
- The similarity solution showed that $d[P_{\max}/\rho V^2)]/d\beta$ is large only for $\beta >\sim 60^\circ$ and is small for $\beta <\sim 40^\circ$. In the last case V represents the most important factor influencing the maximum pressure as a squared power. Here $P_{\max}$ is the maximum pressure.
- In the later stages, when gravity matters, a similarity solution overpredicts the pressure along the wall.
- In addition to the pressure peak caused by the initial water impact with the superstructure, the experiments showed a second peak of the same order of magnitude in the evolution of the pressure along the wall. This one occurs in the later stages and is related to the occurrence of a backward overturning of water, plunging on the wetted deck. Therefore, also these late events are important for green-water loading on the superstructure. Since the present numerical method does not handle free-surface fragmentation phenomena, it is not possible to predict the second pressure peak.
- The stem overhang reduces the water level along the deck but increases the involved flow velocities. Due to this, it is difficult to find a conclusive statement about its positive or negative effects on water impacts with a superstructure.
- A trim angle (a quasi-steady pitch angle) has a small effect on the water level and the velocity of the water flow propagating along the deck, and therefore on the water impact loading on a deck house.
- Reducing the inclination of the wall reduces the water loading during the run-up. When an angle $\alpha = 40^\circ$ (relative to the vertical direction) is considered, the maximum normal force becomes $\sim 50\%$ of the maximum normal force in the case of vertical wall. In the considered range of angles, the force reduction seems to be almost linear with α.
- The effect of hydroelasticity during the impact on a deck house may in general be neglected.

Simplified methods The use of dam-breaking models and shallow-water approximations of the flow on the deck has been investigated. Since a theoretical dam-breaking model does not account for the horizontal fluid motion caused by the flow external to the ship, it can only qualitatively describe the flow on the deck.

Shallow-water approximations can in principle be used in certain domains along the deck. However, they require initial and boundary conditions that are dependent on the external flow, which are not available without solving the complete ship-wave interaction problem.

9.1 Future Perspectives

The table 9.1 summarizes the parameters influencing green-water loading in the bow area of a FPSO, and their role as determined by the present study is qualitatively shown.

RELATIVE IMPORTANCE

parameter	small — large
Freeboard	
Stem Angle	
Local Flow at the Bow	
Relative Vertical Motion	
Trim Angle	
Coupled Flow Between Deck and Outside	
Local Design of Deck House	
Hydroelasticity during Impact	
Wave Steepness	
3-D Effects	

Table 9.1 Qualitative evaluation of factors influencing green-water loading, based on 2-D studies.

Several aspects of the phenomenon need to be further investigated to achieve a complete quantitative understanding. They require more general models relative to the one used in present work. In the following, relevant studies to develop are indicated and, for some of them, possible methods to attack the problem are suggested.

a) External flow. At present, the actual ship motions, resulting from the interaction with the incoming waves, is not modeled. Clearly, these and the dynamic rise of the water in the bow region have profound effects in determining wet-deck occurrence. While ship motion can be probably accurately predicted by simplified models, finer details of the flow in the bow region will require a three-dimensional nonlinear analysis.

   On this ground, a domain-decomposition method can represent the proper approach, balancing accuracy requirements, assumptions on the problem of interest, and computational costs. Within this philosophy, the physical domain can be divided in a suitable number of subdomains. Where appropriate, some of the assumptions can be relaxed and the problem can be simplified applying in each subdomain the proper numerical model.

   Since the problem of interest is time dependent, and the instantaneous solution of each region depends on the solution in the others, time-by-time a "patching" procedure has to be carried out. This represents the main challenging factor. In the case of a FPSO unit, for instance, a possible decomposition could be the one shown in figure 9.1. When the

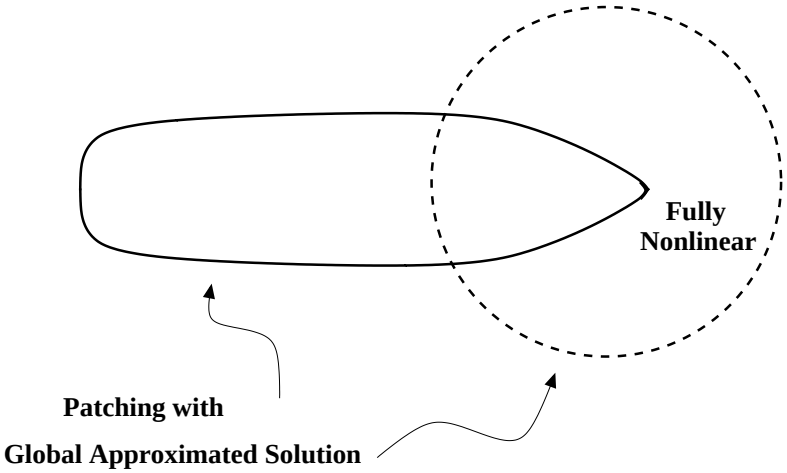

Figure 9.1 Sketch of a possible patching in the case of a FPSO unit. Top view.

nonlinearities associated with incoming waves are not extreme, ship-wave interactions can be described by a second-order method with the exception of a near-bow domain where the fully-nonlinear problem has to be solved to describe the run-up and to predict the water shipping. In this discussion, it is implicitly assumed that the wave-induced body motions are properly described by this simplified model.

b) On-deck hydrodynamics. For dam breaking-type flow, a three-dimensional shallow-water analysis could represent a reasonable compromise between efficiency and accuracy. This simplified description should be used to solve the problem in the deck-subdomain, within the domain-decomposition approach. In this case, the structural response under the action of impacting masses of water should be taken into account, may be through local analysis.

   Another possibility, more computationally demanding, is represented by a suitable field method for studying wave splashing. In this case, local wave breaking, cavity formations, and other phenomena can be treated. Limits are related both to the computational costs and to the accuracy, which still have to be assessed for large-scale problems where impact loads and multi-phase flows are expected.

c) Deck wetness for advancing ships. Forward speed affects occurrence and severity of water-on-deck phenomena. Depending on the ship-loading conditions, this can have either positive or negative effects. Related analyses have to account for interactions between steady and unsteady flows which are expected to be relevant near the ship.

d) Ship dynamics with green water on deck. The behavior of the whole vessel can be seriously modified by the motion of the shipped water, leading to reduced stability, capsize and sinking. This is relevant for smaller vessels. For larger ships it is important to investigate the effect on global hull-girder loads, like midship bending moment. A "direct simulation" of such complex behavior would be valuable to provide a global understanding and to give a better basis for ship design and development of classification rules.

e) Water shipping on damaged ships. When the ship hull is damaged water shipping phenomena can more easily occur. Related characteristics and possible damages for the vessel

can be quite different relative to the case of water on deck on undamaged ships and require dedicated studies (*cf.* Dodworth 2000). Main features of the problem can be investigated by using the numerical method developed in this work.

References

Belytschko, T., Y. Krongauz, D. Organ, M. Fleming, and P. Krysl (1996). Meshless methods: an overview and recent developments. *Comp. Meth. Appl. Mech. Engng. 139*, 3–47.

Benjamin, T. B. (1967). Instability of periodic wavetrainsin nonlinear dispersive systems. In *Proc. of Royal Society Serie A*, Volume 299, pp. 59–75.

Benjamin, T. B. and E. Feir (1967). The disintegration of wavetrain in deep water. *J. Fluid Mech. 27*, 417–430.

Bryant, P. J. (1983). Wavesand wavegroups in deep water. In L. Debnath (Ed.), *Nonline arwaves*. Cambridge University Press.

Buchner, B. (1995). On the impact of green water loading on ship and offshore unit design. In *Proc. Int. Symp. Practical Design of Ships and Mobile Units, PRADS'95*, Seoul, pp. 430–443. The Society of Naval Architects of Korea.

Buchner, B. and J. L. Cozijn (1997). An investigation in to the numerical simulation of green water. In *Proc. Int. Conf. on the Behaviour of Offshore Structures, BOSS'97*, Volume 2, Delft, pp. 113–125. Elsevier Science.

Byatt-Smith, J. G. B. (1971). An integral equation for unsteady surface waves and a comment on the Boussinesq equation. *J. Fluid Mech. 49*, 625–633.

Camfield, F. E. and R. L. Street (1967). An investigation of the deformation and breaking of solitary waves.Technical Report 81, Stanford Univ.

Campbell, I. M. C. and P. A. Weynberg (1980). Measurement of parameters affecting slamming. Final report. Technical Report 440, Technology Reports Centre No. OT-R-8042, Southampton University: Wolfson unit for marine technology.

Cao, Y., R. F. Beck, and W. Schultz (1993). An absorbing beach for numerical simulations of nonlinear wavesin a wavetank. In *Proc. 8th Int. Workshop on Water Waves and Floating Bodies*.

Chaplin, J. R., R. C. T. Rainey, and R. W. Yemm (1997). Ringing of a vertical Cylinder in Waves.*J. Fluid Mech. 350*, 119–147.

Clément, A. (1996). Coupling of two absorbing boundary conditions for 2d time-domain simulations of free surface gravity waves.*Journal of Computational Physics 126*, 139–151.

Cointe, R. (1989a). Nonlinear simulation of transient free surface flows. In *Proc. of 5th Symp. on Numerical Ship Hydrodynamics*, pp. 239–250.

Cointe, R. (1989b). *Quelques aspects de la simulation numerique d'un canal à houle*. Ph. D. thesis, Ecole nationale des ponts et chaussées, France.

Cozijn, J. L. (1995). Development of a calculation tool for green water simulation. Technical report, MARIN Wageningen / Delft Univ. of Technology, Delft, the Netherlands.

Dillingham, J. (1981, Jan.). Motion studies of a vessel with water on deck. *Marine Technology 18*(1).

Dillingham, J. T. and J. M. Falzarano (1988). A numerical method for simulating three-dimensional sloshing. In *The Society of Naval Architects and Marine Engineers*.

Dodworth, K. (2000). *The application of potential flow theory to damaged hull dynamics*. Ph. D. thesis, University of Strathclide, England.

Dommermuth, D. G. and D. K. P. Yue (1987). Numerical simulations of nonlinear axisymmetric flows with a free surface. *J. Fluid Mech. 178*, 195–219.

Dressler, R. F. (1954). Comparison of theories and experiments for the hydraulic dam-break wave. In *Assemblee Generale de Rome*. Tome III.

Dussan, E. B. V. (1979). On the spreading of liquids on solid surfaces: static and dynamic contact lines. In J. L. Lumley, M. V. Dyke, and H. L. Reed (Eds.), *Ann. Rev. Fluid Mech. 11*, pp. 371–400.

Ersdal, G. and A. Kvitrud (2000). Green water on Norwegian production ships. In *Proc. 10th Int. Conf. Offshore and Polar Engg, ISOPE'2000*, Seattle.

Faltinsen, O. M. (1977). Numerical solutions of transient nonlinear free–surface motion outside or inside moving bodies. In *Proc. of 2nd Int. Conf. Num. Ship Hydr.*

Faltinsen, O. M. (1990). *Sea loads on ships and offshore structures*. Cambridge, England: Cambridge University Press.

Faltinsen, O. M. (2001). Hydroelastic slamming. *J. Marine Science and Technology 5*(2).

Fekken, G., A. E. P. Veldman, and B. Buchner (1999). Simulation of green water loading using the Navier-Stokes equations. In Piquet (Ed.), *Proc. 7th Int. Conf. Num. Ship Hydrod.*, Nantes, France, pp. 6.3–1, 9.

Fenton, J. D. (1988). The numerical solution of steady water wave problems. *Comput. Geosci. 14*, 357–368.

Glimm, J. (1965). Solutions in the large for nonlinear hyperbolic systems of equations. *Communications on Pure and Applied Mathematics 18*.

Greco, M. (1997). Forze idrodinamiche e formazione ondosa nel moto di veicoli marini. Master's thesis, University La Sapienza, Rome, Italy.

Grochowalski, S. (1989). Investigation into the physics of the ship capsizing by combined captive and free running model tests. *Trans. SNAME 97*.

Hall, J. V. and G. M. Watts (1953). Laboratory investigation of the vertical rise of solitary waves on impermeable slopes. Technical Report 33, U. S. Army Corps of Engineers Beach Erosion Board.

Huang, Z. and C. C. Hsiung (1996, Dec.). Nonlinear shallow water on deck. *J. of Ship Research 40*(4).

Israeli, M. and S. Orszag (1989). Approximation of radiation boundary conditions. *J. of Computational Physics*, 41:115–135.

Korobkin, A. (1995). Acoustic effects on water impact. In 10^{th} *Int. Workshop of Water Waves and Floating Bodies*, Oxford, England.

Kothe, D. B. (1998). Perspective on Eulerian finite volume methods for incompressible interfacial flows. In H. C. KUHLMANN and H. J. RATH (Eds.), *Free surface flows, CISM Courses and Lectures*, Volume 391. Springer Verlag.

Landrini, M., G. Grytøyr, and O. M. Faltinsen (1999). A B-Spline based BEM for unsteady free surface flows. *J. of Ship Research 43*(1), 1–12.

Lloyd, A. R. J. M., J. Salsich, and J. Zseleczky (1985). The effect of bow shape on deck wetness in head seas. *Trans. RINA*, 9–25.

Longuett-Higgins, M. S. (1953). Can sea waves cause microseisms? In *Proc. Symp. on Microseisms*, Number 306, pp. 74–93.

Longuett-Higgins, M. S. and E. D. Cokelet (1976). The deformation of steep surface waves on water. I A numerical method of computation. In *Proc. R. Soc. London A*, Volume 350, pp. 1–26.

MARINTEK (2000). Review No. 1 April.

Maruo, H. and W. Song (1994). Nonlinear analysis of bow wave breaking and deck wetness of a high speed ship by the parabolic approximation. In *Proc. 20^{th} Symp. on Naval Hydrod.* National Academy Press.

McLean, J. W., Y. C. Ma, D. U. Martin, P. Saffman, and H. Yuen (1981). A new type of three-dimensional instability of finite amplitude gravity waves. *Phys. Rev. Lett. 46*, 817–820.

Mei, C. C. (1983). *The applied dynamics of ocean surface waves*. Singapore: World Scientific.

Milne-Thomson, M. N. (1967). *Theoretical hydrodynamics*. MacMillan.

Mizogushi, S. (1989). Design of freeboard height with the numerical simulation on the shipping water. In *Proc. Int. Symp. on Practical Design of Ships and Mobile Units PRADS'89*, Varna, pp. 103–1,8. Bulgarian Ship Hydrodynamics Centre.

Newman, J. N. (1977). *Marine hydrodynamics*. Cambridge, Massachusetts: MIT Press.

Newton, R. N. (1960). Wetness related to freeboard and flare. *Trans. RINA 102*, 40–81.

Ochi, M. K. (1964). Extreme behavior of a ship in rough Seas - Slamming and shipping of green water. In *SNAME*, New York, pp. 143–202. Annual Meeting of the Society of Naval Architects and Marine Engineerings.

O'Dea, J. F. and D. A. Walden (1984). The effect of bow shape and nonlinearities on the prediction of large amplitude motions and deck wetness. In *Proc. 15th Symp. on Naval Hydrod.*, pp. 163–176. National Academy Press.

Ogilvie, T. F. (1967). Nonlinear high-Froude-number free surface problems. *J. of Engineering Mathematics 1*(3), 215–235.

Ohkusu, M. (1996). Hydrodynamics in ships waves. In M. Ohkusu (Ed.), *Advances in marine hydrodynamics*.

Pantazopoulos, M. S. (1987). *Numerical solution of the general shallow water sloshing problem* Ph. D. thesis, University of Washington, Seattle, USA.

Penney, W. G. and C. K. Thornhill (1952). Part III: the dispertion under gravity, of a column of fluid supported on a rigid horizontal plane. *Phil. Trans. Royal Society Serie A 244*, 285–311.

Pohle, F. V. (1950). *The Lagrangian equations of hydrodynamics: solutions which are analytic functions of the time*. Ph. D. thesis, Graduate School of Arts and Science of New York University, New York, USA.

Rienecker, M. M. and J. D. Fenton (1981). A Fourier approximation method for steady water waves. *J. Fluid Mech.* (104), 119–137.

Ritter, A. (1892). *Die fortpflanzung der wasserwellen*, Volume 36. Z. Ver. deut. Ing.

Salvesen, N., E. O. Tuck, and O. M. Faltinsen (1970). Ship motions and sea loads. *Trans.SNAME 78*, 250–287.

Schwartz, L. W. (1974). Computer extension and analytic continuation of Stokes' expansion for gravity waves. *J. Fluid Mech. 62*.

Skomedal, N.G. (1985). Application of a vortex tracking method to three-dimensional flow past lifting surfaces and blunt bodies. Technical report, Dept. of Marine Technology / The Norwegian Institute of Technology, Trondheim, Norway.

Stansby, P. K., A. Chegini, and T. C. D. Barnes (1998). The initial stages of a dam-break flow. *J. Fluid Mech. 374*, 407–424.

Storch, R. L. (1978). Alaskan king crab boat casualties. *Marine Technology* (1), 75–83.

Tanizawa, K. (1999). A numerical simulation method of hydroelastic water surface impact based on acceleration potential. In *Proc. FEDSM99, 3rd ASME/JSME Joint Fluids Eng. Conf.*, San Francisco.

Wagner, H. (1932). Uber stoss- und gleitvorgange an der oberflache von flussigkeiten. *ZAMM 12*(4), 192–235.

Wan, D. C. and G. X. Wu (1999). The numerical simulation of the green water effect. In *Proc. 14th Int. Workshop on Water Waves and Floating Bodies*, Michigan.

Wang, Z., J. J. Jensen, and J. Xia (1998). On the effect of green water on deck on the wavebending moment. In *Practical Design if Ships and Mobile Units*.

Welch, S., C. Levi, E. Fontaine, and M. P. Tulin (1999). Experimental study of the ringing response of a vertical cylinder in breaking wave groups. *Int. J. Off. Pol. Eng. 9*(4), 276–282.

Wetzel, J. M. (1958). Ven tilationof bodies piercing a free surface. In *Proc. 2nd Symp. on Naval Hydro d.* National Academy Press.

Yeung, R. W. (1982). Numerical methods in free–surface flows. *Annual review of fluid mechanics* (14), 395–442.

Zhang, S., D. K. P. Yue, and K. Tanizawa (1996). Simulation of plunging wa v e impact on a vertical wall. *J. Fluid Mech. 327*, 221–254.

Zhao, R. and O. M. F altinsen (1993). Water entry of two-dimensional bodies. *J. Fluid Mech. 243*, 593–612.

Zhao, R., O. M. F altinsen, and J. Aarnes (1997). Water en try of arbitrary two-dimensional sections with and without flow separation. In *Pro c. of 21rd Symp. on Naval Hydro d.*, T rondheim,Norwa y .National Academy Press.

Zhou, Z. Q., J. Q. D. Kat, and B. Buchner (1999). A nonlinear 3-d approach to simulate green water dynamics on deck. In Piquet (Ed.), *Pro c. 7th Int. Conf. Num. Ship Hydro d.*, Nantes, F rance,pp. 5.1–1, 15.

Appendix A

Details of the Numerical Method

A.1 Tangential Velocity along the Domain Boundary

In the numerical method the tangential velocity $\partial\varphi/\partial\tau$ along the boundary $\partial\Omega$ is in general determined by using the central finite-difference operator

$$\left.\frac{\partial\varphi}{\partial\tau}\right._j = a_{j-1}\varphi_{j-1} + a_j\varphi_j + a_{j+1}\varphi_{j+1} \,. \tag{A.1}$$

The coefficients a_{j-1}, a_j and a_{j+1} are given by

$$a_{j-1} = -\frac{a^2}{den}\,,\; a_j = \frac{a^2-b^2}{den}\,,\; a_{j+1} = \frac{b^2}{den}\,, \tag{A.2}$$

where

$$a = \tau_{j+1} - \tau_j\,,\; b = \tau_j - \tau_{j-1}\,,\; den = a\,b\,(a+b)\,.$$

They are substituted by

$$a_j = -\frac{2\,a\,b+b^2}{den}\,,\; a_{j+1} = \frac{2\,a\,b+b^2+a^2}{den}\,,\; a_{j+2} = -\frac{a^2}{den}\,, \tag{A.3}$$

with

$$a = \tau_{j+1} - \tau_j\,,\; b = \tau_{j+2} - \tau_{j+1}\,,\; den = a\,b\,(a+b)\,,$$

and, respectively ,by

$$a_j = \frac{2\,a\,b+b^2}{den}\,,\; a_{j-1} = -\frac{2\,a\,b+b^2+a^2}{den}\,,\; a_{j-2} = \frac{a^2}{den}\,, \tag{A.4}$$

with

$$a = \tau_{j+1} - \tau_j\,,\; b = \tau_j - \tau_{j-1}\,,\; den = a\,b\,(a+b)\,,$$

when a forward or backward derivative is needed.

A.2 Velocity Potential and Velocity Components

When both φ and $\frac{\partial\varphi}{\partial n}$ are known along $\partial\Omega$, the velocity potential can be evaluated everywhere inside the domain by using the integral representation (3.3), which in discrete form results

$$2\pi\varphi \simeq \sum_j \left\{ \varphi_{j+1} \frac{I_4 - \xi_j I_2}{\xi_{j+1} - \xi_j} + \varphi_j \frac{I_2 \xi_{j+1} - I_4}{\xi_{j+1} - \xi_j} \right\} - \sum_j \left\{ \psi_{j+1} \frac{I_3 - \xi_j I_1}{\xi_{j+1} - \xi_j} + \psi_j \frac{I_1 \xi_{j+1} - I_3}{\xi_{j+1} - \xi_j} \right\}, \quad \text{(A.5)}$$

where $\psi = \partial\varphi/\partial n$. The terms $I_1, .., I_4$ in equation (A.5) are defined as follows

$$\begin{aligned}
I_1 &:= \int_{\xi_1}^{\xi_2} \ln(\sqrt{x^2+\eta^2})\, dx \\
&= \frac{1}{2}\xi_2 \ln({\xi_2}^2+\eta^2) - \xi_2 + \eta \arctan\left(\frac{\xi_2}{\eta}\right) - \frac{1}{2}\xi_1 \ln({\xi_1}^2+\eta^2) + \xi_1 - \eta \arctan\left(\frac{\xi_1}{\eta}\right) \\
I_2 &:= \int_{\xi_1}^{\xi_2} \frac{\eta}{x^2+\eta^2}\, dx \\
&= \arctan\left(\frac{\xi_2}{\eta}\right) - \arctan\left(\frac{\xi_1}{\eta}\right) \\
I_3 &:= \int_{\xi_1}^{\xi_2} x \ln(\sqrt{x^2+\eta^2})\, dx \\
&= \frac{1}{4}{\xi_2}^2 \ln({\xi_2}^2+\eta^2) + \frac{1}{4}\eta^2 \ln({\xi_2}^2+\eta^2) - \frac{1}{4}{\xi_2}^2 - \frac{1}{4}{\xi_1}^2 \ln({\xi_1}^2+\eta^2) - \frac{1}{4}\eta^2 \ln({\xi_1}^2+\eta^2) + \frac{1}{4}{\xi_1}^2 \\
I_4 &:= \int_{\xi_1}^{\xi_2} \frac{\eta\, x}{x^2+\eta^2}\, dx \\
&= \frac{1}{2}\ln({\xi_2}^2+\eta^2)\,\eta - \frac{1}{2}\ln({\xi_1}^2+\eta^2)\,\eta
\end{aligned}$$

Further, from derivation of φ the velocity is obtained in the form

$$2\pi\nabla\varphi \simeq \sum_j \left\{ \varphi_{j+1} \frac{\vec{I}_8 - \xi_j \vec{I}_6}{\xi_{j+1} - \xi_j} + \varphi_j \frac{\vec{I}_6 \xi_{j+1} - \vec{I}_8}{\xi_{j+1} - \xi_j} \right\} - \sum_j \left\{ \psi_{j+1} \frac{\vec{I}_8 - \xi_j \vec{I}_6}{\xi_{j+1} - \xi_j} + \psi_j \frac{\vec{I}_6 \xi_{j+1} - \vec{I}_8}{\xi_{j+1} - \xi_j} \right\} \quad \text{(A.6)}$$

where $\vec{I}_5, .., \vec{I}_8$ are given by

$$\begin{aligned}
\vec{I}_5 &:= \int_{\xi_1}^{\xi_2} -\frac{\vec{\tau}\, x + \vec{\nu}\, \eta}{x^2+\eta^2}\, dx \\
&= -\frac{1}{2}\vec{\tau} \ln({\xi_2}^2+\eta^2) - \vec{\nu} \arctan\left(\frac{\xi_2}{\eta}\right) + \frac{1}{2}\vec{\tau} \ln({\xi_1}^2+\eta^2) + \vec{\nu} \arctan\left(\frac{\xi_1}{\eta}\right)
\end{aligned}$$

$$\vec{I}_6 := \int_{\xi_1}^{\xi_2} \left[2\,\frac{\eta\,(\vec{\tau}\,x + \vec{\nu}\,\eta)}{(x^2+\eta^2)^2} - \frac{\vec{\nu}}{x^2+\eta^2} \right] dx$$

$$= -\frac{-\xi_2\,\vec{\nu}\,{\xi_1}^2 - \xi_2\,\vec{\nu}\,\eta^2 + \eta\,\vec{\tau}\,{\xi_1}^2 + \xi_1\,\vec{\nu}\,{\xi_2}^2 + \xi_1\,\vec{\nu}\,\eta^2 - \eta\,\vec{\tau}\,{\xi_2}^2}{({\xi_2}^2+\eta^2)\,({\xi_1}^2+\eta^2)}$$

$$\vec{I}_7 := \int_{\xi_1}^{\xi_2} -\frac{x\,(\vec{\tau}\,x + \vec{\nu}\,\eta)}{x^2+\eta^2}\,dx$$

$$= -\vec{\tau}\,\xi_2 - \frac{1}{2}\,\vec{\nu}\,\eta\ln({\xi_2}^2+\eta^2) + \eta\,\vec{\tau}\arctan\left(\frac{\xi_2}{\eta}\right) + \vec{\tau}\,\xi_1 + \frac{1}{2}\,\vec{\nu}\,\eta\ln({\xi_1}^2+\eta^2) - \eta\,\vec{\tau}\arctan\left(\frac{\xi_1}{\eta}\right)$$

$$\vec{I}_8 := \int_{\xi_1}^{\xi_2} \left[2\,\frac{x\,\eta\,(\vec{\tau}\,x + \vec{\nu}\,\eta)}{(x^2+\eta^2)^2} - \frac{x\,\vec{\nu}}{x^2+\eta^2} \right] dx$$

$$= \frac{1}{2}(-2\,\eta\,\vec{\tau}\,\xi_2\,{\xi_1}^2 - 2\,\eta^3\,\vec{\tau}\,\xi_2 - 2\,\vec{\nu}\,\eta^2\,{\xi_1}^2 + 2\,\vec{\tau}\arctan\left(\frac{\xi_2}{\eta}\right)\,{\xi_2}^2\,{\xi_1}^2 + 2\,\vec{\tau}\arctan\left(\frac{\xi_2}{\eta}\right)\,{\xi_2}^2\,\eta^2$$
$$+ 2\,\vec{\tau}\arctan\left(\frac{\xi_2}{\eta}\right)\,\eta^2\,{\xi_1}^2 + 2\,\vec{\tau}\arctan\left(\frac{\xi_2}{\eta}\right)\,\eta^4 - \vec{\nu}\ln(\%2)\,{\xi_2}^2\,{\xi_1}^2 - \vec{\nu}\ln(\%2)\,{\xi_2}^2\,\eta^2$$
$$- \vec{\nu}\ln(\%2)\,\eta^2\,{\xi_1}^2 - \vec{\nu}\ln(\%2)\,\eta^4 + 2\,\eta\,\vec{\tau}\,\xi_1\,{\xi_2}^2 + 2\,\eta^3\,\vec{\tau}\,\xi_1 + 2\,\vec{\nu}\,\eta^2\,{\xi_2}^2$$
$$- 2\,\vec{\tau}\arctan\left(\frac{\xi_1}{\eta}\right)\,{\xi_1}^2\,{\xi_2}^2 - 2\,\vec{\tau}\arctan\left(\frac{\xi_1}{\eta}\right)\,{\xi_1}^2\,\eta^2 - 2\,\vec{\tau}\arctan\left(\frac{\xi_1}{\eta}\right)\,\eta^2\,{\xi_2}^2$$
$$- 2\,\vec{\tau}\arctan\left(\frac{\xi_1}{\eta}\right)\,\eta^4 + \vec{\nu}\ln(\%1)\,{\xi_1}^2\,{\xi_2}^2 + \vec{\nu}\ln(\%1)\,{\xi_1}^2\,\eta^2 + \vec{\nu}\ln(\%1)\,\eta^2\,{\xi_2}^2$$
$$+ \vec{\nu}\ln(\%1)\,\eta^4)/(\%2\,\%1)$$
$$\%1 := {\xi_1}^2 + \eta^2$$
$$\%2 := {\xi_2}^2 + \eta^2$$

A.3 Numerical Features of the Method

In water-on-deck simulations, the free surface is discretized by at least sixty points per wavelength. In the vicinity of the ship and on the deck, where a higher accuracy is required, a local refinement has been introduced with a factor from 5 to 15 times the initial discretization.

Once the local refinement during the simulation is started, the free-surface regridding has been independently made for the outer and the inner zone. In each of these, the regridding was dynamically made when the size of some element became too large or too small relative to the mean size of the free-surface panel.

The computational time and memory space requirements vary according to the specific problem studied. For example, computations reported in chapter 4 to study wave and ship parameter analysis, typically require 20 Mb memory and about 4 hours CPU time on a PC Pentium III 350 MHz.

A.4 Example of Convergence Test

All the numerical solutions presented have been verified for independence of the two main discretization parameters: the number of points per reference length, and the number of steps per reference time. Usually, for water shipping caused by incoming waves, the wavelength and the wave period are reasonable reference quantities to be used. For time discretization, step of the order of 1/50-1/80 the wave period is used as initial time step but this is greatly varied during the wave-body interaction by the dynamic procedure to tune the time step. A similar consideration can be done for the spatial discretization because of the dynamic grid refinement.

Therefore, a systematic grid-independence analysis can be easily performed only for cases without the body. In the following, an example of convergence test is reported. The considered case refers to the experimental set-up discussed in chapters 7 and 8, without the ship model in the wave flume. The motion of the physical wavemaker has been set for waves with $H = 0.16$ m and $\lambda = 2$ m, and the measured flap motion has been used to drive the wavemaker in the numerical simulation. Results are presented in figure A.1 through the evolution of the wave

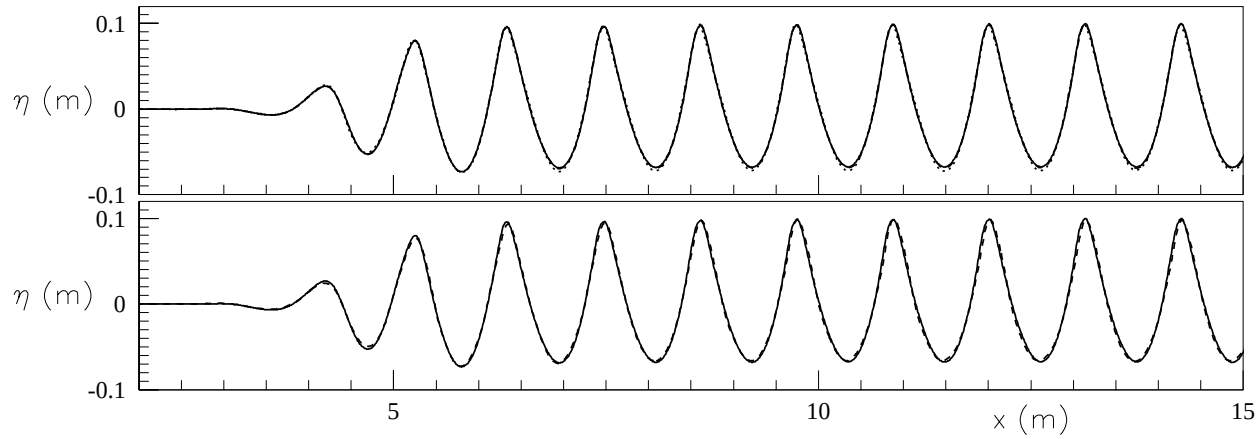

Figure A.1 Example of convergence test. Evolution of the wave elevation at 0.765 m from the wavemaker. Prescribed incoming wave with $H = 0.16$ m and $\lambda = 2$ m. Top: numerical results with 25 (dotted line), 50 (dashed line) and 100 (solid line) points per wavelength. The corresponding time step Δt is 1/32, 1/64 and 1/128 the wave period, respectively. Bottom: numerical results with 100 nodes along one wavelength (solid line) and experimental results (dashed line).

elevation at 0.765 m from the vertical position of the wavemaker. In the top figure, results are superimposed for 25 (dotted line), 50 (dashed line) and 100 (solid line) points per wavelength, and $T/\Delta t = 32, 64, 128$ steps per period T of the incoming wave. From a practical point of view, the results are superimposed. An enlarged view would show small differences around the minima between the coarsest and the most refined grid. No differences are detectable between simulations with 100 nodes and 200 points (not shown) along one wavelength.

In the bottom of the figure the simulation with 100 points per wavelength is compared with the experimental data measured at the same location. The experimental data have been shifted to correct a systematic constant phase delay. This error source in the experiments is discussed in section 7.4. The agreement with the numerical results is satisfactory, though a certain difference in amplitude can be observed from an enlarged view (not shown) at the beginning of the phenomenon.

Appendix B

Boundary Value Problem for ψ

Here the boundary-value problem for the function $\psi(\vec{P},t) = \partial\varphi/\partial t + \vec{V}_P \cdot \nabla\varphi$ is determined. In particular, it is shown that this is formally identical to the problem (3.1) for the velocity potential[1]. This means that: (i) ψ is a harmonic function, (ii) with a Neumann condition along the wetted surface of the ship, and (iii) a Dirichlet condition along the free surface.

ψ is a harmonic function By applying the Laplace operator ∇^2 to the Bernoulli equation (2.4), we have

$$\nabla^2 \underbrace{\left(\frac{\partial\varphi}{\partial t} + \vec{V}_P \cdot \nabla\varphi\right)}_{\psi = D_{BO}\varphi/Dt} - \nabla^2\vec{V}_P \cdot \nabla\varphi + \nabla^2\left(\frac{1}{2} \mid \nabla\varphi \mid^2 + gz + \frac{p}{\rho}\right) = 0 \quad \forall\vec{P} \in \Omega\,.$$

Here the second term gives

$$\nabla^2(V_G \cdot \nabla\varphi + \vec{\omega} \times \vec{GP} \cdot \nabla\varphi) \;=\; V_G \cdot \nabla(\nabla^2\varphi) + \vec{\omega} \times \vec{GP} \cdot \nabla(\nabla^2\varphi) + \vec{\omega} \times \nabla^2\vec{GP} \cdot \nabla\varphi\,,$$

which is zero. By taking the divergence of the Euler equation and by using $\nabla \cdot \vec{u} = 0$ we see that also the third term is zero. Therefore ψ is harmonic.

Free-surface boundary condition By adding and subtracting the term $\vec{V}_P \cdot \nabla\varphi$ to the dynamic free-surface condition

$$\frac{\partial\varphi}{\partial t} + \frac{1}{2} \mid \nabla\varphi \mid^2 + g\eta = 0 \qquad\qquad \forall\vec{P} \in \partial\Omega_{FS}\;, \forall t$$

we obtain

$$\psi \;=\; \vec{V}_P \cdot \nabla\varphi - \frac{1}{2} \mid \nabla\varphi \mid^2 - g\eta\,. \tag{B.1}$$

The right-hand-side of equation (B.1) can be evaluated at each time instant, after the problem for φ has been solved and if the body motion is known. Therefore, (B.1) gives a Dirichlet condition along the free surface for the field of ψ.

[1] See chapters 2 and 3 for the definition of the used symbols.

Body boundary condition First, we note that

$$\frac{\partial \psi}{\partial n} = \frac{\partial}{\partial n}\left(\frac{D_{BO}\,\varphi}{Dt}\right) \equiv \frac{D_{BO}}{Dt}\left(\frac{\partial \varphi}{\partial n}\right) . \tag{B.2}$$

Indeed,

$$\begin{aligned}
\frac{D_{BO}}{Dt}\left(\frac{\partial \varphi}{\partial n}\right) &= \frac{D_{BO}}{Dt}\left(\vec{n}\cdot \nabla\varphi\right) \\
&= \vec{n}\cdot \frac{D_{BO}\nabla\varphi}{Dt} + \frac{D_{BO}\,\vec{n}}{Dt}\cdot\nabla\varphi \\
&= \vec{n}\cdot\left[\frac{\partial \nabla\varphi}{\partial t} + (\vec{V}_P\cdot\nabla)\nabla\varphi\right] + (\vec{\omega}\times\vec{n})\cdot\nabla\varphi\,,
\end{aligned}$$

where the term $(\vec{V}_P\cdot\nabla)\nabla\varphi$ can be rewritten as

$$\begin{aligned}
(\vec{V}_P\cdot\nabla)\nabla\varphi &= \nabla(\vec{V}_P\cdot\nabla\varphi) - (\nabla\varphi\cdot\nabla)\vec{V}_P - \nabla\varphi\times(\nabla\times\vec{V}_P) \\
&= \nabla(\vec{V}_P\cdot\nabla\varphi) - \vec{\omega}\times\nabla\varphi + 2\vec{\omega}\times\nabla\varphi\,,
\end{aligned}$$

thus

$$\begin{aligned}
\frac{D_{BO}}{Dt}\left(\frac{\partial \varphi}{\partial n}\right) &= \vec{n}\cdot\left[\nabla\left(\frac{\partial\varphi}{\partial t}\right) + \nabla(\vec{V}_P\cdot\nabla\varphi) + \vec{\omega}\times\nabla\varphi\right] + (\vec{\omega}\times\vec{n})\cdot\nabla\varphi \\
&= \vec{n}\cdot\nabla\left(\frac{\partial\varphi}{\partial t} + \vec{V}_P\cdot\nabla\varphi\right) + \vec{n}\cdot\vec{\omega}\times\nabla\varphi - \vec{n}\cdot\vec{\omega}\times\nabla\varphi \\
&= \frac{\partial}{\partial n}\left(\frac{D_{BO}\varphi}{Dt}\right) = \frac{\partial\psi}{\partial n}\,.
\end{aligned} \tag{B.3}$$

Second, by using the impermeability condition $\partial\varphi/\partial n = \vec{V}_P\cdot\vec{n} = \vec{n}\cdot(V_G + \vec{\omega}\times\vec{GP})$, we can write the left-hand-side of equation (B.3) as

$$\begin{aligned}
\frac{D_{BO}}{Dt}\left(\frac{\partial \varphi}{\partial n}\right) &= \frac{D_{BO}}{Dt}[\vec{n}\cdot(V_G + \vec{\omega}\times\vec{GP})] \\
&= \frac{D_{BO}\,\vec{n}}{Dt}\cdot(V_G + \vec{\omega}\times\vec{GP}) + \vec{n}\cdot\frac{D_{BO}}{Dt}(V_G + \vec{\omega}\times\vec{GP}) \\
&= \vec{\omega}\times\vec{n}\cdot(V_G + \vec{\omega}\times\vec{GP}) + \vec{n}\cdot\left(\dot{\vec{V}}_G + \frac{D_{BO}\vec{\omega}\times\vec{GP}}{Dt}\right) \\
&= V_G\times\vec{\omega}\cdot\vec{n} + \vec{\omega}\times\vec{GP}\times\vec{\omega}\cdot\vec{n} + \vec{n}\cdot\dot{\vec{V}}_G + \vec{n}\cdot\dot{\vec{\omega}}\times\vec{OP} - \vec{\omega}\times\vec{OP}\times\vec{\omega}\cdot\vec{n}\,.
\end{aligned}$$

Each term can be evaluated at any time instant if the body motion is known, and therefore the equation (B.2) is a Neumann condition along the ship wetted surface[2].

[2] $\dot{\vec{V}}_G$ is the acceleration of G.

Appendix C

Verification and Validation of the Method in Shallow-Water Conditions

In green-water loading studies, one has to cope with the wave-body interaction problem in which waves interact with a floating body, and, if shipping of water occurs, with the development of a free-surface flow along the ship deck. This appendix is devoted to some verification and validation studies relevant to the latter part of the problem.

C.1 Case 1: Collapse of a Semi-Circular Water Column

In the following, the collapse under the action of gravity of a semi-circular body of water is studied. The mass of water is limited by a horizontal rigid and smooth wall, as shown in figure C.1.

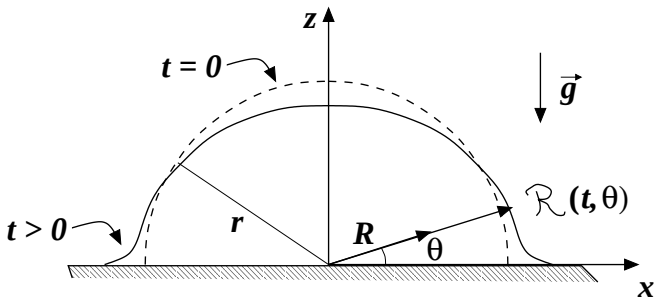

Figure C.1 Gravitational collapse of a semi-circular water column. Sketch of the problem and nomenclature adopted.

Free-surface evolution Within a potential flow model, the bubble evolution at very small times after the collapse can be found analytically. In Penney and Thornhill (1952) this is obtained by using a series of the form

$$\sum_{n=0}^{\infty} \mathcal{A}_{2n} \left(\frac{R}{r}\right)^{2n} \cos 2n\theta \,, \tag{C.1}$$

to describe both the geometrical and the fluid-dynamic variables. The problem is then solved by introducing a small-time expansion of the unknown terms $\mathcal{A}_{2n}$ which are only time dependent. More specifically, the evolution of $\mathcal{A}_{2n}$ can be found (i) by substituting in the problem equations the series expansion, and (ii) by solving for the coefficients in the small-time expansions of $\mathcal{A}_{2n}$. The resulting analytical free-surface evolution for sufficiently small times reads

$$\begin{cases} \mathcal{R}(\theta,t) \;=\; \mathcal{R}(\theta,0) \;-\; \frac{gt^2}{\pi}\left[1 \;+\; \sin\theta \log\tan(\tfrac{1}{4}\pi \;-\; \tfrac{1}{2}\theta)\right] \\ \\ \mathcal{R}(\theta,0) \;=\; const. = r \end{cases} , \tag{C.2}$$

where r is the radius of the initial semi-circular configuration of the bubble. This solution is compared with our numerical results in figure C.2 with satisfactory agreement, and the two

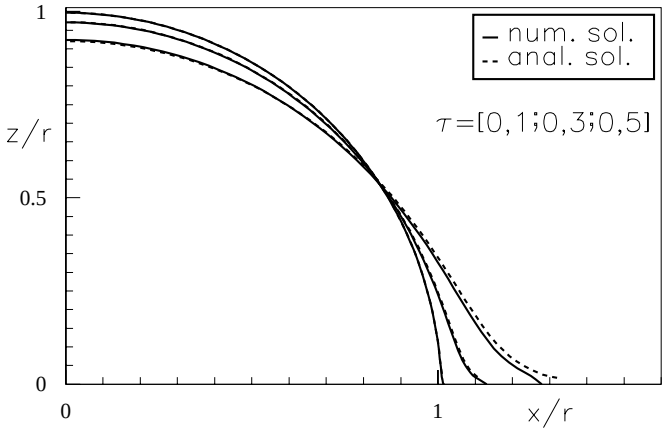

Figure C.2 Evolution of an initially semi-circular water column: numerical results (solid lines) and analytical solution (dashed lines) based on the small-time expansion by Penney and Thornhill (1952).

results start to diverge after the non-dimensional time $\tau = t \cdot \sqrt{g/r} \simeq 0.5$. This is reasonable since the applicability of expression (C.2) decreases as time increases. The numerical evolution of the water bubble on a longer time scale ($\tau = t\sqrt{g/r} \leq 8$) is presented in figure C.3.

Mass and energy conservation On a longer time scale, the small time expansion is no longer applicable and a first test available to verify the fully-nonlinear numerical method is checking mass ($\mathcal{M}$) and energy ($\mathcal{E}$) conservation[1]. These are shown in the table of figure C.3 through the

[1] Mass and energy are given by

$$\mathcal{M} \;=\; \int_\Omega \rho \,\mathrm{d}S \quad \text{and} \quad \mathcal{E} \;=\; \int_\Omega \rho \left(g\,z \;+\; \frac{1}{2}\,|\vec{u}|^2\right) \mathrm{d}S \,, \tag{C.3}$$

respectively. Here ρ is the water density, Ω is the fluid domain and $\vec{u}$ is the fluid velocity.

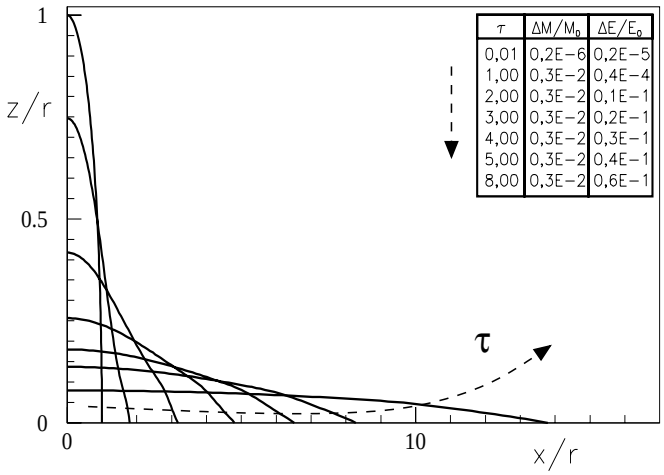

Figure C.3 Evolution of an initially semi-circular water column: free-surface configurations and relative mass and energy errors by the present method. $\mathcal{M}_0$ is the initial mass, $\mathcal{E}_0$ is the initial energy, and $\tau = t \cdot \sqrt{g/h}$ is the non-dimensional time. The plot is not in natural scale.

relative errors

$$\Delta\mathcal{M}/\mathcal{M}_0 = (\mathcal{M} - \mathcal{M}_0)/\mathcal{M}_0 \qquad \Delta\mathcal{E}/\mathcal{E}_0 = (\mathcal{E} - \mathcal{E}_0)/\mathcal{E}_0$$

$\mathcal{M}_0$ and $\mathcal{E}_0$ being the initial mass and energy, respectively. The free-surface configurations shown in the same figure correspond to the time instants reported in the table. The mass error is roughly constant and equal to the 0.3% during the whole presented evolution. The energy error increases with the time, reaching about the 6% for the latest time considered, which corresponds to a rather large deformation of the bubble.

In the attempt to ov ercome the limits inherent in the small-time expansion approach, Penney and Thornhill (1952) solved the problem b y considering a truncated series (C.1) at $N < \infty$, and obtaining numerically the coefficients from the exact boundary v alue problem. The results (Penney) for $N = 4$ are compared with our n umerical results (present) in tables C.1, through the mass and energy ratios for $\tau \leq 1$.

τ	P enney	present
0.0	1.000	1.000
0.2	1.001	0.998
0.4	1.005	0.998
0.6	1.022	0.998
0.8	1.054	0.998
1.0	1.059	0.998

τ	P enney	present
0.0	1.000	1.000
0.2	1.006	1.002
0.4	1.012	0.998
0.6	1.039	1.000
0.8	1.111	1.000
1.0	1.204	1.000

Table C.1 Evolution of an initially semi-circular water column: mass ratio $\mathcal{M}/\mathcal{M}_0$ (left table), and energy ratio $\mathcal{E}/\mathcal{E}_0$ (right table) for increasing value of the non-dimensional time $\tau = t \cdot \sqrt{g/h}$. $\mathcal{M}_0$ and $\mathcal{E}_0$ are the initial mass and energy, respectively.

With this approach, mass and energy are better conserved at the very initial time, and error increases with time more than for the present method, may be indicating the need of a larger number of terms in the truncated series.

Pressure evolution Suddenly after the bubble release, the pressure becomes different than the hydrostatic one. In more detail, for $R = 0$ (see sketch C.1) Penney and Thornhill's numerical solution gives a pressure of $0.622\rho gr$ when $N = 4$ and of $0.628\rho gr$ when $N = 5$, while the present numerical method gives $0.637\rho gr$, which is very close to the analytical solution $(2/\pi)\rho gr \simeq 0.6366\rho gr$ found by Pohle (1950).

The evolution of the pressure distribution along the wall is analyzed in figure C.4, where the numerical pressure at four time instants is given together with the corresponding hydrostatic contribution $\rho g\eta$. The atmospheric pressure is set zero. The evolution shows that, at the

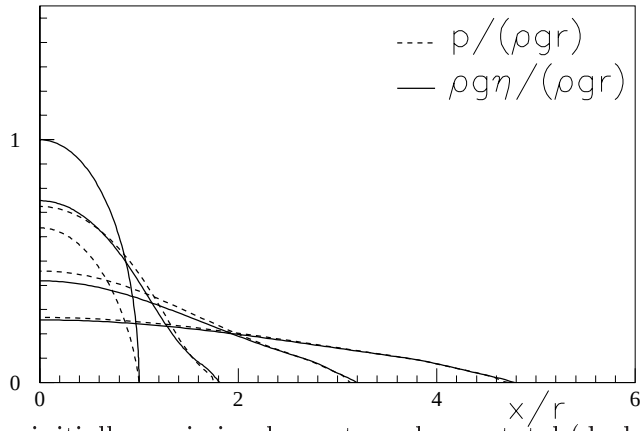

Figure C.4 Evolution of an initially semi-circular water column: total (dashed lines) and hydrostatic (solid lines) pressure distributions at four time instants.

beginning, along the whole wetted wall the pressure is smaller than the hydrostatic contribution. Later on the pressure exceeds this value in some parts of the wall, and then approaches it as the time increases.

C.2 Case 2: Collapse of a Rectangular Water Column

The collapse of a rectangular water column $2L$ long can physically be interpreted as the breaking of a dam delimiting a reservoir of water with length L. In the following this problem is discussed by assuming that, after the breaking, the water invades a dry and smooth region.

In left plot of figure C.5 the evolution of a water column with height h and length $2L = 2h$ is presented. Here, the x-axis is along the horizontal wall and the z-axis is vertically upwards along the axis of symmetry of the water column. To avoid numerical difficulties, in the simulation the upper corner at the dam position has been rounded with a local radius of curvature of $0.065h$. The non-dimensional time of the free-surface configurations shown is given in the table, together with the corresponding relative mass and energy errors, which are fairly conserved. The right plot in the same figure shows the pressure evolution along the horizontal wall. The global behavior is qualitatively similar to that of the circular water column. The gravitational collapse appears now faster, and the tendency of the pressure to reach the hydrostatic pressure is slower.

In figure C.6, our numerical free-surface evolution is compared with results by a field method based on a finite difference scheme, given in Penney and Thornhill (1952). According to the

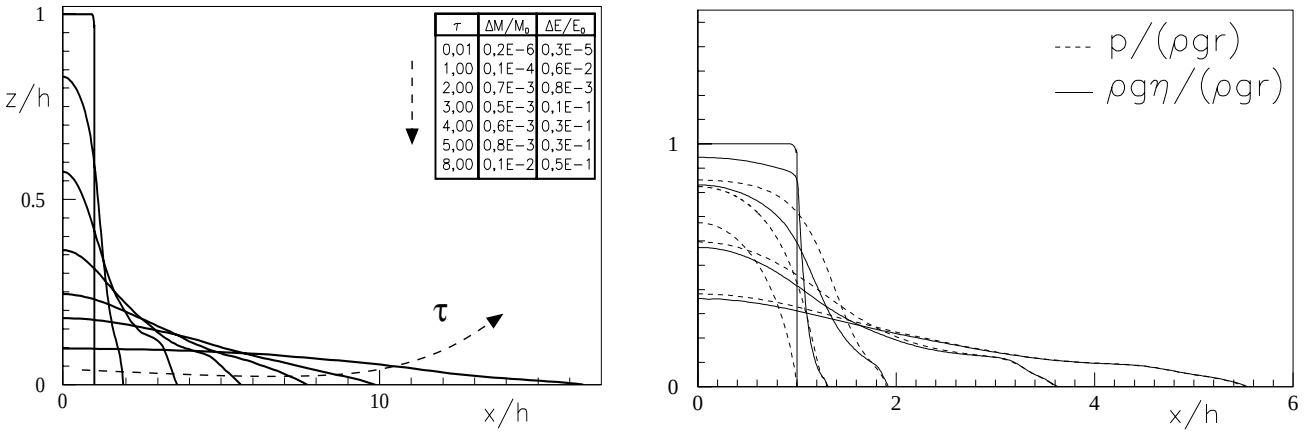

τ	ΔM/M0	ΔE/E0
0,01	0,2E−6	0,3E−5
1,00	0,1E−4	0,6E−2
2,00	0,7E−3	0,8E−3
3,00	0,5E−3	0,1E−1
4,00	0,6E−3	0,3E−1
5,00	0,8E−3	0,3E−1
8,00	0,1E−2	0,5E−1

Figure C.5 Collapse of an initially rectangular water column. Left: snapshots of the free surface by present method. The corresponding time instants are given in the table, together with the relative errors of mass and energy. $\mathcal{M}_0$ is the initial mass, $\mathcal{E}_0$ is the initial energy and $\tau = t \cdot \sqrt{g/h}$. The plot is not in natural scale. Right: total (dashed lines) and hydrostatic (solid lines) pressure distributions at different time instants.

authors, their data agree with experimental results, not shown in the paper. Limiting ourselves to this comparison, it is apparent an initial agreement of the two simulations. Later on the velocity near the wall-free surface contact point becomes faster in the finite difference method, and the predicted water level is higher in a large portion of the domain. Since mass and energy are well conserved by the present method, this suggests that the finite difference scheme does not conserve mass and energy at this stage.

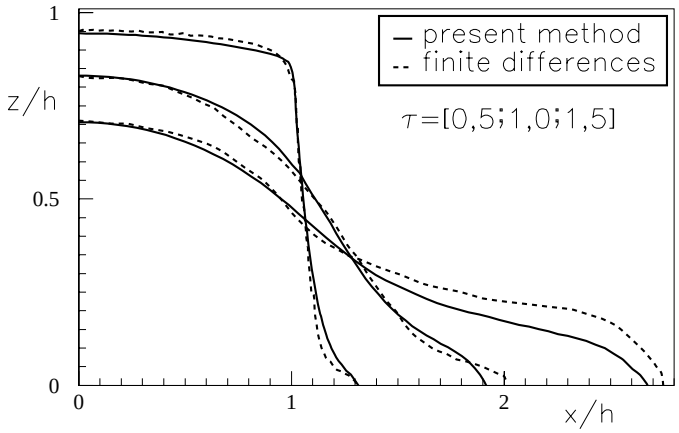

Figure C.6 Collapse of an initially rectangular water column: free-surface configurations at three time instants. Present method (solid lines) and finite difference method (dashed lines) by Penney and Thornhill (1952). The plot is not in natural scale.

C.3 Case 3: Dam Breaking with an Semi-Infinite Water Reservoir

In the following, we consider the breaking of a dam delimiting a reservoir of water with length $L \to \infty$. In particular, Pohle (1950) studied the first stages of the phenomenon by using a small-time expansion method and found for the pressure field immediately after the breaking

$$p^0(x,z) = \rho\, g\,(h - z) - \tfrac{8\rho g h}{\pi^2} \sum_{n=0}^{\infty} \left\{ \frac{1}{(2n+1)^2}\, e^{\frac{+(2n+1)\pi x}{2h}}\, \cos\left(\frac{2n+1}{2h}\right) \pi z \right\}$$

The adopted coordinate system is indicated in sketch C.7, further h represents the initial water height. The pressure along the horizontal wall can be obtained from previous expression by

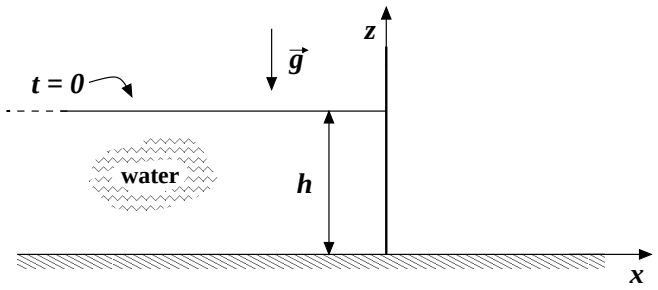

Figure C.7 Dam breaking: sketch of the problem.

setting $z = 0$. This is represented by the triangles in the left plot of figure C.8. In the same plot numerical results for L/h equal to 1, 2 e 3 are shown (solid lines). In the numerical simulations,

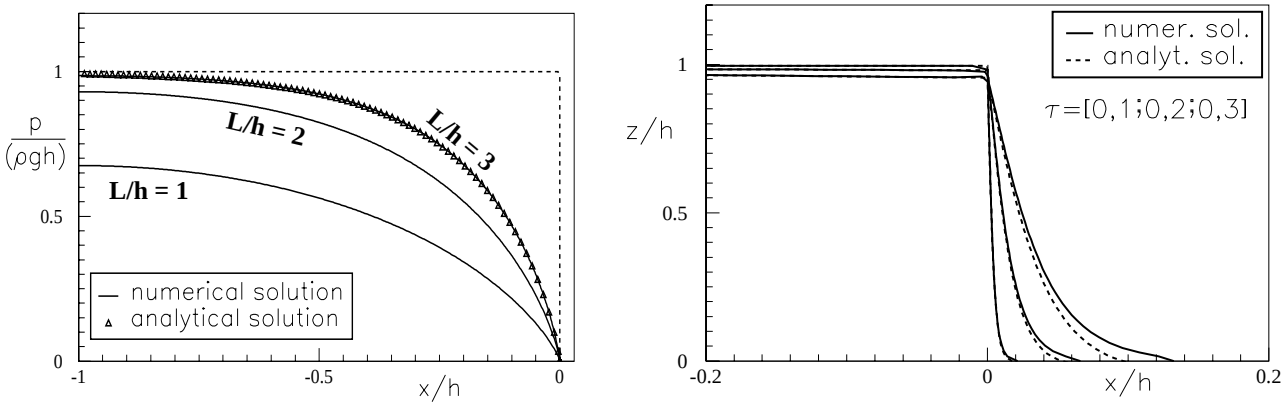

Figure C.8 Dam breaking. Left: analytical pressure distribution along the horizontal wall by Pohle (1950, triangles) and numerical results (solid lines). The dashed line represents the initial free-surface configuration ($\tau = t \cdot \sqrt{g/h} = 0$) used in the numerical simulation. This is characterized by a local radius of curvature of $0.01h$ at the upper corner at the dam position ($x/h = 0$). Right: free-surface configurations obtained by the small-time expansion in Pohle (1950, dashed lines) and by present method (solid lines). In the numerical case $L = 3h$ is used.

the upper sharp corner at the dam position (see dashed curve in the figure) has been rounded

with a radius of curvature of $0.01h$. Results by using $L = 3h$ fit quite well the analytical pressure. This gives both a confidence in the numerical pressure evaluation and shows that the actual value of L is practically ininfluent provided $L/h > 3$, and in the numerical simulation a finite length of the reservoir can be considered, reducing the computational costs. The right plot of the same figure shows the agreement between analytical and numerical ($L/h = 3$) free surfaces at the first stages of the release. Free-surface profiles at larger times after the breaking are given by figure C.9. In the numerical simulation the initial upper corner at the dam position is characterized

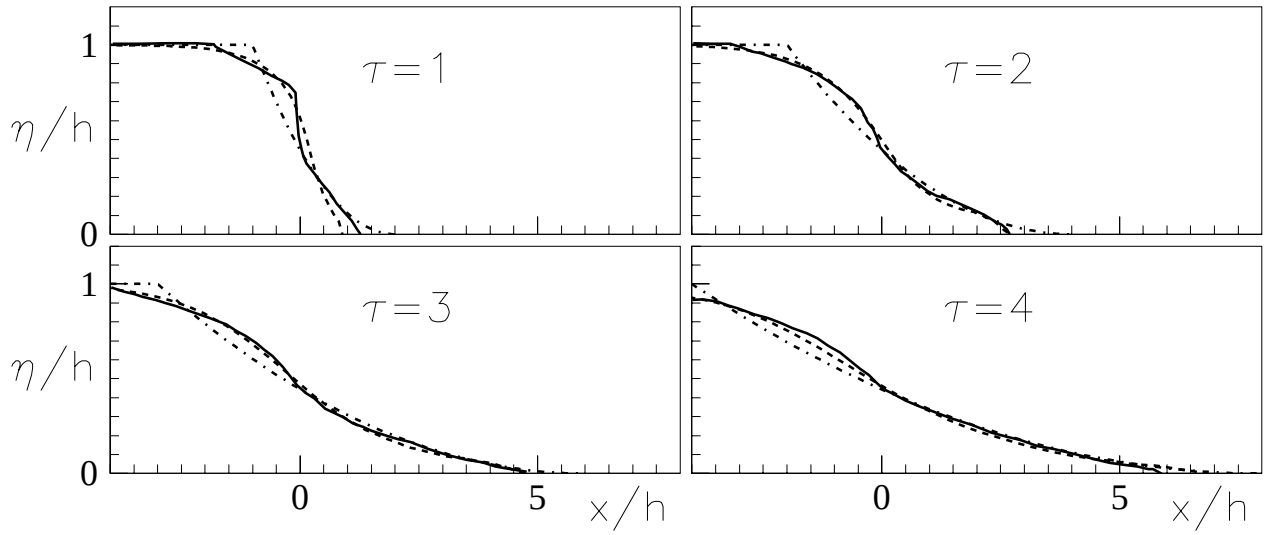

Figure C.9 Water evolution after the dam breaking: experiments by Dressler (1954, solid lines), numerical results (dashed lines) and shallow water results (dashed-dot lines). $\tau = t \cdot \sqrt{g/h}$, where h is the initial height of the water reservoir.

by a radius of curvature of 0.065 h. We verified that the evolution of the free surface for small times after the breaking (not shown) is practically the same as when a radius of 0.01 h is used. In the simulations reported hereafter, we prefer to use the largest radius which allows a simpler handling of the later free-surface evolution because of the smaller initial curvature. In sequence C.9 the numerical solution (dashed lines) is compared with experiments by Dressler (1954, solid lines), with satisfactory agreement during the whole considered time interval. At the beginning of the evolution, dispersive-wave effects matter, while for larger times the evolution can be adequately described by the shallow-water solution by Ritter (1892), also presented in the figure (dashed-dot lines). In the later stages of the evolution, fully-nonlinear "exact" and shallow-water solutions overpredict the experimental wave-front velocity. This may be caused by surface-tension effects during the experiments (*cf.* section 4.2), and the development of turbulent flow influencing the free-surface evolution, as discussed by Dressler (1954). The author observed that this phenomenon appeared later when a smooth bottom (case of the experimental data shown in figure C.9) was used than in the case of a rough surface.

C.4 Case 4: Run-up of Long Waves on a Flat Wall

Experimental data for solitary waves along flat inclined structures are available in literature. The solitary-wave solution can be found analytically (*cf. e.g.* Mei 1983), and elevation and velocity potential have been used in the numerical simulation as initial conditions. The studied problem is shown in sketch C.10: a tank with a vertical wall on the left side and an inclined wall

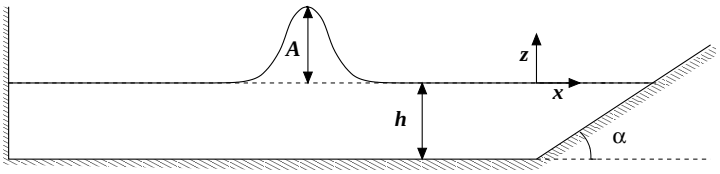

Figure C.10 Run-up of solitary waves on a flat wall: sketch of the problem and nomenclature adopted.

on the right side. The tank, with depth h, is taken sufficiently long so that the no-penetration boundary condition on the left wall will not alter significantly the initial evolution of the solitary wave, which starts closer to that side of the tank.

The run-up of the solitary wave along walls with different inclinations have been studied. As an example, figure C.11 shows the free-surface evolutions for inclinations of $\alpha = 15°$ (left) and $45°$ (right). In both cases, the amplitude of the incident wave is $A = 0.2\ h$, with the crest of the

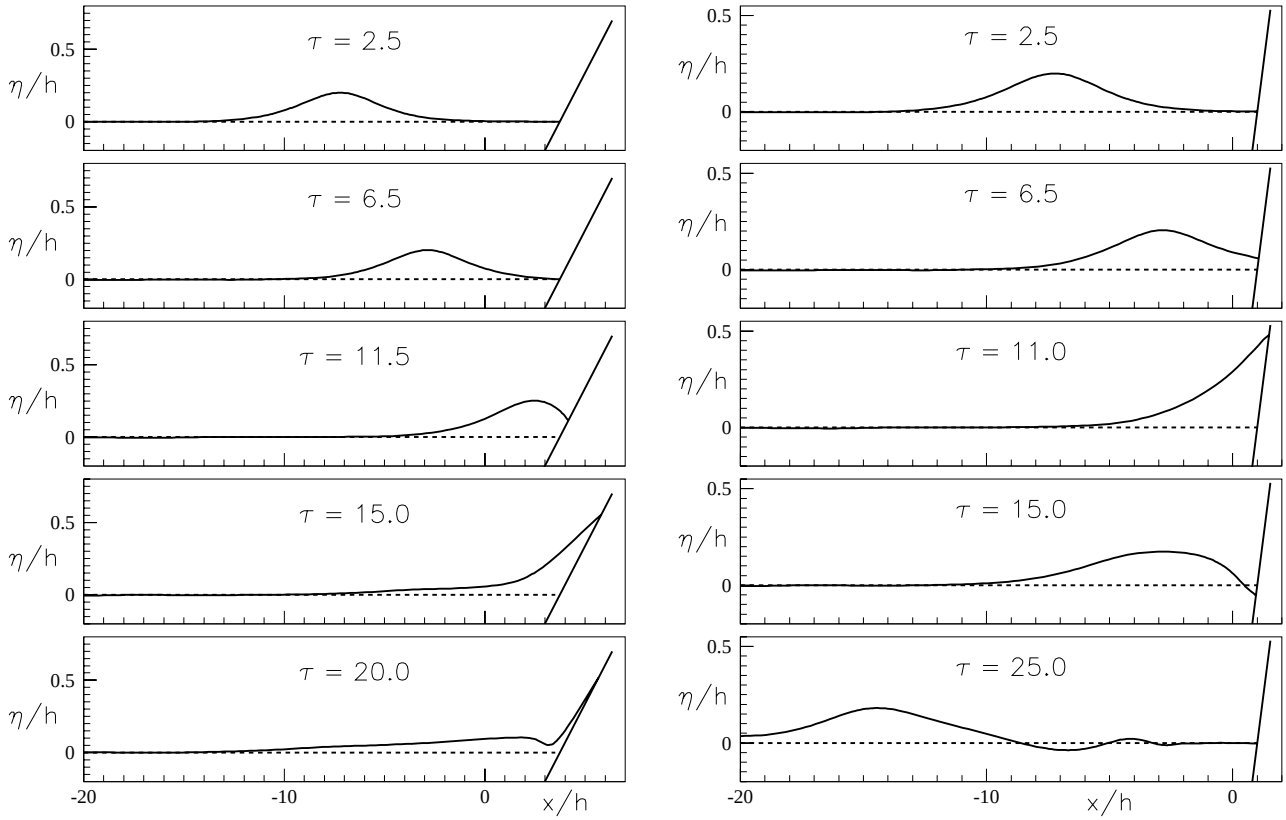

Figure C.11 Run-up of solitary waves ($A = 0.2\ h$) on a flat wall: numerical solution. Left: $\alpha = 15°$. Right: $\alpha = 45°$. The plots are not in natural scale. $\tau = t\sqrt{g/h}$.

solitary wave located initially at a distance 8 h from z-axis (*cf.* the sketch C.10).

To emphasize the free surface profiles, in the plots the vertical scale has been exaggerated. Qualitatively, by keeping constant the ratio A/h, as the wall inclination reduces (smaller α) the water run-up becomes faster and interests a thinner fluid layer. In practice, a wall with a small inclination behaves as a beach reached by the wave. The water depth becomes locally shallower and wave-breaking phenomena can occur. In the presented cases, the incident wave is strongly deformed by the interaction with the wall. This is apparent, for instance, from the sequence on the right where the water conditions near the wall are shown both before and after the run-up. The reflection from the wall destroys the symmetry of the solitary wave and during the water run-down a second crest appears, though very small relative to the primary crest.

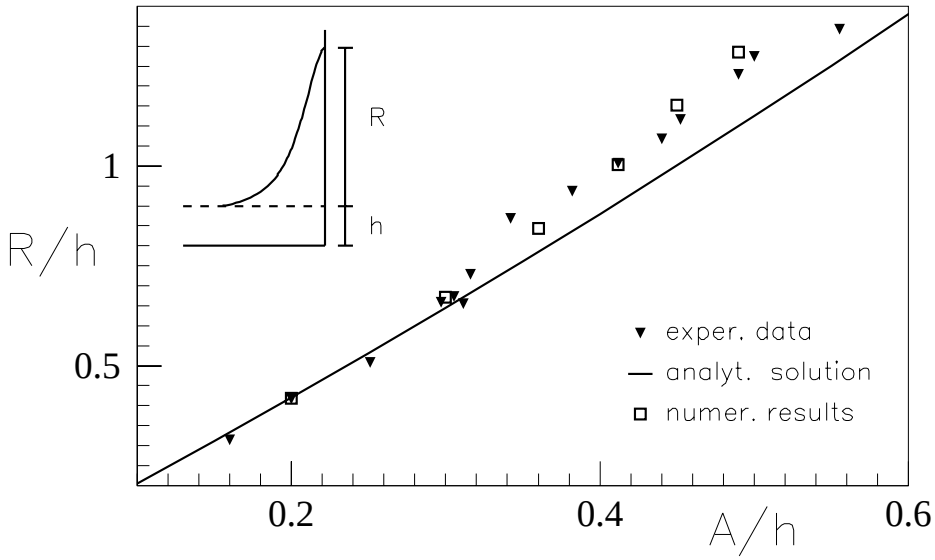

Figure C.12 Run-up of solitary waves on a flat vertical wall ($\alpha = 90°$): maximum run-up. Numerical results (empty squares) are compared with experiments by Camfield and Street (1967, full triangles) and with analytical solution by Byatt-Smith (1971, solid line).

For these cases, the experimental maximum run-up, R, is given by Hall and Watts (1953). In more detail, the maximum run-up is defined as the maximum vertical distance between the still water level and the intersection between wall and free surface, and the best-fit of the measured data read

$$R_{ex} \;=\; 3.75\,A^{1.12} \quad , \quad \text{for} \quad \alpha \;=\; 15^0 \quad \text{and}$$

$$R_{ex} \;=\; 2.15\,A^{0.81} \quad , \quad \text{for} \quad \alpha \;=\; 45^0 \;.$$

If we consider the case $A = 0.2\ h$, we have

$$R_{ex} \;\simeq\; 0.6\,h \quad \text{and} \quad R_{nu} \;\simeq\; 0.7\,h \quad (\alpha \;=\; 15^0)$$

$$R_{ex} \;\simeq\; 0.6\,h \quad \text{and} \quad R_{nu} \;\simeq\; 0.5\,h \quad (\alpha \;=\; 45^0) \;,$$

for the experimental (R_{ex}) and numerical (R_{nu}) solutions, respectively.

We now consider the case of a vertical wall ($\alpha = 90°$). The maximum run-up is given in figure C.12 as a function of A/h. Here, numerical results are compared with experiments by Camfield and Street (1967) and with the weakly-nonlinear analytical solution

$$\frac{R}{h} = 2\frac{A}{h} + \frac{1}{2}\left(\frac{A}{h}\right)^2$$

obtained by Byatt-Smith (1971), with an error $\mathcal{O}[(A/h)^3]$. For (initial) wave amplitude-to-depth ratio A/h sufficiently small all the results are in a reasonable agreement, while for larger amplitudes only the numerical results follow the experiments.

For the same geometry the pressure evolution along the vertical wall is shown in figure C.13 for $A/h = 0.36$, where, as can be expected, the resulting pressure deviates from the hydrostatic pressure.

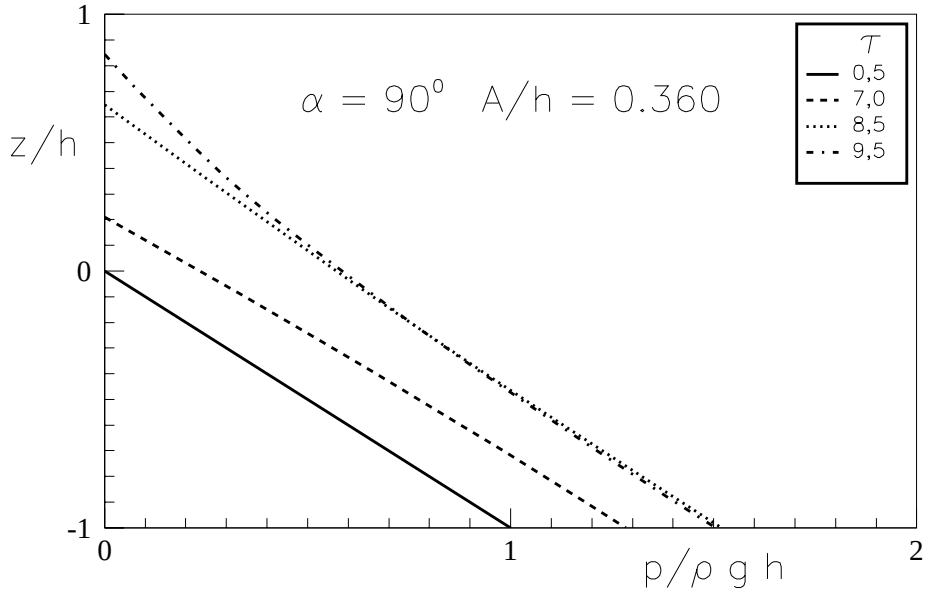

Figure C.13 Run-up of solitary waves on a flat vertical wall ($\alpha = 90°$): pressure along the wall for a solitary wave with $A/h = 0.36$ ($\tau = t \cdot \sqrt{g/h}$).

Appendix D

Liquid Wedge-Flat Wall Impact: Similarity Solution

The similarity solution of a liquid wedge impacting nonsymmetrically a flat wall is discussed here. The problem of interest is sketc hed in figure D.1, where a wedge of water hits at $t = t_{\text{imp}}$ a straight horizontal wall with velocity $(U, -V)$, U and V being positive quantities. The procedure here described follo wsthe one presented in Zhang *et al.* (1996) for the case with $U = 0$. The wedge has an angle 2β and an inclination γ from the z-axis. Both the gravity and the fluid

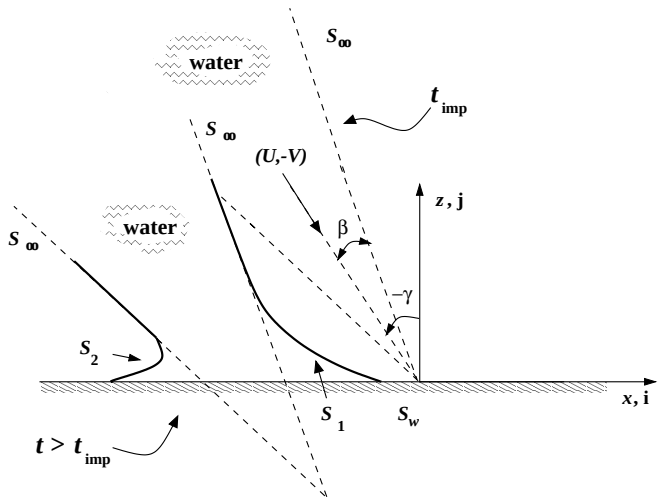

Figure D.1 Impact of a liquid wedge against a flat wall: sk etc h of the problem and adopted nomenclature.

viscosity are neglected, and the problem is solved in terms of the velocity potential φ due to the

impact. The related boundary value problem is in the form

$$\begin{cases} \nabla^2\varphi(x,z,t) \;=\; 0 & \forall \vec{P} \in \Omega \\ \nabla\varphi \;=\; U\vec{i} - V\vec{j} & \text{on } S_\infty \\ \frac{\partial\varphi}{\partial z} \;=\; 0 & \text{on } z \;=\; 0 \\ \dfrac{\partial\varphi}{\partial x} \;=\; \dfrac{\partial S_i}{\partial t} + \dfrac{\partial\varphi}{\partial z}\dfrac{\partial S_i}{\partial z} & \text{on } x \;=\; S_i(z,t) \\ \dfrac{\partial\varphi}{\partial t} + \dfrac{1}{2}\left[\left(\dfrac{\partial\varphi}{\partial x}\right)^2 + \left(\dfrac{\partial\varphi}{\partial z}\right)^2\right] \;=\; 0 & \text{on } x \;=\; S_i(z,t) \end{cases} \tag{D.1}$$

where the symbols are defined in sketch D.1. Once the non-dimensional variables

$$\xi = \frac{x}{Vt}\,,\ \eta = \frac{z}{Vt}\,,\ \Phi = \frac{\varphi}{V^2 t}\,,\ \zeta_i = \frac{S_i}{Vt}\,,\ (i = 1,\,2)$$

are introduced, the problem can be rewritten as

$$\begin{cases} \nabla^2\Phi(\xi,\eta) \;=\; 0 & \forall \vec{P} \in \Omega \\ \nabla\Phi \;=\; \frac{U}{V}\vec{i} - \vec{j} & \text{as } \eta \to \infty \\ \dfrac{\partial\Phi}{\partial\eta} \;=\; 0 & \text{on } \eta \;=\; 0 \\ \dfrac{\partial\Phi}{\partial\xi} \;=\; \zeta_i - \eta\dfrac{d\zeta_i}{d\eta} + \dfrac{\partial\Phi}{\partial\eta}\dfrac{d\zeta_i}{d\eta} & \text{on } \xi \;=\; \zeta_i(\eta) \quad (A) \\ \Phi - \xi\dfrac{\partial\Phi}{\partial\xi} - \eta\dfrac{\partial\Phi}{\partial\eta} + \dfrac{1}{2}\left[\left(\dfrac{\partial\Phi}{\partial\xi}\right)^2 + \left(\dfrac{\partial\Phi}{\partial\eta}\right)^2\right] \;=\; 0 & \text{on } \xi \;=\; \zeta_i(\eta) \quad (B) \end{cases} \tag{D.2}$$

In this way the free-surface velocity components

$$u_i(\eta) \;=\; \left.\frac{\partial\Phi}{\partial\xi}\right|_{\xi=\zeta_i(\eta)} \qquad \text{and} \qquad v_i(\eta) \;=\; \left.\frac{\partial\Phi}{\partial\eta}\right|_{\xi=\zeta_i(\eta)}$$

remain associated with the equations

$$u_i \;=\; \zeta_i \;+\; (v_i - \eta)\,\frac{d\zeta_i}{d\eta} \tag{D.3}$$

and

$$\frac{dv_i}{d\eta} \;=\; \frac{(\eta - v_i)\,\dfrac{d\zeta_i}{d\eta}\,\dfrac{d^2\zeta_i}{d\eta^2}}{1 + \left(\dfrac{d\zeta_i}{d\eta}\right)^2}\,, \tag{D.4}$$

respectively . The former is simply equation (D.2.A). The latter is obtained by differentiating equation (D.2.B) with respect to η and by eliminating u_i through equation (D.3). This means that the problem can be solved once $\zeta_i(\eta)$ is known.

At this stage, we assume that the solution is self-similar, and the problem (D.2) becomes function of the variable η. Further, we assume the relation

$$\zeta_i \;=\; a_i \;+\; \eta\, b_i \;+\; d_i\, e^{-c_i\,\eta} \tag{D.5}$$

between η and ζ_i (i=1, 2), as done in the work by Zhang *et al.* (1996). In (D.5), as $\eta \to \infty$, only the linear contribution remains, implying that the free surface is wedge shaped far from the wall. Close to the wall an exponential behavior is assumed. The unknown coefficients a_i-d_i can be determined so that problem (D.2) is satisfied. In particular, the asymptotic condition permits to determine a_i and b_i as follows

$$\zeta_i \;\to\; (\eta \,+\, 1)\, \tan(\alpha_i) \,\pm\, \frac{Ut}{Vt} \quad \text{as} \quad \eta \to \infty \qquad \Rightarrow \qquad \begin{cases} a_i \;=\; \tan(\alpha_i) \\ \\ b_i \;=\; \tan(\alpha_i) \pm \frac{U}{V} \end{cases} \qquad (\alpha_i = \gamma \pm \beta)$$

By introducing the expression of ζ_i in (D.4), we can solve analytically the ordinary differential equation for v_i. This yields an integration coefficient C_0 also to be found. The five unknowns c_i, d_i and C_0 are determined by enforcing the conditions

$$v_i|_{\eta=0} = 0 \quad \text{(a)} \qquad\qquad v_i|_{\eta\to\infty} = -1 \quad \text{(b)}$$

and by requiring the conservation of fluid mass and of fluid momentum in the ξ-direction during the impact (see sketch D.2). By combining conditions (a) and (b), C_0 can be eliminated from

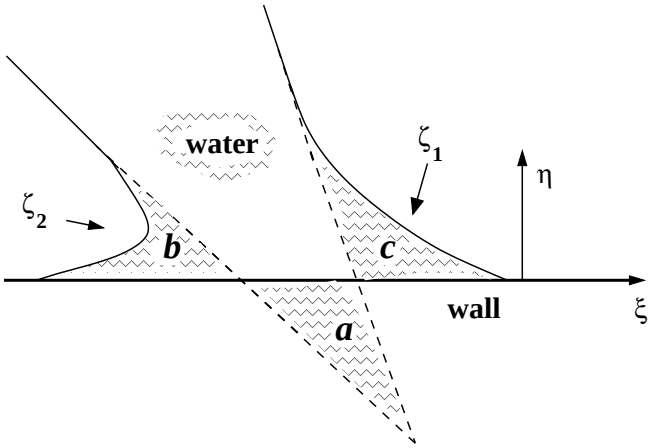

Figure D.2 Impact of a liquid wedge against a flat wall. For the mass conservation: $\text{mass}_a = \text{mass}_b + \text{mass}_c$. For the fluid momentum conservation in the ξ-direction: $\text{mom}_{\xi a} = \text{mom}_{\xi b} + \text{mom}_{\xi c}$. Non-dimensional variables are used.

the first-step unknowns, then the equations for c_i, d_i become

$$
\begin{aligned}
1-2: \quad & \frac{1}{c_i}\left(1-\frac{\lambda_i}{h_i}\right) - \frac{\lambda_i}{h_i} + \frac{a_i\, e_i}{c_i\, h_i} \ln \frac{\lambda_i - a_i\, e_i}{h_i - a_i\, e_i + c_i\, d_i\, e_i} + \frac{\lambda_i}{c_i\, h_i} \ln 4\,\lambda_i^2 \\
& - \frac{\lambda_i}{c_i\, h_i} \ln 2\,[\lambda_i\, h_i + a_i\,(a_i - c_i\, d_i) + 1] = 0 \qquad (i = 1, 2) \\
3: \quad & \frac{d_1}{c_1} - \frac{d_2}{c_2} - \frac{1}{2}(a_1 - a_2) = 0 \\
4: \quad & \frac{3}{4}\left(\frac{d_1^2}{c_1} - \frac{d_2^2}{c_2}\right) + \frac{3\, a_1\, d_1}{c_1}\left(\frac{1}{c_1} + 1\right) - \frac{3\, a_2\, d_2}{c_2}\left(\frac{1}{c_2} + 1\right) - \frac{1}{2}(a_1^2 - a_2^2)
\end{aligned}
\tag{D.6}
$$

where $e_i = d_i/|d_i|$, $h_i = \sqrt{1 + (a_i - c_i\, d_i)^2}$ and $\lambda_i = \sqrt{1 + a_i^2}$. Equations (D.6.1-2) do not coincide exactly with the corresponding relations in Zhang *et al.* (1996), which do not satisfy the asymptotic conditions of the problem, probably because of misprints. The solution of equations (D.6) requires an iterative procedure, and in this work a Newton-Raphson algorithm has been applied.

To evaluate the pressure distribution along the wall, the velocity potential along the structure is needed and a specific boundary value problem is solved, with boundary data obtained from the similarity solution discussed above (Φ and its normal derivative along the free surface, and the no-penetration boundary condition on the wall). Once Φ on the wall is known, the pressure can be evaluated from the Bernoulli equation

$$
\frac{p}{\rho\, V^2} = -\left\{ \Phi - \eta \frac{\partial \Phi}{\partial \eta} - \xi \frac{\partial \Phi}{\partial \xi} + \frac{1}{2}\left[\left(\frac{\partial \Phi}{\partial \xi}\right)^2 + \left(\frac{\partial \Phi}{\partial \eta}\right)^2 \right] \right\}. \tag{D.7}
$$

Appendix E

Simplified Method for Water-Wedge Impacts

A simplified solution of the problem of a water half-wedge hitting a flat wall at 90 degrees is derived here. Some verifications of the method have been presented in section 5.2.1 through comparison with a similarity solution.

The problem of interest is sketched in figure E.1 where β is the half-wedge angle and V is the fluid impact velocity. The potential flow theory is used and the gravity effects are neglected

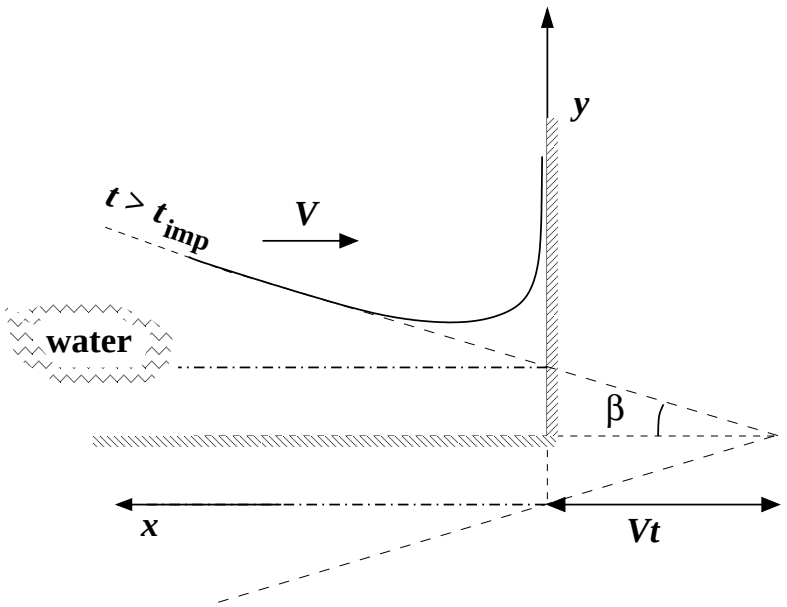

Figure E.1 Sketch of the problem of interest.

by assuming sufficiently large fluid accelerations during the impact. On the free surface (the half-wedge profile) the common "slamming" condition $\varphi = 0$ is enforced, φ being the velocity

potential caused by the impact. This boundary condition expresses the flow deviation of 90° at the wall. Both the "deck" (horizontal wall) and the impacted wall are taken rigid. Finally, the half-wedge angle is assumed asymptotically small. With these assumptions, the boundary value problem for φ is solved at each time instant t after the impact ($t = t_{\text{imp}}$). The influence of the deck is modeled by imposing the symmetry about the axis along it and studying the equivalent problem of a fluid wedge with angle 2β hitting the wall. Within the assumption of an asymptotically small β, the free surface condition is transfered along the horizontal lines at $y = 0$ and $y = 2Vt\,\tan\beta$ (dash-dotted lines in the sketch E.1). The resulting boundary value problem is shown in the top plot of figure E.2, where $a = 2Vt\,\tan\beta$ and z is the complex variable $x + \mathrm{i}y$. The body boundary condition is $\frac{\partial\varphi}{\partial x} = V$ on $x = 0$ between $y = 0$ and $2Vt\,\tan\beta$. A

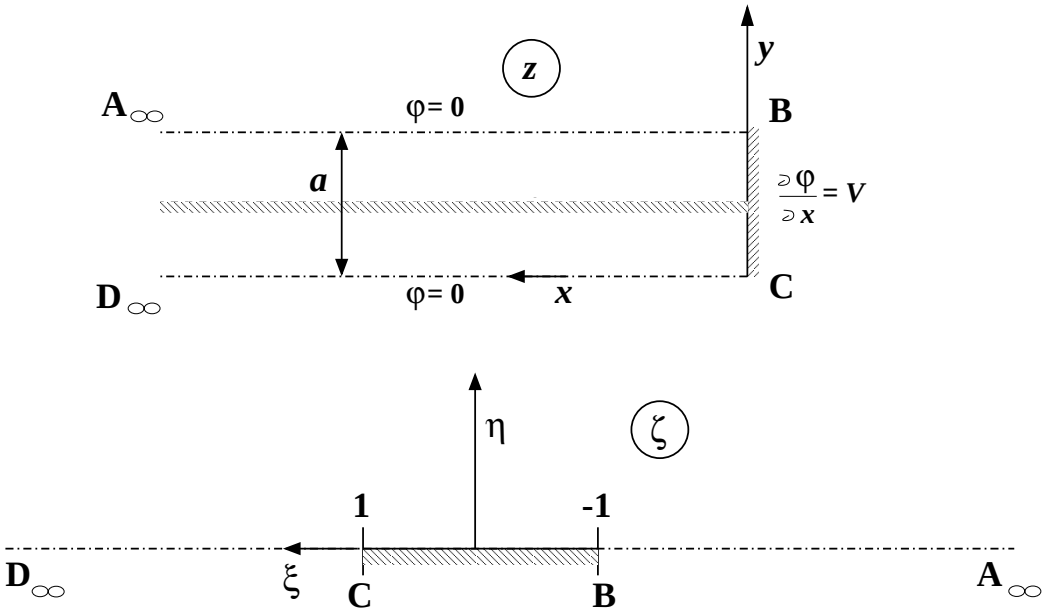

Figure E.2 Conformal mapping used in the asymptotic solution for small β.

solution can be found by conformal mapping (*cf.* Milne-Thomson 1967) between the physical plane z and an auxiliary complex ζ-plane ($\zeta = \xi + \mathrm{i}\eta$) by the transformation $\zeta = \cosh\frac{\pi z}{a}$. The complex velocity $dw/dz = u - iv$ in the physical plane is related to the corresponding velocity in the auxiliary plane by

$$\frac{d\,w}{d\,\zeta} = \overline{u} - i\,\overline{v} = \frac{d\,w}{d\,z}\,\frac{d\,z}{d\,\zeta}\,. \tag{E.1}$$

By using this relationship, the boundary conditions

$$\begin{cases} \overline{v} = \dfrac{V\,a}{\pi\sqrt{1-\zeta^2}} & \text{along BC} \\ \overline{u} = 0 & \text{along } \mathrm{A}_\infty\ ,\ \mathrm{B}_\infty \end{cases} \tag{E.2}$$

are obtained in the ζ-plane. This means that the solution can be found by a distribution of

vortices on $\eta = 0$ between $\xi = -1$ and 1 (*cf.* Newman 1977) with strength

$$\overline{\gamma}(\xi) \;=\; \frac{2}{\pi}\,\frac{1}{\sqrt{1\,-\,\xi^2}}\,\fint_{-1}^{1}\,\frac{V\,a}{\pi\,\sqrt{1\,-\,\xi_1^2}}\,\frac{\sqrt{1\,-\,\xi_1^2}}{\xi_1\,-\,\xi}\,\mathrm{d}\xi_1\,. \tag{E.3}$$

This integral equation[1] can be analytically solved and yields

$$\overline{u} \;=\; -\,\frac{\overline{\gamma}}{2} \;=\; -\,\frac{2\,V\,a}{\pi^2\,\sqrt{1\,-\,\xi^2}}\,\ln\left\{\tan\frac{\pi\,y}{2\,a}\right\}\,,$$

for the velocity component in ξ direction. By transforming back to the physical plane we find the complex fluid velocity. In particular, the vertical velocity on the wall is $v = \frac{2V}{\pi}\ln(\tan\frac{\pi y}{2a})$. This suggests a uniformly valid solution on the form

$$\frac{d\,w}{d\,z} \;=\; -\,\frac{2\,V}{\pi}\,\log\left\{\tanh\frac{\pi\,z}{2\,a}\right\}\,, \tag{E.4}$$

where $\log f(z) \;=\; \ln|f(z)| \;+\; \mathrm{i}\arg[f(z)]$. The total pressure on the wall is then obtained by Bernoulli equation

$$p \;=-\rho\left\{\frac{\partial\varphi}{\partial t}+\frac{1}{2}\left[(-\,V\,+\,u)^2\,+\,v^2\,+\,V^2\right]\right\}_{x=0} \tag{E.5}$$

and by using $\varphi \;=\; -\int_y^a v\mathrm{d}y_1$. We must note that equation (E.5) is not consistent with the used free surface condition, where the velocity component v is singular. The maximum pressure occurring at $y = a$ is on the form (triangles in figure 5.11)

$$\frac{p|_{y=a}}{\rho\,V^2} \;=\; \frac{8\,\tan\beta}{\pi^2}\,\int_{\pi/4}^{\pi/2}\,\ln(\tan\underbrace{l}_{l\,=\,\frac{\pi\,y_1}{2\,a}})\mathrm{d}l\,+\,\frac{1}{2}\,.$$

By introducing solution (E.4) in the kinematic free surface condition $\partial\eta/\partial t = \partial\varphi/\partial z$ and by integrating the latter, the free surface elevation (dashed lines in figure 5.10) can be obtained as

$$\eta \;=\; \underbrace{(x\,+\,Vt)\,\tan\beta}_{\eta|_{t=t_{\mathrm{imp}}}}\,-\,\int_{t_{\mathrm{imp}}}^{t}\,\frac{2V}{\pi}\ln\left(\tanh\frac{\pi x}{2a}\right)\,\mathrm{d}t\,. \tag{E.6}$$

The expression for the pressure is logarithmically singular at $y = a$ (and $y = 0$). The same is true for η at $x = 0$. This is a consequence of that the body boundary condition, $\partial\varphi/\partial x = V$, is not consistent with the boundary condition $\varphi = 0$ on $y = a$ (and $y = 0$). The latter implies zero horizontal velocity at B (and C).

[1] Symbol $\fint$ in equation (E.3) indicates a principal value integral.

Appendix F

Simplified Problem to Evaluate the Added Masses

In the following the solution of the simplified problem B discussed in section 5.2.3 is presented. The definition of the used symbols is given in that section and is not repeated here.

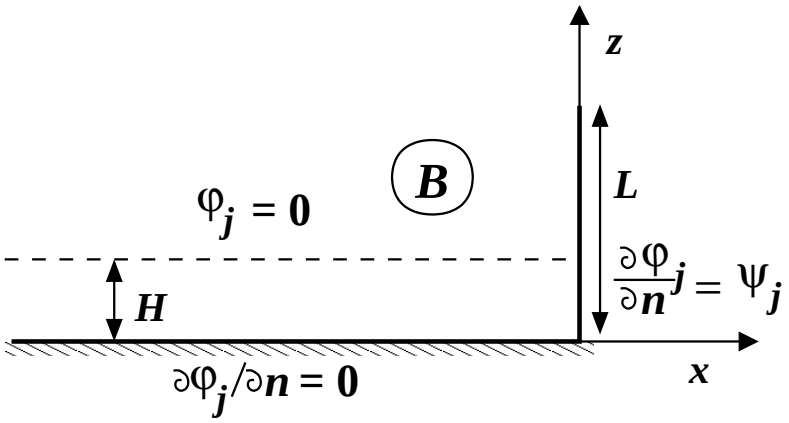

Figure F.1 Sketch of the problem of interest.

It can be shown that the solution of the problem of interest (see sk etc hF.1) can formally be written as

$$\varphi_j(x,z) \;=\; \sum_{n=0}^{\infty} a_{jn} \sin\left[\frac{2n+1}{2H}\,\pi\,(z\;-\;H)\right] e^{\frac{2n+1}{2H}\,\pi\,x}\,. \tag{F.1}$$

This expression satisfies the free surface condition, the bottom condition and the asymptotic condition for $x \to -\infty$. The value of the unknown coefficients a_{jn} is thus obtained by enforcing the impermeability condition along the wetted portion (H) of the beam. In particular, the normal velocity component along the beam, $\psi_j \;=\; a\,\sin p_j z \;+\; b\,\cos p_j z \;+\; c\,\sinh p_j z \;+\; d\,\cosh p_j z$, is

here described as series of the independent functions $\sin[\frac{2n+1}{2H}\pi\,(z\,-\,H)]$. The coefficients v_{jn} of this series are expressed by

$$v_{jn}\;=\;\frac{\int_0^H\;\psi_j(z)\;\sin\,\frac{2n+1}{2H}\pi\,(z\,-\,H)]\,dz}{\int_0^H\,\sin[\frac{2n+1}{2H}\pi\,(z\,-\,H)]\,dz}$$

and can be analytically evaluated. By imposing then the impermeability condition $\partial\varphi_j/\partial n\;=\;\psi_j$, the unknowns a_{jn} can be easily obtained as

$$a_{jn}\;=\;v_{jn}\,\frac{2H}{(2n+1)\,\pi}\,.$$

Once φ_j is known, the added mass terms,

$$A_{jn}\;=\;\int_0^H\;\psi_j(z)\,\varphi_n(0,z)\,dz\,, \tag{F.2}$$

can also be analytically calculated.

To estimate the distance x^* from where the fluid is not affected by the beam (*cf.* section 5.2.3), the boundary value problem is modified by introducing a rigid vertical wall at a distance x from the beam. The solution can be found also in this case by using the same procedure as discussed above. In particular, the added mass terms can be calculated. By progressively increasing x, we can find the distance x^* as the smallest x from where onthe actual position of the wall is not important for the terms A_{jn}.

Appendix G

Wavemaker: Experimental Time Histories

Figures G.1–G.3 show typical recorded time histories of the measured wavemaker motion in terms of the oscillation angle α. The latter is positive for a rotation towards the wave flume. The basic ship model (case a of figure 7.2) was used in the shown tests. The prescribed incoming waves are indicated in the captions. A ramp function of 2 seconds was used at the beginning of the motion. Figure G.4 shows the typical recorded time histories of the wavemaker motion when the basic model, and the two alternative bow geometries (case b and c of figure 7.2) are considered. The prescribed incoming waves are 2 m long and with a 0.16 m crest-to-trough height. The different wave reflection from the ship model when varying the bow geometry is not evident looking at the evolution of α.

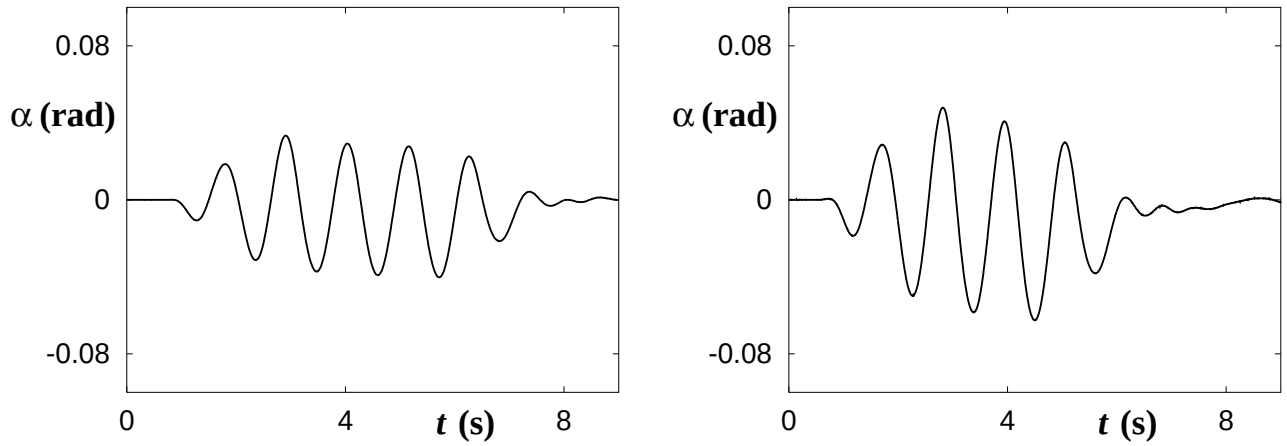

Figure G.1 Wavemaker motion: angle of oscillation. Nominal incoming waves with $\lambda = 2$ m and $H = 0.08$ m (left) and with $\lambda = 2$ m and $H = 0.12$ m (right).

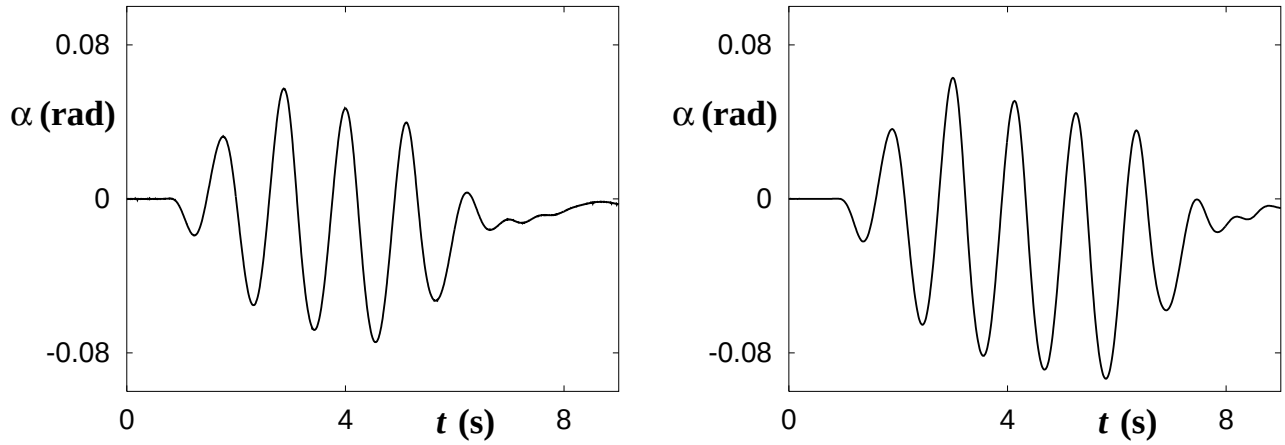

Figure G.2 Wavemaker motion: angle of oscillation. Nominal incoming waves with $\lambda = 2$ m and $H = 0.14$ m (left) and with $\lambda = 2$ m and $H = 0.16$ m (right).

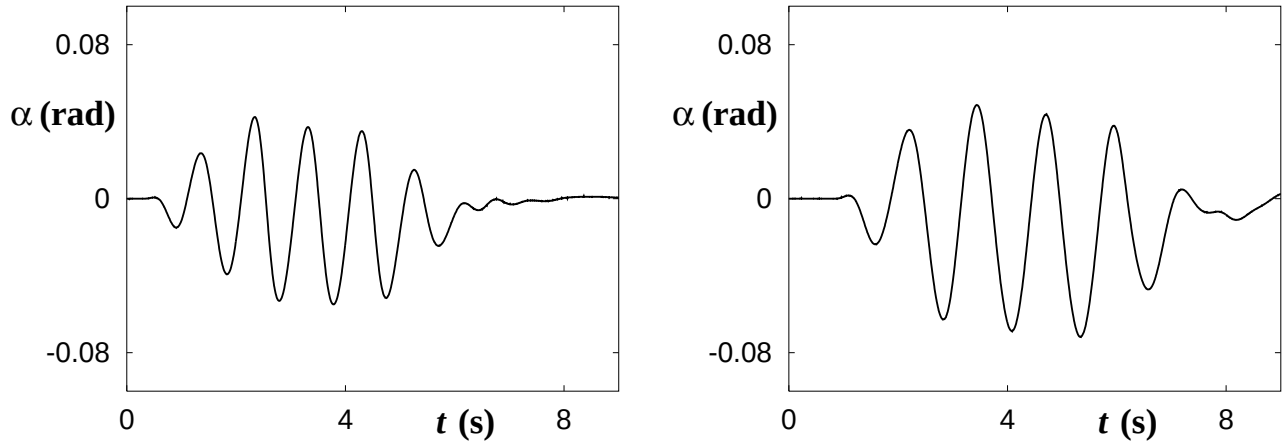

Figure G.3 Wavemaker motion: angle of oscillation. Nominal incoming waves with $\lambda = 1.5$ m and $H = 0.12$ m (left) and with $\lambda = 2.5$ m and $H = 0.12$ m (right).

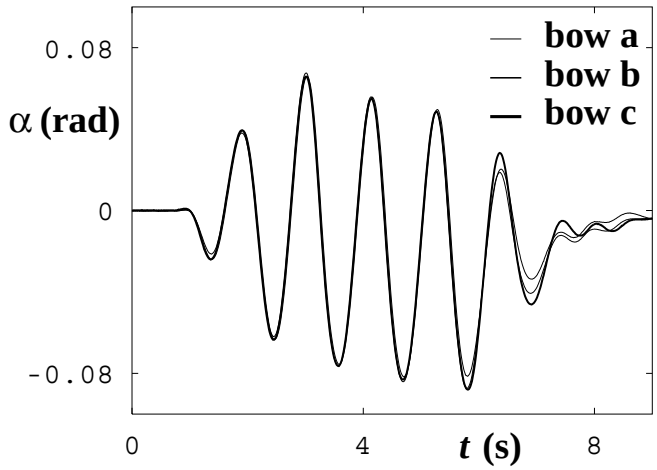

Figure G.4 Wavemaker motion: angle of oscillation in the case of vertical bow (case a), bow inclined at 45 degrees (case b) and bow inclined at -45 degrees (case c). Nominal incoming waves with $\lambda = 2$ m and $H = 0.16$ m.